



NASA Technical Memorandum 4737

Second United States Microgravity Payload: One Year Report

P.A. Curreri, Editor
Marshall Space Flight Center • MSFC, Alabama

D.E. McCauley, Editor
University of Alabama • Huntsville, Alabama

National Aeronautics and Space Administration
Marshall Space Flight Center • MSFC, Alabama 35812

April 1996

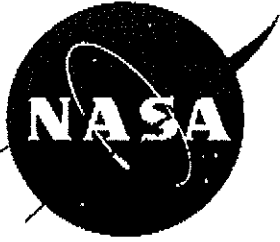
Handwritten scribbles

NASA Technical Memorandum 4737

REDSTONE SCIENTIFIC INFORMATION CENTER



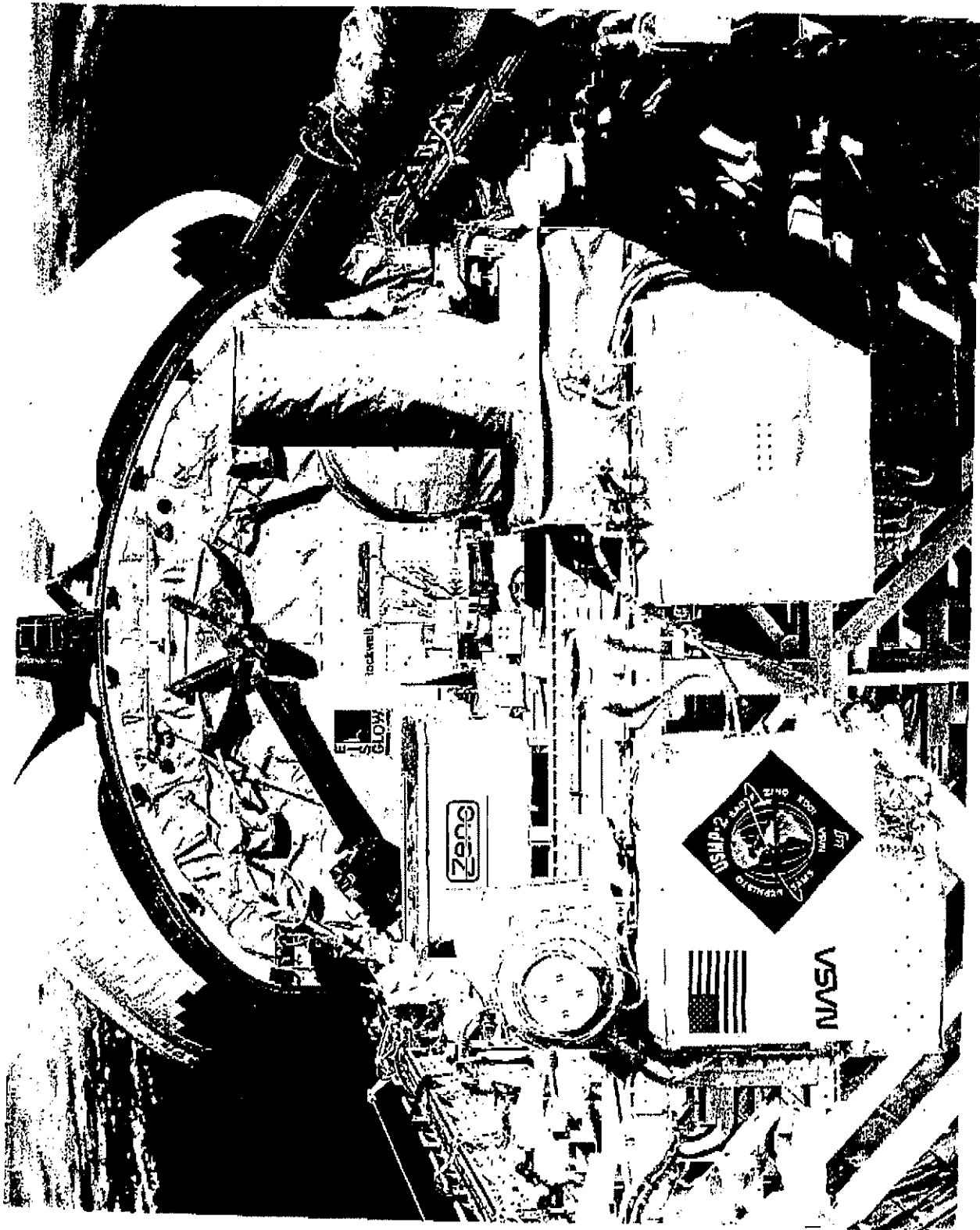
5 0510 00138202 4



Second United States Microgravity Payload: One Year Report

P.A. Curreri and D.E. McCauley, Editors

JUL 15 1985 *CY 1*
Loan Copy Only - Do Not Destroy
Property of
Redstone Scientific Information Center



S1

TABLE OF CONTENTS

	<u>Page</u>
INTRODUCTION	xvii
SECTION I. ONE-YEAR REPORT FOR SAMS AND OARE ON STS-62/USMP-2	1-1
1.1 Introduction	1-3
1.2 Accelerometer Systems	1-3
1.3 <i>Columbia</i> Low-Gravity Environment—STS-62	1-3
1.3.1 Crew Sleep	1-4
1.3.2 Crew Exercise	1-4
1.3.3 Flash Evaporator System	1-4
1.3.4 Circulation Pumps	1-4
1.3.5 Thrusters	1-4
1.3.6 Space Shuttle Attitude	1-5
1.4 Summary	1-5
1.5 Publications	1-6
SECTION II. ISOTHERMAL DENDRITIC GROWTH EXPERIMENT	2-15
2.1 Introduction	2-17
2.2 Background on Dendritic Growth	2-18
2.3 The Isothermal Dendritic Growth Experiment (IDGE)	2-20
2.3.1 IDGE Growth Chamber	2-21
2.3.2 Flight Experiment Procedure	2-22
2.4 Results	2-22
2.4.1 Dendritic Growth Velocities	2-23
2.4.2 Dendritic Tip Radii	2-24
2.4.3 Growth Péclet Number	2-24
2.4.4 Kinetic Scaling Parameter	2-24
2.5 Teleoperations	2-25
2.5.1 IDGE Operating Plans	2-25
2.5.2 Flight Operations	2-26
2.6 Summary and Conclusions	2-27
2.7 Work in Progress	2-28
2.8 References	2-29
2.9 Publications and Presentations	2-30
SECTION III. IN SITU MONITORING OF CRYSTAL GROWTH USING MEPHISTO	3-45
3.1 Overview	3-47
3.2 Background	3-47
3.3 USMP-2 Mission Description	3-48
3.3.1 Experimental Facility and Techniques	3-48
3.3.2 Flight Summary	3-48
3.4 Microstructural and Data Analysis	3-49
3.4.1 Microstructural Analysis	3-49
3.4.2 Kinetics Data Analysis	3-49

3.4.3	Microstructural Analysis	3-49
3.4.4	Kinetics Data Analysis	3-52
3.5	Summary	3-56
3.6	References	3-57
SECTION IV. GROWTH OF SOLID SOLUTION SINGLE CRYSTALS		4-89
4.1	Introduction	4-92
4.2	Study Rationale	4-93
4.3	Driving Force for Convection	4-93
4.4	Previous Results for Compositional Redistribution	4-94
4.5	Problems Associated With Growth Interface Shape Control	4-94
4.6	Advantages of Microgravity Growth	4-95
4.7	Ground-Based Results	4-95
4.8	Flight Results	4-96
4.9	Flight Timeline	4-96
4.10	Residual Acceleration Results	4-97
4.11	Radiography	4-97
4.12	Photography	4-98
4.13	X-Ray Diffraction	4-98
4.14	Scanning Electron Microscopy (SEM)	4-100
4.15	Energy Dispersion Spectrometry (EDS)	4-100
4.16	Cutting Strategy	4-101
4.17	Optical Microscopy	4-102
4.18	Wavelength Dispersive Spectrometry	4-102
4.19	Synchrotron Radiation Studies	4-103
4.20	Summary and Preliminary Conclusions	4-103
4.21	References	4-105
SECTION V. HIGHLIGHTS OF THE ZENO RESULTS FROM THE USMP-2 MISSION		5-135
5.1	Introduction	5-137
5.2	Timeline	5-138
5.3	Instrument Performance	5-138
	5.3.1 Thermostat and Thermometry	5-138
	5.3.2 The Light-Scattering Spectrometer	5-139
5.4	Determining T_c On Orbit	5-140
5.5	Turbidity Measurements and Related Effects	5-141
5.6	Critical-Point Fluctuation Decay Rates	5-143
5.7	Conclusion	5-145
5.8	Selected Bibliography	5-146

LIST OF ILLUSTRATIONS

Figure	Title	Page
STS-62	Onboard Photo: Shuttle Cargo Bay	ii
	USMP-2 Payload	xix
Figure 1-1.	Orbital acceleration research experiment data from STS-62	1-7
Figure 1-2.	Crew sleep period	1-8
Figure 1-3.	Crew active time with exercise period	1-8
Figure 1-4.	Time domain vector magnitude of SAMS data for Unit F, Head B, MET 012/00:45:00–012/00:47:10	1-9
Figure 1-5.	Power spectral density vector magnitude of SAMS data for Unit F, Head B, MET 012/00:45:00–012/00:47:10	1-9
Figure 1-6.	Time domain vector magnitude of SAMS data for Unit F, Head B, MET 008/14:19:30–008/14:21:40. Circulation pump activation	1-10
Figure 1-7.	Time domain vector magnitude of SAMS data for Unit F, Head B, MET 009/17:09:00–009/17:11:10. OMS	1-10
Figure 1-8.	Time domain vector magnitude of SAMS data for Unit F, Head B, MET 010/17:12:00–010/17:14:10. Primary reaction control system activity	1-11
Figure 1-9.	Power spectral density vector magnitude of SAMS data for Unit F, Head B, MET 010/17:12:00–010/17:14:10. Primary reaction control system activity	1-11
Figure 1-10.	Space shuttle attitudes for USMP-2 on STS-62	1-12
Figure 1-11.	Attitude transition during USMP-2 operations (–ZLV/+YVV to –XLV/–ZVV)	1-13
Figure 1-12.	Attitude transition during USMP-2 operations (–XLV/–ZVV to –XLV/+ZVV)	1-13
Figure 2-1.	IDGE flight growth chamber	2-33
Figure 2-2.	IDGE temperature controlled tank and optic system	2-34
Figure 2-3.	Examples of 35-mm photographic images and low-resolution, binary, digitized electronic images	2-35
Figure 2-4.	Dendritic growth tip velocity as a function of supercooling	2-36
Figure 2-5.	Dendritic growth tip velocity as a function of supercooling at the lower supercoolings	2-37
Figure 2-6.	Dendritic growth tip radius as a function of supercooling	2-38

Figure 2-7.	Dendritic growth tip Péclet numbers as a function of supercooling.....	2-39
Figure 2-8.	Dendritic growth tip Péclet numbers as a function of supercooling in the diffusion-limited supercooling range.....	2-40
Figure 2-9.	Dendritic growth scaling parameter as a function of supercooling.....	2-41
Figure 2-10.	The first telescience measured velocity calculated from the SSTV data.....	2-42
Figure 2-11.	Dendrite tip displacement versus time data from the SSTV data.....	2-43
Figure 2-12.	Extension of the velocity data range that was obtained through the use of telescience	2-44
Figure 3-1.	(a) MEPHISTO core assembly	3-62
Figure 3-1.	(b) Arrangement of the experimental samples in MEPHISTO. Shows three rod-shaped samples processed in parallel, the location of thermocouples, and the two solid/liquid (s/l) interfaces from which a differential Seebeck electro motive force (emf) is measured. Also shown is the overall temperature distribution in the apparatus during processing (schematic)	3-62
Figure 3-2.	Initial microstructure showing a faceted cellular/dendritic morphology. Samples grown via directional solidification at a rate of 0.2 cm/s. Optical micrograph, differential interference contrast (DIC) illumination	3-63
Figure 3-3.	(a) Summary of sample sections preserved during final solidification. Also shows the orientation of microsections of the samples which are taken in a direction pointing to the diffuser center and thus thermally equivalent	3-64
Figure 3-3.	(b) Microstructural evolution starting with the initial microstructure at growth velocities V1 and V2. (c) Continued growth at V2 and V3	3-65
Figure 3-3.	(d) Microstructural evolution during continued growth at V3 and after change in the growth rate to V4. (e) Continued growth at V4	3-66
Figure 3-3.	(f) Microstructural evolution during continued growth at V4 and growth rate changes to V5, V1, and V3. Note the cellular breakdown during growth at V5. (g) Continued growth at V3, followed by a growth rate change to V6. Note the development of a cellular structure at V6	3-67
Figure 3-4.	(a) Microstructural appearance of the interface between the Earth-grown (faceted cellular/dendritic) and microgravity-processed (plane front) portions of the Peltier sample, moving furnace side. The composite micrographs were obtained under a polarized light/sensitive tint illumination and show the emergence of a few dominant orientations during directional solidification in microgravity	3-68

Figure 3-4.	(b) Microstructural appearance of the interface between the Earth-grown (faceted cellular/dendritic) and microgravity-solidified (plane front) portions of the Resistance/Quenching sample, fixed furnace side. The microstructure developed during final cool down. Polarized light/sensitive tint illumination	3-69
Figure 3-4.	(c) Interface between the initial microstructure and microgravity solidification at a growth velocity of 1.85 $\mu\text{m/s}$. Micrograph represents the bottom half of the sample cross section. Note the emergence of two dominant orientations from the initial structure	3-70
Figure 3-5.	Plane front solidification at velocities ranging from 1.85 to 6.71 $\mu\text{m/s}$	3-70
Figure 3-6.	(a) Schematic of the shape of an interface at the transition between V5 and V1. (b) Low magnification micrograph of the interface. The interface is slightly curved at the edges due to the surface tension forces at the solid/liquid/crucible triple junction	3-71
Figure 3-7.	Detail of interface between V5 and V1. Note the changes in grain boundary angles upon decreasing the growth rate. Optical Micrograph, DIC illumination	3-72
Figure 3-8.	Secondary Ion Mass Spectroscopic (SIMS) analysis of the V5/V1 interface illustrating the sharp change in average Sn content at the interface	3-72
Figure 3-9.	(a) Schematic representation of the features of a selective breakdown at a growth velocity of 26.6 $\mu\text{m/s}$. (b) Microstructural appearance of the selective breakdown	3-73
Figure 3-10.	Selective planar to cellular transition at a growth velocity of 26.88 $\mu\text{m/s}$	3-74
Figure 3-11.	(a) Schematic illustration showing the salient features of a cellular transition at a growth velocity of 40 $\mu\text{m/s}$. (b) Low magnification micrograph of V6 breakdown region. (c) Higher magnification view of cellular growth at V6	3-75
Figure 3-12.	(a) Schematic of cellular growth, transverse section. Shows two dominant orientations. (b) Optical micrograph (B.F.) illustrating the cell boundaries. (c) Optical micrograph (P.L.S.T.) showing two dominant grains. (d) Optical micrograph (D.F.) showing cell boundaries	3-76
Figure 3-13.	(a) Typical resistance tracking of interface position and measurement of furnace translation (by linear potentiometer) as a function of processing time. Typical Seebeck measurement cycle (solidification-stabilization-remelting-stabilization). (b) The hysteresis between resistance change during solidification (bottom curve) and that during symmetrical remelting (top curve)	3-77
Figure 3-14.	FFT editing of resistance measurement during a typical Seebeck cycle. Note the removal of superimposed noise so that fine slope changes during the resistance tracking can be detected	3-78

Figure 3-15.	Subtraction of resistance change during solidification from that during symmetrical remelting. FFT edited data. The existence of a negative plateau indicates interfacial retardation during solidification	3-78
Figure 3-16.	Resistance change during the final quench, shows a sharp increase in the resistance at the time of quench. The subsequent decay is due to the slower melting of the portion of the sample pushed into the hot zone during the quench. Also shown are furnace position and outputs of quenching sample thermocouples	3-79
Figure 3-17.	Output of short and long thermocouples in the quenching sample during a typical Seebeck measurement. Also shown is the corresponding furnace movement	3-80
Figure 3-18.	Evolution of differential Seebeck emf due to microstructure/thermal gradient interaction. (a) Initial and directional growth microstructure at two interfaces. (b) Thermal gradient zone during directional solidification. (c) Evolution of the Seebeck emf during translation of a thermal gradient	3-81
Figure 3-19.	The processing sequence of microstructural/Seebeck emf evolution described in figures 20(a)–(e). Shows two melting cycles and two solidification cycles separated by stabilization periods. Each step in the process is identified by a letter (a through e), corresponding to figures 20 (a)–(e)	3-82
Figure 3-20.	(a) Initial interface between the Earth-grown faceted cellular/dendritic microstructure and liquid alloy. The interface is slightly curved at the solid/liquid/crucible triple junction. The baseline Seebeck emf is steady with a mean value of $\sim 70 \mu V$	3-83
Figure 3-20.	(b) Directional 2-mm melting of the initial interface and the corresponding Seebeck signal	3-84
Figure 3-20.	(c) Directional 2-mm solidification resulting in plane-front growth with columnar grains and the corresponding evolution of the Seebeck signal	3-85
Figure 3-20.	(d) Directional 7-mm melting of the plane-front (2 mm) and cellular/dendritic (last 5 mm) region and the corresponding evolution of the Seebeck signal	3-86
Figure 3-20.	(e) Directional 7-mm solidification resulting in plane-front growth with columnar grain structure. Also shown is the disappearance of unfavorable orientations as growth proceeds and the corresponding evolution of the Seebeck signal	3-87
Figure 4-1.	Superconducting magnet furnace	4-110
Figure 4-2.	Estimated compositional profile based on diffusion controlled solidification	4-111
Figure 4-3.	Z-component OARE data during attitude change	4-111
Figure 4-4.	OARE data at instrument for $-ZLV/+YVV$ attitude	4-112
Figure 4-5.	OARE data transformed to AADSF location for $-ZLV/+YVV$ attitude	4-112

Figure 4-6.	Directions of residual acceleration vectors with respect to AADSF and orbiter	4-113
Figure 4-7.	Resolved OARE data for AADSF flight sample	4-114
Figure 4-8.	Radiographs of flight and ground-truth cartridges showing the last to freeze material	4-115
Figure 4-9.	Appearance of ground-truth and flight cartridges after processing	4-116
Figure 4-10.	AADSF flight sample after removal from ampoule—J7 position	4-117
Figure 4-11.	(a) Typical Laue back reflection pattern of surface of flight sample. (b). Broad beam back reflection Laue pattern—same region as figure 11a	4-118
Figure 4-12.	Back scattered electron image (SEM) from flight sample—note the channeling pattern	4-119
Figure 4-13.	(a) Thermal etch pits on surface of flight sample—close to [111]. (b). Thermal etch pits on high index surface	4-120
Figure 4-14.	Surface of flight sample showing interface breakdown during orbiter maneuver	4-121
Figure 4-15.	Surface composition of ground-truth sample along J7+90° orientation	4-122
Figure 4-16.	Surface composition of flight sample along J7 orientation	4-122
Figure 4-17.	Surface composition of flight sample along J7–90° orientation	4-123
Figure 4-18.	Surface composition of flight sample along J7+90° orientation	4-123
Figure 4-19.	Surface composition of flight sample along J7+180° orientation	4-124
Figure 4-20.	Surface composition of flight sample close to J7–90° orientation	4-124
Figure 4-21.	Two-dimensional analysis of a slab of the ground-truth sample cut through the rate change region—EDS results	4-125
Figure 4-22.	Microstructure of the slab shown in figure 21—ground-truth sample etched in Polisar II	4-126
Figure 4-23.	Flight sample cut to show major grain in [111] direction—etched in Polisar II	4-127
Figure 4-24.	Ground-truth sample cut at right angles to growth axis—etched in Polisar II	4-128
Figure 4-25.	Composition across diameter of ground-truth sample—EDS results	4-129
Figure 4-26.	Composition across diameter of flight sample with superimposed diffusion profile	4-129

Figure 4-27.	Three-dimensional representation of composition of flight sample—WDS results	4-130
Figure 4-28.	Composition map for flight sample in +YVV/−ZLV attitude (62 mm)	4-131
Figure 4-29.	Composition map for flight sample in −XLV/−ZVV attitude (106 mm)	4-131
Figure 5-1.	A schematic of the optical layout of the instrument, showing its main components: Beamsplitter (B1), mirrors (M1, M2, and M3), apertures (A1–A4), photodiodes (PD1 and PD2), and photomultiplier tubes (PMT1 and PMT2). The thermostat is the cylindrical object in the center	5-151
Figure 5-2.	The timeline of the experiment, given as the temperature of the sample (measured in distance from T_c) versus MET in days	5-151
Figure 5-3.	The stability of the sample temperature at 1 mK, over a four-hour period while collecting correlograms. The rms of the variations is $1.7 \mu\text{K}$. (Time is in <i>hhmm</i> format.)	5-152
Figure 5-4.	The temperature of the sample cell during a slow temperature step of -2 mK , shown as distance from T_c . The time constant for thermal relaxation of the sample cell is about 30 minutes. (Time is in <i>hhmm</i> format.)	5-152
Figure 5-5.	The temperature of the sample cell during a fast temperature step of $-200 \mu\text{K}$, shown as distance from T_c . (Time is in <i>hhmm</i> format.)	5-153
Figure 5-6.	A correlogram example showing simple exponential decay on a logarithmic time scale. Taken at $T - T_c = 100 \text{ mK}$ at a laser power of $17 \mu\text{W}$, this is a forward-scattering correlogram	5-153
Figure 5-7.	A section of the zig-zag T_c search, showing the pattern of sample temperature changes: Cooler by $20 \mu\text{K}$, then warmer by $10 \mu\text{K}$. The data are smoothed over a 300-second interval. The turbidity during this same time is shown in figure 8. (Time is in <i>hhmm</i> format.)	5-154
Figure 5-8.	A section of the zig-zag T_c search, showing the response of the sample turbidity to the zig-zag temperature steps shown in figure 7 for the same time period. The data are smoothed over a 300-second interval. (Time is in <i>hhmm</i> format.)	5-154
Figure 5-9.	The turbidity signal during the entire 64-hour zig-zag T_c search. (Time is in day: <i>hhmm</i> format.)	5-155
Figure 5-10.	The temperature of the high-precision control shell of the thermostat, during the first scan for T_c . The temperature of this shell, shown making $-50 \mu\text{K}$ steps, determines the sample temperature, shown in figure 11. (Time is in <i>hhmm</i> format.)	5-155
Figure 5-11.	The sample temperature during the first scan for T_c , in response to the control-shell steps shown in figure 10. The result is a uniform sample cooling of $500 \mu\text{K}/\text{hour}$. (Time is in <i>hhmm</i> format.)	5-156

Figure 5-12.	The turbidity signal during the first scan for T_c . The small feature just past 0600 hours is where the sample crosses T_c ; the large peak is spinodal decomposition. (Time is in <i>hhmm</i> format.)	5-156
Figure 5-13.	Forward-scattering photon count rate during the first scan for T_c , showing from the break in slope that the sample crosses T_c just past 0600 hours. (Time is in <i>hhmm</i> format.)	5-157
Figure 5-14.	The turbidity signal during a 500 $\mu\text{K}/\text{hour}$ scan for T_c done in 1-g during preflight testing. Compare this scan with the $\mu\text{-g}$ scan shown in figure 12	5-157
Figure 5-15.	The turbidity signal, in preflight testing, during a warming sequence between T_c+1 K to T_c+5 K, made in steps of 0.1 K. The sinusoidal shape is due to cell expansion; the small spikes result from changes in fluid density	5-158
Figure 5-16.	Data taken on the engineering model of the instrument show, in the lower curve, the response of the turbidity signal to a change in temperature from $T_c + 0.6$ K to $T_c + 0.7$ K. The upper curve is the change due solely to cell expansion. The vertical units are the phase along the interference curve for the cell	5-158
Figure 5-17.	The difference between the two curves in figure 16, showing the response of the turbidity signal due solely to changes in the fluid density. Compare with figure 18. (These data are from the engineering model of the instrument.)	5-159
Figure 5-18.	The time derivative of the temperature change which produced the turbidity signal shown in figure 16; this curve has the same shape as the curve in figure 17. (These data are from the engineering model of the instrument.)	5-159
Figure 5-19.	The turbidity response to a temperature change of -70 mK, starting at $T_c+0.1$ K, showing cell interference, adiabatic response, and an as-yet unidentified feature	5-160
Figure 5-20.	Dual correlogram taken at $T_c + 560$ mK with 17 μW of laser power; the integration time was six minutes. Forward scattering (upper curve) had an average count rate of 710 counts/second; backscattering (lower curve) had 435 counts/second	5-160
Figure 5-21.	Dual correlogram taken at T_c+1 mK with 17 μW of laser power; the integration time was ten minutes. Forward scattering (upper curve) had an average count rate of 446,000 counts/second; backscattering (lower curve) had 17,800 counts/second	5-161
Figure 5-22.	Dual correlogram taken at T_c+1 mK with 1.7 μW of laser power; the integration time was fifteen minutes. Forward scattering (upper curve) had an average count rate of 27,100 counts/second; backscattering (lower curve) had 2,200 counts/second	5-161

- Figure 5-23. Dual correlogram taken at $T_c+100 \mu\text{K}$ with $1.7 \mu\text{W}$ of laser power; the integration time was fifteen minutes. Forward scattering (upper curve) had an average count rate of 45,000 counts/second; backscattering (lower curve) had 3,000 counts/second 5-162
- Figure 5-24. Backscattering decay rates as a function of temperature; the vertical scale is linear, the horizontal scale logarithmic. The crosses are 1-g data from preflight testing; the diamonds are the mission data. The curve is our best theoretical estimate. The error bars show the rms of the data 5-162
- Figure 5-25. Forward-scattering decay rates as a function of temperature; both scales are logarithmic. The crosses are 1-g data from preflight testing; the diamonds are the mission data. The curve is our best theoretical estimate. The error bars, generally smaller than the symbols, show the rms of the data 5-163

LIST OF TABLES

Table	Title	Page
Table 3-1.	Summary of Growth Conditions and Shuttle Activities During Final Solidification Steps	3-60
Table 3-2.	Summary of Morphological Changes in USMP-2 Samples	3-61
Table 4-1.	OARE Data Transformed to AADSF Coordinates	4-132
Table 4-2.	Quality of Surface on Flight Sample	4-132
Table 4-3.	Orientation of Flight Sample—Transformed Laue Patterns	4-133

USMP-2 Acronyms

AADSF	Advanced Automatic Directional Solidification Furnace
BCC	Body Centered Cubic
CENG	Centre d'Etudes Nuclaires National de Grenoble
CNES	Centre National d'Etudes Spatiales
DSO	Detailed Supplementary Objective
EAC	Experiment Apparatus Container
EDS	Energy Dispersion Spectrometry
EMF	Electro Motive Force
ETR	Experiment Tape Recorders
FES	Flash Evaporator System
JSC	Johnson Space Center
ICP	Inductively Coupled Plasma
IDGE	Isothermal Dendritic Growth Experiment
MEPHISTO	Material por l'Etude des Phenomenes Intéressants la Solidification sur Terre et en Orbite
MET	Mission Elapsed Time
MPRESS	Mission Peculiar Experiment Support Structure
MSFC	Marshall Space Flight Center
NIST	National Institute of Standards and Technology
NLS	National Synchrotron Light Source
NRA	NASA Research Announcement
OARE	Orbital Acceleration Research Experiment
OAST	Office of Aeronautics and Space Technology
OMS	Orbital Maneuvering System
PIMS	Principal Investigator Microgravity Sciences
POCC	Payload Operations Control Center
RCS	Reaction Control System
RPI	Rensselaer Polytechnic Institute
SAMS	Space Acceleration Measurement System
SCN	Succinonitrile
SCU	System Control Unit
SEM	Scanning Electron Microscope
SIMS	Secondary Ion Mass Spectroscopy
S/L	Solid/Liquid
SSTV	Slow Scan Television
STS	Space Transportation System
SUNY	State University of New York
USMP	United States Microgravity Payload
WDS	Wavelength Dispersion Spectrometry
XLV, YVV, ZLV, ZVV	Orbiter Attitudes (plus or minus)
Zeno	Light-Scattering Spectrometer Experiment

USMP-2 Mission Information

Orbiter	<i>Columbia</i>
Mission Number	STS-62
Dates of Flight	March 4–18, 1994
Crew Size	Five
Number of Shifts	One
Accelerometers	OARE—Measures low-level accelerations in the frequency range below 1 Hertz down to essentially steady state and is mounted near the center of gravity of the Orbiter. SAMS—Measures low-level accelerations from about 0.01 Hertz up to 100 Hertz and is mounted in or near the science experiment equipment.
Co-Manifested Payload	Office of Aeronautics and Space Technology's experiment OAST-2

l'Etude des Phenomenes Intéressants la Solidification sur Terre et en Orbite (MEPHISTO), and the Critical Fluid Light Scattering Experiment (Zeno). The mission was highly successful and resulted in full operation of all four apparatus.

Experience and Lessons

USMP-2 required the second largest command load (through March 1994) directed through Marshall Space Flight Center's Payload Operations Control Center (POCC). The system control unit (SCU) routed approximately 10,000 commands to USMP-2 and relayed some 27 gigabits of experiment data to the ground for real-time and postflight analyses. All data were also recorded on the flight data recorders aboard USMP-2 with the experiment tape recorders (ETR) serving as backup. The ETR failed an hour before the end of USMP-2 microgravity operations, but flight recorders and downlink captured all the remaining data. Overall, the USMP carrier performed exceptionally well during the mission.

Telescience. IDGE and Zeno provided the most extensive demonstrations of telescience. IDGE investigators controlled conditions as they watched crystal growth through the two TV cameras, then commanded the film cameras to take high-resolution pictures at the appropriate times. While photography was suspended for 3 days to conserve film, the investigators collected valuable data via slow-scan TV. Zeno demonstrated telescience as the principal investigation team controlled temperature ranges, manually stepping changes in extremely small increments and observing the xenon film's responses. This added flexibility was critical since some of the experiment time constants proved to be longer than expected in space. The AADSF team created a demarcation point on the sample to establish the position and shape of the solid-liquid growth interface before the orbiter attitude changed 150 hours into the microgravity portion of the flight. MEPHISTO utilization of telescience was greatly enhanced by near real-time Seebach and resistivity data which provided information on the samples' responses to gravity perturbations and on the interfacial morphological stability. This information was utilized to set the fixed and moving furnace temperature, solidification rates, and conditions for Peltier markings.

USMP-2's success sets a new standard in the U.S. Microgravity Sciences and Applications program. The anticipated scientific results are expected to expand our understanding of fundamental aspects of materials behavior with and without gravity as a factor. Already, the extensive operational experience has expanded our confidence and capabilities in manned and telescience operations in space.

INTRODUCTION

Peter A. Curreri

USMP Mission Scientist
George C. Marshall Space Flight Center, Huntsville, Alabama 35812

The second United States Microgravity Payload (USMP-2), flown in March 1994, carried four major microgravity experiments plus a sophisticated accelerometer system. The USMP program is designed to accommodate experiments requiring extensive resources short of a full Spacelab mission. The four USMP-2 experiments dealt with understanding fundamental aspects of materials behavior, three with the formation of crystals from melts, and one with the critical point of a noble gas. This successful, scientifically rich mission also demonstrated telepresence operations.

USMP Overview

The USMP program grew out of early automated materials payloads carried by the space shuttle during 1983–1986. Of special value was the Materials Science Laboratory flown on STS-24 (Space Transportation System) in 1986. USMP supports up to 2,268 kg of experiment apparatus mounted on the Mission-Peculiar Experiment Support Structure (MPESS), an aluminum truss structure which spans the shuttle payload bay and occupies less than 1 meter of length. For USMP, two MPESS units are connected to provide mounting spaces (up to 86×102 cm) and utilities for up to six experiments. Payload services include electrical power (450 W @ 28 V), active and passive cooling, and command and data handling. The latter is routine through the shuttle orbiter and provides the potential for remote operations or telepresence.

Candidate flight experiments are selected by NASA from among the broad range of proposals submitted in response to NASA Research Announcements (NRAs) issued for various microgravity disciplines. Experiments are assigned to Spacelab, USMP, or other carriers based on the best match between investigators' needs and facility services. USMP experiments generally have needs between the resources of the middeck and Spacelab, and which can also be packaged for exposure to the space environment. At least two more USMP missions are planned through the late 1990s.

The USMP-2 mission included the Space Acceleration Measurement System (SAMS) which was comprised of five sets of triaxial sensor heads, each with three orthogonal accelerometers, located at several positions on the payload. Gravity's effects are not totally eliminated in space; some acceleration occurs at any position removed from the spacecraft center of mass. Additional micro-accelerations are caused by "normal" spacecraft activities: Crew movement, antenna pointing, shuttle maneuvers, atmospheric drag, etc. Some accelerations are intermittent while others are quasi-steady or periodic and can have subtle, unwanted effects on experiments. SAMS was designed to measure and record the microgravity environment during USMP-2 operations and provide high-resolution, time-tagged data which can be correlated with events aboard the shuttle and within experiment events and features on specimens. Data are stored on optical disk and transmitted to the ground.

USMP-2 Experiments

Four experiments flown on USMP-2 represent a range of investigations from crystal formation to fundamental physics. Their common need was extended operations in an extremely quiet microgravity environment. This was provided during the STS-62 mission, March 4–18, 1994, aboard Space Shuttle *Columbia*. Of the 14 days in orbit, USMP-2, the prime payload, was allocated 9.25 days of microgravity starting shortly after orbital insertion. USMP-2 experiments were the Advanced Automated Directional Solidification Furnace (AADSDF), the Isothermal Dendrite Growth Experiment (IDGE), the Material por

1.3.1. Crew Sleep

The five-member crew of STS-62 worked on a single-shift schedule. The vibration environment is reduced during crew sleep periods compared to periods of crew activity because some equipment is turned off and crew push-off forces are minimal or nonexistent. Figure 1 shows OARE data for the extent of the STS-62 mission. Crew sleep times appear as periodic, relatively quiet regions of the plot, especially evident in the first half of the mission. Other characteristics of this plot will be described later.

The spectrogram in figure 2 shows the SAMS data from a 2-hour period (mission elapsed time MET 012/06:00 to 08:00) in one of the crew sleep periods. It can be seen in this data that the environment is very quiet across the frequency range of interest (25 Hz).

1.3.2. Crew Exercise

The spectrogram in figure 3 shows the SAMS data from a 2-hour period (MET 012/00:00 to 02:00) during a typical crew active time. This data includes nominal operations (from MET 012/00:50 to 02:00) and the beginning of a sequence of crew exercise activities (from 00:10 to 00:50).

Figure 4 shows an example of the vibration environment as recorded by SAMS while a crew member was exercising on the bicycle ergometer. In this figure note the increased acceleration level at MET 012/00:46:00 indicating an increase in crew exertion level. In figure 5 the exercise activity is identified by the excitation of 1.2 and 2.4 Hz frequencies. These frequencies correspond to the pedaling and body motion frequencies of the crew member.

1.3.3. Flash Evaporator System

Some heat rejection is provided on-orbit by the flash evaporator system (FES) of the space shuttle. FES activity was noted during STS-62 and the effect on the microgravity environment was similar to previous missions.

1.3.4. Circulation Pumps

The electric motor-driven pumps of the three independent space shuttle hydraulic subsystems have an impact on the low-gravity environment. The pumps must be activated periodically on-orbit. Figure 6 shows SAMS data collected when circulation pump 2 was activated during STS-62. Note the relatively large magnitude, short duration transient at MET 008/14:19:55, and the two lower magnitude transients that occur about 75 and 85 seconds later. This data signature appears to be characteristic of the initiation of circulation pump activity.

1.3.5. Thrusters

The space shuttle orbital maneuvering system (OMS) and reaction control system are used to provide thrust on-orbit. OMS thrust is used to modify an orbit for payload rendezvous or deploy, or to change orbit. During Office of Aeronautics and Space Technology-2 (OAST-2) operations on STS-62, three OMS burns (designated OMS-3, OMS-4, and OMS-5) occurred. Figure 7 shows SAMS data collected during the OMS-4 burn. Note the 3×10^{-2} g shift of the acceleration mean level during the burn, followed by a return to the original mean upon burn completion. This signature is typical of OMS engine burns.

SECTION I. ONE-YEAR REPORT FOR SAMS AND OARE ON STS-62/USMP-2

Richard DeLombard

PIMS Project Manager
NASA Lewis Research Center, Cleveland, Ohio 44135

1.1. INTRODUCTION

The second United States Microgravity Payload (USMP-2) flew on the Space Shuttle *Columbia* on mission STS-62 (Space Transportation System) in March 1994. The USMP-2 part of STS-62 was dedicated to low-gravity experiments. To support these experiments, two accelerometer systems were flown in the Orbital Acceleration Research Experiment (OARE) and the Space Acceleration Measurement System (SAMS).

The Principal Investigator Microgravity Services (PIMS) project supports principal investigators of microgravity experiments in the evaluation of the effects of varying acceleration levels on their experiments. A summary report was prepared by PIMS to furnish interested experiment investigators with a guide to evaluate the acceleration environment during STS-62 and as a means of identifying areas which require further study. The summary report provides an overview of the STS-62 mission, describes the accelerometer systems flown on STS-62, discusses some specific analysis of the accelerometer data in relation to the various activities which occurred during the mission, and presents plots resulting from this analysis as a snapshot of the environment during the mission.

Numerous activities occurred during the STS-62 mission that are of interest to the low-gravity community. Specific activities of interest during STS-62 were crew exercise, experiment latch operations, closed circuit camera motion, radiator latch operations, flash evaporator system and water dump operations, circulation pump activity, Ku band antenna activity, orbital maneuvering system and primary reaction control system firings, and attitude changes. The low-gravity environment related to these activities is discussed in the summary report.

1.2. ACCELEROMETER SYSTEMS

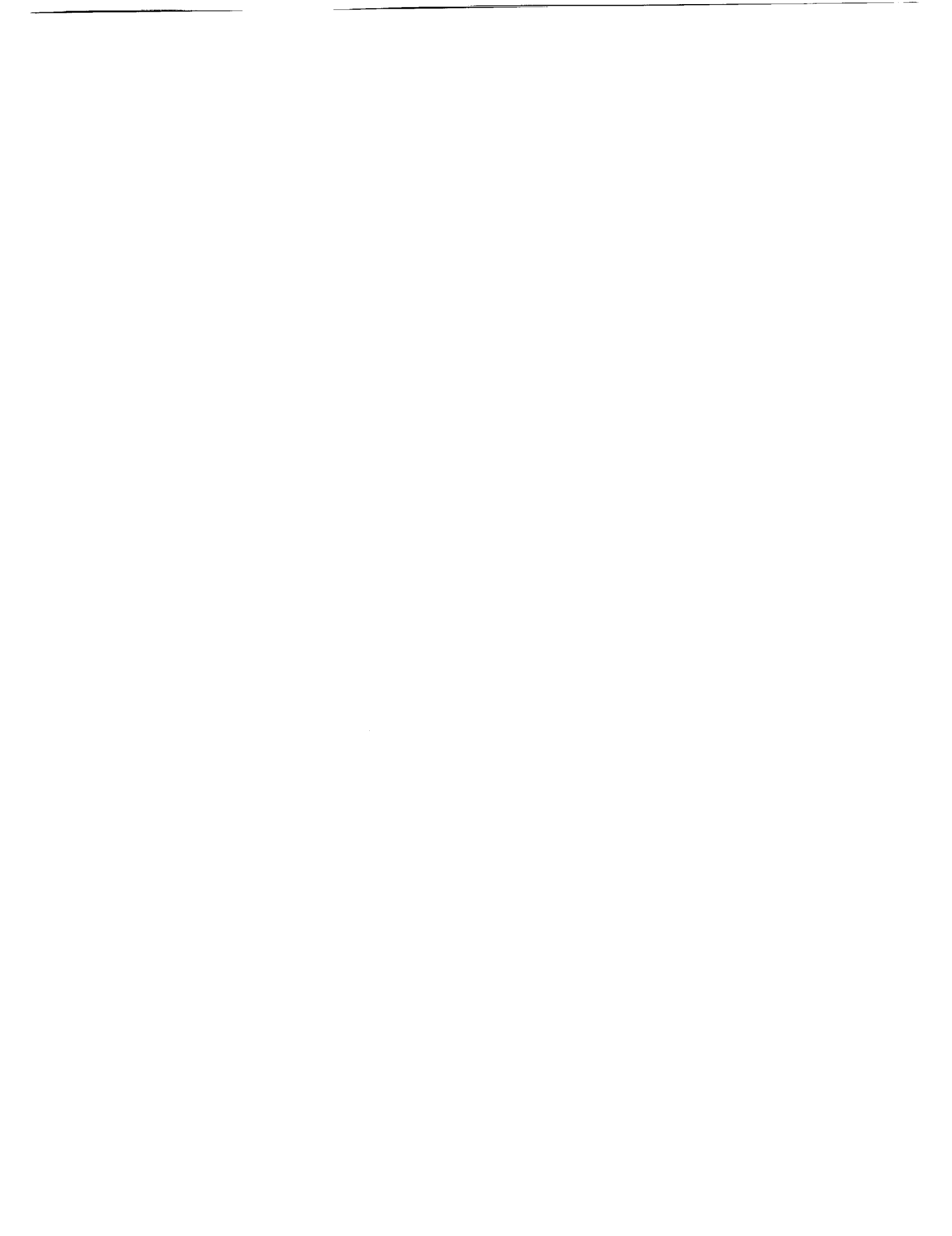
Two accelerometer systems, OARE and SAMS, measured the low-gravity environment of the Space Shuttle *Columbia* during the STS-62 mission. The OARE instrument measures low-level accelerations in the frequency range below 1 Hz down to essentially steady-state. It is mounted near the center of gravity of the space shuttle vehicle. The SAMS units have the capability of measuring low-level accelerations from about 0.01 Hz up to 100 Hz. The SAMS sensors are mounted in or near the science experiment equipment.

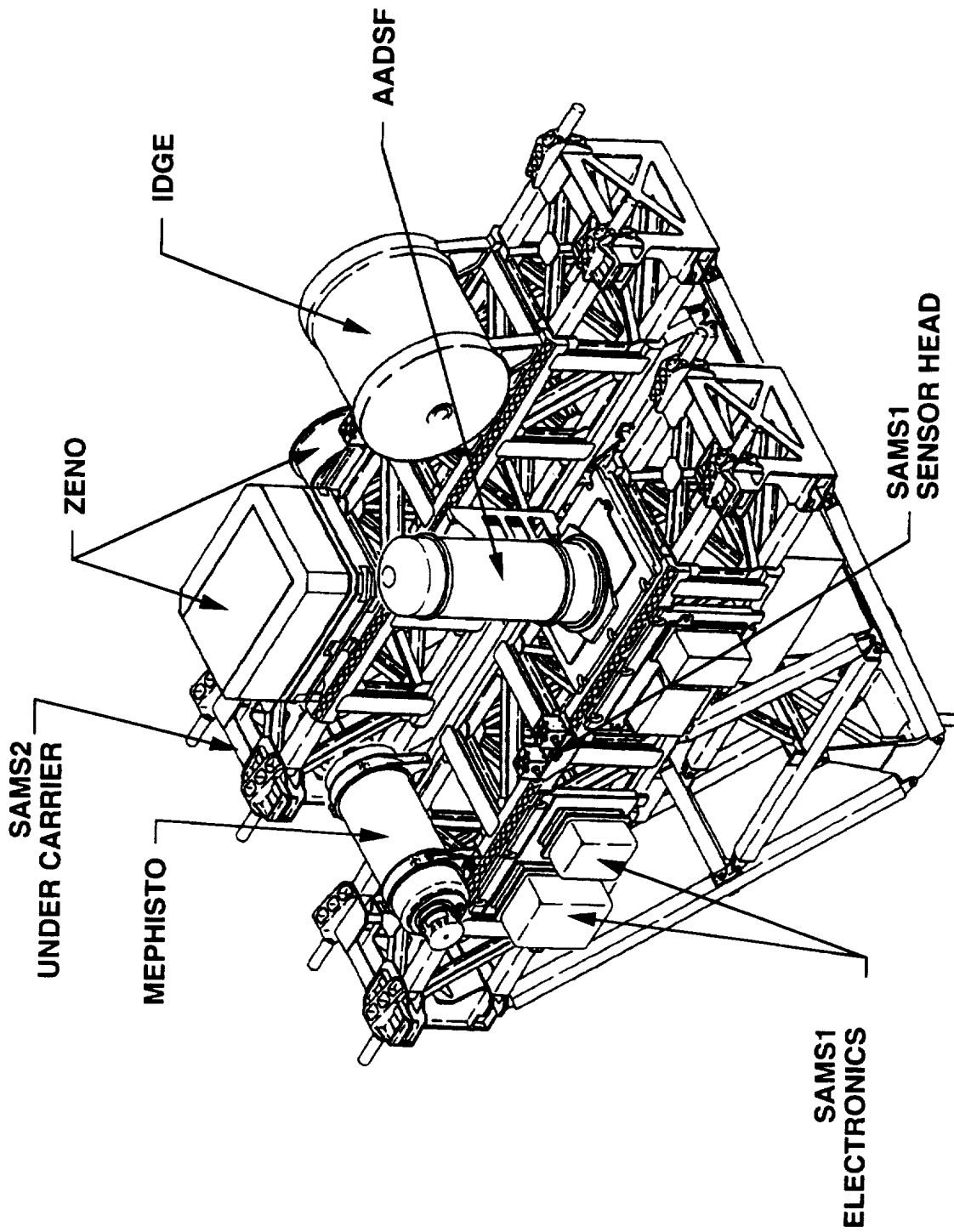
1.3. COLUMBIA LOW-GRAVITY ENVIRONMENT – STS-62

The acceleration environment measured by an accelerometer system on the space shuttle is contributed to by numerous sources. All ongoing operations of crew life support systems and activities and operations of the space shuttle, crew, carrier, and experiments tend to have vibratory and/or oscillatory components that contribute to the “background” acceleration environment. The following sections describe several significant areas of the microgravity environment.

SECTION I.

**ONE-YEAR REPORT FOR SAMS AND OARE
ON STS-62/USMP-2**





USMP-2 PAYLOAD

Figure 8 shows SAMS data collected during Detailed Supplementary Objective-324 (DSO-324), a NASA Johnson Space Center (JSC) DSO aimed at evaluating the payload on-orbit, low-frequency environment. For this DSO, the primary reaction control system engines were fired numerous times over a period of 6 minutes. Note that the time domain magnitudes are on the order of 10^{-2} g and that the power spectral density representation in figure 9 shows an increase in energy level across the entire frequency spectrum.

1.3.6. Space Shuttle Attitude

For a typical microgravity science mission, the attitude is maintained to optimize certain secondary parameters, such as the net quasi-steady acceleration, duration and frequency of thruster firings, and attitude changes during the course of the mission.

The STS-62 mission had several primary attitudes defined for the two primary payloads, USMP-2 and OAST-2. The attitude flown for the USMP-2 payload during the majority of the first 7 days of the mission was the $-ZLV/+YVV$, figure 10. This attitude was chosen to minimize attitude changes and the amount of thruster firings. Two additional attitudes, $-XLV/-ZVV$ and $-XLV/+ZVV$ (figure 10), were flown at the end of the USMP-2 timeline before the OAST-2 attitudes. During the OAST-2 operations from MET 009/16:45 through MET Day 012, the attitude of the space shuttle was changed frequently in support of various experiments.

The transitions from the $-ZLV/+YVV$ to the $-XLV/-ZVV$ and then to the $-XLV/+ZVV$ attitude can be seen at MET hours 163 and 192 in the OARE data shown in figure 1. Two 20-minute windows which encompass these attitude changes are shown in figures 11 and 12. The large excursions in the acceleration levels at this time are due to the space shuttle thrusters used to change the attitude.

The quasi-steady acceleration vector changes direction as a result of these transitions as can be seen by the x, y, and z levels before and after the attitude transition. This illustrates why some experiments require a certain attitude during their critical operations so that a particular quasi-steady acceleration environment is maintained.

1.4. SUMMARY

There were two primary payloads for the STS-62 mission: USMP-2 and OAST-2. Two SAMS units were on board STS-62 to support the USMP-2 experiments. Five SAMS triaxial sensor heads were mounted at various locations on the carrier among the four science experiments. The OARE instrument was mounted in the space shuttle cargo bay to support the USMP-2 experiments with low-frequency acceleration measurements.

A mission summary report was prepared to describe the microgravity environment of the mission.

1.5. PUBLICATIONS

1. DeLombard, R., M.J.B. Rogers, K. Destro-Sidik, and W.O. Wagar, "Real-Time Acceleration Data Analysis on STS-62 (USMP-2)," AIAA95-0612, January 1995.
2. Matisak, B., L. French, M.J.B. Rogers, K. Destro-Sidik, R. DeLombard, and W.O. Wagar, "Results of the Quasi-Steady Acceleration Environment From the STS-62 and STS-65 Missions," AIAA95-0691, January 1995.
3. Rogers, M.J.B., and R. DeLombard, "Summary Report of Mission Acceleration Measurements for STS-62," NASA TM 106773.

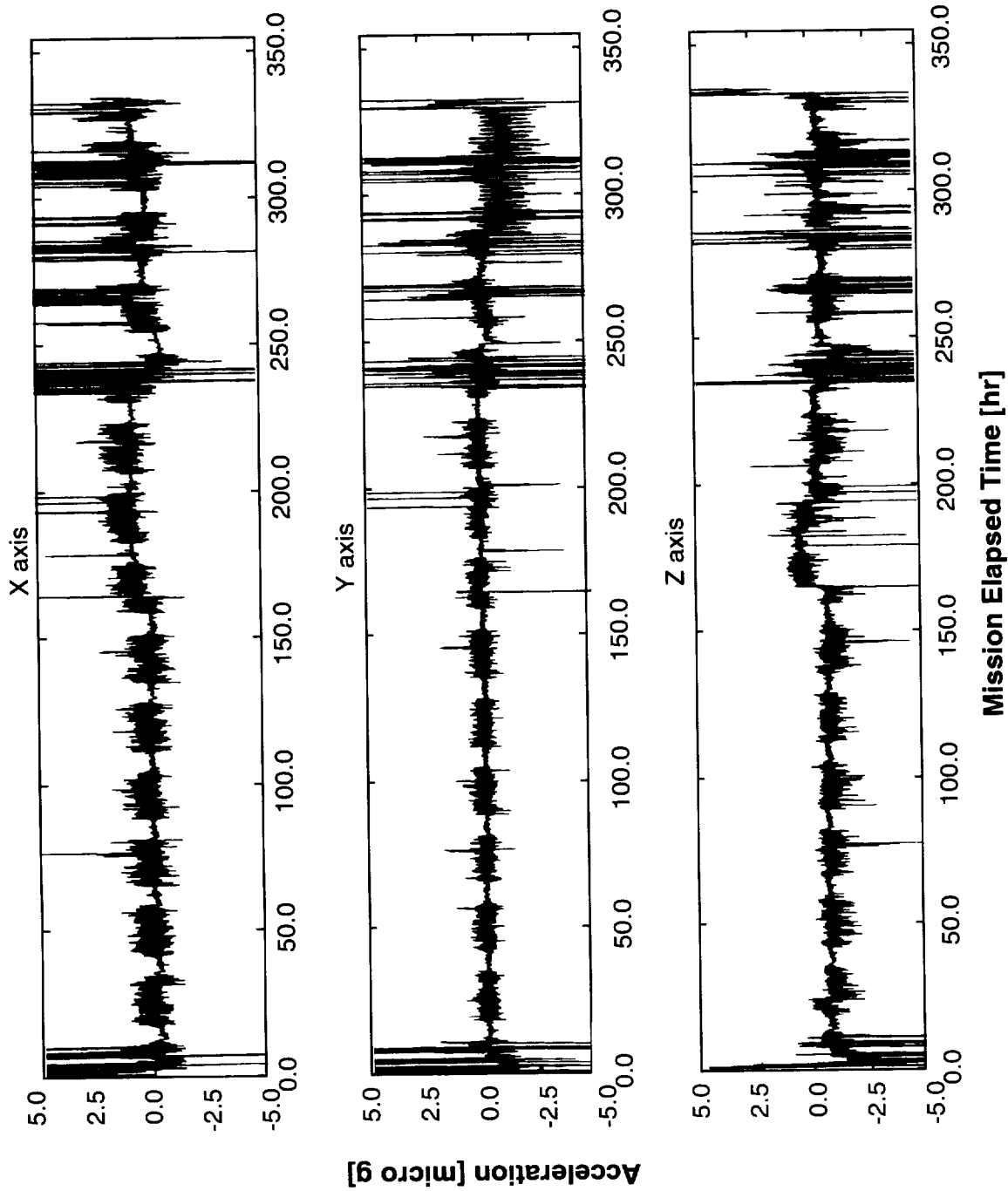


Figure 1. Orbital acceleration research experiment data from STS-62.

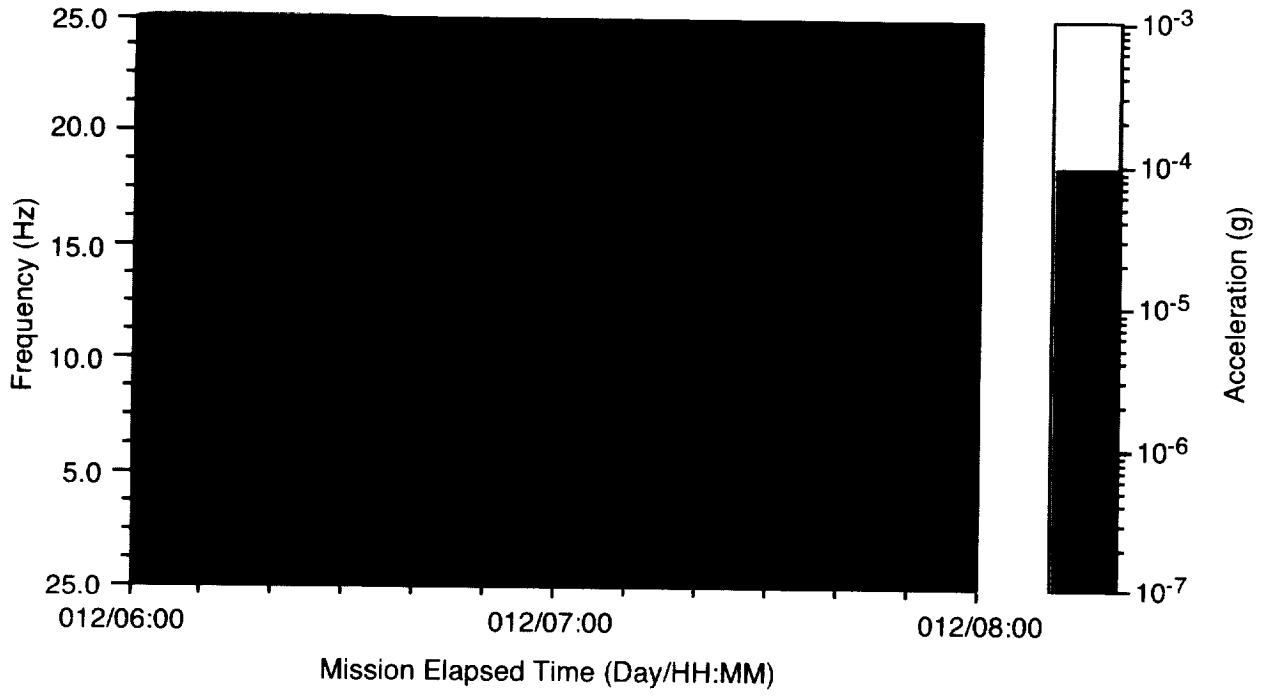


Figure 1-2. Crew sleep period.

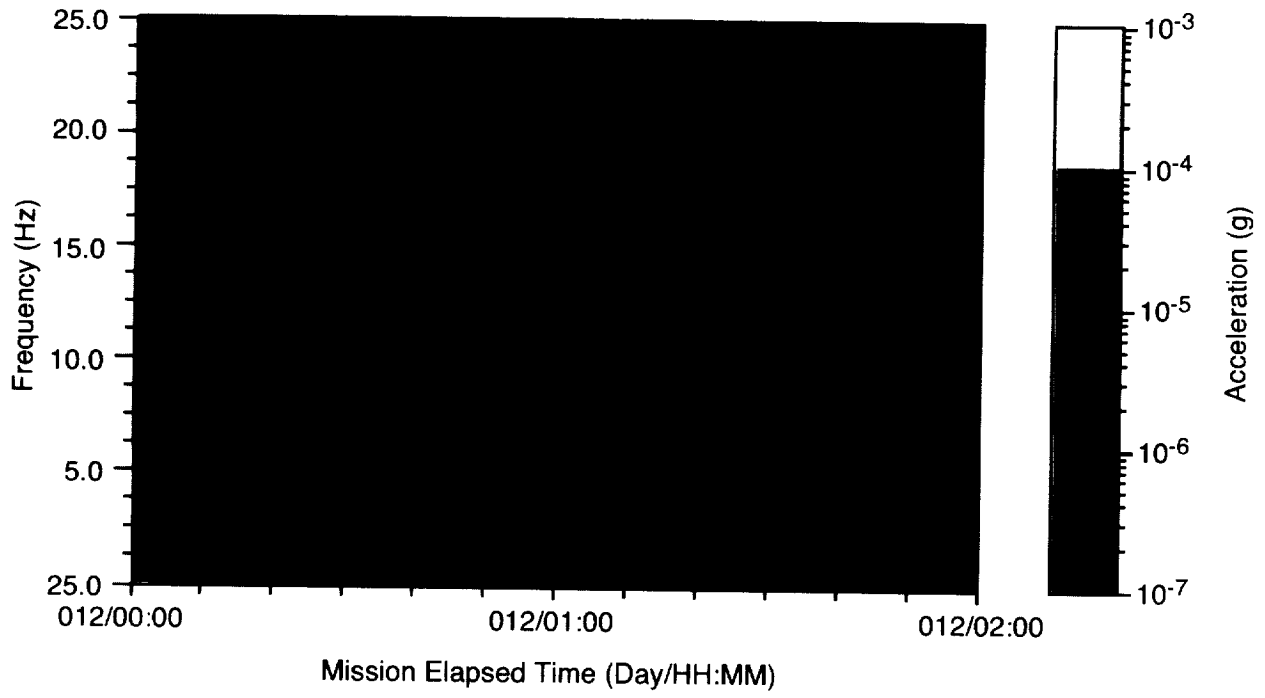


Figure 1-3. Crew active time with exercise period

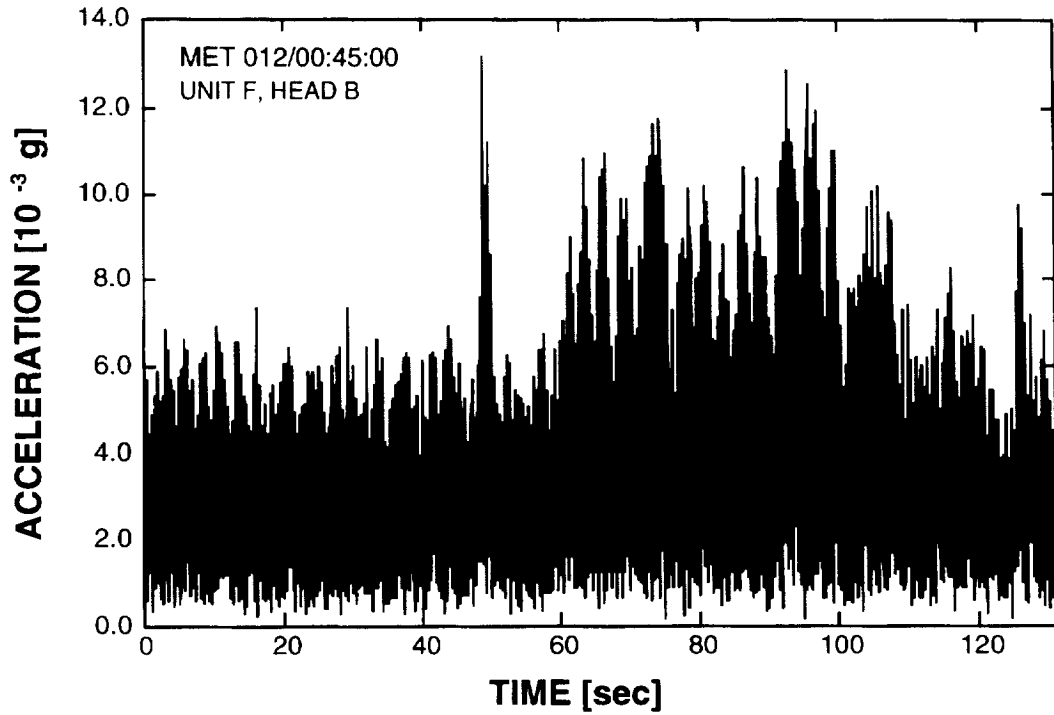


Figure 1-4. Time domain vector magnitude of SAMS data for Unit F, Head B, MET 012/00:45:00–012/00:47:10.

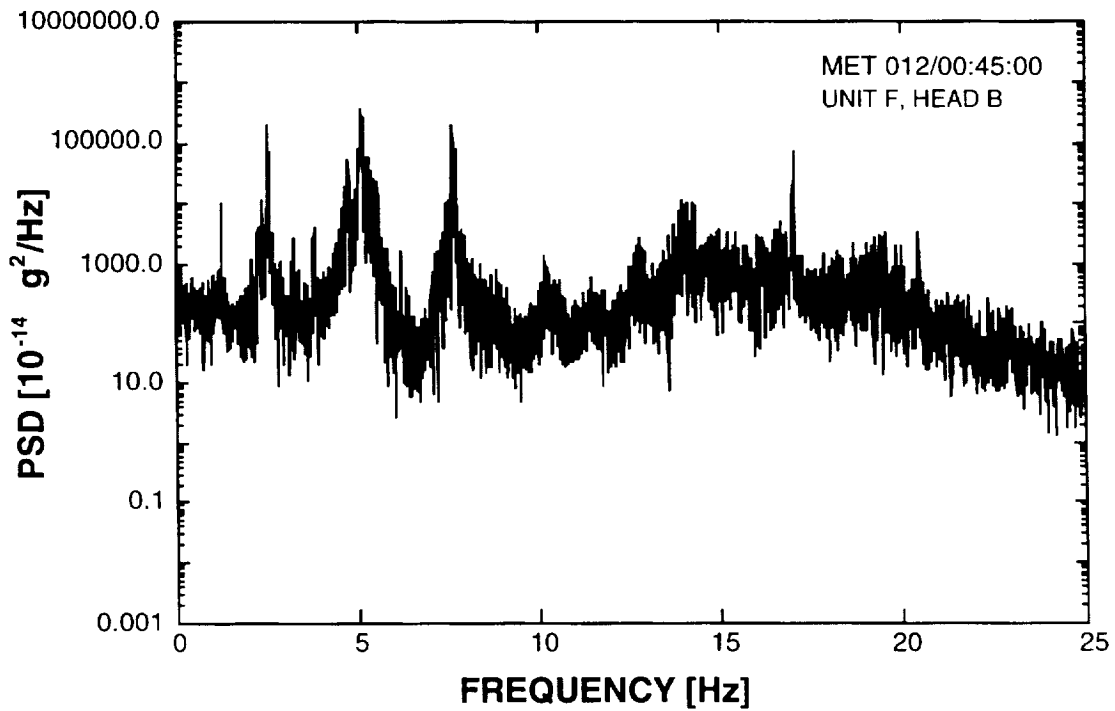


Figure 1-5. Power spectral density vector magnitude of SAMS data for Unit F, Head B, MET 012/00:45:00–012/00:47:10.

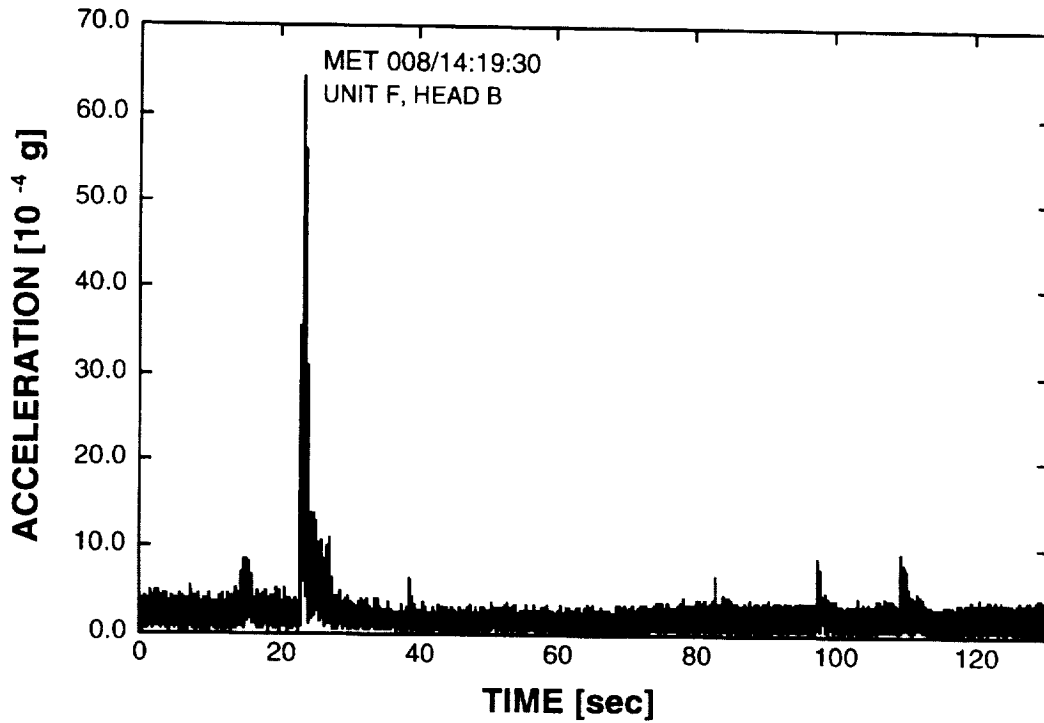


Figure 1-6. Time domain vector magnitude of SAMS data for Unit F, Head B, MET 008/14:19:30–008/14:21:40. Circulation pump activation.

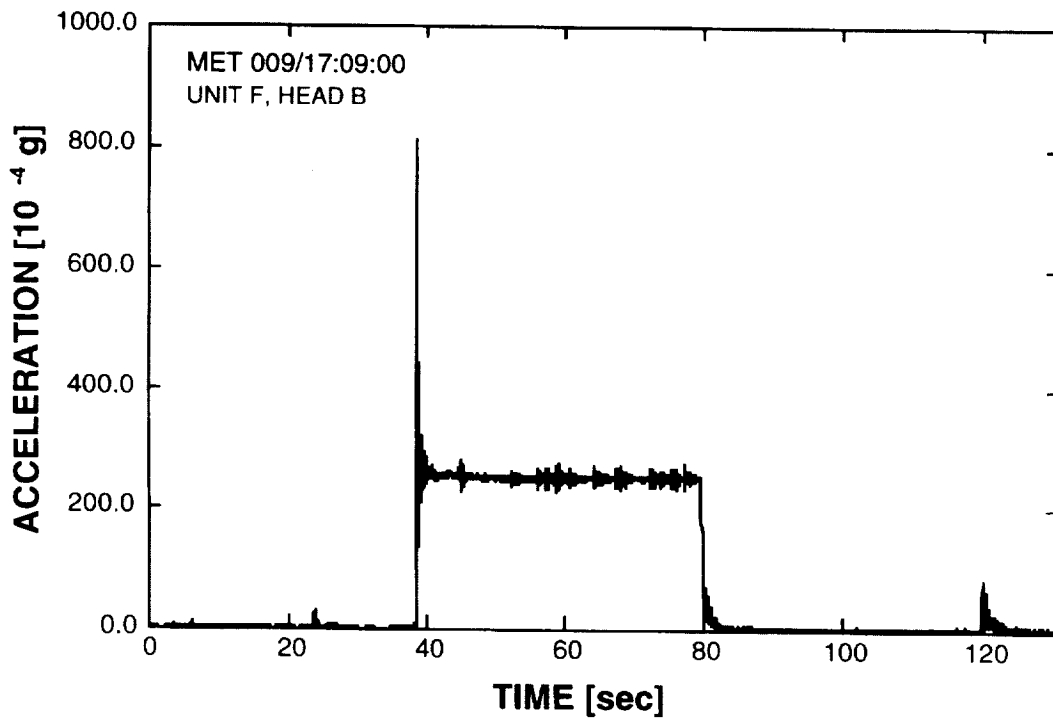


Figure 1-7. Time domain vector magnitude of SAMS data for Unit F, Head B, MET 009/17:09:00–009/17:11:10. OMS.

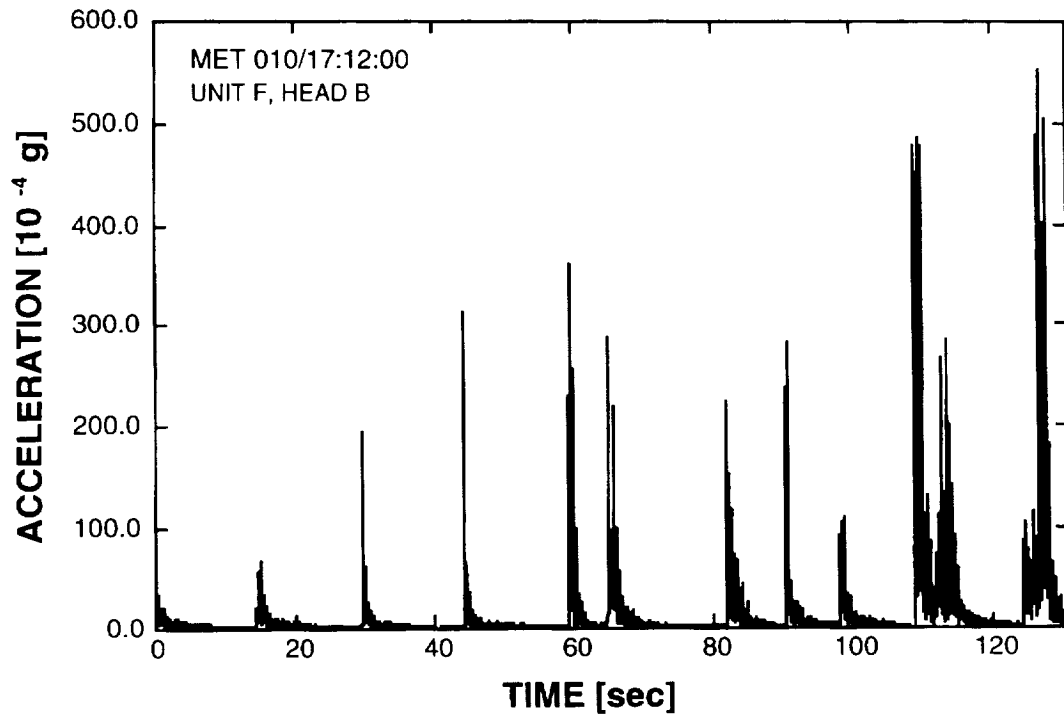


Figure 1-8. Time domain vector magnitude of SAMS data for Unit F, Head B, MET 010/17:12:00–010/17:14:10. Primary reaction control system activity.

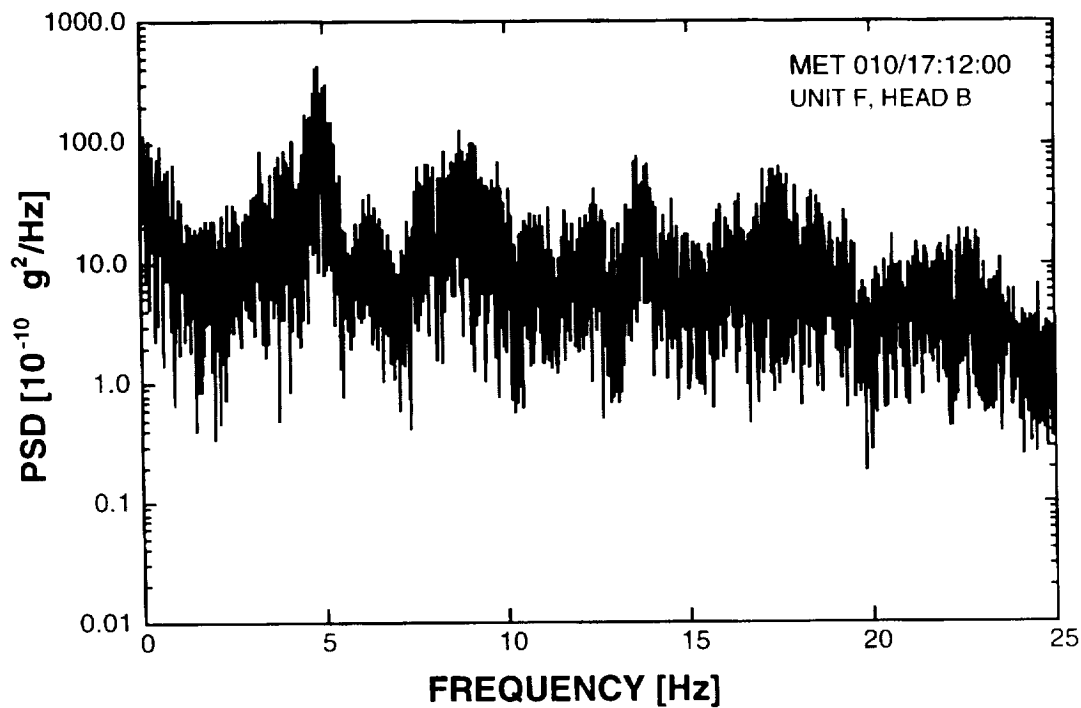


Figure 1-9. Power spectral density vector magnitude of SAMS data for Unit F, Head B, MET 010/17:12:00–010/17:14:10. Primary reaction control system activity.

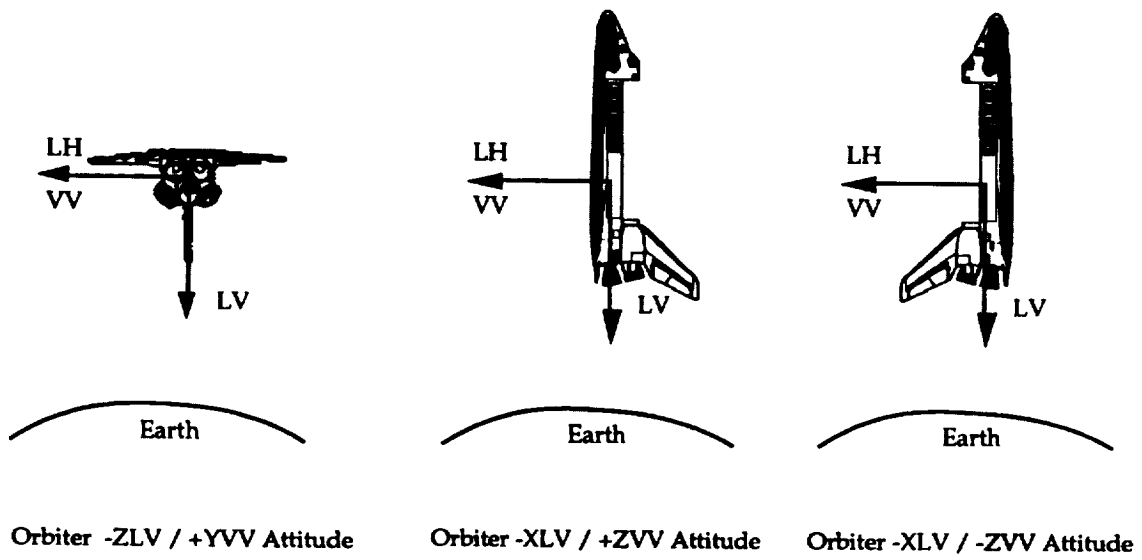


Figure 1-10. Space shuttle attitudes for USMP-2 on STS-62.

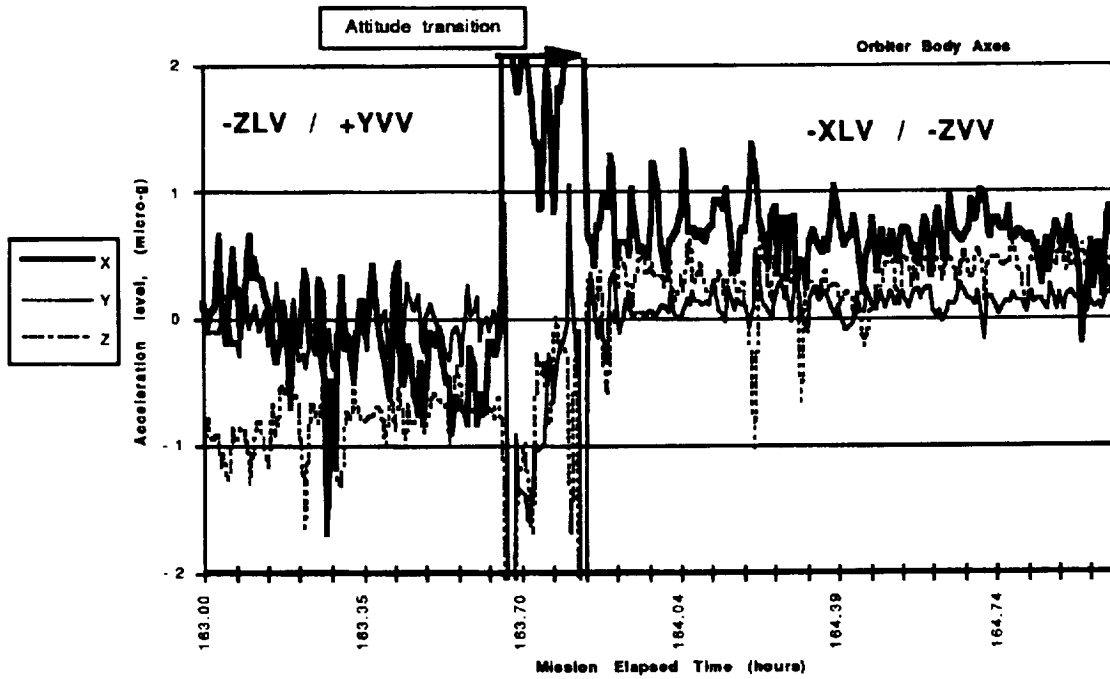


Figure 1-11. Attitude transition during USMP-2 operations (-ZLV/+YVV to -XLV/-ZVV).

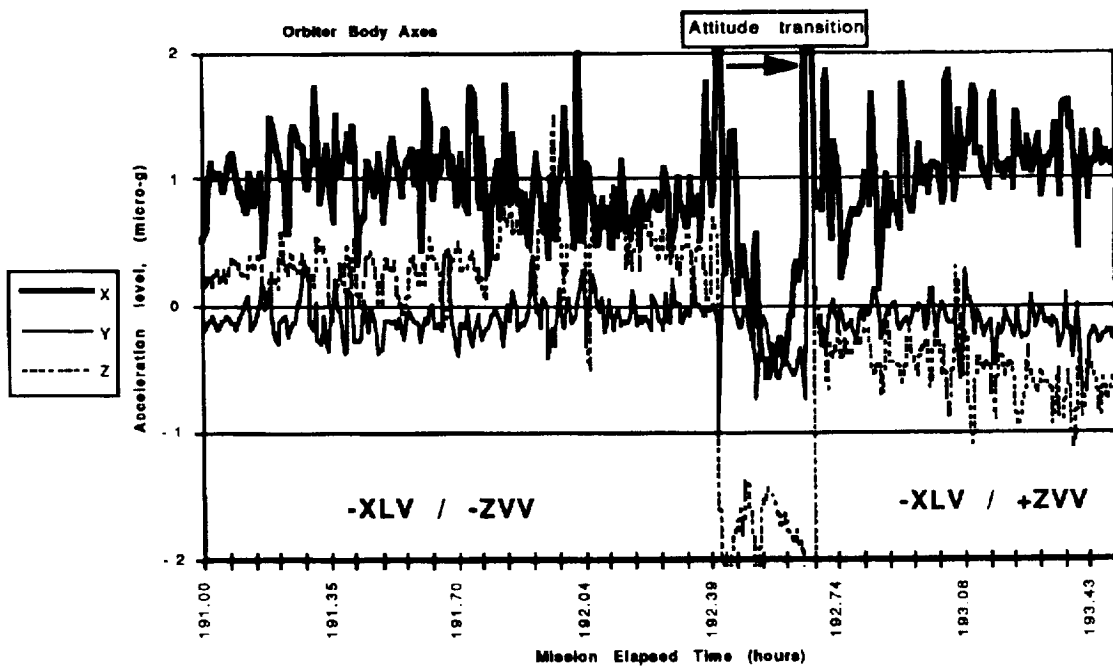


Figure 1-12. Attitude transition during USMP-2 operations (-XLV/-ZVV to -XLV/+ZVV).

SECTION II.

ISOTHERMAL DENDRITIC GROWTH EXPERIMENT

Acknowledgments

The requirements for designing, building, testing, and operating a complex, highly interactive scientific experiment aboard the space shuttle are beyond the skills and resources of any one individual or organization. Diverse teams of dedicated professionals are required. Over the last 10 years the following individuals contributed significantly to the design, construction and operation of this experiment: L.T. Bushnell, R.C. Hahn, B.A. Herbach, P.A. Kobryn, J.C. LaCombe, T.A. Lagrasso, E.R. Rubinstein, N.B. Singh, M.E. Selleck, S.H. Tirmizi, and A. Velosa, at RPI, Troy, NY; and E. Winsa's team: R. Abramczyk, C. Blachly-Olah, D. Burns, A. Fedak, R. Grant, A. Kawecki, F. Kohl, G. Kraft, M. Lehto, L. Levinson, D. Malarik, J. McDade, D. Miller, A. Patel, D. Priebe, J. Robertson, A. Sobota, D. Vachon, G. Weeks, and R. Whittlesey, at or associated with NASA's Lewis Research Center, Cleveland, OH.

Special thanks are due for the continued understanding, interest, and financial support provided by the NASA Life and Microgravity Sciences and Application Division, (Code U), Washington, DC, under Contract NAS3-25368, with liaison provided by the Microgravity Experiments Branch, Space Experiments Division, Lewis Research Center, Cleveland, OH.

The successful operation of the experiment would not have been possible without the efforts of the mission scientist and the mission management team. Thanks also to those who oversaw POCC training and simulations, and the POCC cadre who coordinated and implemented the project's operations. Finally, we also extend our thanks to the crew of STS-62 and the support crews at the NASA research centers involved with the space shuttle's activities.

SECTION II. ISOTHERMAL DENDRITIC GROWTH EXPERIMENT

M.E. Glicksman and M.B. Koss

Materials Science and Engineering Department
Rensselaer Polytechnic Institute, Troy, New York 12180-3590

E. A. Winsa

Space Experiments Division, NASA Lewis Research Center
Cleveland, Ohio 44135

2.1. INTRODUCTION

A vast amount of the products and devices that we use every day—everything from aluminum foil and soda cans, to cars and jet engines—are made from metals and alloys. Early in the creation of these products, the metals are in a liquid, or molten state, that freezes to form a solid, similar to the way water freezes to form ice. If you were to look at some just frozen, or freshly solidified metallic alloy with a strong magnifying glass you would see that its surface is not uniform, but is made up of tiny individual crystalline grains. Moreover, if you were able to look even more carefully at the individual grains through a powerful microscope, you would see that each grain is made up from what looks like tiny metallic pine trees crowding and growing into each other. These metallic tree-like crystals are called dendrites. This description is appropriate because metallic dendrites actually grow analogously in the manner trees grow, with a main branch or trunk, from which grow side branches, from which grow smaller side branches, eventually filling all space.

Dendritic growth is a common mode of crystal growth encountered when metals and alloys solidify under low thermal gradients, as occurs in most casting and welding processes. Furthermore, in engineering materials, the details of the dendritic morphology is directly related to various material responses and properties, such as hot cracking, corrosion resistance, toughness, and yield strength. Although, the effects of the initial dendritic microstructure can be modified by subsequent heat treatments, the final material properties are generally dependent on the details of the original dendritic microstructure. Thus, the understanding and control of dendritic growth in solidification processing is crucial in order to achieve desired physical properties in products created by casting. According to J. S. Langer, writing on dendritic growth in *Physics Today*:

“Metallurgists have long sought to predict and control alloy microstructures. The development of automated, cost effective manufacturing techniques ultimately depends on the precision with which we can solve this problem in non-equilibrium pattern formation. In principle, we would like to incorporate fundamental understanding of microstructures into computer codes that simultaneously help us design materials with made to order properties and optimise their manufacturability and performance.”¹

Of more generic interest, perhaps, dendritic growth is also an archetypical problem in morphogenesis, where a complex pattern evolves from simple starting conditions. Thus, the physical understanding and mathematical description of how dendritic patterns evolve during the solidification process are of interest to scientists and engineers.

In the case of cast alloys that solidify dendritically, the long-term goal is the development of computational methods to elucidate both the microstructure and chemical microsegregation, and the macroscopic end product made up by the agglomeration of millions of dendritic grains. Then, metallurgical engineers can understand and control the metal formation process, and thus be able to make better, less expensive, and more reliable metal products. This requires detailing physical processes over a scale change of at least two orders in magnitude. The mesoscopic dendritic grains, which are strongly influenced by the growth pattern of individual dendrites, are considered the starting point to the problem of micro to macro scale modeling. A full understanding of the behavior of a single, isolated dendrite represents an important step in achieving better understanding and control of the final properties of dendritically solidified materials.

To be sure, remarkable progress has been made recently by numerical simulations of dendritic patterns employing phase field models, and in simulating the grain structure of castings. These types of numerical studies contribute greatly to our understanding of dendritic growth processes and their effect on cast properties. The immediate goal of IDGE's research in dendritic growth is to provide a complete physical and mathematical description of how a single, isolated, dendrite grows.

Over the years, scientists and engineers have learned a great deal about how dendritic crystals grow. Now, the growth of dendrites is known to be controlled by the transport of heat, and/or solute, from the moving solid-liquid interface into the supercooled melt. Under terrestrial conditions, the gradient of the melt density near the solid-liquid interface, caused by the rejection of solutes or latent heat, is acted upon by gravity, resulting in a buoyancy-induced convective flow affecting all the other energy and species transport processes occurring in the liquid phase. The gravity-induced convection severely complicates how dendrites grow, making the study of certain aspects of dendritic growth intractable.

The Isothermal Dendritic Growth Experiment (IDGE), which flew aboard the Space Shuttle *Columbia* (Space Transportation System-62 (STS-62)) in March 1994, was designed, built, and operated to grow dendrites, and photograph them as they grow from the molten state over a range of supercooling, while orbiting the Earth. On orbit, the acceleration field that promotes convection is reduced about one million times from that on Earth. The main scientific objective was to produce data sets of dendritic tip velocities and radii, on orbit, that will become the scientific benchmark for critically testing phenomenological and theoretical models.

2.2. BACKGROUND ON DENDRITIC GROWTH

A number of theories of dendritic crystal growth to predict the dendrite's tip velocity, V , and radius of curvature, R , as a function of the supercooling, ΔT , have been developed over the last 40 years (see the recent review paper).² In 1946, a mathematical solution to the dendritic heat diffusion problem was first analyzed by Ivantsov,³ who, based on thermal transport mechanisms, physical assumptions, and mathematical approximations, modeled the dendrite as a paraboloidal body of revolution, growing at a constant velocity, V . The resultant solution of the partial differential heat diffusion equation can be expressed exactly in paraboloidal coordinates moving at a constant velocity, V , with the dendrite tip as the representative equation,

$$\Delta\Theta = \text{Pe}(e^{\text{Pe}})E_1(\text{Pe}) \equiv \text{Iv}(\text{Pe}). \quad (1)$$

In this formulation, $\text{Iv}(\text{Pe})$ is identified as the Ivantsov function, where

$$\Delta\Theta = \frac{\Delta T}{(\Delta H_f / C_p)}, \quad (2)$$

is the nondimensional scaled supercooling, Pe is the growth Péclet number,

$$Pe = \frac{VR}{2\alpha} \equiv Iv^{-1}(\Delta\Theta), \quad (3)$$

and $E_1(Pe)$ is the first exponential integral function. In these equations, ΔT is the applied supercooling, ΔH_f is the molar latent heat, C_p is the constant pressure molar specific heat, V is the dendrite tip velocity, R is the dendrite tip paraboloidal radius of curvature, α is the thermal diffusivity of the melt phase, and $Iv^{-1}(\Delta\Theta)$ is a formal representation of the inverse of the Ivantsov function (which cannot be expressed in terms of known functions).

This diffusion solution is, however, incomplete, insofar as it specifies only the tip growth Péclet number, $VR/2\alpha$, as a function of the supercooling, and not the explicit dendritic dynamic operating state, V , and R . The Péclet number obtained from the Ivantsov solution for each specified supercooling yields, instead, an infinite manifold of V , and R , ordered pairs (V, R) , that satisfy the diffusion solution at that particular value of ΔT . Specifying the driving force alone through Ivantsov's solution does not uniquely describe the operating state.

The early experimental data on the interface velocity of pure transition metals such as Ni and Co provided more of a qualitative test of theory, inasmuch as there were no corresponding morphology measurements, the velocity measurements themselves had a large experimental scatter (20–50 percent), and the thermophysical properties needed for checking theory were either unavailable or inaccurate.

In the early 1970's, Glicksman and co-workers showed that succinonitrile (SCN), a body centered cubic (BCC) organic plastic crystal, could be used as a model metal analog system for studying dendritic growth.⁴ This was possible because SCN solidifies like the cubic metals, i.e., with an atomically "rough" solid-liquid interface, yet retains advantages because SCN displays convenient properties for solidification experiments, such as a low melting temperature (58.08 °C), optical transparency, and the potential for accurate characterization of its thermophysical properties. The use of SCN greatly facilitated dendritic growth studies over the past 20 years, where now dendritic tip velocities and radii could both be accurately measured and used as a critical test of theory.

The earlier studies convincingly showed that the then current theories of dendritic growth, i.e., combining the Ivantsov solution with the "maximum velocity" hypothesis, was incorrect. Furthermore, one found that unique, steady, operating states (V_{exp}, R_{exp}) are observed at any specified supercooling, ΔT . Considerable theoretical efforts within the physics community have been directed to answering the question as to whether, and under what conditions, a second independent equation or length scale exists, which, when combined with the Ivantsov diffusion solution, mathematically selects the unique (i.e., observed) dynamic operating state^{2 5} which nature seems to have no trouble selecting.

This effort to find a second lengthscale has in large part been shaped by the observations that for several materials undergoing unconstrained dendritic growth, VR^2 , is constant, or very weakly varying, as a function of the supercooling. Two of the candidates for the additional crystal growth physics that provide the second crucial equation are the effects from the solid-melt interfacial energy, the influence of temperature fluctuations in the melt, or both. Furthermore, the scaling equation derived from these additional physical considerations may be based on several different dynamical considerations, such as

morphological stability, microscopic solvability, shape anisotropy, noise amplification, trapped waves, etc. Although the underlying mechanisms, or even the physics, for these “theories of the second length scale” might in fact be quite different, their results are often encapsulated with a scaling constant,

$$\sigma^* = \frac{2\alpha d_o}{VR^2}. \quad (4)$$

Here, σ^* is usually referred to as the stability, selection, or scaling constant, and d_o is the capillary length scale, a material parameter defined as,

$$d_o = \frac{\Omega_s \gamma}{\Delta S_f} \left(\frac{C_p}{\Delta H_f} \right), \quad (5)$$

where Ω_s is the molar volume, ΔS_f is the molar entropy of fusion, and γ is the solid-liquid interfacial energy. Solving equations (3) and (4) for V and R yields,

$$V = \frac{2\alpha\sigma^* I v^{-2}(\Delta T)}{d_o}, \quad (6)$$

and

$$R = \frac{d_o}{\sigma^* I v^{-1}(\Delta T)}, \quad (7)$$

where now, V and R are unique functions of the supercooling.

An experimental requirement to test dendritic growth theories fully is then to measure *simultaneously* the dendrite tip velocity and radius of curvature, and then test the validity of equations (6), (7), and (1). Early SCN dendritic growth data showed that heat transfer due to natural convection might be modifying the diffusional heat transfer, i.e., the shape of the dendritic growth chamber, and the direction of [100] growth of the primary dendrite with respect to gravity, affected the measurements. It became necessary to characterize dendritic velocity and radius measurements not only as a function of the applied supercooling, but also parameterized by the growth orientation with respect to gravity.

2.3. THE ISOTHERMAL DENDRITIC GROWTH EXPERIMENT (IDGE)

Unfortunately, more detailed subsequent work showed that gravity-induced convection actually *dominates* dendritic growth, particularly in the lower supercooling range typical of industrial castings.^{6 7} Convection confounds any straightforward analysis based on diffusive heat transfer. There have been some attempts to estimate the effects of natural or forced convection on dendritic growth,⁸ but these calculations are themselves coupled to yet unproven elements of basic dendritic growth theory, and, consequently, cannot provide an independent test of the theory. In the higher supercooling range, where convective influences diminish in comparison to thermal conduction, the morphological scale of dendrites becomes too small to be resolved optically at the high growth speeds encountered.

The experimental situation prior to the microgravity experiment reported here, was that there appeared to be too narrow a range of supercoolings in any crystal-melt system studied terrestrially that remains both free of convection effects, and also permits an accurate determination of the dendrite tip

radius of curvature. Thus, a low-gravity dendritic growth experiment was proposed to measure definitively the kinetics and morphology of dendritic growth, and to measure the effects of natural convection on dendritic growth. Such a test requires that a single, clearly defined experimental parameter, namely, the supercooling, fully determine the resulting steady-state dendritic growth velocity, V , and tip size, R . NASA's Microgravity Science and Applications Division supported the development of a critical microgravity space flight experiment to evaluate dendritic growth theories.⁸⁻¹⁰ Designated the IDGE, the first flight, manifested on the second United States Microgravity Payload (USMP-2) mission, was launched and operated on the STS-62 on March 4-18, 1994. The IDGE enabled the acquisition of accurate dendritic growth speed and morphology data under diffusion-controlled conditions, while greatly reducing buoyancy-induced convective heat transport through the reduction of gravity.¹¹ As shown, the microgravity environment broadens this range of supercoolings and permits for the first time a critical assessment of both the heat transport theory and the interfacial kinetics behavior.

2.3.1. IDGE Growth Chamber

The techniques for accomplishing simultaneous kinetic and morphological measurements for SCN dendrites are well established.⁴⁻⁶ However, the constraints of an autonomous, or tele-operational, microgravity experiment require extensive modifications of established ground-based laboratory techniques.⁹⁻¹⁰ This is most evident in the design and construction of the flight growth chamber (figure 1), which is physically and metaphorically central to the operation of the IDGE apparatus.

In order to withstand the $5 g_0$ launch acceleration, and the other rigors of space flight, the usual, delicate, all glass laboratory growth chamber was replaced with a more rugged combination of glass and metal. The flight chamber provides an unobstructed view of the growing dendrites through four windows, set perpendicularly, which allow for stereographic correction of the measurements. This type of chamber requires that the dendrites grow within the field of view of the windows. This requirement is accomplished by providing a thin capillary injector tube, called the stinger. Dendritic growth is initiated by energizing thermoelectric coolers attached to one end of the stinger. The other end of the stinger, where the dendrite emerges in the center of the chamber, is notched, much like the tip of a fountain pen. This helps isolate the leading dendrite and reduces the time needed until the leading dendrite is isothermal and has achieved steady state.

Two stable thermistors (the second thermistor is redundant) monitor the temperature inside the chamber. The phase change volume expansion and the thermal expansion of the melt are compensated by stainless-steel bellows which prevents either stray vapor cavities from forming or overpressuring the growth chamber. The growth chamber is sealed under vacuum, and the external pressure which is transmitted through the bellows from the thermostatic bath is sufficient to prevent any free surface formation due to cavitation. The attachment of all components, joints, and seals used in the growth chamber that come in contact with SCN employs autogenous electron beam welds. This joining method preserves the purity of the SCN from contamination by avoiding the introduction of any solder, fluxes, elastomers, or other alloying components that could contaminate the SCN.¹²

The growth chamber is mounted inside a temperature-controlled tank (figure 2) or thermostat inside an experiment apparatus container (EAC). Also inside the EAC is the modified shadowgraphic optic and photographic system, the dendrite growth detection system utilizing optic ram chips, and the control electronics. The inner pressurized vessel of the EAC is controlled in an atmosphere of moist nitrogen at 15 lb/in^2 and $25 \text{ }^\circ\text{C}$. The temperature control tank is filled with a mixture of ethylene glycol and water in a proportion such that its index of refraction matches that of molten SCN. Index matching enhances the capability of the optic system. Two heaters (one redundant) and a rotating propeller permit temperature

control to the desired level (within 2 mK of the set point) both temporally and spatially. All control, including data acquisition is performed by on-board computers.

2.3.2. Flight Experiment Procedure

The IDGE flight experiment was divided into 60 operational cycles. The first cycle, the warm-up cycle, consists of bringing the system up to the operational temperature where all system components are checked and initialized. Also, the purity of the SCN test specimen was confirmed by examining the flatness of the melting plateau. The second cycle measured the liquidus temperature of the SCN as a calibration point from which all subsequent supercoolings are measured. The remaining cycles were dendritic growth cycles where dendrites are grown and photographed at varying supercoolings.

For each dendritic growth cycle, the thermostatic bath is heated to over 3 K above the SCN melting temperature. The bath is maintained at this elevated temperature until the SCN inside the chamber reaches, and becomes stable, at this temperature. This insures that all the SCN in the chamber is melted and that no stray crystals are present. The bath temperature is then reduced to the temperature that will produce the desired supercooling in the SCN. After the molten SCN has cooled and stabilized at the prescribed supercooling, thermoelectric coolers initiate solidification at the capped end of the stinger. The solidifying SCN grows down the inside wall of the stinger until it emerges as a dendritic crystal from the stinger in the center of the growth chamber, which is still molten and spatially uniform in temperature at the prescribed supercooling.

For each dendritic growth cycle, the experiment obtained a time series of stereo-pairs of 35-mm photographic images, low-resolution, binary, digitized electronic images (figure 3), and various data streams characterizing the dendrite's growth conditions during the cycle. For each image pair, either 35-mm film negative or digitized image, we measured the position of the dendrite tip, and the associated time that the image was recorded. We determined the dendritic velocity by calculating the slope of the displacement-time curve from the steady-state regime of the growth cycle. The velocity is then adjusted by appropriate stereographic and magnification factors. This procedure yields a set of dendrite velocity measurements accurate to about ± 2 percent.

The overall experimental task of measuring the size and shape of steady-state dendritic crystal's tips is more complex. The complexity is evidenced by noting that the typical experimental uncertainty encountered in the best terrestrial laboratory-based tip radii measurements is typically ± 10 percent. Some of the details of our tip shape analysis methods are described elsewhere,¹³ although additional important changes for improving radii measurements are currently under development in our laboratory. In summary, the grey-scale film image is digitized to locate the solid-liquid interface, which is reduced to a list of ordered coordinate pairs that define the dendrite profile or edge. The data describing the dendrite profile is regressed to an equation for the model of a dendrite, from which it is straightforward to calculate the radius of curvature at the tip. The tip radii data from the IDGE are usually accurate to better than ± 5 percent for supercoolings less than 1.0 K.

2.4. RESULTS

The IDGE apparatus, from the multilayer thermal insulation blanket to the succinonitrile dendritic growth chamber, worked flawlessly during the USMP-2 mission, and the 9 days of dedicated microgravity time was employed to the fullest. At mission completion, the IDGE had obtained scientific data comprising approximately 450 photo negatives, over 1000 slow scan TV (SSTV) images, and numerical data characterizing the temperature environment of the dendritic growth cycles, spanning the supercooling

range from circa 0.05 to 2.0 K—a dynamic data range of almost 40, greatly exceeding preflight expectations.

To date, we have completed the reconstruction of the experiment monitoring printouts for each dendritic growth cycle, and calculated the steady-state temperatures, pressures, and corrected supercooling for each of 59 cycles. We have completed detailed calculations of dendritic velocities from the SSTV images and from the 35-mm photo negatives. We have completed calculations of the stereographic corrections, dendrite projection view orientation, dendrite unit vectors, and the start time, end time, and duration of steady-state growth time, for all applicable growth cycles. Finally, we have completed the selection, image capture, image processing, and radius calculation of the best focused, steady-state photo negatives, for each growth cycle. A complete “canonical” data set is being prepared at this time (March 1995).

2.4.1. Dendritic Growth Velocities

The two ground-based dendritic growth velocity data sets used for comparison with the microgravity data (Glicksman/Huang and IDGE terrestrial) are in close agreement over the entire supercooling range (figure 4). Thus, negligible differences exist between these two data sets arising from the different chamber size and shape, the different SCN specimens employed, and the different eulerian angles (between 0° and 45°) of the [100] growth direction with respect to gravity. However, there are dramatic differences in the observed growth rates, particularly at the lower supercoolings, between terrestrial and microgravity conditions. At about 1.7 K supercooling there still appears to be a slight reduction in the growth velocity under microgravity conditions as compared to terrestrial conditions. This reduction in velocity becomes more evident at 1.3 K supercooling, where the velocity measured in microgravity is approximately 15 percent lower than the terrestrial data, increasing to almost 200 percent reduction at small supercoolings. These particular results show that there are substantial convective effects at 1 g₀, even at the highest supercoolings for which the solidification microstructures can be resolved during in situ observations.

The slope of the microgravity data changes from being steeper than the terrestrial data at the higher supercoolings, to being almost parallel to it at the lower supercoolings (less than ca. 0.4 K (figure 5)). This reveals that even in microgravity, substantial convective effects reappear at the lower supercoolings. The scatter in the microgravity data at the lower supercoolings may be ascribed (although not yet proven) to variations in the magnitude of the acceleration environment, or to variations of the direction of growth of the measured dendrite with respect to the direction of the local net microgravity acceleration, or perhaps to some combination of the two effects.

The discussion of the radii results (figure 6) parallels that already given on the velocity data, except that here the radius is not as strong a function of supercooling as the velocity, so that the ratios between the terrestrial and microgravity results are smaller, although still evident. An experimentally determined microgravity scaling constant, $\sigma^* = 2\alpha d_p / (VR^2)$, calculated from the microgravity measurements of V and R , at high supercoolings where convection affects are assumed minimal, yields $\sigma^* = 0.0194$. Curiously, this value of σ^* is almost exactly the same as the terrestrially measured value of σ^* , and this surprising agreement will be discussed in more detail later.

Theoretical velocity calculations using the microgravity measured σ^* and Ivantsov's transport theory do not describe the microgravity velocity data over *any* supercooling range (figure 4). The theoretical predictions are, however, parallel to and above the microgravity data at the higher supercoolings. If instead of directly calculating σ^* , we treat σ^* as an adjustable scaling parameter, which

we designate, σ_v , we are able to fit the observed microgravity velocity data at supercoolings of 0.47 K and above with $\sigma_v = 0.0164$. The deviations between the microgravity data at the lower supercoolings and the fit at the larger supercoolings using σ_v provide quantitative evidence that the quasi-static residual microgravity level of approximately $0.7 \mu g_o$ has a significant, and eventually dominant, effect on dendritic growth. Thus, at sufficiently low supercoolings, even in microgravity, convection effects substantially alter the growth velocity from what would be expected by heat diffusion alone (figure 5). The excellent agreement of velocity calculations with σ_v with the microgravity data over the range of supercoolings from 0.47 to 1.7 K show that this is the supercooling range over which one must test dendritic growth theories which employ heat conduction as the rate limiting transport process.

2.4.2. Dendritic Tip Radii

Theoretical radii calculations also using the microgravity measured value of σ^* and Ivantsov's transport theory do not describe the microgravity radius data over *any* supercooling range either (figure 6). Again, however, a one-parameter fit to the radii data over the supercooling range from 0.47 to 1.57 K yields the adjustable scaling parameter $\sigma_R = 0.0179$, which describes the microgravity radii data at higher supercooling. Thus there appears to be no *single* scaling parameter, whether calculated directly from the velocity and radius data combined or inferred as an adjustable parameter from the velocity or radius data separately that when coupled to the Ivantsov heat transfer results, properly describes *both* the velocity and radius data. This suggests strongly that the Ivantsov function combined with a *unique* scaling constant is not an accurate description of the dendritic growth process.

2.4.3. Growth Péclet Number

The failure of Ivantsov's diffusion solution, when combined with a unique scaling rule to describe the diffusion-limited growth regime, is apparent from the differences found between the experimentally determined growth Péclet number data calculated from the velocity and tip radius data sets from both the microgravity and terrestrial experiments, and the theoretical Péclet numbers (figures 7 and 8). This theory has *no* adjustable parameters. The microgravity measured Péclet number data set is clearly separated from the terrestrial data. Most importantly, even in the diffusion-limited regime, the microgravity data are systematically lower than that predicted for paraboloidal dendrites as the Ivantsov theory curve.

Before the IDGE, it was not possible to separately test the Ivantsov solution and the scaling rule hypothesis. To our knowledge, this is the first clear evidence gathered that shows that Ivantsov's formulation for paraboloidal dendritic growth does not accurately describe dendritic growth in SCN. The approximate agreement achieved between the transport theory and the microgravity data indicates that dendritic growth is indeed most likely governed by the diffusion of latent heat from the crystal-melt interface, but the detailed Ivantsov formulation to describe that diffusion process is in need of some modification.

2.4.4. Kinetic Scaling Parameter

Nonetheless, it remains instructive to examine the scaling law data (figure 9). The scatter, both within and among the three data sets, is significant. There appears to be a trend where σ^* increases inversely with supercooling. If σ^* has a dependence on supercooling, that dependence is rather weak compared to the scatter observed in the new dendritic growth data, especially in the diffusion-limited regime established by the microgravity velocity data. Thus, assuming σ^* remains constant over this limited supercooling range would only introduce a slight error in any quantity that depends on σ^* . Most striking is the observation that although the terrestrial and microgravity velocity and radii data are markedly different,

the terrestrial and microgravity σ^* values are virtually indistinguishable. This surprising finding is in agreement with our earlier observation that the average of σ^* from the diffusion-limited microgravity data is almost exactly the same as the average value of σ^* derived from terrestrial measurements.

2.5. TELEOPERATIONS

2.5.1. IDGE Operating Plans

As a default, the IDGE had an autonomous preprogrammed experimental protocol. The IDGE autonomous flight protocol is divided into 38 cycles. The initial warm-up cycle consists of heating the system up to the operational temperature, where all system components are checked and initialized. A slow melting plateau is performed as a check of specimen purity. Cycle 01 provides a freezing plateau, which yields the precise liquidus temperature of the SCN (± 0.001 K) in the chamber, and serves as the calibration point from which all subsequent supercoolings are measured. Cycles 02–11 provides dendritic growth data acquisition, where dendrites were grown and photographed at each of 10 programmed supercoolings taken in logarithmic steps between 0.1 and 1.0 K. Cycles 12–31 repeat the cycle 02–11 sequence twice more, so that each prescribed supercooling in the nominal range is performed three times.

An additional seven cycles are scheduled for repeating some of the growths at the larger supercoolings, where, because of the difficulties in measuring small tips ($< 25 \mu\text{m}$), redundant data would be beneficial. These cycles also provide the option to extend the supercooling range of the experiment above and below the nominal preprogrammed range. The protocol specifies that a sequence of six photographs are exposed for each camera view during each growth cycle. The photo intervals for each growth cycle were determined from theory based on the assumptions of diffusion-limited heat transfer and a paraboloidal tip shape coupled to the simple scaling rule that $VR^2 = \text{const.}$, where V and R are the speed and radius during steady-state growth.

The IDGE operating plans allowed the initial 12 cycles to run autonomously. Then, based on the data analyses performed during those initial 12 cycles, minimal parameter changes were made to the experiment protocol for the next 10 cycles. For example, when necessary, we changed the photo times and nothing else. Finally, after these 22 cycles were completed, we used the full telescience capabilities of the IDGE to maximize the quantity and quality of the data return. Specifically, we were able to improve the data return by modifying the photo timing intervals, the number of photographs per growth cycle, and the selection of supercoolings to be examined. The telescience operations must manage all these changes to produce the optimal data return under the constraint of two limiting resources: (1) Time, limited to approximately 9 days of microgravity with priority commanding when the USMP-2 payload was designated as the primary payload of STS-62; and (2) film, limited to approximately 225 *usable 35-mm photo frames* available on each camera. The IDGE operations are *terminated* when either of these two limiting resources are exhausted. Therefore, the optimal strategy was to use all the film before the microgravity time was completed, and to complete the microgravity time without any unexposed frames remaining in the cameras.

The IDGE science team could, by obtaining telescience data, and performing the analysis outlined above, monitor the progress of the experiment, and, where needed, revise the protocol parameters in accordance with the replanning operations. Once a day, at the completion of the first shift consol duties, the science team then integrated all the data generated and analyzed at the Payload Operations Control Center (POCC) and transmitted from Rensselaer Polytechnic Institute (RPI), and replanned the mission for the next 30 hours.

2.5.2. Flight Operations

On March 4, 1994, 8:53 AM EST, the Space Shuttle *Columbia* (STS-62), lifted off from the Kennedy Space Center, Cape Canaveral Florida, into a low Earth orbit of approximately 163 nautical miles. On board the *Columbia*, as part of the USMP-2 was the IDGE. The IDGE powered up four hours after launch, ran through the calibrations cycles, and then commenced the dendritic growth cycles. Cycle 03, at a supercooling of approximately 0.17 K, afforded the first opportunity to get critical feedback from the experiment. The initial velocity analysis, completed around day 01, hour 08 Mission Elapsed Time (MET), showed a significant departure from theory.

The velocity calculated from the SSTV in microgravity was about 3.6 μm seconds, as compared to 9.8 μm seconds at terrestrial gravity, and 2.8 μm seconds as predicted by theory (figure 10). Based on the preprogrammed photo intervals for this growth cycle, the disparity between the predicted velocity and the observed velocity, meant that three of the six programmed photographs were taken when the dendrite was beyond the camera's field of view. Later, a more detailed analysis revealed that steady-state growth ceased after only 5.5 mm of growth (figure 11), rather than after 10 mm of growth experienced under terrestrial conditions. This unexpected occurrence, combined with the error in the estimated velocity, resulted in only one photograph being exposed during the steady-state regime. Thus, insufficient film data were available to calculate the steady-state velocity from this growth cycle.

A similar analysis conducted for all analyzable data obtained through growth cycle 11, for supercoolings between 0.1 and 1.0 K, revealed four significant trends that were used in subsequent mission replanning: (1) The measured velocity in microgravity is different from the theoretical estimates; (2) steady-state dendrite growth ceases in microgravity over a total growth distance smaller than under terrestrial conditions; (3) the total steady-state growth distance is proportional to the supercooling; and (4) the growth transient prior to achieving steady-state growth is smaller in microgravity than in terrestrial gravity, and that displacement decreases as the supercooling is increased.

Many of the experimental parameters for the subsequent growth cycles were adjusted using the empirical "rules" developed from the analysis of the initial preprogrammed growth cycles. During cycles 12–21, we revised the photo times only. These changes provided two advantages: (1) Accurate velocity and radius data from the film data could be obtained because we were now using precise photo timing intervals; and (2) with these revised photo timing intervals, each dendritic growth cycle took significantly less time than had been allocated in the preprogrammed flight protocol. Therefore, besides improving the quality and quantity of the data we were now obtaining, one of the IDGE's limiting resources, time in low Earth orbit, was effectively increased. However, while making these changes to the photo timing intervals, we discovered that the time to enter, uplink, and verify a command sequence that implemented the parameter change, took four times as long as what we experienced while training for the IDGE mission. Slow commanding increased the time and effort expanded by IDGE team members who planned and executed the commanding sequences during the flight.

The telescience analysis performed during cycles 12–21 convinced the team to "stretch" the IDGE film resources to match the increased on-orbit time by readjusting the experimental parameters to expose only four photos per growth cycle through cycle 30, and then to expose only two photos per cycle from cycle 31 on. These changes saved two photos per growth through cycle 30, and four per growth from cycle 31–37. At two photos per cycle, there was enough film for more than 60 growth cycles. Also, the telescience results known at that point in the mission suggested that the best strategy for the remainder of the experiment was to extend the range of supercooling both above and below that selected originally. Also, a different selection of supercoolings was sampled within the specified range rather than at the 10 preprogrammed supercoolings from which data had already been adequately acquired.

The IDGE experiment unfolded according to the revised plans until cycle 33, when it was realized that the operating software would not function properly after cycle 37—the last preprogrammed growth cycle. The experiment was repeatedly interrupted by executing an uplinked “pause” command, while the team verified that this was in fact true. The experiment was suspended until a solution to this problem was determined and implemented. The solution chosen was to set the photo times and the number of photos so that the required data could be obtained, and then a command was sent to reboot the computer before the start of the next growth cycle. Since, the cycle index recorded by the software only updated at the end of a growth cycle, the cycle counter never incremented. When the computer finally rebooted, the software read the current disk memory, and acted as if the current growth cycle still needed to be performed. However, during the first part of the growth cycle, a set of commands was sent to the IDGE to change the supercooling and the photo times. Then, when the “new” required data had been collected, we again sent the reboot command. In this manner, the IDGE continued to operate successfully well beyond 37 growth cycles without advancing the cycle index and reaching the shut-down condition which would have occurred after the cycle count exceeded 37.

The limitation to this scheme was that it was not possible to perform dendritic growths at supercoolings above 0.2 K, because the photo intervals were too short to insure that the computer reboot command could be entered, uplinked, and executed in time before the cycle count would increment. We were, nonetheless, able to obtain critical microgravity growth data at three supercoolings above 0.2 K, by using three of the remaining five cycles in the uninterrupted, and incrementing mode.

At completion of the USMP-2 flight, where 38 experimental cycles were originally planned, 60 cycles had actually been completed. Fifty-seven of the 60 were dendritic growth cycles, from which 56 SSTV velocities were calculated. Of those, photographic sequences were attempted for 52, of which 40 useful velocity measurements were made, and 12 failed. Of the 12 where velocity measurements were not possible, 3 had incorrect preprogrammed photo intervals based on theory, so that only 1 photo was exposed during steady-state growth. Nine of the last 24 cycles (all with only 2 photos exposed) also failed to yield a steady-state velocity measurement. Either the first photo was taken before steady-state began, or the second photo was taken after steady-state ended. In both cases, it was known that these measurements should not be included in any final data set, and two photo cycles could be attempted, because the SSTV telescience data located the steady-state regime. The reliable and accurate “canonical” data obtained in microgravity describe dendritic growth over a supercooling range from about 0.06 to 1.9 K. Without teleoperations, that range would have been from 0.22 to 1.3 K supercooling, as shown in the inner rectangle of figure 12.

2.6. SUMMARY AND CONCLUSIONS

We measured the dendritic growth velocities and tip radii of curvature of succinonitrile in microgravity using the IDGE instrument flown on the USMP-2 platform in the payload bay of the Space Shuttle *Columbia* (STS-62). The on-orbit microgravity data, when compared to terrestrial dendritic growth data, demonstrate that (1) convective effects under terrestrial conditions cause growth speed increases of a factor of 2 at lower supercoolings ($\Delta T < 0.5$ K), and remain significant even up to values as high as $\Delta T = 1.7$ K supercooling; (2) in the supercooling range from 0.47 to 1.7 K, the data remain virtually free of convective effects, and may be used reliably for examining diffusion-limited dendritic growth theories; (3) a diffusion solution to the dendrite problem, combined with a unique (measured) scaling constant, σ^* , does not yield individual growth velocity and radius predictions consistent with the observed dendritic growth velocities and radii as a function of supercooling; and (4) the failure of this conventional formulation is currently attributed to departures from the Ivantsov diffusion solution, which is formulated for paraboloidal dendrites. Ivantsov’s theory describes the overall dependence of Péclet number on

supercooling, but predicts a value higher (5–15 percent) than the data we observed in the diffusion-limited regime.

We offer here two speculations that might account for the discrepancy between the IDGE data and the Ivantsov solution. The first is that the diffusion field of the Ivantsov formulation is based on a dendrite tip which is a paraboloid of revolution, which is only strictly true at the tip itself. In addition, it has also been assumed that all the available supercooling is consumed by the heat conduction field. If a small portion of this temperature drop is used, say, in the “creation” of interfacial energy as the dendrite propagates, then the value of the supercooling used to plot the data in figures 7 and 8 would be too high, and to correct for this, the data would need to be shifted slightly to the left. Although neither of these speculations have yet to be examined in quantitative detail, both seem reasonable hypotheses, consistent with the current microgravity data.

When modeling dendritic growth terrestrially, the effect of convection on dendritic growth must also be included. With a working model of diffusion-limited dendritic growth, one can use the data provided here at the lower supercoolings to compare quantitatively diffusion-limited theory with dendritic growth at two well-characterized different gravity levels (0.7×10^{-6} and $1 g_0$). This feature must also be solved before computer codes will simulate dendritic growth terrestrially.

Based in part on the description of the experiment operations narrated in this report, an experiment’s operations are as important as the experiment’s apparatus, and should be treated accordingly with respect to both effort and expenditures. Furthermore, telescience—the remote observation, and operation of an experiment—can greatly enhance experiment operations, and remains an important tool for future microgravity spaceflight experiments

2.7. WORK IN PROGRESS

The IDGE team has completed the bulk of the data measurements and analysis for a complete and detailed archival journal publication on the IDGE flight on USMP-2. We have begun preparing this paper, which will include the canonical microgravity data from the IDGE flight on USMP-2, and plan to have it submitted to *Phys. Rev. E.*, by the end of September 1995.

In addition we are pursuing improved image processing methods to examine and extract radii data at the highest supercooling (above 1.0 K) performed on the flight. We did not expect to be able to measure dendritic radii at these elevated supercoolings, however, advances in available image processing techniques suggest that we should attempt this. We are also preparing to perform measurements on the sidebranching that occurs in dendritic growth. These issues, and others, are interesting and important, and will be pursued after the submittal of the archival publication on the IDGE that describes the data and analysis of this report.

2.8. REFERENCES

1. Langer, J.S., "Issues and Opportunities in Materials Research," *Physics Today*, 24, October 1992.
2. Glicksman, M.E., and S.P. Marsh, "The Dendrite," Handbook of Crystal Growth, edited by D.J.T. Hurle, Elsevier Science Publishers B.V., Amsterdam, 1993, vol. 1b, p. 1077.
3. Ivantsov, G.P., "Temperature Field Around Spherical, Cylindrical, and Needle-Shaped Crystals Which Grow in Supercooled Melts," *Dokl. Akad. Nauk, USSR*, 58, 56, 1947.
4. Glicksman, M.E., R.J. Schaefer, and J.D. Ayers, "Dendritic Growth—A Test of Theory," *Met. Trans. A*, 7A, 1747, 1976.
5. Brener, E.A., and V.I. Mel'nikov, "2-Dimensional Dendritic Growth at Arbitrary Péclet Number," *Adv. Phys.* 40, 53, 1991.
6. Huang, S C., and M.E. Glicksman, "Fundamentals of Dendritic Solidification: I. Steady State Tip Growth," *Acta Metall.*, 29, 701, 1981.
7. Glicksman, M.E., and S.C. Huang, "Convective Heat Transfer During Dendritic Growth," Convective Transport and Instability Phenomena, ed. Zierp and Ortel, Karlsruhe, 557, 1982.
8. Ananth, R., and W.N. Gill, "Self-Consistent Theory of Dendritic Growth with Convection," *J. Crystal Growth*, 91, 587, 1988; and "Dendrite Growth with Thermal Convection," *J. Crystal Growth*, 108, 173, 1991.
9. Glicksman, M.E., E.A. Winsa, R.C. Hahn, T.A. LoGrasso, S.H. Tirmizi, and M.E. Selleck, "Isothermal Dendritic Growth—A Proposed Microgravity Experiment," *Met. Trans. A*, 19A, 1945, 1988.
10. Glicksman, M.E., R.C. Hahn, M.B. Koss, S.H. Tirmizi, A. Velosa, and E.A. Winsa, "Isothermal Dendritic Growth Experiment: Science, Engineering, and Hardware Development for USMP Space Flights," *Advances in Space Research*, 11, 53, 1991.
11. Glicksman, M.E., M.B. Koss, and E.A. Winsa, "Dendritic Growth Velocities in Microgravity," *Phys. Rev. Lett.*, 73, 573, 1994.
12. Rubinstein, E.R., S.H. Tirmizi, and M.E. Glicksman, "Long Term Purity Assessment of SCN," *J. Crystal Growth*, 106, 89, 1990.
13. Glicksman, M.E., M.B. Koss, V.E. Fradkov, M.E. Rettenmayer, and S.S. Mani, "Quantification of Crystal Morphology," *J. Crystal Growth*, 137, 1, 1994.

2.9. PUBLICATIONS AND PRESENTATIONS

Peer Reviewed Journal Articles

1. Glicksman, M.E., M.B. Koss, and E.A. Winsa, "Dendritic Growth Velocities in Microgravity," *Phys. Rev. Lett.*, 73(4), 573, 1994.

Review Articles

1. Smith, R.N., M.E. Glicksman, and M.B. Koss, "Effects of Buoyancy on the Growth of Dendritic Crystals," *Annual Review of Heat Transfer*, vol. VII, in press, 1995.

Proceedings and Other Articles

1. Glicksman, M.E., M.B. Koss, L.T. Bushnell, J.C. LaCombe, P. Kobryn, and E.A. Winsa, "The Tele-Operational Capabilities of the IDGE," 6th International Symposium on Experimental Methods for Microgravity Science, edited by R.A. Schiffman and J.B. Andrews, The Minerals, Metals & Materials Society, p. 141, 1994.
2. Winsa, E.A., D.C. Malarik, M.E. Glickmsan, M.B. Koss, L.T. Bushnell, and J.C. LaCombe, "Operation of the Isothermal Dendritic Growth Experiment on USMP-2," Reprint AIAA 95-0610, 33rd Aerospace and Sciences meeting and exhibit, Reno NV, January 9-12, 1995.
3. Glicksman, M.E., M.B. Koss, L.T. Bushnell, J.C. LaCombe, and E.A. Winsa, "Space Flight Data From the Isothermal Dendritic Growth Experiment," *Adv. Space Res.*, 16(7), 181, 1995.
4. Glicksman, M.E., M.B. Koss, L.T. Bushnell, J.C. LaCombe, and E.A. Winsa, "Dendritic Growth of Succinontrile in Terrestrial and Microgravity Conditions as a Test of Theory," *ISIJ International*, 35(6), 1216, 1995.
5. Smith, R.N., M.E. Glicksman, M.B. Koss, L.T. Bushnell, and J.C. LaCombe, "Experimental Study of Dendrite Growth in an Undercooled Melt Under Microgravity Conditions," Heat Transfer Session at the 1994 ASME Winter Annual Meeting in Chicago, in press, 1995.
6. Glicksman, M.E., M.B. Koss, L.T. Bushnell, J.C. LaCombe, and E.A. Winsa, "Dendritic Growth in Terrestrial and Microgravity Conditions," Material Research Society (MRS) Fall Meeting, Symposium P, Boston, MA, in press, 1995.
7. Glicksman, M.E., M.B. Koss, L.T. Bushnell, and J.C. LaCombe, "The Isothermal Dendritic Growth Experiment: Implications for Theory," Modeling of Casting, Welding, and Advanced Solidification Processes VII, The Minerals, Metals & Materials Society, in press, 1995.
8. Glicksman, M.E., M.B. Koss, L.T. Bushnell, J.C. LaCombe, and E.A. Winsa, "Evaluation of Teleoperating the IDGE on STS-62," 7th International Symposium on Experimental Methods for Microgravity Science, edited by R. A. Schiffman, The Minerals, Metals & Materials Society, in press, 1995.

Presentations

1. Glicksman, M.E., "Dendritic Growth in Microgravity: IDGE Flight 1," Aachen Foundry Institute, Aachen, Germany, March 1994.
2. Glicksman, M.E., "Dendritic Growth in Microgravity: IDGE Flight 1," DLR, Space Simulation Institute, Koln-Portz, Germany, March 1994.
3. Glicksman, M.E., "The Isothermal Dendritic Growth Experiment: First Results from USMP-2," Pittsburgh Chapter of the ACCG, Pittsburgh, PA, May 1994.
4. Glicksman, M.E., "The Isothermal Dendritic Growth Experiment: First Results from USMP-2," Microgravity Materials Science Conference, Von Braun Civic Center, Huntsville, AL, May 1994.
5. LaCombe, J.C., "Dendritic Solidification in a Microgravity Environment," Joint Meeting of the Eastern New York Chapter of ASM International and the Hudson-Mohawk Section of TMS, Latham, NY, May 1994.
6. Koss, M.B., "Preliminary Results from the Isothermal Dendritic Growth Experiment," at the Space Experiments Division Awards Ceremony, NASA Lewis Research Center, Cleveland, OH, July 1994.
7. Glicksman, M.E., "Space Flight Data From the Isothermal Dendritic Growth Experiment," at 26th COSPAR, Hamburg, Germany, July 1994.
8. Glicksman, M.E., "Space Flight Data From the Isothermal Dendritic Growth Experiment," Giesserei Institut, RWTH Aachen, Aachen, Germany, July 1994.
9. Glicksman, M.E., "The Isothermal Dendritic Growth Experiment: Implications for Theory," NIST, Gaithersburg, MD, August 1994.
10. Glicksman, M.E., "Space Flight Data From the Isothermal Dendritic Growth Experiment: What Have We Learned?," Materials Engineering Department Seminar, Rensselaer Polytechnic Institute, Troy, NY, September 1994.
11. Bushnell, L.T., "Effects of Convection on Dendritic Growth in Microgravity," ACCG-East/9, Atlantic City, NJ, October 1994.
12. LaCombe, J.C., "Three Dimensional Characteristics of Dendrites," ACCG-East/9, Atlantic City, NJ, October 1994.
13. Smith, R.N., "Experimental Study of Dendrite Growth in an Undercooled Melt Under Microgravity Conditions," ASME Winter Annual Meetings, Chicago IL, November 1994.
14. Glicksman, M.E., "Convection in Microgravity: First Flight of the Isothermal Dendritic Growth Experiment," AIChE meeting in San Francisco, CA, November 1994.
15. Glicksman, M.E., "Isothermal Dendritic Growth Experiment USMP-2,3,4," Raumsimulation Institut, DLR, Koln, Germany, November 1994.

16. Glicksman, M.E., "Dendritic Growth in Terrestrial and Microgravity Conditions," Material Research Society (MRS) Fall Meeting, Boston, MA, November 1994.
17. Winsa, E.A., "Operation of the Isothermal Dendritic Growth Experiment on USMP-2," Paper 95-0610, 33rd Aerospace and Sciences Meeting and Exhibit, Reno NV, January 1995.
18. Koss, M.B., "Evaluation of Teleoperating the IDGE on STS-62," 7th International Symposium on Experimental Methods for Microgravity Science, TMS Annual Meeting and Exhibit, Las Vegas, NV, February 1995.
19. Glicksman, M.E., "The Isothermal Dendritic Growth Experiment: Anniversary Review of Space Flight Result," Burgess Memorial Lecture, Washington, DC Chapter, ASM, March 1995.

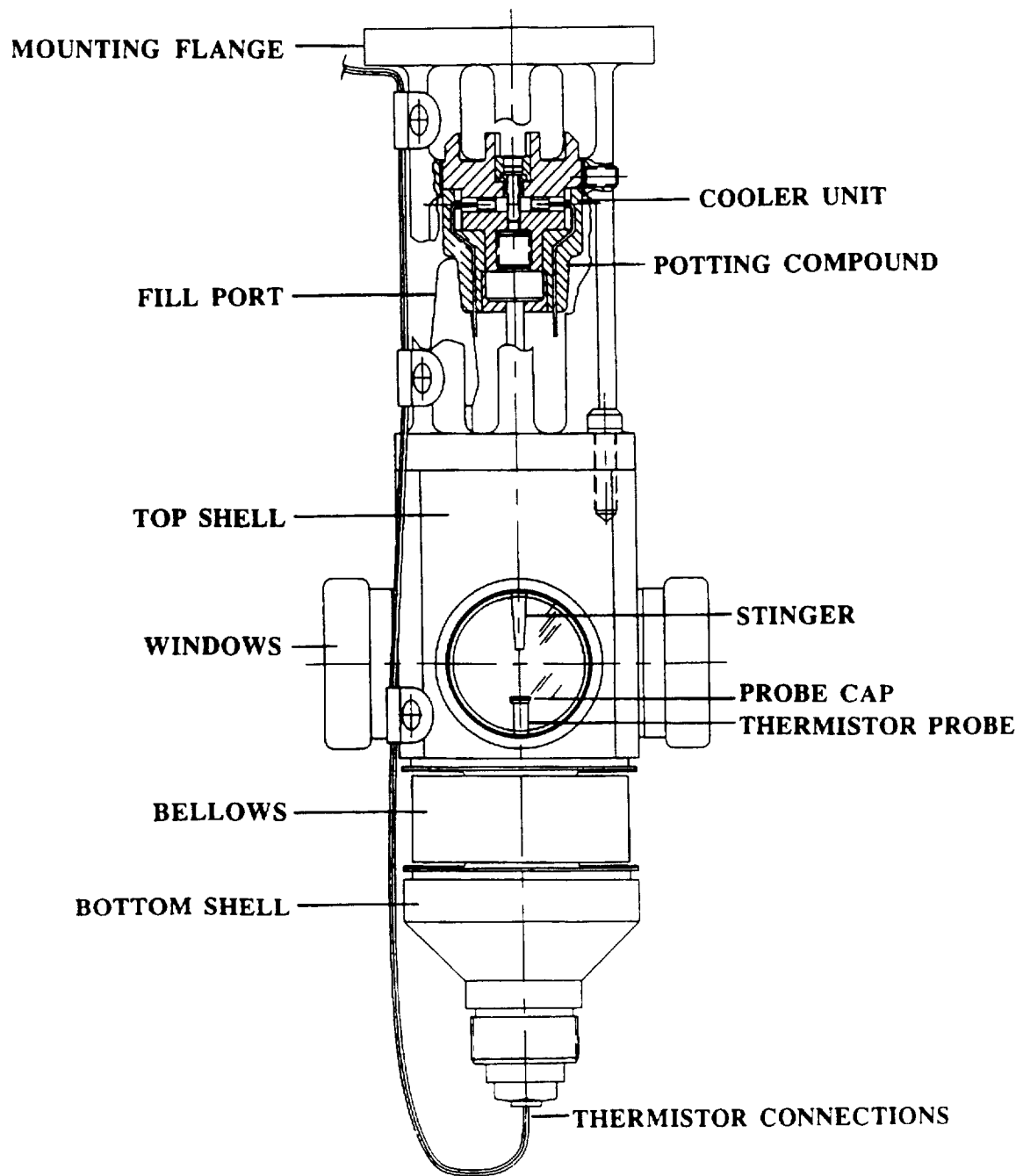


Figure 2-1. IDGE flight growth chamber.

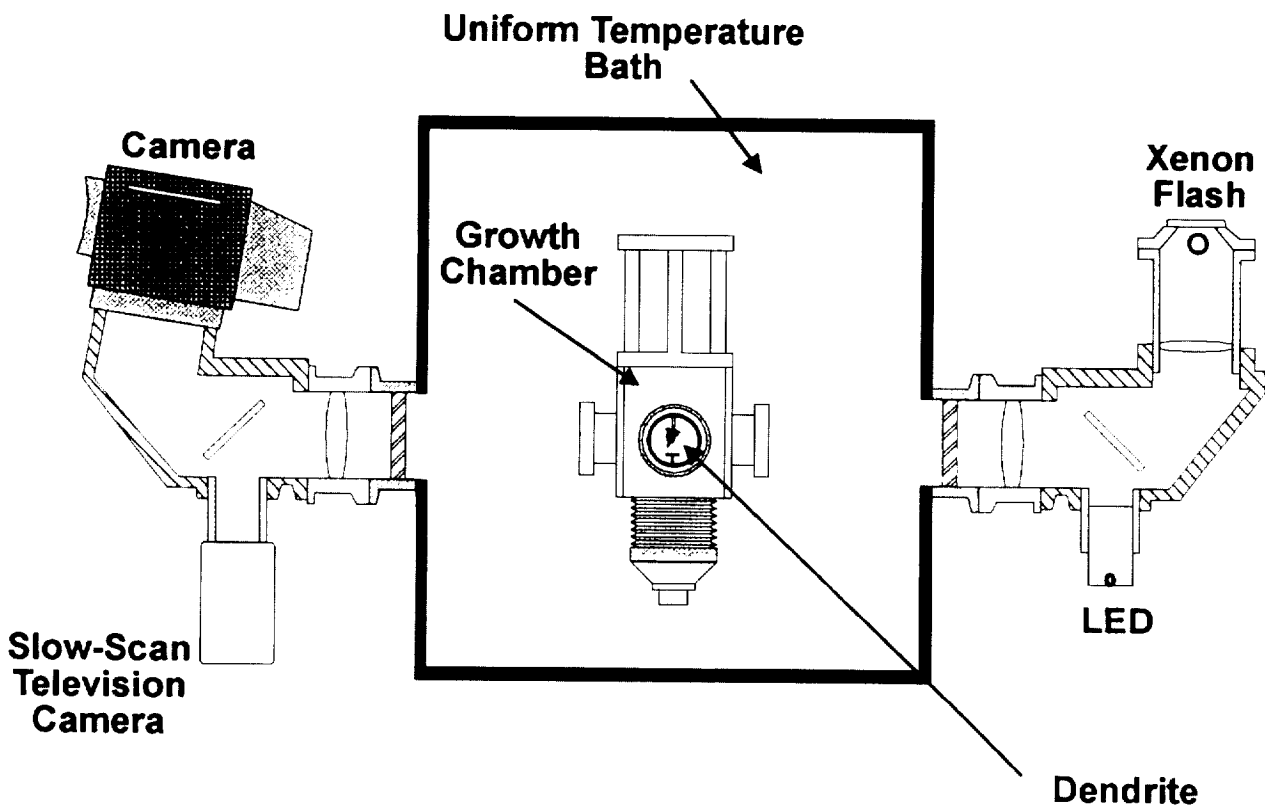


Figure 2-2. IDGE temperature controlled tank and optic system.

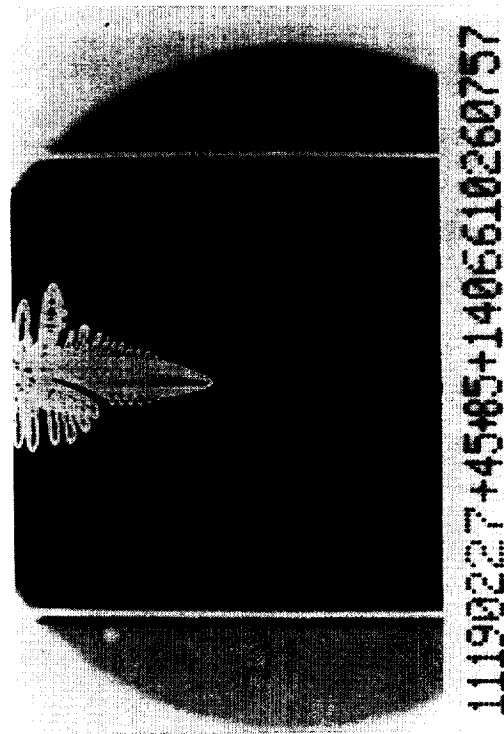
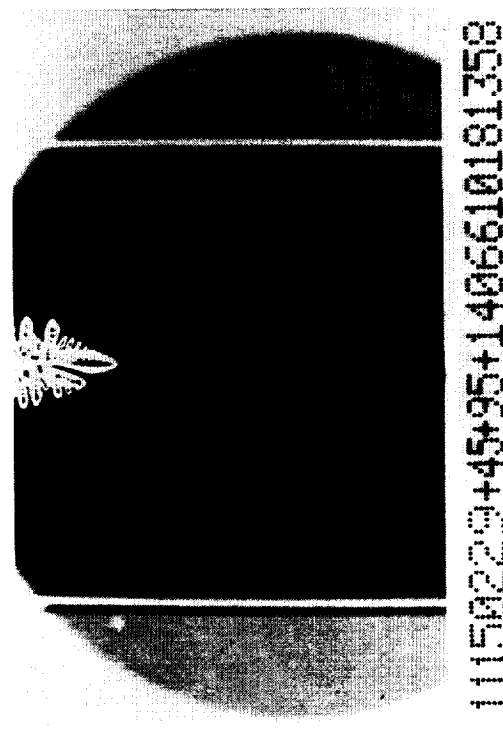
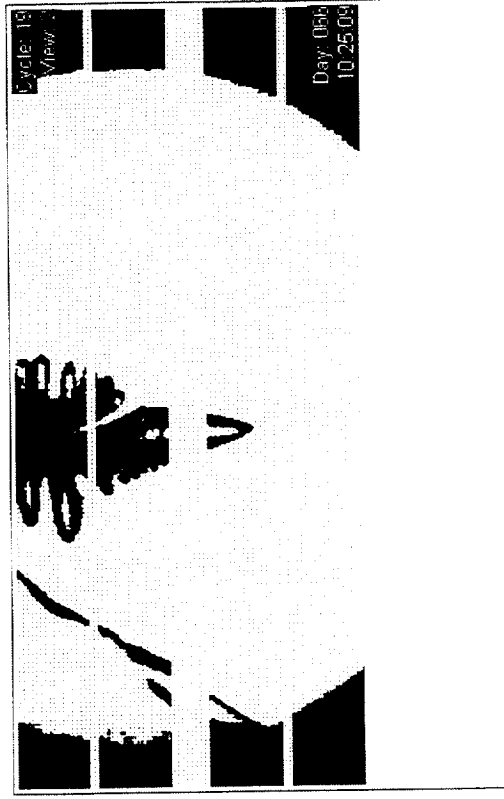
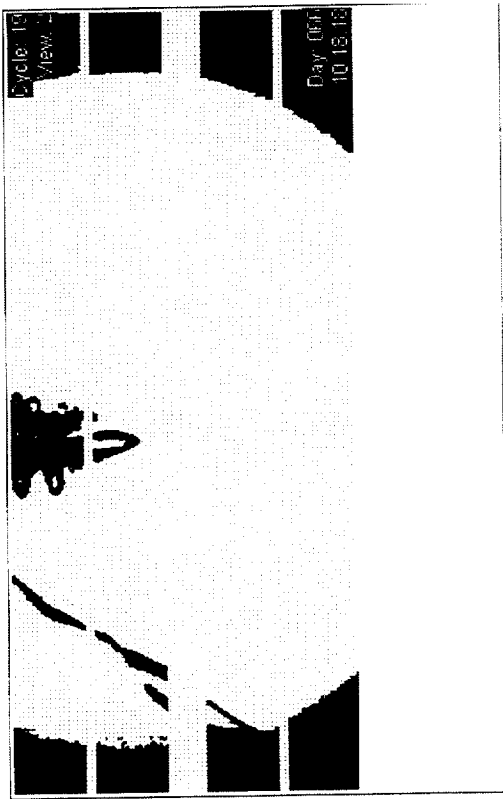


Figure 2-3. Examples of 35-mm photographic images and low-resolution, binary, digitized electronic images.

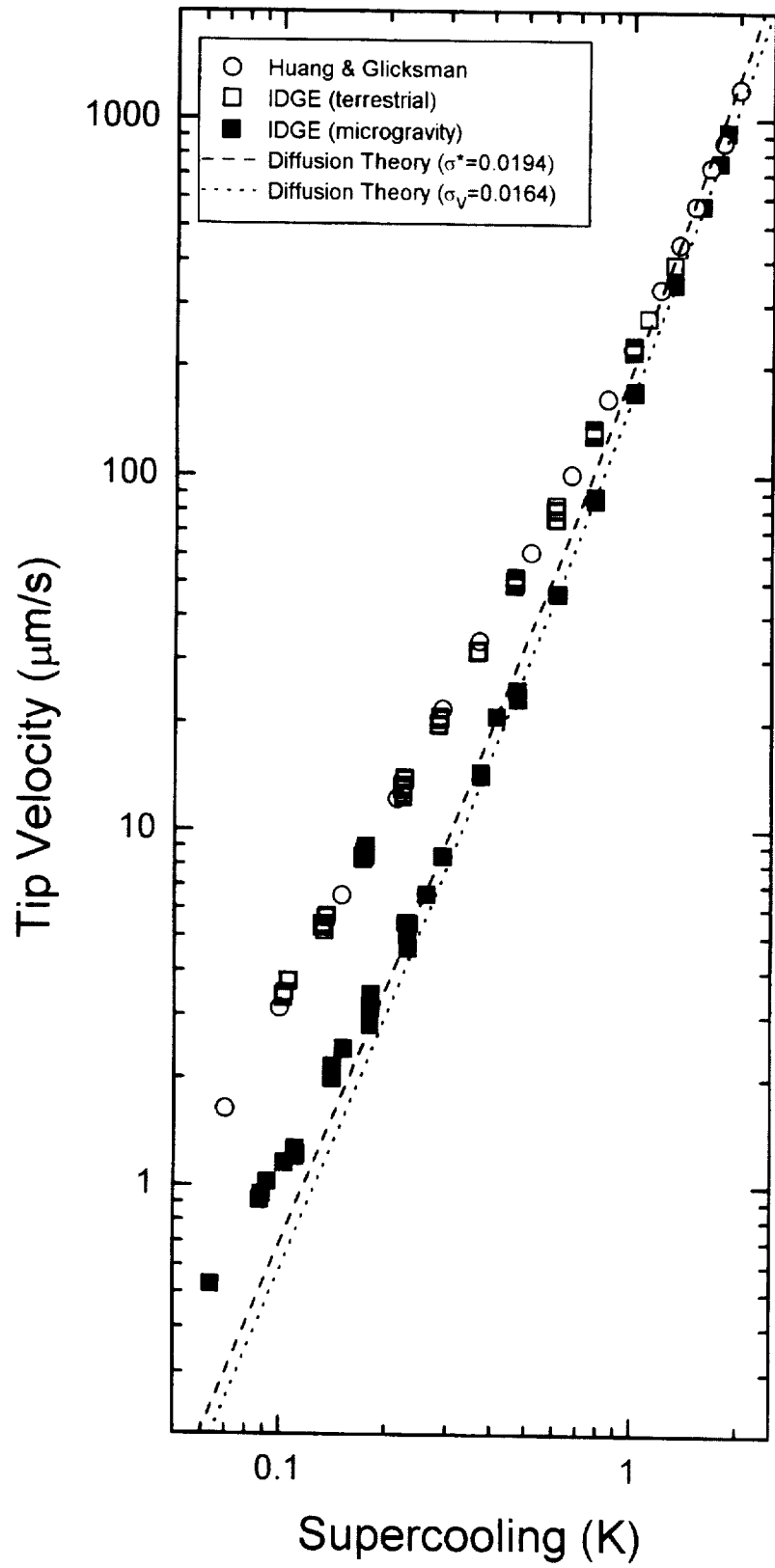


Figure 2-4. Dendritic growth tip velocity as a function of supercooling.

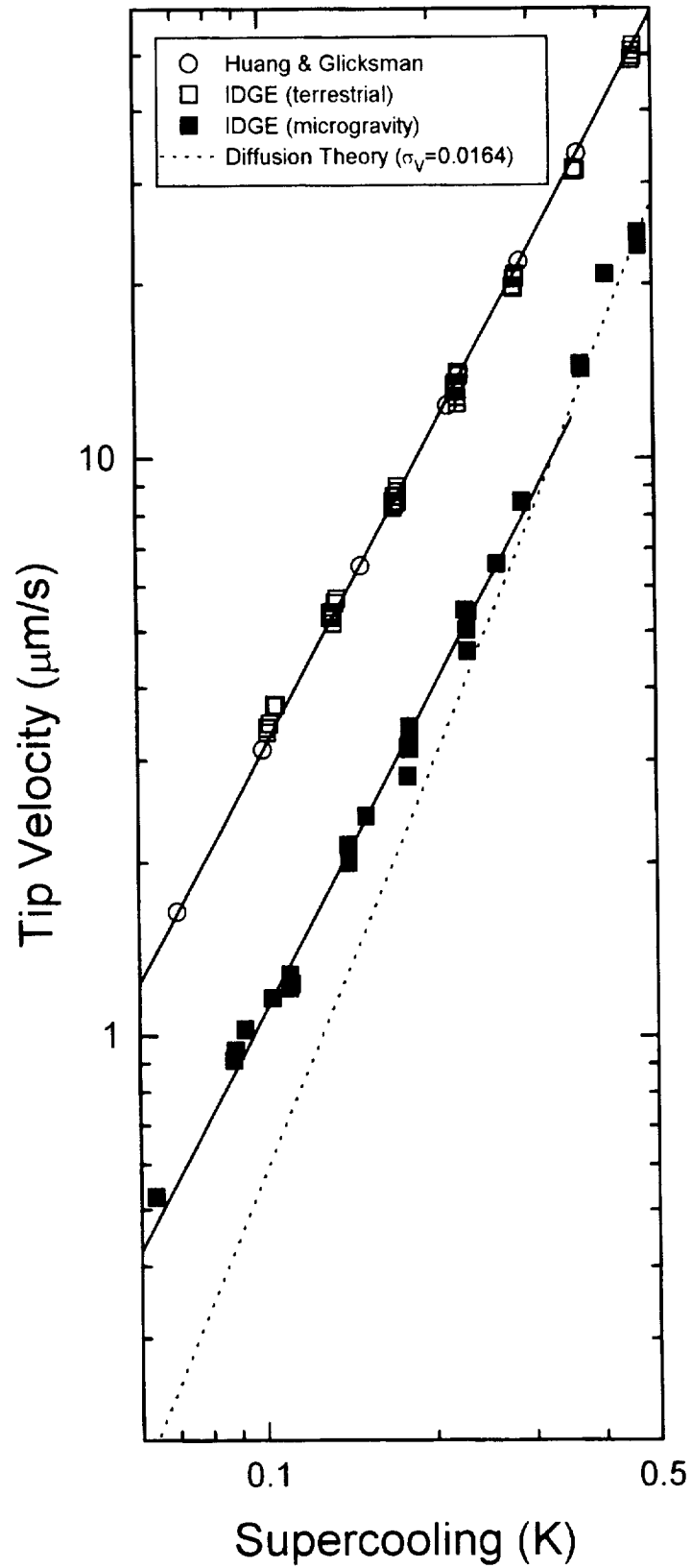


Figure 2-5. Dendritic growth tip velocity as a function of supercooling at the lower supercoolings.

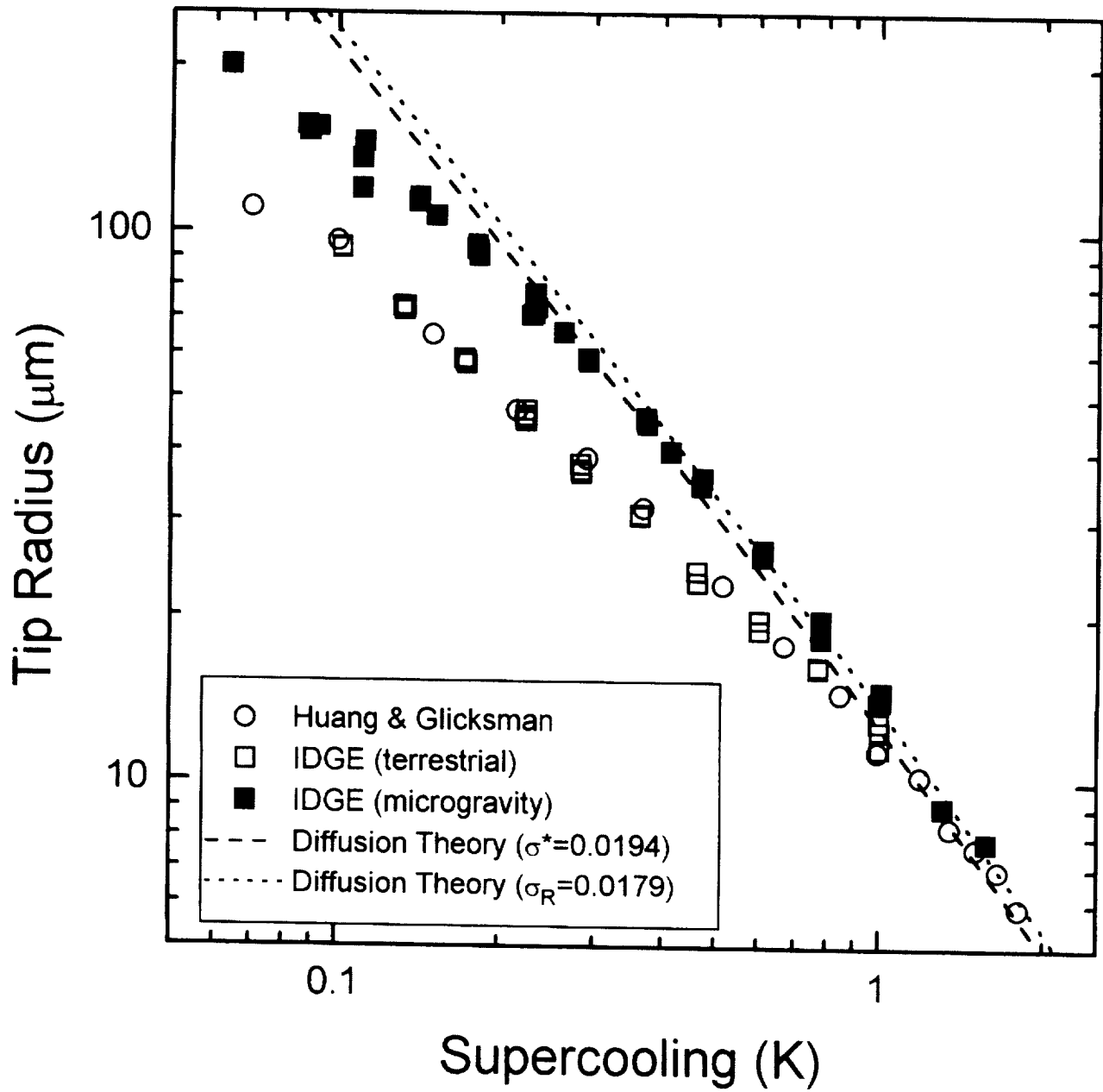


Figure 2-6. Dendritic growth tip radius as a function of supercooling.

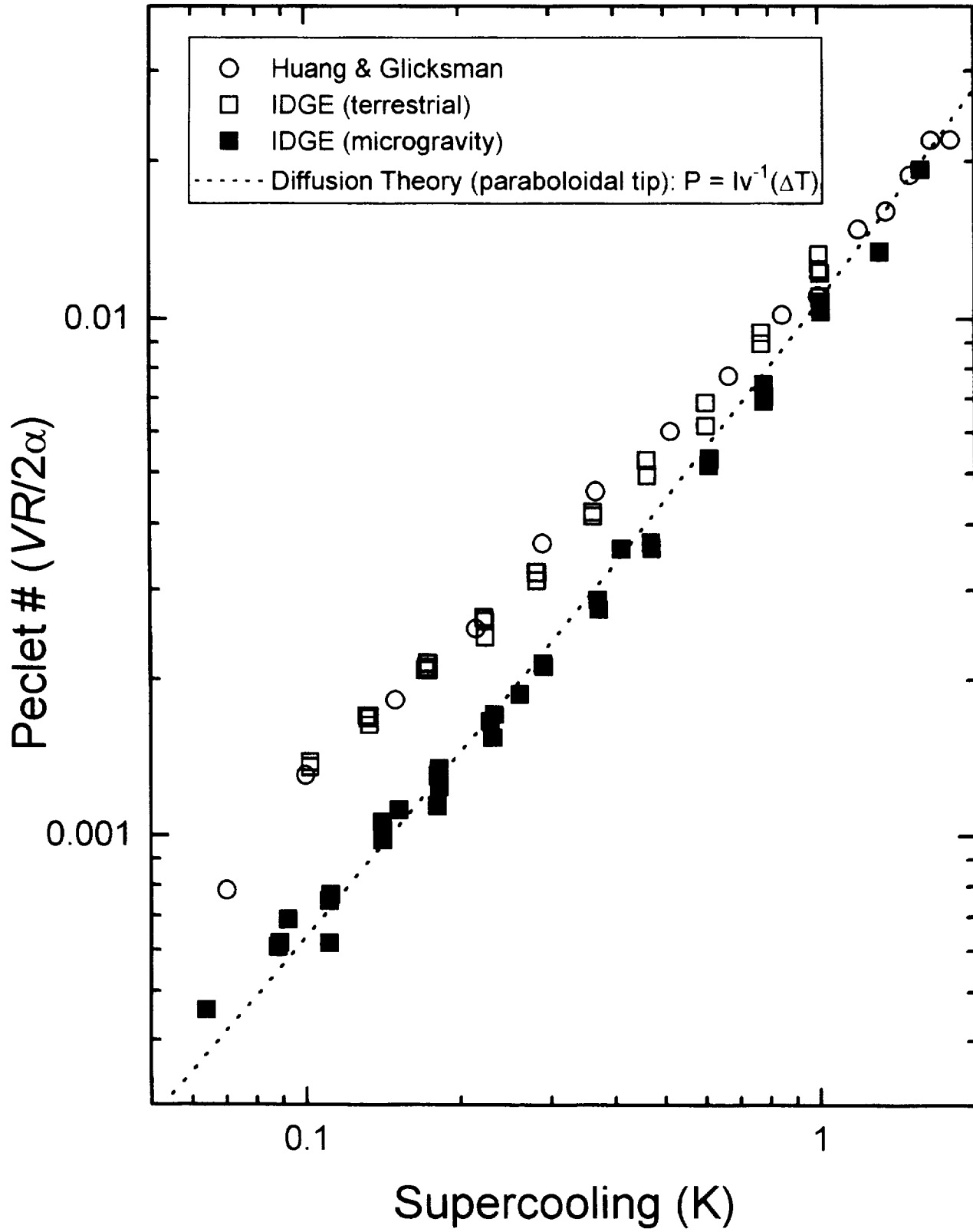


Figure 2-7. Dendritic growth tip Péclet numbers as a function of supercooling.

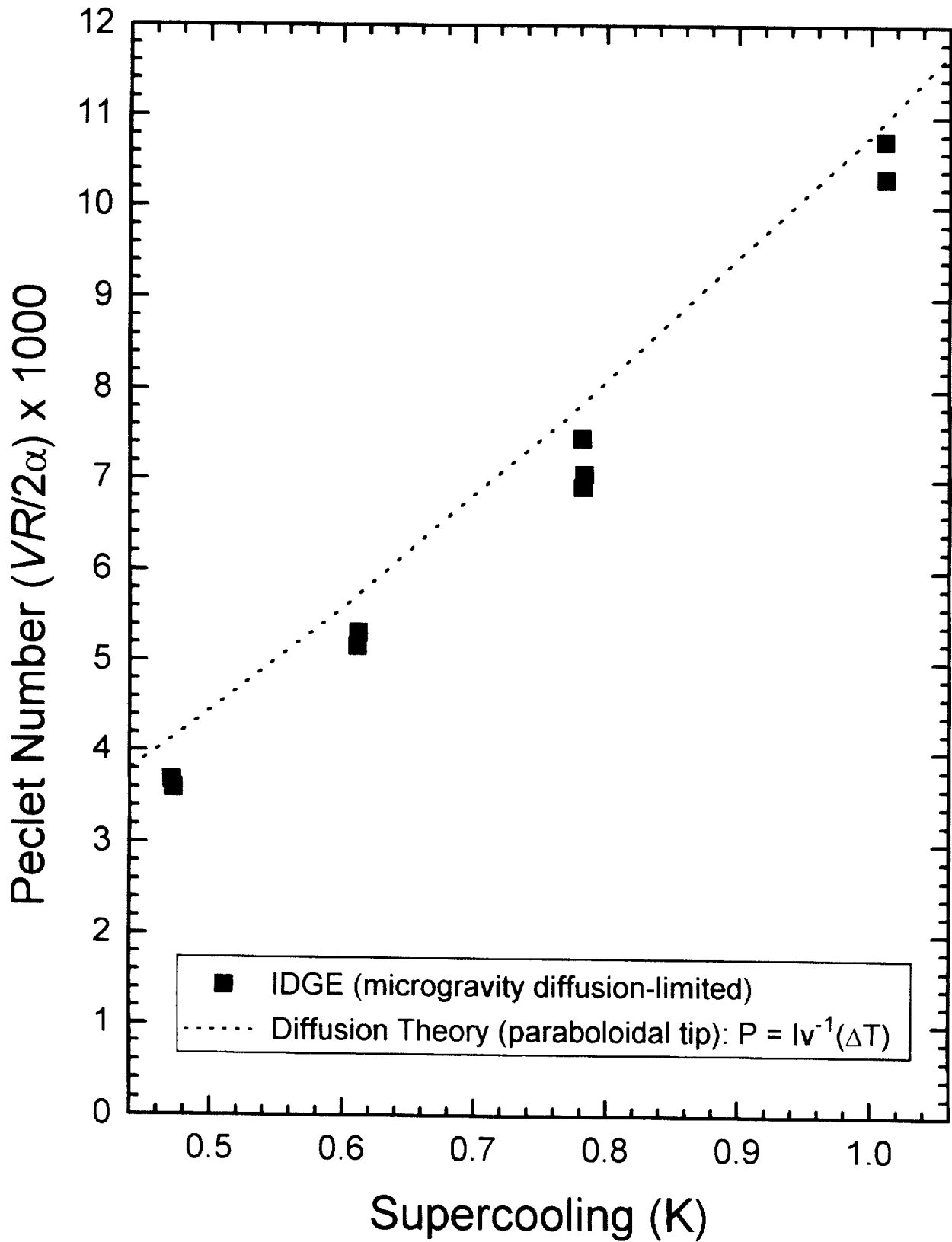


Figure 2-8. Dendritic growth tip Péclet numbers as a function of supercooling in the diffusion-limited supercooling range.

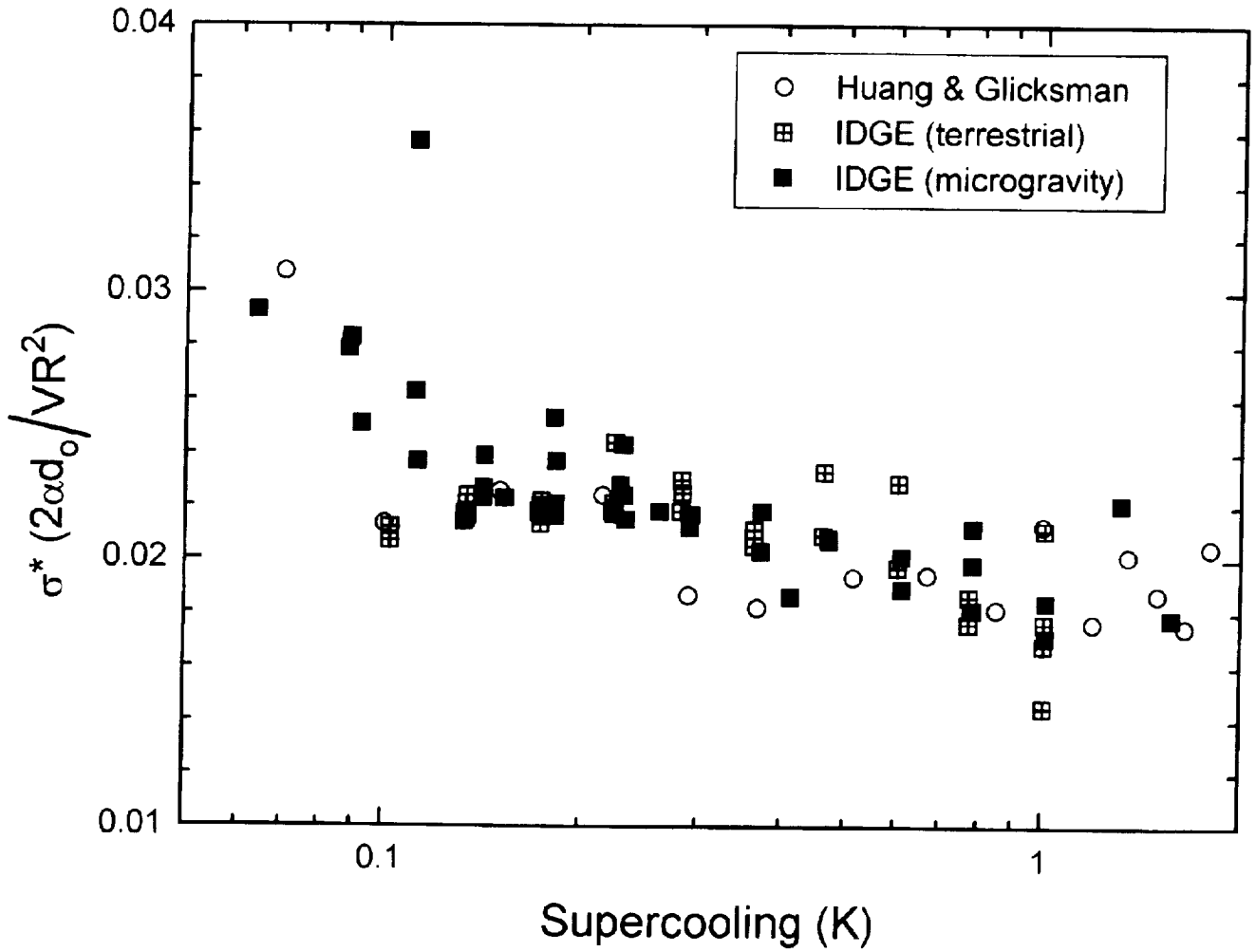


Figure 2-9. Dentritic growth scaling parameter as a function of supercooling.

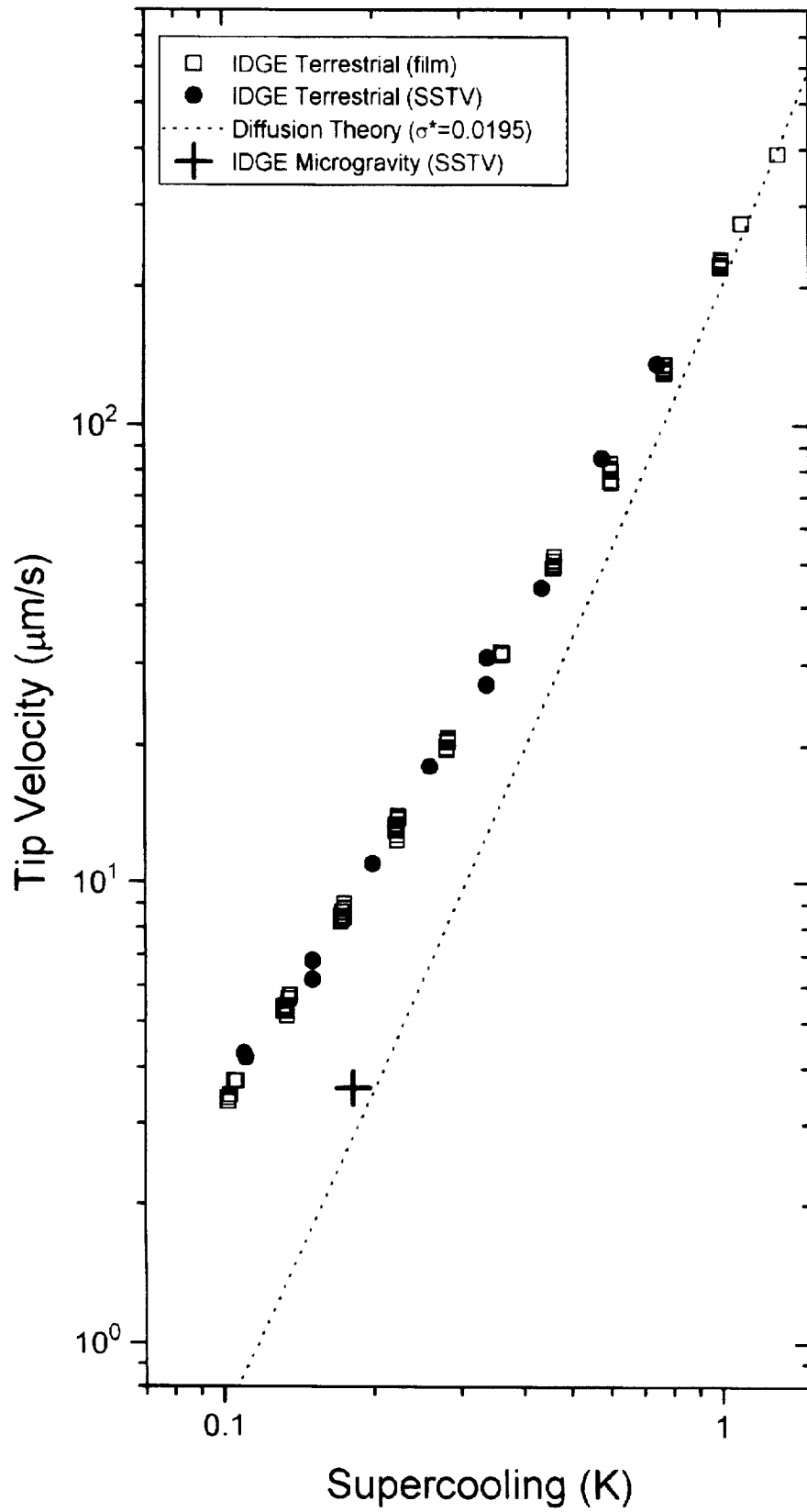


Figure 2-10. The first telescience measured velocity calculated from the SSTV data.

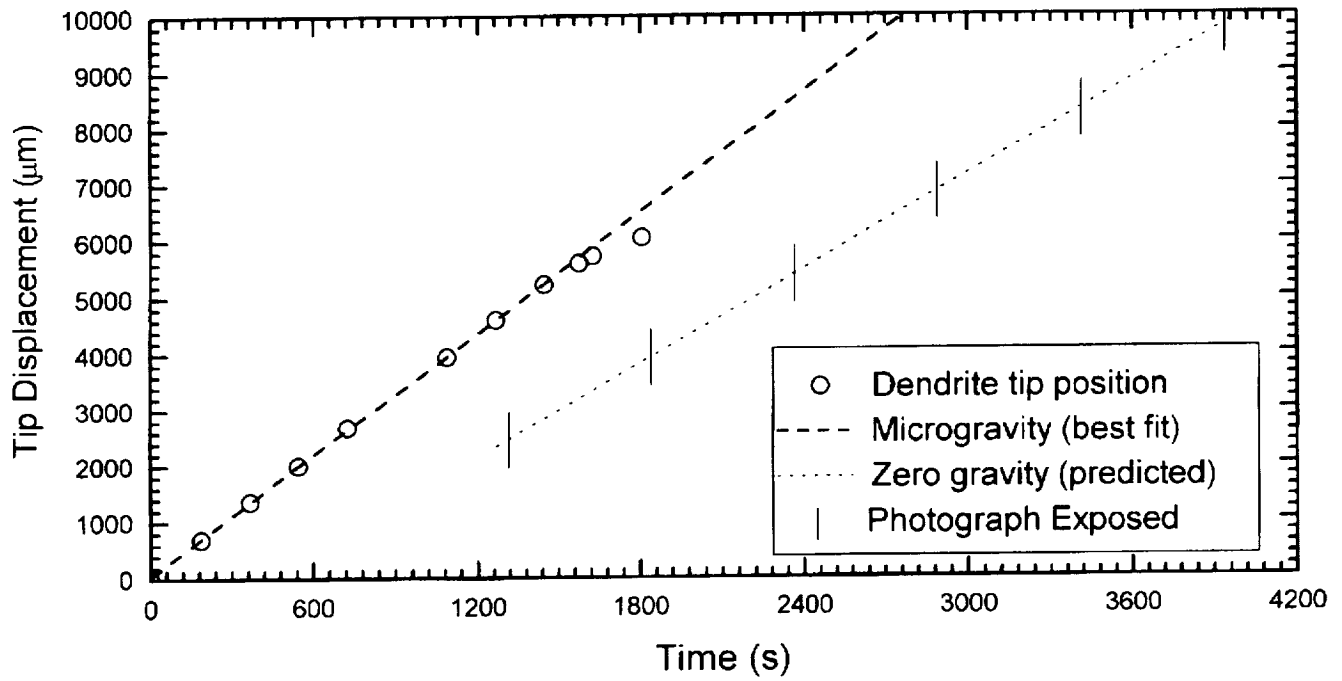


Figure 2-11. Dendrite tip displacement versus time data from the SSTV data.

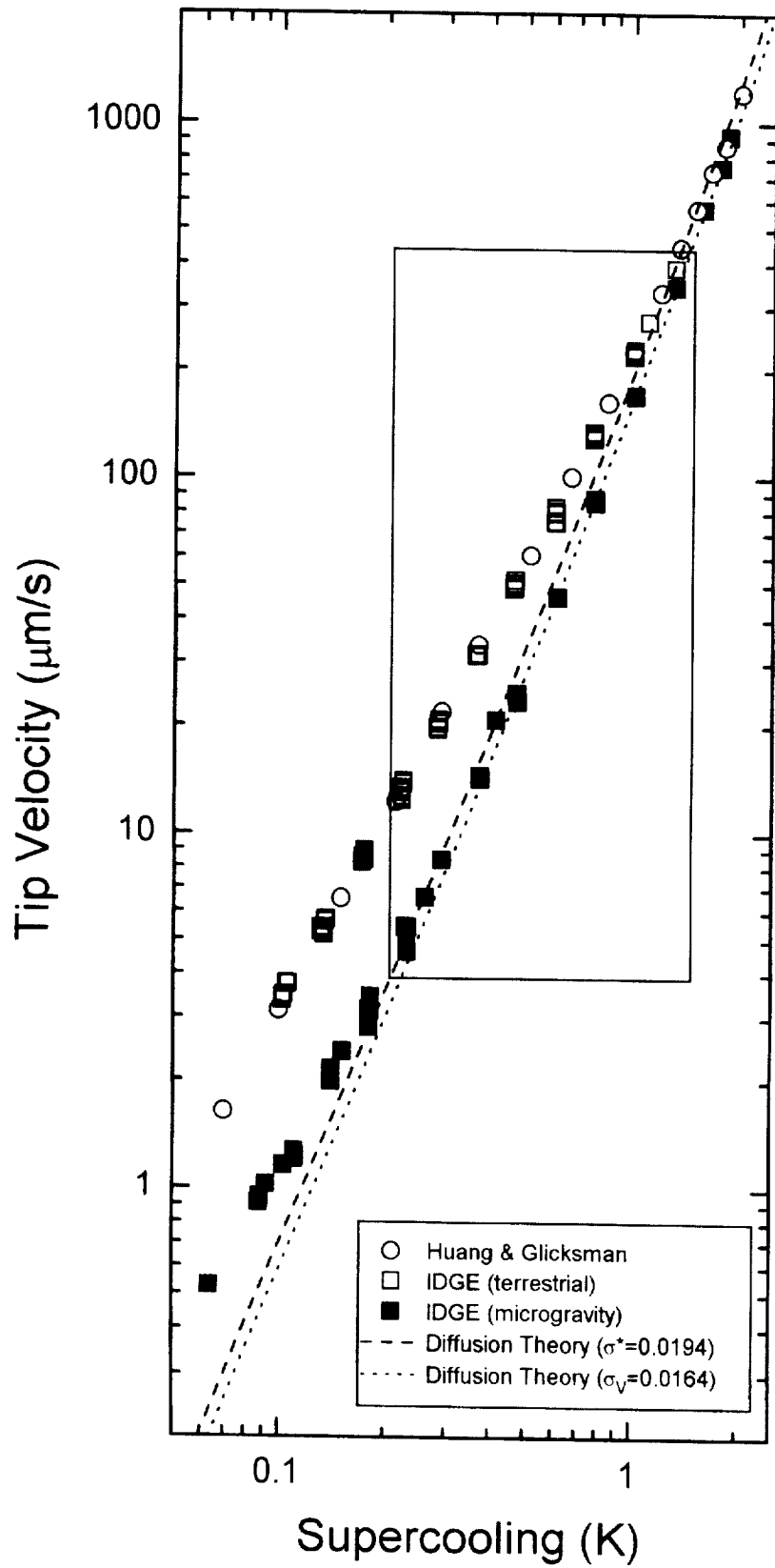


Figure 2-12. Extension of the velocity data range that was obtained through the use of telescience.

SECTION III.

**IN SITU MONITORING OF CRYSTAL GROWTH
USING MEPHISTO**

Acknowledgments

We would like to extend our special appreciation (in alphabetical order) to B. Angelier, M. Bodaert, P. Bioulez, J. Comera, P. Contamin, C. Fenwick, D. Gadonniex, G. Hieu, F. Herbillon, R. Krishnasamy, J.E. Mazille, B. Merkel, R. Panchapakesan, J.P. Praizey, A. Rouzaud, and G. Santoro for their efforts. We would also like to gratefully acknowledge the financial support from NASA (grant NAG-3-1096) for this program.

**SECTION III. IN SITU MONITORING OF CRYSTAL GROWTH
USING MEPHISTO
Mission STS 62 – Program USMP-2
Experiment Analysis**

Reza Abbaschian

Professor and Chairman, Department of Materials Science and Engineering
University of Florida, Gainesville, Florida 32611

3.1. OVERVIEW

This report summarizes the results of the *In situ Monitoring of Crystal Growth Using MEPHISTO* (*Material pour l'Etude des Phenomenes Intéressants de la Solidification sur Terre et en Orbite*) experiment on USMP-2 after 8 months of data and microstructural analysis. It consists of an analysis of the microstructural evolution of microgravity processed samples and of the telemetry data. The flight experiment was accomplished with the collaboration of the University of Florida, the Centre National d'Etudes Spatiales (CNES), the Centre d'Etudes Nucleaires de Grenoble (CENG), the National Institute of Standards and Technology (NIST), and NASA (P.I.: R. Abbaschian, Co-P.I.'s: A.B. Gokhale, J.J. Favier, and S.R. Coriell). The MEPHISTO Project Manager was G. Cambon (CNES) and the NASA Project Scientist and Project Manager were H.C. de Groh III and R. DeWitt (NASA-Lewis Research Center (LeRC)), respectively.

The research program has yielded a wealth of scientific data. A total of more than 45 cm of directionally solidified alloy were recovered. Metallurgical analysis of the samples has shown that the interfacial kinetics play a key role in controlling the morphological stability of faceted alloys. We believe this to be the first unambiguous demonstration of such an effect during directional solidification under diffusion-dominated conditions. In addition, analysis of the differential Seebeck thermoelectric signals for very slow growth velocities was carried out. The analysis indicates that it is possible to calculate the kinetic undercooling from the Seebeck signal decay at the end of solidification. Such information is not accessible from ground-based studies due to effects associated with convective destabilization.

3.2. BACKGROUND

The In situ Monitoring of Crystal Growth experiment, flown aboard USMP-2 using the MEPHISTO flight hardware, was a fundamental investigation of the directional solidification of a faceted metallic alloy. The experiment was carried out on-board *Columbia* (Mission STS-62, Program USMP-2, March 4–18, 1994). The hardware used was MEPHISTO Flight Model 2, which was developed by CNES and flown for the first time on this mission. The hardware is similar to MEPHISTO-I which was flown aboard USMP-1 for Sn-Bi alloys by J.J. Favier and his colleagues.

This research program was initiated by the University of Florida (NASA grant NAG-3-1096) in January 1990. As such, the ground-based experiments as well as sample preparation and integration for the microgravity study were carried out in the relatively short period of approximately four years after the start of the program. This was accomplished by the establishment of a collaborative effort involving the CENG, CNES, and NIST, with program scientist and management provided by LeRC.

The experiments were performed to gain a detailed understanding of two fundamental and interrelated aspects of the liquid to solid transformation in faceted alloys: (a) Morphological stability of the solid/liquid (s/l) interfaces and the resulting macro- and microsegregation patterns, and (b) atomic attachment kinetics at the freezing interface, deduced via measurement of the growth rate-interface supercooling relationship(s). The alloy system used was Bi doped with 0.1 at.% Sn.

3.3. USMP-2 MISSION DESCRIPTION

3.3.1. Experimental Facility and Techniques

The experiments used the MEPHISTO directional solidification facility which processes three samples in parallel, each approximately 900 mm long and 6 mm in diameter. One sample was used for interfacial temperature measurements (termed the Seebeck sample), another for resistance and thermal gradient measurements (termed the resistance sample), and the third for demarcation of the interface shape during directional solidification (termed the Peltier sample). A 2-cm length of the resistance sample was also quenched at the end of the microgravity experiment.

The core structure of the MEPHISTO facility is shown schematically in figure 1(a), while the arrangement of the experimental samples along with important dimensions, positions of the two s/l interfaces, locations of thermocouples and the overall temperature profile are shown schematically in figure 1(b). The general experimental procedure consisted of melting the middle ~500-mm length of the samples using two furnaces, thus creating two s/l interfaces. One of the furnaces was kept stationary and the other moved back and forth at specified rates in order to melt or solidify at that side of the samples. In addition, the sample ends were maintained at a controlled and constant temperature in order to facilitate the measurement of a differential voltage from the two interfaces and the resistance change during solidification and melting.

3.3.2. Flight Summary

The experiment was monitored and controlled using real-time telemetry. After a nominal hardware initialization sequence, the condition of the samples was checked by monitoring a variety of sensors (Seebeck electro motive force (emf), resistance, Peltier circuit continuity, thermocouple outputs, microfurnace heating rates, heat sink behavior, etc.). It was found that all three samples were nominal, without any evidence of loss of integrity. However, during the first 31 hours of the mission, three main anomalies were encountered: (1) An apparent indication of a "grounding" of the Peltier sample, followed by an indication of a loss of the sample continuity; (2) anomaly occurred in the temperature output of the thermocouples in the Peltier sample; and (3) anomaly manifested itself as a saturation of the Seebeck signal after the completion of two melting/solidification cycles. Following this, the Seebeck signals saturated at either the positive or negative voltage limits of the amplifier, with intermittent, highly amplified signals which could not be correlated with any microstructure-related phenomena. These anomalies have been described previously in detail in our postlaunch, 6-month report.

Over 55 melting and solidification cycles with different thermal and velocity conditions were performed. The total experimentation time was 326 hours 14 minutes. After the mission, over 45 cm of directionally solidified alloy was recovered in good condition. As discussed below, the metallurgical analyses of these samples have started to provide valuable information on the morphological stability of faceted alloys.

Also, despite the Seebeck anomalies, the first 30 hours of Seebeck signal nevertheless provided valuable data on the interfacial undercooling of the faceted alloy during plane-front solidification at a low growth velocity. As presented later, the measurement of such low levels of kinetic undercooling are not feasible on Earth.

The final solidification sequence for the samples is given in table 1, summarizing the lengths of the regions which were preserved after controlled directional solidification at the specific growth velocities listed. Also included are the shuttle attitude and possible sources of g-perturbations.

3.4. MICROSTRUCTURAL AND DATA ANALYSIS

The following main themes were identified for the postflight analysis:

3.4.1. Microstructural Analysis

- Plane front growth
- Plane front to cellular transition
 - Orientation-dependence of transition thresholds
 - Direction of cell growth with respect to the growth direction
 - Cell spacing as a function of growth velocity
- Compositional changes.

3.4.2. Kinetics Data Analysis

- Resistance measurements
- Temperature gradient in the liquid and solid (G_l , G_s)
- Seebeck thermoelectric measurements.

3.4.3. Microstructural Analysis

Overview of Microstructural Evolution—The initial (Earth-grown) microstructure of the samples is shown in figure 2. The samples were produced from a homogeneous master alloy via directional solidification at a growth velocity of 0.2 cm/s. The high growth velocity was used to avoid macrosegregation along the length of the grown sample. This was further verified by inductively coupled plasma (ICP) analysis of the sample ends after the flight. The optical micrograph (differential interference contrast (DIC) illumination) in figure 2 shows relatively uniform cross sections with a faceted cellular/dendritic morphology; the growth is radially inward.

An overview of the microstructural evolution of the samples grown in space is obtained from the low magnification (x10) composite of a microsection of the quenched sample, figures 3(a)–(g), while the microstructural changes observed are summarized in table 2. Figure 3(a) shows schematically a summary

of processing lengths and velocities as well as the microstructure in each section. Also shown is the location and orientation of the microsection with respect to the furnace graphite diffuser center. Note that the microsection orientations of all the samples are such that they are thermally equivalent. The micrographs in figures 3(b)–(g) show the successive development of the microstructure as a function of the distance solidified and the growth velocity. As detailed later, for solidification at velocities ranging from V1 to V3 (see table 2 for velocity values), the growth occurs in a planar mode, while a distinct cellular morphology is seen at the V5 and V6 velocities. The planar to cellular transitions at V5 and V6 reveal many important aspects of the solidification of faceted materials in microgravity as discussed later. The microstructural evolution at the intermediate V4 velocity appears to be selectively cellular, with the transition to cellular mode detected in one of the grains, but not the others, after approximately 14 mm of directional solidification. The other grains continued to grow in a plane-front mode until the end of the solidification cycle (30 mm). This behavior is currently being investigated further. The Peltier and Seebeck samples generally had microstructures similar to those shown in figure 3, except that no cellular growth was observed at V4 in these samples, as discussed in more detail in the following sections.

Plane Front Solidification—The comparative development of a plane-front microstructure is illustrated in figures 4(a)–(b) which show the transition from a faceted cellular/dendritic structure of the Earth-grown portion of the samples to a plane-front morphology at the moving furnace interface (Peltier sample) and at the fixed furnace interface (during final cool down, quenching sample), respectively. At both interfaces, the initial cellular to plane-front transition interface was sharply delineated, as seen clearly by the low magnification micrograph in figure 4(c). The optical micrograph shows that only a few dominant orientations emerge from the initial (rapidly cast) microstructure, which was found to be a common feature of all three samples.

The microstructural appearance of continued growth in the plane-front mode (V1, V2, and V3) is shown in figure 5. Only a few orientations again dominate the growth front and the microstructure is characterized by a complete absence of microsegregation patterns (Sn-rich areas), indicating plane-front solidification. Our recent preliminary bulk orientation analysis via combined electron channeling/backscattered electron imaging (measurements at 600 points) indicates that the dominant growth direction was the trigonal $\langle 111 \rangle$ axis, with the grains rotated with respect to each other by a few degrees around this axis.

S/L Interface Shape—In all cases where an interface was revealed, for example during cellular to plane-front transition upon decreasing the growth rate, it was found that the interface was nearly flat, with a slight curvature (concave toward solid) near the s/l/crucible triple junction. The general shape of the interface is illustrated in figures 6(a)–(b) and 7. Figure 6(a) shows a schematic of the interface, while figure 6(b) shows a micrograph of the interface between steps 11M and 11V (table 1), where the growth rate was decreased from 26.9 to 1.85 $\mu\text{m/s}$. Upon closer examination, the boundary across each grain appears to be fairly flat, with the small angles between them giving the appearance of an overall slight curvature of the interface, as shown by the higher magnification micrograph of the interface center, figure 7. It can be seen from this differential interference contrast illumination micrograph that a distinct feature of the microstructural morphology at these interfaces is the sharp changes in the angles of columnar grain boundaries upon reducing the growth rate. The result is the disappearance of some of the orientations because of the net effect of the anisotropy of thermal conductivities and interfacial kinetics. It was found also that the interface was associated with a sharp compositional change, detected via secondary ion mass spectroscopy (SIMS) analysis, figure 8.

We note that in the absence of a Peltier interface demarcation capability, the above analysis provides only marginal information on the shape of the interface during growth at various velocities.

Notwithstanding, the results indicated that, in spite of the sharp temperature gradients imposed across the interface, the interface for each grain remains faceted.

In order to overcome the inability to pass Peltier pulses through the sample, attempts were made to demarcate the growing interfaces by closing the MEPHISTO isolation valve at predetermined times toward the end of the mission, thus providing short-term g-perturbations. The compositional analysis of these regions has so far not provided conclusive evidence of solute banding. More detailed analysis using SIMS is currently underway.

Transition to a Cellular Growth Mode—Microstructural examination of the microgravity-processed sections indicated that those regions of the samples grown at the V5 and V6 velocities exhibited a morphological transition to a cellular growth mode. One of the most interesting aspects of the transition at the V5 (26.9 $\mu\text{m/s}$) velocity was the existence of a distinct bias toward preferential breakdown of some grains. The preferential breakdown is shown schematically in figure 9(a) and via a low magnification micrograph in figure 9(b). Referring to these figures, it can be seen that one grain continues to grow in the plane-front mode for a significant distance while the other orientation is growing in a cellular mode. The distance of separation between the morphological instability of the two grains at this velocity is approximately 1.2 cm. The microstructural appearance of a preferential transition at a higher magnification is shown in figure 10. Figures 9 and 10 additionally show that the orientation which exhibits the cellular transition early is also the one that is tilted more with respect to the heat flow direction (6.5° ; in comparison, the tilting of cells in the other orientation was weak and close to zero). These observations clearly suggest an influence of the anisotropy in interface properties on the morphological stability of this alloy.

Cellular transition at a higher growth velocity (V6: 40 $\mu\text{m/s}$) exhibited features which were similar to that at V5, except that the differential instability of the neighboring grains was not as pronounced, resulting in a significantly narrower planar to cellular transition zone, as shown in figures 11(a)–(c). Figure 11(a) shows schematically the main features of cellular breakdown at this velocity, while the microstructural appearance of the cellular breakdown for the entire cross section of the sample is shown in figure 11(b) and at a higher magnification in figure 11(c). In this region also, two dominant grain orientations were present, albeit with additional subgrain boundaries. The cell spacing was significantly finer (0.179-mm average), with a cell tilt of 4.5° with respect to the heat flow direction for one grain. For the other grain, the growth orientation was even closer to the dominant growth direction. The cross-sectional view of cell geometry on a transverse section is shown in figures 12(a)–(d). Figure 12(a) shows schematically the appearance of cell boundaries in the two dominant orientations detected in this region, while 12(b) shows an optical micrograph in the bright field mode. The dominant orientations are clearly revealed under a sensitive-tint polarized light illumination, figure 12(c), while the cell boundaries are delineated by a dark-field illumination, figure 12(d). It can be seen that the microstructure consists of long plate-like cells, with only a marginal difference in the cell spacings of the two orientations. A measurement of the extinction angles under polarized light indicated that the two orientations were axially rotated by an angle not greater than 15° from each other. It may thus be concluded that while the two regions are separated by a large-angle boundary, both orientations are close to the dominant growth direction.

The microstructural analysis presented above indicates that selected orientations are morphologically more stable than others, resulting in a staggered planar to cellular transition. In general, anisotropic interfacial properties are expected to play a role in the morphological stability of planar interfaces, as well as the evolution of cellular and dendritic structures; this has been predicted theoretically by Coriell and Sekerka [1976], Coriell et al. [1994] by extending the linear stability analysis of Mullins and Sekerka [1964], and by Young et al. [1987] in the weakly nonlinear regime. These treatments indicate

that such anisotropies tend to stabilize the growth of a planar interface. Experimental observations reported by Tiller and Rutter [1956] for lead-tin alloys and by Trivedi [1990] and Trivedi et al. [1991] for transparent organic systems have been found to be generally consistent with the theoretical predictions.

The most important aspect of the present observations is the extremely long extension of the plane-front stability in one grain with respect to the neighboring grain(s). We believe that it is the anisotropy in interfacial kinetics, rather than in the surface energy or thermal conductivity, which is exerting such a strong influence on the morphological stability.

In addition, as shown above in figures 11(a)–(c), it was found that the extent of staggered cellular transition diminished at a higher growth velocity (V_6 , 40 $\mu\text{m/s}$). This observation is contrary to the theoretical predictions, which indicate that the stabilizing influence of interface kinetics should become more pronounced with increasing growth velocity. It is our belief that when the growth rate increases, the faceted interface(s) go through a kinetic roughening transition, become nonfaceted, and reduce the stabilizing effect of interfacial kinetics. Additional considerations include factors such as dislocation assisted versus dislocation free growth.

3.4.4. Kinetics Data Analysis

Resistance Measurements—Internal tracking of the interface movement was carried out by measuring the resistance change across the sample as the moving interface translated at preset velocities. The resistance change as a function of the processing time during a typical Seebeck measurement cycle* is shown in figure 13(a), along with the furnace (external) movement, which was tracked through a linear potentiometer. It can be seen that while the correlation between the external measurement of interface position and the internal measurement is good, there appears to be a slight lag in the resistance change at the beginning of solidification. The lag can be seen clearly when the melting and solidification parts of the cycle are plotted as a function of the distance, as shown in figure 13(b). It should be noted that the signals contain a superimposed (analog-to-digital conversion related) “noise” which can be removed via a full spectrum Fourier analysis, as illustrated in figure 14. Note that the slope changes in the resistance can now be seen without ambiguity. The difference between the resistance change during solidification and reverse (symmetrical) melting ($\Delta R = dR|_s - dR|m$) is shown in figure 15 using the filtered data. The figure shows that during solidification, the ΔR increases continuously until a steady plateau is reached after about 15 mm of solidification. After the external furnace translation is stopped, the difference diminishes back to nearly zero. Such behavior seems to be consistent with the retardation of the interfacial temperature from solute buildup and/or kinetics sources. However, since the corresponding Seebeck data are not available, a more definite conclusion cannot be reached at this time.

It may be recalled that the sample which was used to measure the resistance change during processing was also used to quench a 2-cm section at the end of the microgravity experimentation period. The quenching behavior was monitored through the resistance change, as illustrated by the plot in figure 16, showing the sharp increase in the resistance at the instant of quench. Also shown on this figure is the furnace position and the output from two thermocouples in the resistance sample, which were located approximately 40 and 90 mm from the interface. The subsequent decrease in the resistance after quenching indicates a melting of that 2-cm section of the sample which was pushed from the cold zone into the hot zone at the fixed interface. Note that the time constant for melting is appreciably larger in this case.

*The processing sequence during Seebeck measurements typically consisted of solidification/stabilization (i.e., no furnace movement)/reverse melting/stabilization.

Thermal Gradient Measurements—The temperature gradients were measured continuously during solidification and melting by using thermocouples in the quenching sample, designated as T1 and T3. A typical thermal measurement is shown in figure 17. Also shown in the figure are the corresponding furnace position and the melting temperature. For these thermocouples, the preflight predicted positions after volume compensation were 105 and 61 mm. The positions deduced from the thermal data were 100.3 ± 1.4 mm and 61.9 ± 1.6 mm, respectively.

The data were linearized in the vicinity of the melting temperature (~ 271.4 °C) separately for the solid and the liquid. The thermal gradients are represented as:

$$\begin{aligned} \frac{dT}{dX} &= \frac{dT}{dt} \cdot \frac{dt}{dX} \\ &= \frac{1}{V} \frac{dT}{dt} \end{aligned} \quad (1)$$

The gradients were found to be: $(G_L, G_S)_{\text{solidification}} = 216$ and 219 °C/cm and $(G_L, G_S)_{\text{melting}} = 213$ and 219 °C/cm.

Seebeck Measurements—The interfacial undercooling was measured using the Seebeck technique in which the differential thermo-emf is measured from two s/l interfaces,⁸⁻¹⁰ one stationary and the other moving. The stationary interface acts as a reference junction, against which the temperature changes of the moving interface can be measured from a differential signal at the sample ends. For isotropic materials or single crystals, the differential voltage is directly proportional to the difference in the temperatures of the moving and stationary interfaces, while for polycrystals and particularly for anisotropic materials, additional terms are introduced from effects associated with thermo-emfs of grain boundaries and orientations in the gradient zone. Thus,

$$E_s = \eta_{s/l} \Delta T_i + \int \nabla T(x) \sum_{i=1}^n \eta_{\theta_i / \theta_{i+1}} dx \quad (2)$$

where $\eta_{s/l}$ is the difference in the Seebeck coefficients of the solid and liquid, ΔT_i is the interfacial undercooling, $\nabla T(x)$ is the temperature change as a function of distance in the solid, and $\eta_{\theta_i / \theta_{i+1}}$'s are the crystallographic orientation-dependent Seebeck coefficients.[†] The summation is implied over the range of orientations in the microstructure. Therefore, because of the interaction between microstructural features (e.g., grain boundaries) and the temperature gradients generated during processing, the contribution to the overall Seebeck emf can vary if the microstructure undergoes changes during interface migration. This situation is shown schematically in figures 18(a) to 18(c), illustrating the passage of a temperature gradient converting an equiaxed cellular structure to a columnar one during plane-front directional solidification. As the gradient zone passes over the microstructure, there is a corresponding change in the differential Seebeck emf, associated with the changes in the growth morphology, grain shapes, and orientations, as shown schematically in figure 18(c). Obviously, when the microstructure forming at the interface is the same as that leaving the gradient zone, the change in the Seebeck signal due to structural contributions must diminish.

[†] In order to eliminate such structural effects and determine the interfacial contributions, Favier and Rouzaud used a technique of subtracting the Seebeck signals during melting from those during solidification for Sn-Bi alloys processed on USMP-1. For anisotropic Bi-Sn alloys, however, we found the technique to be inaccurate.

The interfacial temperature depression is made up of contributions from three sources: Chemical (ΔT_c), kinetic (ΔT_k), and capillarity (curvature-related, ΔT_r). For plane-front solidification, the capillarity contribution can be ignored, while, as discussed below, the chemical contribution can be calculated provided the convecto-diffusive state of the liquid can be quantified. The kinetic undercooling in the case of dislocation assisted growth is generally related to the growth velocity by

$$V = a\Delta T_k^n \quad (3)$$

where V is the growth velocity and a and n are constants. In order to compare with microgravity experiments, the kinetic law for pure Bi single crystals was previously determined based on 72 measurements at growth velocities ranging from 2×10^{-4} to 9.5×10^{-3} cm/s. The resulting values for a and n were 0.0274 cm/s(K)^n and 1.65, respectively,¹¹ which agreed fairly well with those reported in the literature.¹²⁻¹⁴

Seebeck Signals During Plane Front Solidification—Two melting/solidification cycles were performed at the beginning of microgravity processing prior to the Seebeck anomalies. The melting/solidification sequence of these cycles is shown schematically in figure 19, while the corresponding microstructural evolution is shown in figures 20(a)–(e), along with the Seebeck signals obtained during each processing step. The microstructural evolution sketched in figure 20 was based on the microstructures obtained during final solidification of the sample under nearly identical growth conditions, as shown earlier in figures 4(a)–(c).

As noted earlier and shown in figure 20(a), the interface that formed after thermal stabilization of the furnace is nearly flat with very slight curvature at the triple-junction between the solid, liquid, and the crucible (fused quartz) wall. The corresponding Seebeck emf during this stationary state is constant with a mean value of $\sim 70 \mu V$, representing the baseline for the measurements. During melting at a velocity of 26.7×10^{-4} cm/s, figure 20(b), the Seebeck emf is seen to decrease to $55 \mu V$ at a rate of $\sim 7.5 \mu V/\text{mm}$. Upon stopping the furnace translation, the signal goes through a transient and increases by $7.5 \mu V$ to a stable level of $62.5 \mu V$. This transient, lasting approximately 200 seconds after the furnace had stopped, is related to local adjustments in the thermal fields as well as stabilization of the microstructure near the interface. Thus, for the initial faceted dendritic microstructure, the net Seebeck change during melting is $3.75 \mu V/\text{mm}$.

During the reverse 2-mm solidification at a velocity of 1.85×10^{-4} cm/s at the same location, figure 20(c), the Seebeck signal decreases from 62.5 to $22.5 \mu V$, and upon stopping the furnace translation, the signal increases through a transient by $10.5 \mu V$. The time interval for the transient in this case is, however, much longer than that after melting (~ 900 seconds versus ~ 200 s), indicating an additional slower decaying component. The transient in the Seebeck signal at the end of solidification is related primarily to the solutal decay (diffusional decay of the solute-rich boundary layer and concurrent decay of the chemical undercooling), with some early contributions from thermal and kinetics adjustments when the interface comes to rest. As discussed later, the decay can be used to determine the kinetic undercooling at the interface. It should be noted that even though the same 2 mm which was melted was solidified again, the Seebeck signals behave differently. This is due to the fact that two important changes take place during this plane-front solidification: (1) A solute-rich boundary layer begins to build up at the interface, and (2) the new structure formed comprises predominantly of columnar grains aligned parallel to the heat flow direction (figures 4(a)–(c)) and therefore is appreciably different from the microstructure which was melted.

The reverse melting of 7 mm at a velocity of 26.7×10^{-4} cm/s, figure 20(d), shows many interesting features which give quantitative information on the microstructural evolution. First, for the initial 2-mm of melting, the section that had been solidified in space (columnar grains) is melted back. In this case, the Seebeck signal tracks the initial solidification, except in reverse order (figure 20(c)). After melting of the space-grown section, there is an inversion in the Seebeck signal, as it begins to track the melting of the ground-grown portion of the sample, with the same slope as the first 2-mm melting (figure 20(b)) of the ground-grown sample. It should be noted that the first 2-mm of solid contained a concentration of Sn ranging from kC_0 (0.0029 at.%) to 0.0048 at.%, whereas the latter section contains C_0 (0.1 at.%). In addition, the first section contained only a few directionally grown grains, while the latter section is faceted cellular/dendritic. The behavior of the signal thus clearly suggests a very sensitive response of the Seebeck emf to the microstructure as well as the interface temperature. Upon stopping the furnace translation (after 7 mm), the signal undergoes a transient, and stabilizes back to a level observed after the first melting (62.5 μV), indicating the establishment of an interface very similar to the one encountered after 2-mm melting.

The directional solidification following this melting is shown in figure 20(e). The evolution of the Seebeck emf is identical to the first 2-mm solidification (figure 20(c)), indicating nearly identical structural development. However, the signal shows an inflection point after approximately 4.6-mm solidification and continuously decreases in slope thereafter, resulting in a lower rate of change at the end of the solidification cycle (7 mm). The behavior of the signal for this measurement as well as the first solidification shown in figure 20(c) can be described empirically by an error function of the form

$$E_s = a + \frac{1}{2}b \left[1 + \frac{\text{erf}(t - c)}{\sqrt{2d}} \right], \quad (4)$$

where a , b , c , and d are constants and t is the time in seconds.

Based on our earlier discussion (figure 18), the decrease in slope indicates a change in the contribution from microstructure/thermal field interaction related effects. It is clear that, as the oriented plane-front microstructure develops, as shown in figure 4(a), the Seebeck emf from gradient affected zone decreases accordingly. Upon stopping the furnace translation (after a solidification of 7-mm), the signal is seen to decay in a characteristic manner, until a stable thermosolutal and interface profile is attained.

The temperature depression due to compositional changes for the purely diffusive state can be calculated using the classical Tiller et al. [1953] approach. The governing equation for the plane-front solidification in initial transient (for the present velocity, a steady state would be achieved at a distance > 15 cm) is

$$C_1^* = C_0 \left\{ \frac{1-k}{k} \left[1 - \exp\left(-k \frac{V}{D_1} x\right) \right] + 1 \right\} . \quad (5)$$

The chemical contribution is then given by

$$\Delta T_c = m_1 (C_1^* - C_0) \quad (6)$$

where C_1^* is the composition of the liquid at the interface, C_0 is initial alloy composition (0.1 at.%), k is the equilibrium partition coefficient (0.029), V is the growth velocity (1.85×10^{-4} cm/s), D_1 is the liquid

diffusivity ($5.315 \times 10^{-5} \text{ cm}^2/\text{s}$ for Sn in Bi for an average temperature in the gradient zone of 435.5°C),¹⁶ x is the distance solidified, and m_1 is the liquidus slope ($-2.32 \text{ K/at.}\%$).

Based on equations (5) and (6), the temperature depression due to compositional changes after 2-mm and 7-mm solidification is 0.155 and 0.533 K, respectively, from which we can deduce the magnitude of nonsolutal contributions, such as the kinetic undercooling. The resulting values of 2.75 and 3.5 μV corresponded to a kinetic undercooling of 0.055 and 0.07 K after 2-mm and 7-mm solidification, respectively.

The above determined interface kinetics supercoolings compare well with those calculated based on the kinetic undercooling for pure Bi single crystals (0.048 K), using equation (3) and the values of constants given earlier. However, it should be emphasized that the constants in equation (3) were derived for pure Bi single crystals, which can be appreciably different for the rate equation for alloys, as discussed by Abbaschian and Mehrabian [1978]. Unfortunately, because of the Seebeck signal anomalies, additional data could not be gathered during the rest of the mission to determine the effect of compositional changes on interfacial kinetics.

We note that, because of thermosolutal convection, accurate measurements of the kinetic undercooling in alloys are not feasible on Earth, particularly when the growth velocities are on the order of a few $\mu\text{m/s}$. As shown above, the kinetic measurements can however be performed in a high-quality microgravity environment.

3.5. SUMMARY

We report two major findings based on the first 8 months of data and microstructural analysis:

(1) The morphological stability of various crystallographic orientations is significantly affected by the anisotropy of interface kinetics and surface energies. The effect was clearly demonstrated via postflight microstructural analysis. The analysis showed that the growth of one orientation occurred in a plane-front mode while the neighboring orientations exhibited a transition to a cellular mode. The most interesting aspect of such a staggered breakdown was the relatively large extent to which the plane-front growth continued in one orientation. It is clear that the anisotropy in interfacial properties of the faceted alloy in general, and the interface kinetics in particular, play a major role in stabilizing plane-front growth. The very significant interplay between the crystallography-dependent thermophysical properties (e.g., interface kinetics coefficients, surface energy, and thermal conductivity) of the faceted alloy and effects associated with any possible solute diffusion parallel to the interface (resulting from a staggered morphological transition) thus warrant further experimental and theoretical investigation.

(2) The differential Seebeck signals allowed the monitoring of interfacial phenomena. While these signals are extremely sensitive to the interaction between thermal gradients and local microstructural details, the magnitude of kinetic undercooling could nevertheless be calculated from the decay in the Seebeck signal at the end of solidification. Using this method, the kinetic undercooling was measured even at very slow growth rates. We note that such measurements are not possible on Earth because of thermosolutal convective effects.

3.6. REFERENCES

1. Coriell, S.R., and R.F. Sekerka, "The Effect of Anisotropy of Surface Tension and Interface Kinetics on Morphological Stability," *J. Crystal Growth*, 34(2), 157, 1976.
2. Coriell, S.R., B.T. Murray, and A.A. Chernov, "Kinetic Self-Stabilization of a Stepped Interface: Binary Alloy Solidification," *J. Crystal Growth*, 141, 219, 1994.
3. Mullins, W.W., and R.F. Sekerka, "Stability of a Planar Interface During Solidification of a Dilute Binary Alloy," *J. Appl. Phys.*, 35, 444, 1964.
4. Young, G.W., S.H. Davis, and K. Brattkus, "Anisotropic Interface Kinetics and Tilted Cells in Unidirectional Solidification," *J. Crystal Growth*, 83, 560, 1987.
5. Tiller, W.A., and J.W. Rutter, "The Effect of Growth Conditions Upon the Solidification of a Binary Alloy," *Can. J. Phys.*, 34, 96, 1956.
6. Trivedi, R., "Effects of Anisotropy Properties on Interface Pattern Formation," *Appl. Mech. Rev.*, 43(5), Part 2, S79, 1990.
7. Trivedi, R., V. Seetharaman, and M.A. Eshelman, "The Effects of Interface Kinetics Anisotropy on the Growth Direction of Cellular Microstructures," *Met. Trans. A*, 22A, 585, 1991.
8. Favier, J.J., "Etude des Cinetiques Cristallisation par Application de l'Effet Thermoelectrique Analyse de la Temperature d'une Interface de Solidification," Ph.D. Dissertation, Grenoble, 1977.
9. Alvarez, J., S.D. Peteves, and G.J. Abbaschian, "Thermoelectric Effects Across Solid-Liquid Gallium Interface," *Thin Solid Films and Interfaces*, edited by J.E.E. Baglin et al., MRS Symp. Proc. 25, 345, 1984.
10. Peteves, S.D., and G.J. Abbaschian, "Growth Kinetics of Faceted Solid-Liquid Interfaces and Kinetic Roughening," *J. Crystal Growth*, 79, 775, 1986.
11. Abbaschian, R., A.B. Gokhale, J.J. Favier, G. Cambon, S.R. Coriell, H.C. de Groh III, and R.L. DeWitt, "A Study of Directional Solidification of Faceted Bi-Sn Alloys in Microgravity," AIAA 95-0608, Washington, DC, 1995.
12. Kobayashi, K.F., M. Kumikawa, and P.H. Shingu, "Growth Rate of Crystals of Pure Metals Nucleated From the Undercooled Melt," *J. Crystal Growth*, 67, 85, 1984.
13. Alfintsev, G.A., and D.E. Ovsienko, "Study of the Growth Mechanism of Certain Metal Crystals From the Melt," in *Growth and Imperfections in Metallic Crystals*, edited by D.E. Ovsienko, Consultants Bureau, NY, p. 32, 1968.
14. Sixou, B., A. Rouzaud, and J.J. Favier, "Growth Kinetics in Ultra-Pure Bismuth Using a Thermoelectric Method for Interface Temperature Measurements," *J. Crystal Growth*, 137, 605, 1994.

15. Tiller, W.A., K.A. Jackson, J.W. Rutter, and B. Chalmers, "The Redistribution of Solute Atoms During Solidification of Metals," *Acta. Met.*, *1*, 428, 1953.
16. Niwa, K., M. Shimoji, S. Kado, Y. Watanabe, and T. Yokokawa, "Studies on Diffusion in Molten Metals," *J. of Metals*, *91*, 96, 1957.
17. Abbaschian, G.J., and R. Mehrabian, "Effect of Aluminum on the Solidification Kinetics and Morphology of Gallium," *J. Crystal Growth*, *43*, 433, 1978.

Publications/Presentations from the Current Research Program

1. Gokhale, A.B., R. Krishnasamy, and R. Abbaschian, "In situ Monitoring of Solid-Liquid Interfaces During Crystal Growth," MRS Spring Meeting, San Francisco, CA, April 28, 1992.
2. de Groh, H.C. III, "A Numerical and Experimental Study of Natural Convection and Interface Shape in Crystal Growth," First International Conference on Transport Phenomena in Processing, 1993.
3. Gadonneix, D., A.B. Gokhale, and R. Abbaschian, "Morphological Stability of Faceted Solid/Liquid Interfaces in Dilute Bi-Sn Alloys," AIAA 94-0791, 32nd Aerospace Sciences Meeting & Exhibit, Reno, NV, January 10–13, 1994.
4. de Groh, H.C. III, and E.S. Nelson, "On Residual Acceleration During Space Experiments," in *Heat Transfer in Microgravity Systems*, edited by S.S. Sadhal and A. Gopinath, HTD-290, pp. 23–33, ASME, 1994.
5. Abbaschian, R., NASA Research Summaries: Microgravity Materials Science Conference, Huntsville, AL, May 24–25, 1994.
6. Gokhale, A.B., "USMP-2 Preliminary Results," NASA-Lewis Research Center, Cleveland, OH, July 5, 1994.
7. Abbaschian, R., A.B. Gokhale, J.J. Favier, S.R. Coriell, H.C. de Groh III, and R. DeWitt, "Directional Solidification of Faceted Bi-Sn Alloys in Microgravity," AIAA 95-0608, 33rd Aerospace Sciences Meeting and Exhibit, Reno, NV, January 9–12, 1995.
8. Yao, M., R. Raman, and H.C. de Groh III, "Numerical Modeling of Bridgman Growth in Space with MEPHISTO," International Conference on Computational Engineering Science, Presented at the 1995 ICES Meeting, July 30–August 3, 1995.
9. Gadonneix, D., "Morphological Stability of Faceted Bi-Sn Alloys During Directional Solidification," Master's Thesis, University of Florida, 1995.
10. Yeoh, G.H., G. de Vahl Davis, E. Leonardi, H.C. de Groh III, and M. Yao, "A Numerical and Experimental Study of Natural Convection and Interface Shape by Crystal Growth," *J. Crystal Growth*, accepted, 1995.

11. Yao, M., R. Raman, and H.C. de Groh III, "Numerical Simulation of Heat and Mass Transport During Space Crystal Growth with MEPHISTO," NASA TM, in review, 1995.

Table 3-1. Summary of Growth Conditions and Shuttle Activities During Final Solidification Steps

Step #	Start Position, mm	End Position, mm	Velocity mm/Hr ($\mu\text{m/s}$)	Start Time MET	End Time MET	FF Temp., °C	MF Temp. °C	Shuttle Attitude	Orbiter Activities
11C	001	011	V1: 06.66 (1.85)	08/06:30:37	08/08:00:42	706	690	-XLV,+ZVV	Crew Sleep
11G	011	026	V2: 12.17 (3.38)	08/17:18:15	08/18:32:11	703	690	-XLV,+ZVV	Crew Off-Duty, NOP
11H	026	056	V3: 24.16 (6.71)	08/20:19:21	08/21:33:52	703	690	-XLV,+ZVV	Crew Off-Duty, NOP, Fan Checks
11I	056	086	V4: 48.00 (13.34)	08/23:06:04	08/23:43:34	703	690	-XLV,+ZVV	Crew Exercise, SIMO Dump Init., Filter Cleaning
11M	086	116 (104)	V5: 96.77 (26.88)	09/02:33:35	09/02:52:11	703	690	-XLV,+ZVV	Crew Exercise
11V	104	106	V1: 06.66 (1.85)	11/03:54:21	11/04:12:22	700	690	-ZLV,+YVV	Pre-Sleep, -ZLV Maneuver
11W	106	120	V3: 24.42 (6.78)	11/10:09:18	11/10:43:42	713	690	-ZLV,+YVV	Crew Sleep, MEPHISTO Relief Valve Open/Close, NOP
16	120	149	V6: 144.2 (40.01)	11/14:09:15	11/14:21:19	709	690	-ZLV,+YVV	Post Sleep, Metabolic Studies
17	149	169	QUENCH	11/14:21:20	11/14:21:21	709	690	-ZLV,+YVV	

Notes:

Start and End Positions in MEPHISTO Coordinates

MET: Mission Elapsed Time

FF: Fixed Furnace

MF: Moving Furnace

NOP = No Other Perturbations

Table 3-2. Summary of Morphological Changes in USMP-2 Samples

Sample	Growth Conditions						
	Earth Grown	V1 1.85 $\mu\text{m/s}$	V2 3.38 $\mu\text{m/s}$	V3 6.71 $\mu\text{m/s}$	V4 13.34 $\mu\text{m/s}$	V5 26.88 $\mu\text{m/s}$	V6 40.01 $\mu\text{m/s}$
Quench	A	B	B	B	B1	C1	C3
Seebeck	A	B	B	B	B	C2	C4
Peltier	A	B	B	B	B	D	D

- A: Faceted cellular/dendritic with radially inward growth. Microstructure shown in figure 2.
- B: Plane front. Columnar grains. Microstructure shown in figure 5.
- B1: Predominantly plane front. Columnar grains. One grain shows preferential cellular breakdown.
- C1: Two dominant grains. Transition of one grain to cellular mode after 2.54-mm growth at V5. Cellular breakdown in the second grain occurs in a stepwise sequence, with the first breakdown ~ 0.18 mm after the breakdown in the first grain and the last breakdown 1.7 mm after that in the first grain. The grain which breaks down first shows a cell tilt of 4° with respect to the heat flow direction and an average cell spacing of 0.356 mm. The second grain shows a cell tilt close to zero and an average cell spacing of 0.517 mm.
- C2: Two dominant grains. One grain breaks down ~ 0.6 mm after growth at V5, the second grain continues plane-front growth for an appreciable length of time (12.22 mm) before transitioning to a cellular mode. The cells in the grain which breaks down first are tilted 6.5° with respect to the heat flow direction, with an average cell spacing of 0.265 mm, while the cell tilt in the second grain is close to zero, with an average cell spacing of 0.276 mm. Microstructure shown in figure 9.
- C3: Two dominant grains. The entire cross section shows a transition to a cellular growth mode almost immediately after the start of growth at this velocity. The cells are tilted $\sim 4.5^\circ$ with respect to the heat flow direction, with an average cell spacing of 0.279 mm.
- C4: Two dominant grains. The entire cross section shows a transition to a cellular growth mode ~ 3.2 mm after the start of growth at this velocity. The cells are tilted $\sim 4.5^\circ$ with respect to the heat flow direction, with an average cell spacing of 0.179 mm. Microstructure shown in figure 11.
- D: Under investigation.

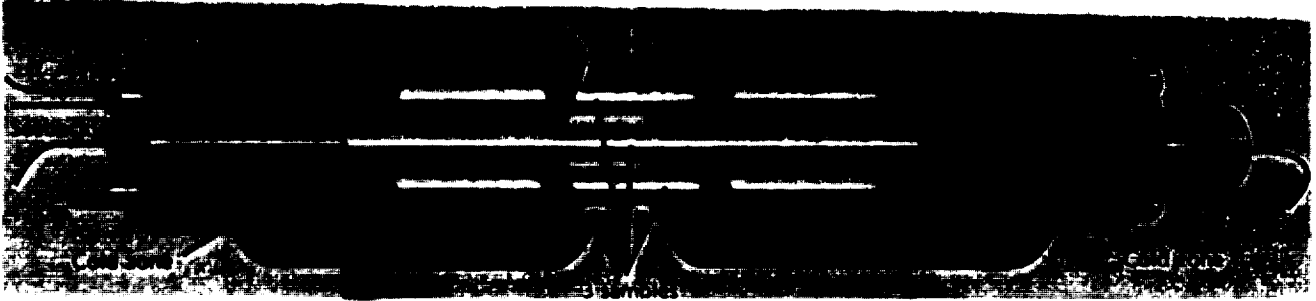


Figure 3-1. (a) MEPHISTO core assembly.

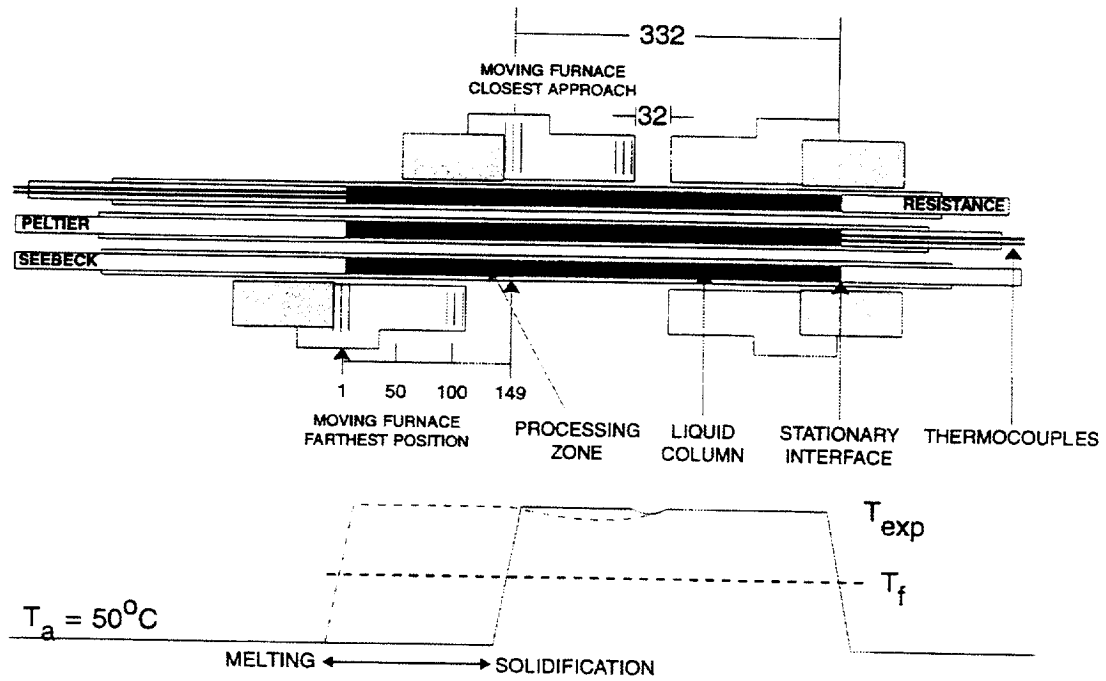
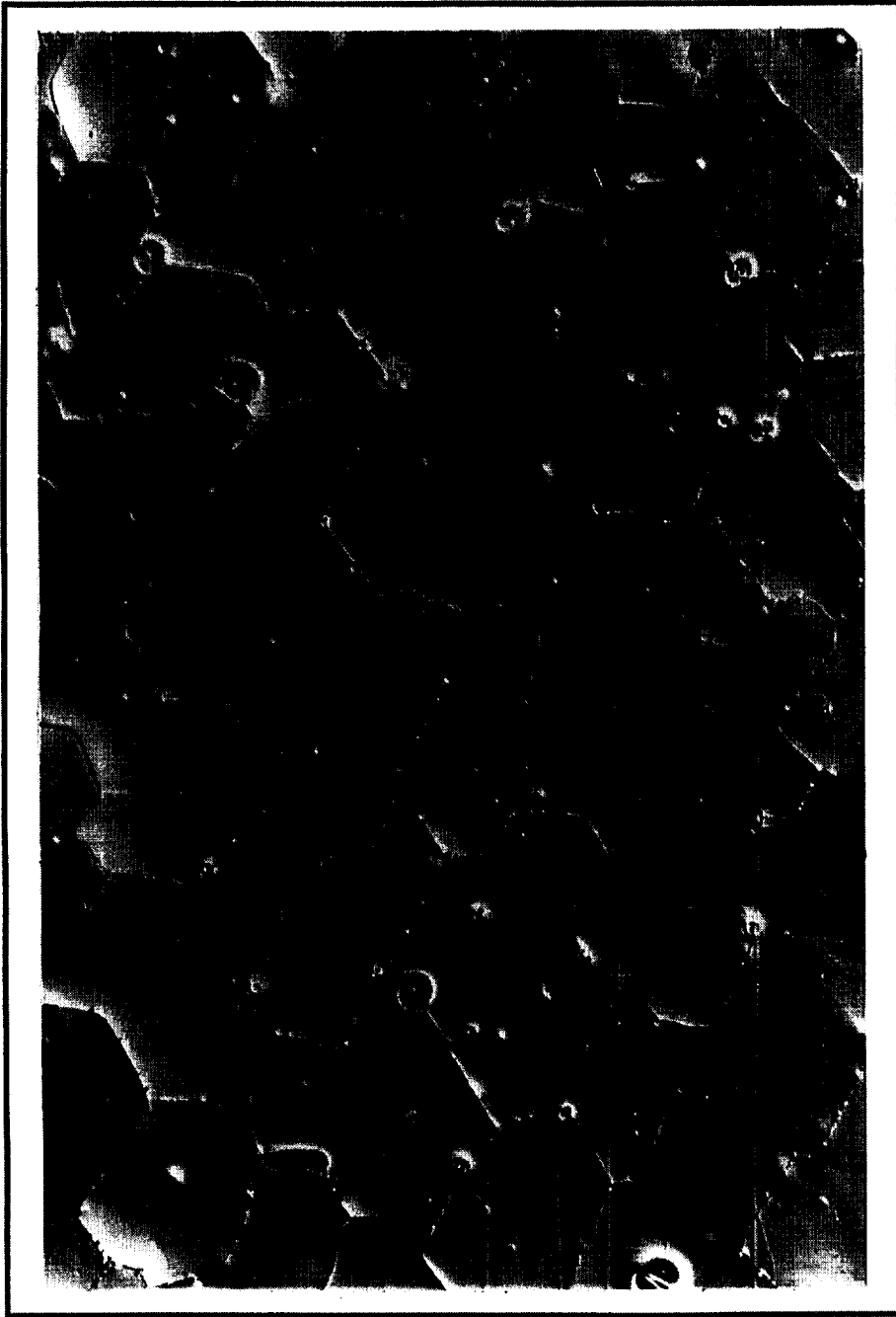


Figure 3-1. (b) Arrangement of the experimental samples in MEPHISTO. Shows three rod-shaped samples processed in parallel, the location of thermocouples, and the two solid/liquid (s/l) interfaces from which a differential Seebeck electro motive force (emf) is measured. Also shown is the overall temperature distribution in the apparatus during processing (schematic).



75 μm

Figure 3-2. Initial microstructure showing a faceted cellular/dendritic morphology. Samples grown via directional solidification at a rate of 0.2 cm/s. Optical micrograph, differential interference contrast (DIC) illumination

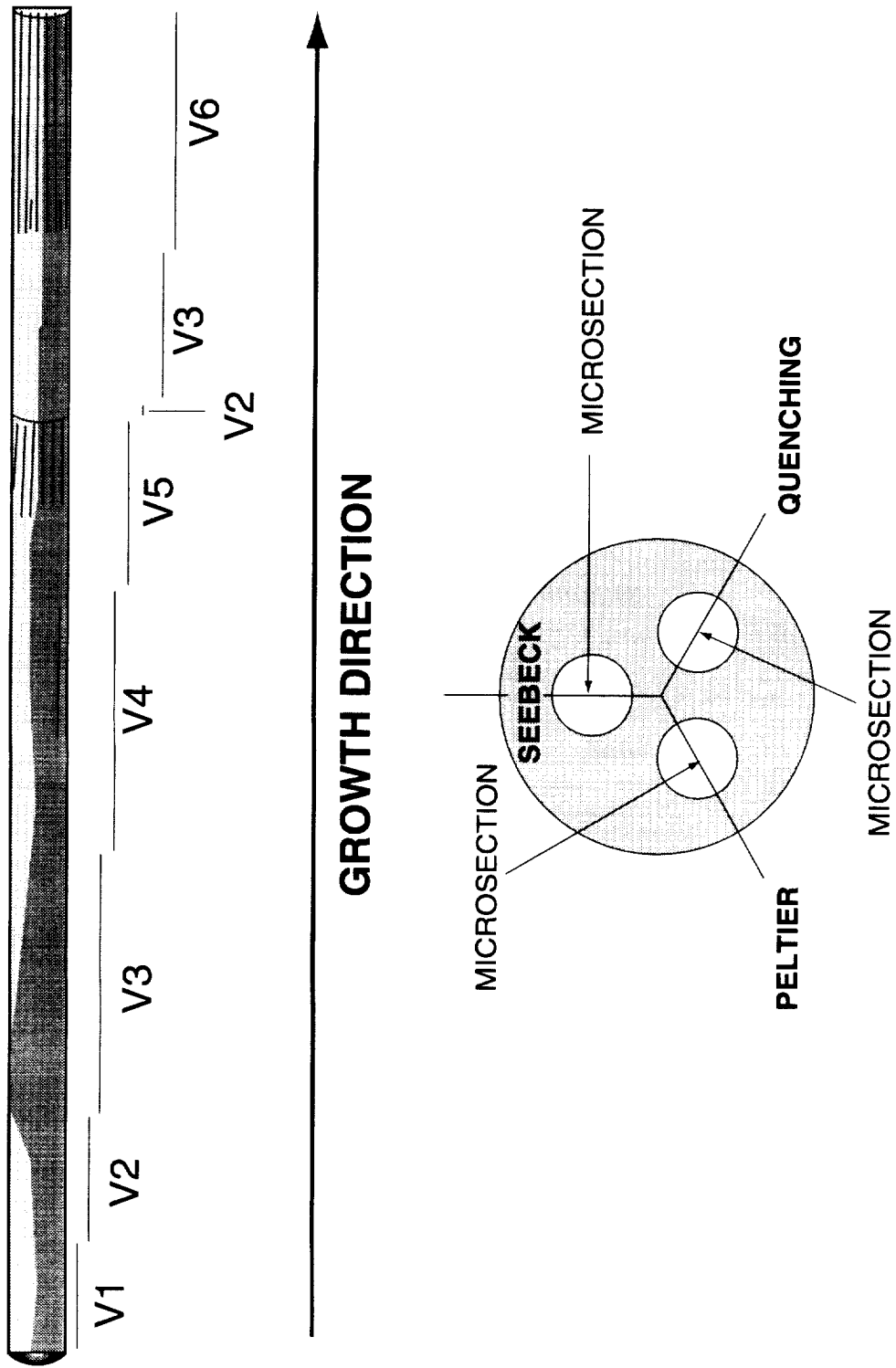


Figure 3-3. (a) Summary of sample sections preserved during final solidification. Also shows the orientation of microsections of the samples which are taken in a direction pointing to the diffuser center and thus thermally equivalent.

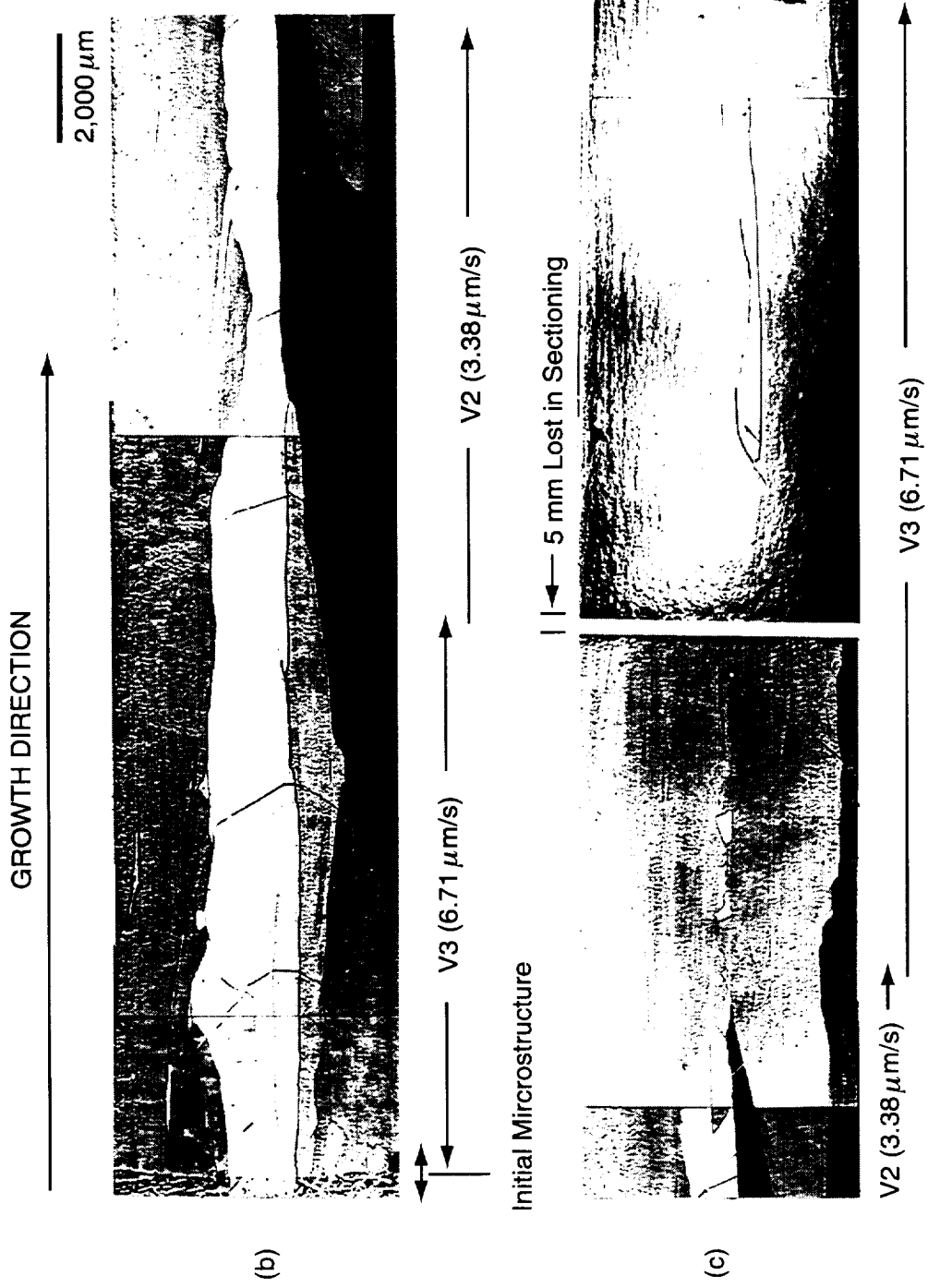


Figure 3-3. (b) Microstructural evolution starting with the initial microstructure at growth velocities V1 and V2.
 (c) Continued growth at V2 and V3.

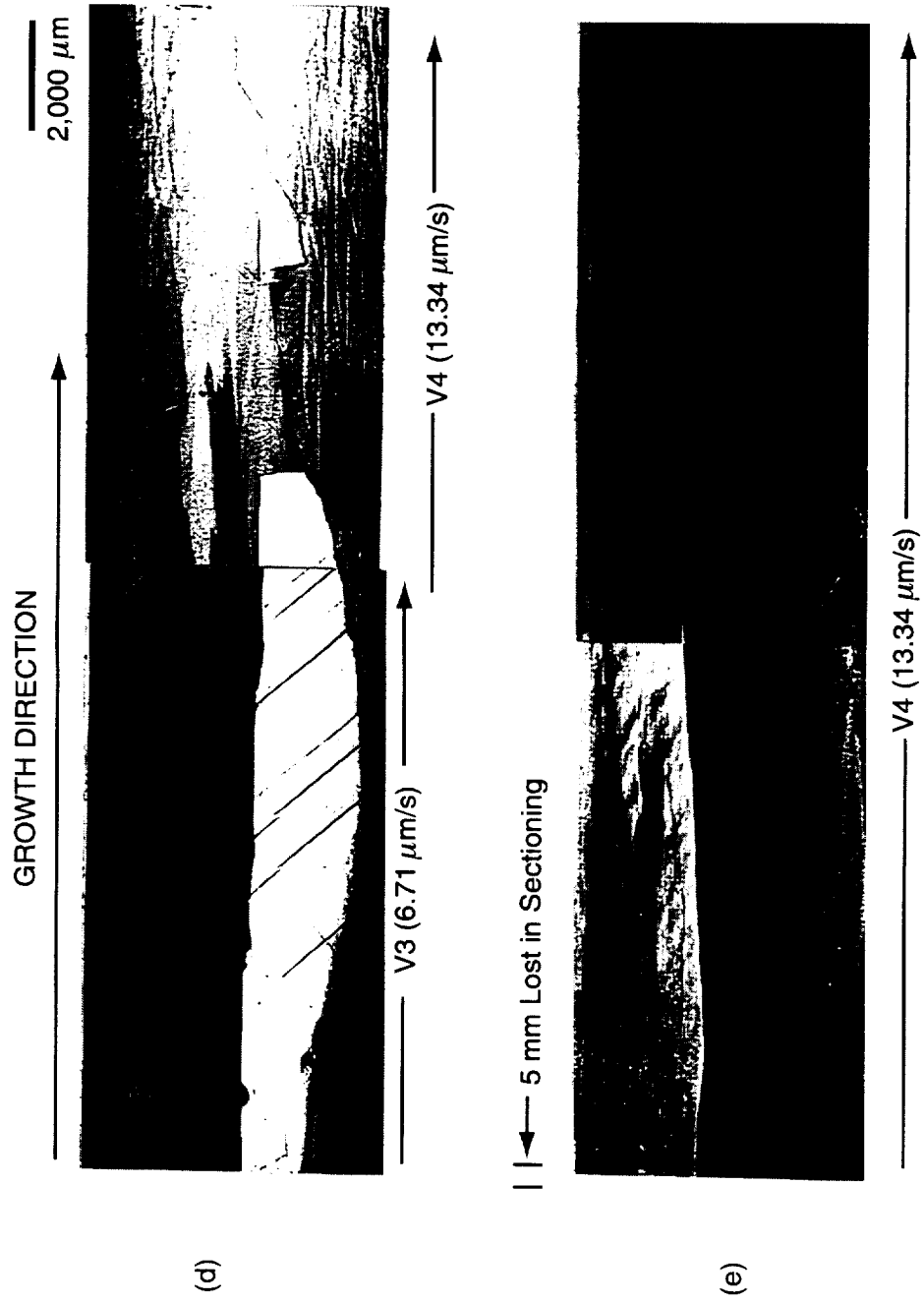


Figure 3-3. (d) Microstructural evolution during continued growth at V3 and after change in the growth rate to V4. (e) Continued growth at V4.

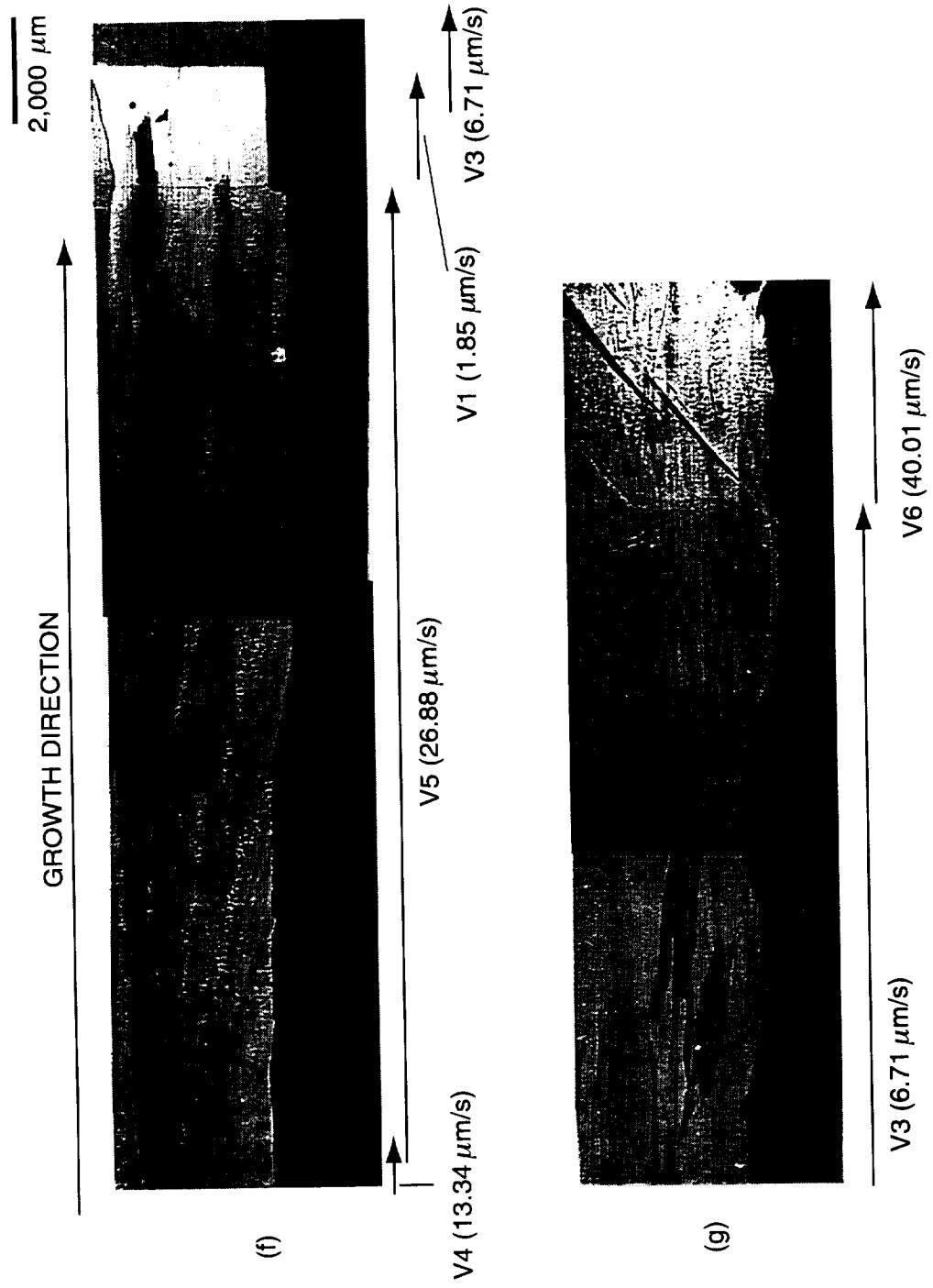


Figure 3-3. (f) Microstructural evolution during continued growth at V4 and growth rate changes to V5, V1, and V3. Note the cellular breakdown during growth at V5. (g) Continued growth at V3, followed by a growth rate change to V6. Note the development of a cellular structure at V6.

Plane Front Growth, Peltier Sample, Moving Furnace

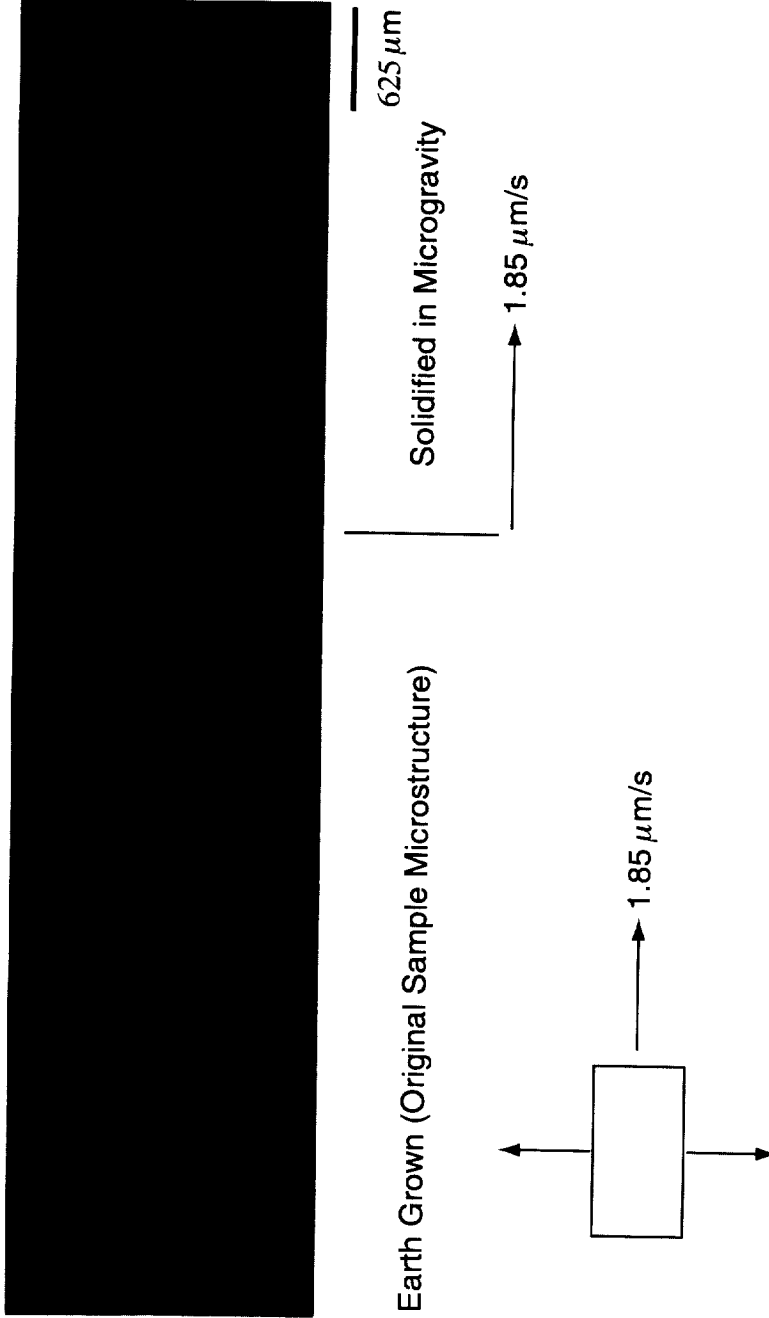


Figure 3-4. (a) Microstructural appearance of the interface between the Earth-grown (faceted cellular/dendritic) and microgravity-processed (plane front) portions of the Peltier sample, moving furnace side. The composite micrographs were obtained under a polarized light/sensitive tint illumination and show the emergence of a few dominant orientations during directional solidification in microgravity.

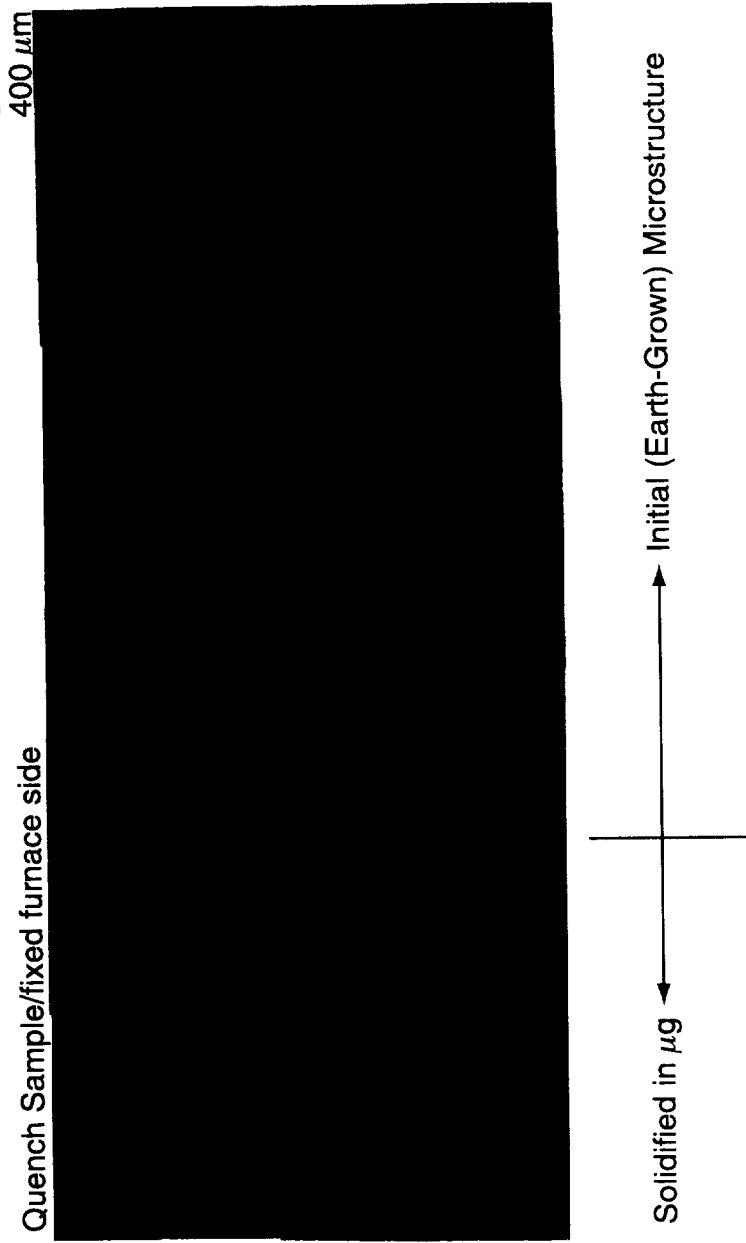


Figure 3-4. (b) Microstructural appearance of the interface between the Earth-grown (faceted cellular/dendritic) and microgravity-solidified (plane front) portions of the Resistance/Quenching sample, fixed furnace side. The microstructure developed during final cool down. Polarized light/sensitive tint illumination.

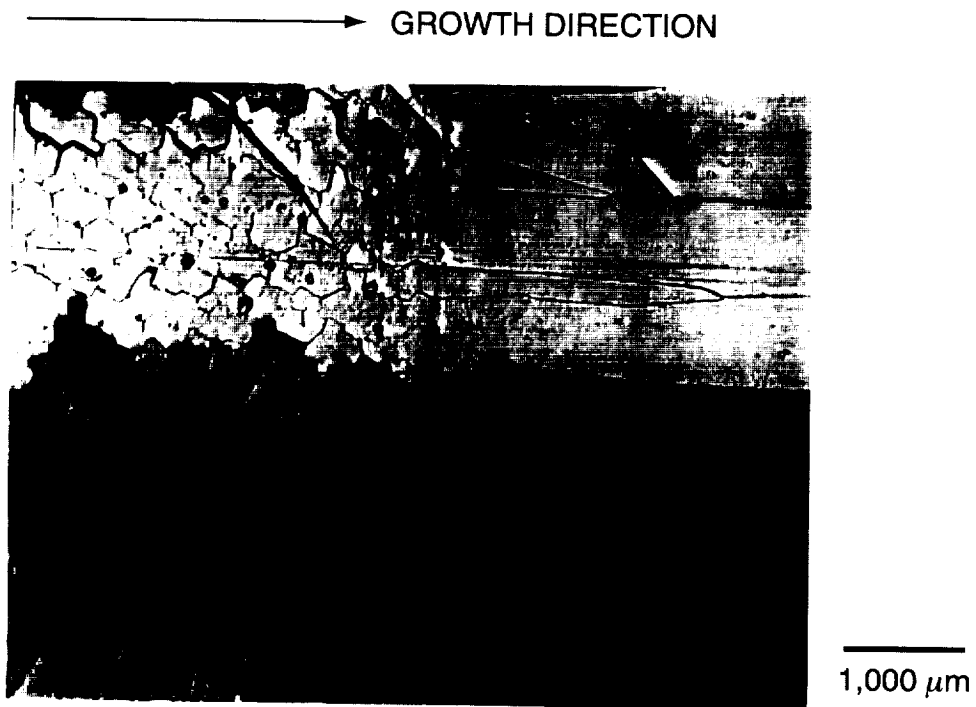


Figure 3-4. (c) Interface between the initial microstructure and microgravity solidification at a growth velocity of $1.85 \mu\text{m/s}$. Micrograph represents the bottom half of the sample cross section. Note the emergence of two dominant orientations from the initial structure.

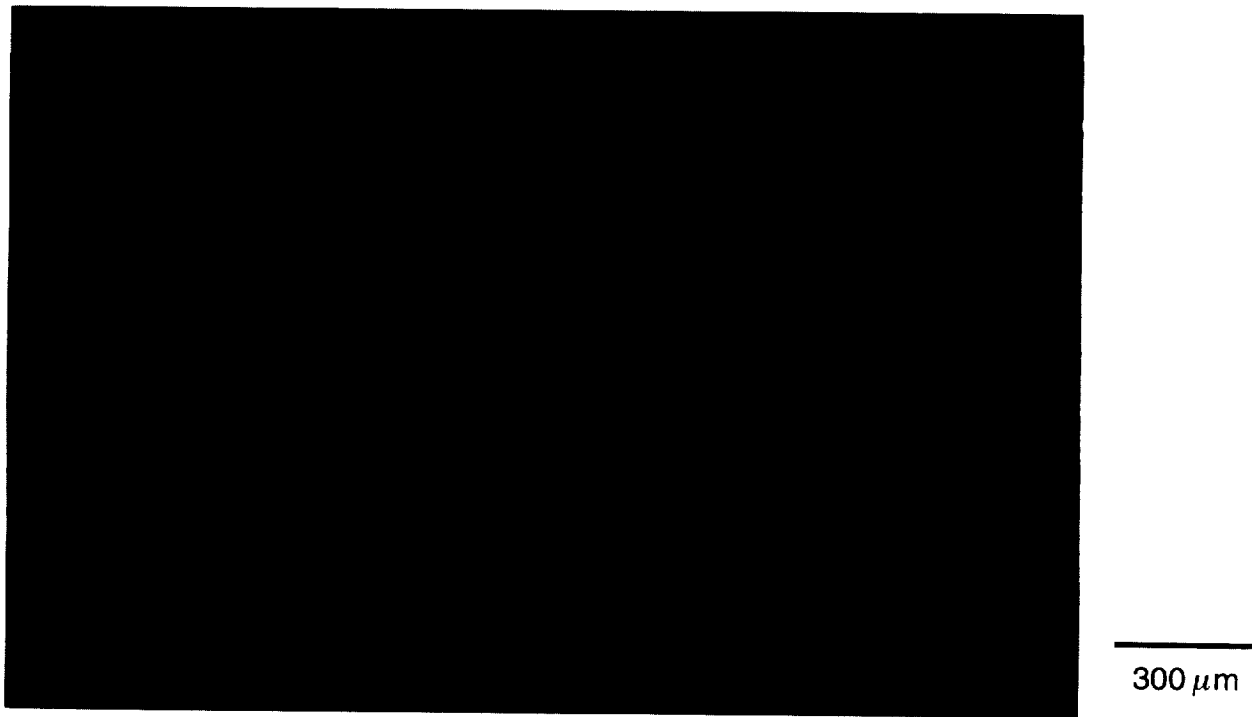


Figure 3-5. Plane front solidification at velocities ranging from 1.85 to $6.71 \mu\text{m/s}$.

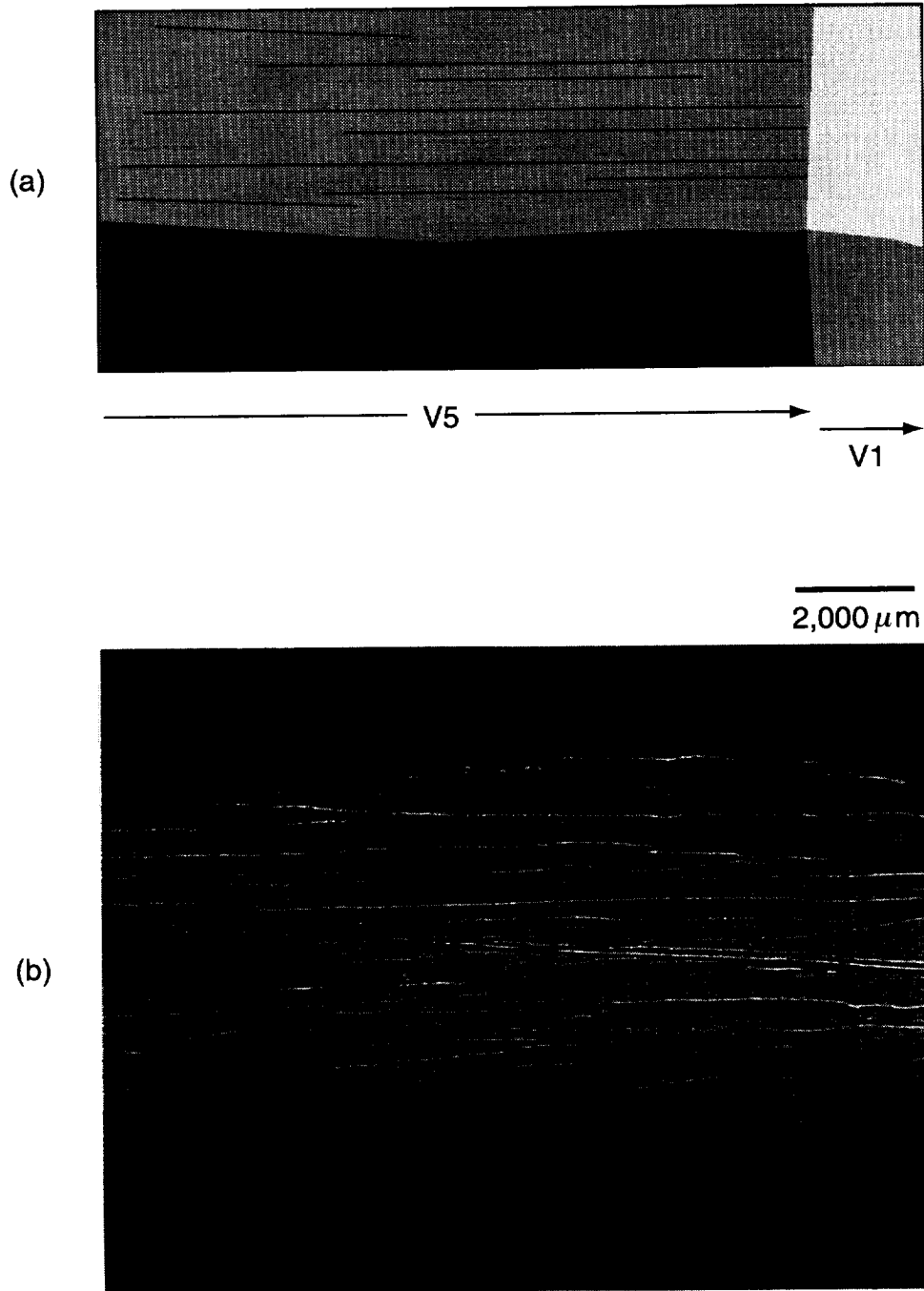


Figure 3-6. (a) Schematic of the shape of an interface at the transition between V5 and V1. (b) Low magnification micrograph of the interface. The interface is slightly curved at the edges due to the surface tension forces at the solid/liquid/crucible triple junction.

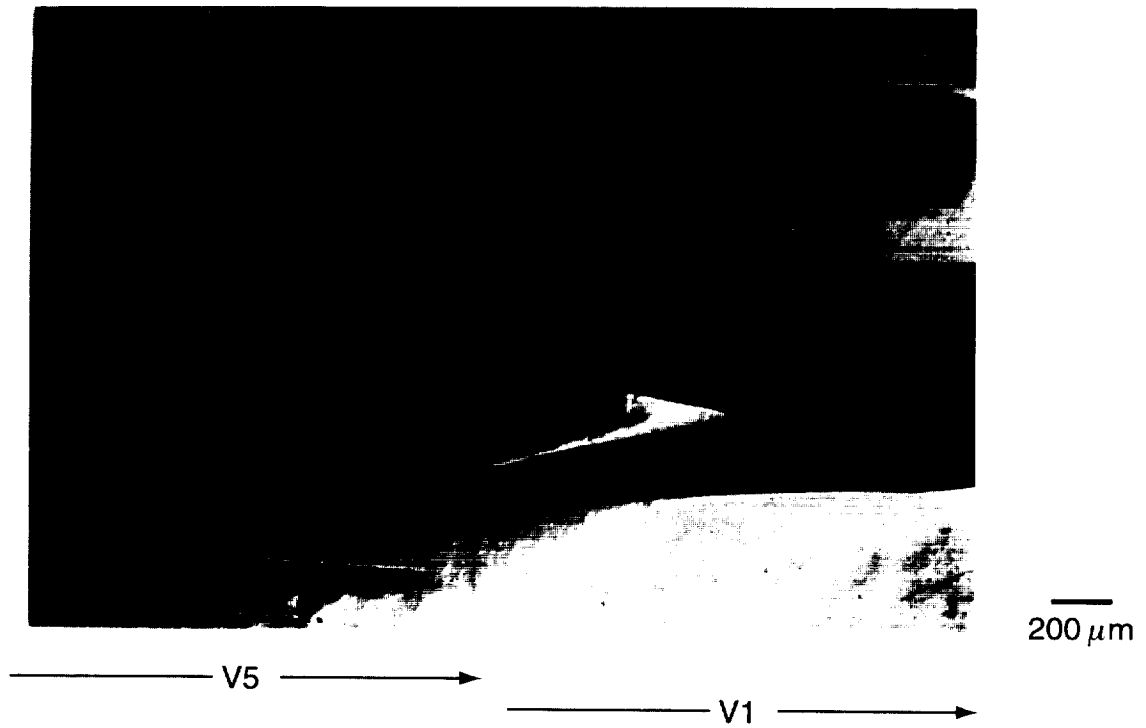


Figure 3-7. Detail of interface between V5 and V1. Note the changes in grain boundary angles upon decreasing the growth rate. Optical Micrograph, DIC illumination.

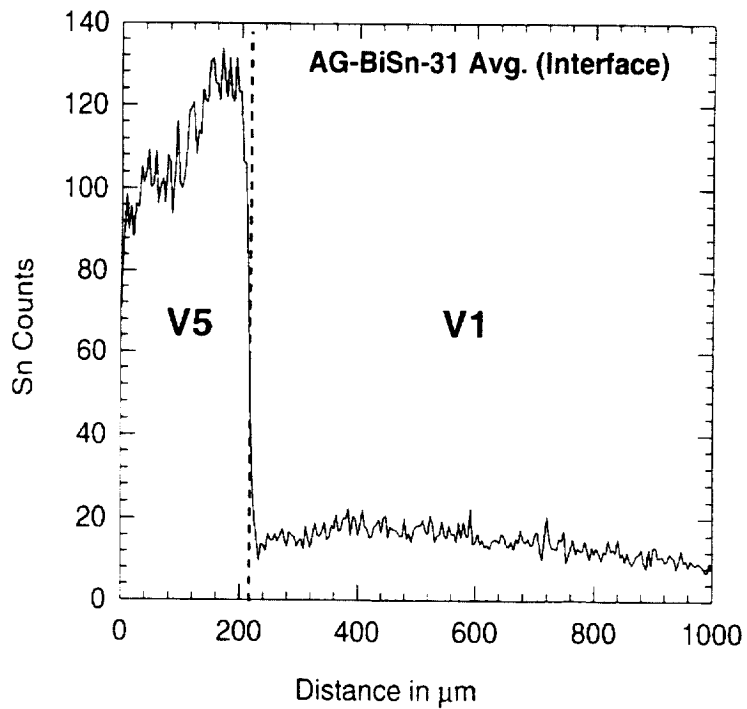
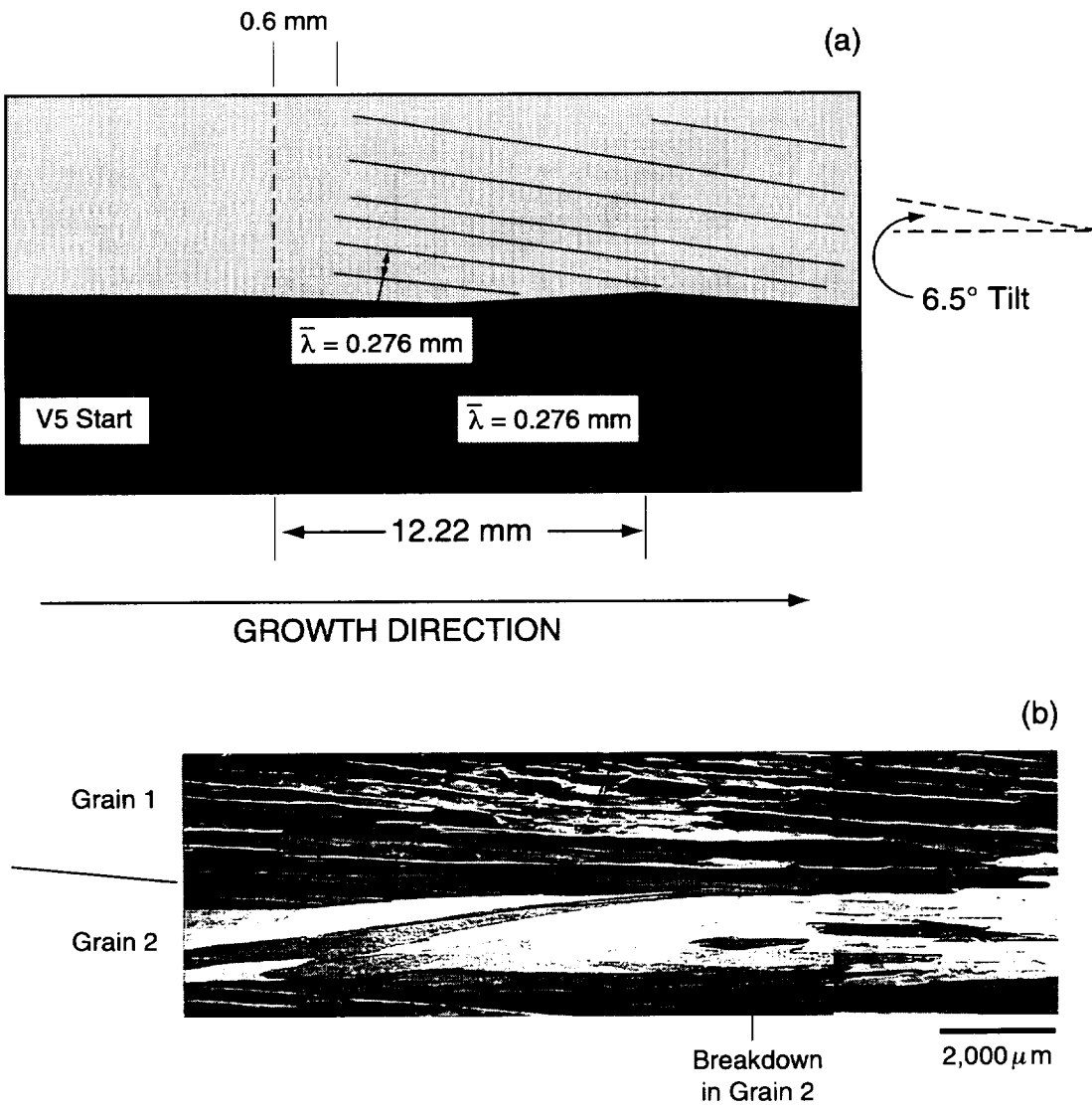
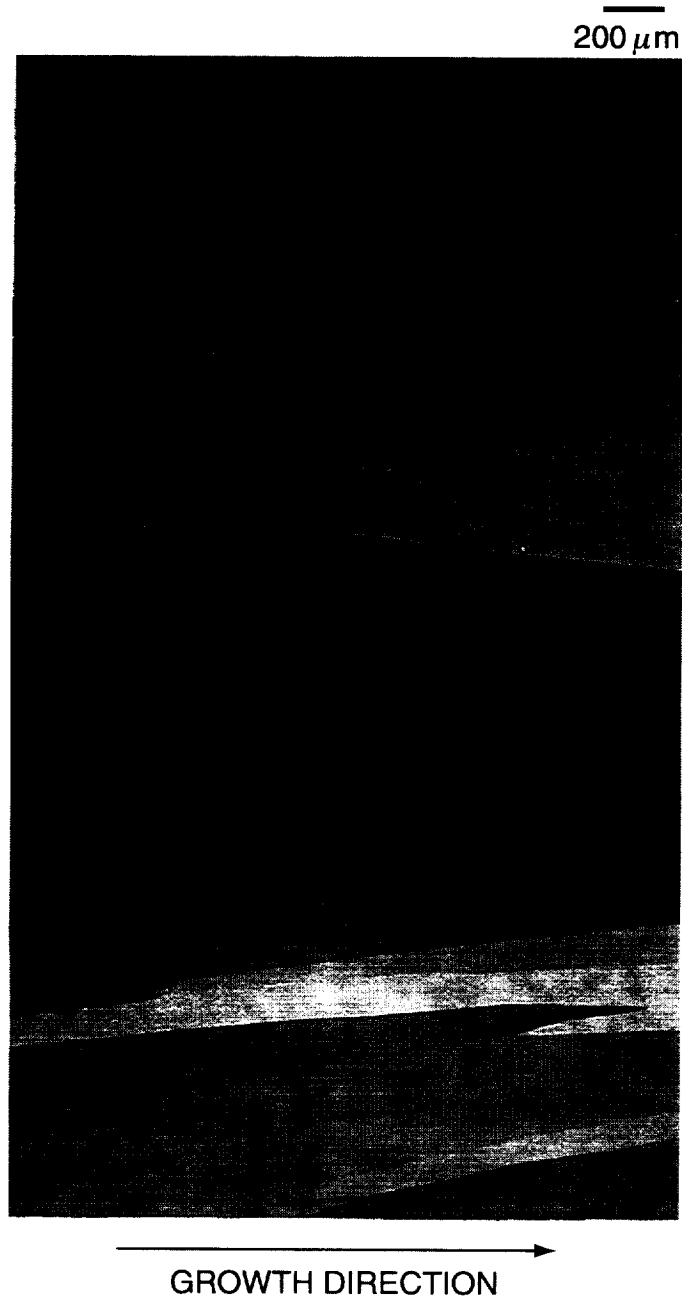


Figure 3-8. Secondary Ion Mass Spectroscopic (SIMS) analysis of the V5/V1 interface illustrating the sharp change in average Sn content at the interface.



Note: the top grain is cellular while the bottom grain continues in a plane-front mode for a significant distance (12.22 mm) before a transition to the cellular mode.

Figure 3-9. (a) Schematic representation of the features of a selective breakdown at a growth velocity of $26.6 \mu\text{m/s}$. (b) Microstructural appearance of the selective breakdown.



Note: the bottom grain is growing in the plane front mode while the top orientation is growing in a cellular mode with cells tilted with respect to the heat flow direction.

Figure 3-10. Selective planar to cellular transition at a growth velocity of $26.88 \mu\text{m/s}$.

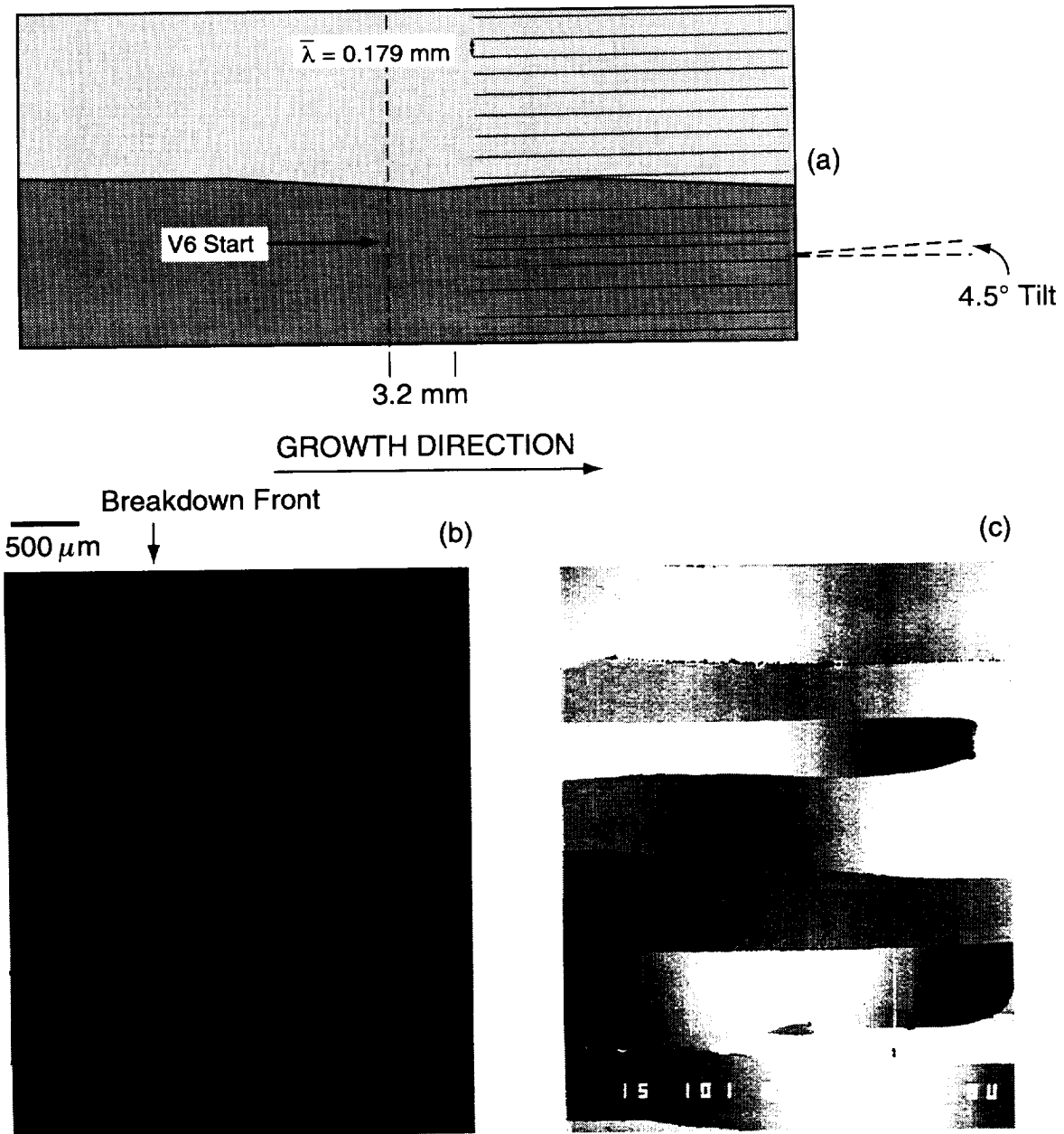


Figure 3-11. (a) Schematic illustration showing the salient features of a cellular transition at a growth velocity of $40 \mu\text{m/s}$. (b) Low magnification micrograph of V6 breakdown region. (c) Higher magnification view of cellular growth at V6.

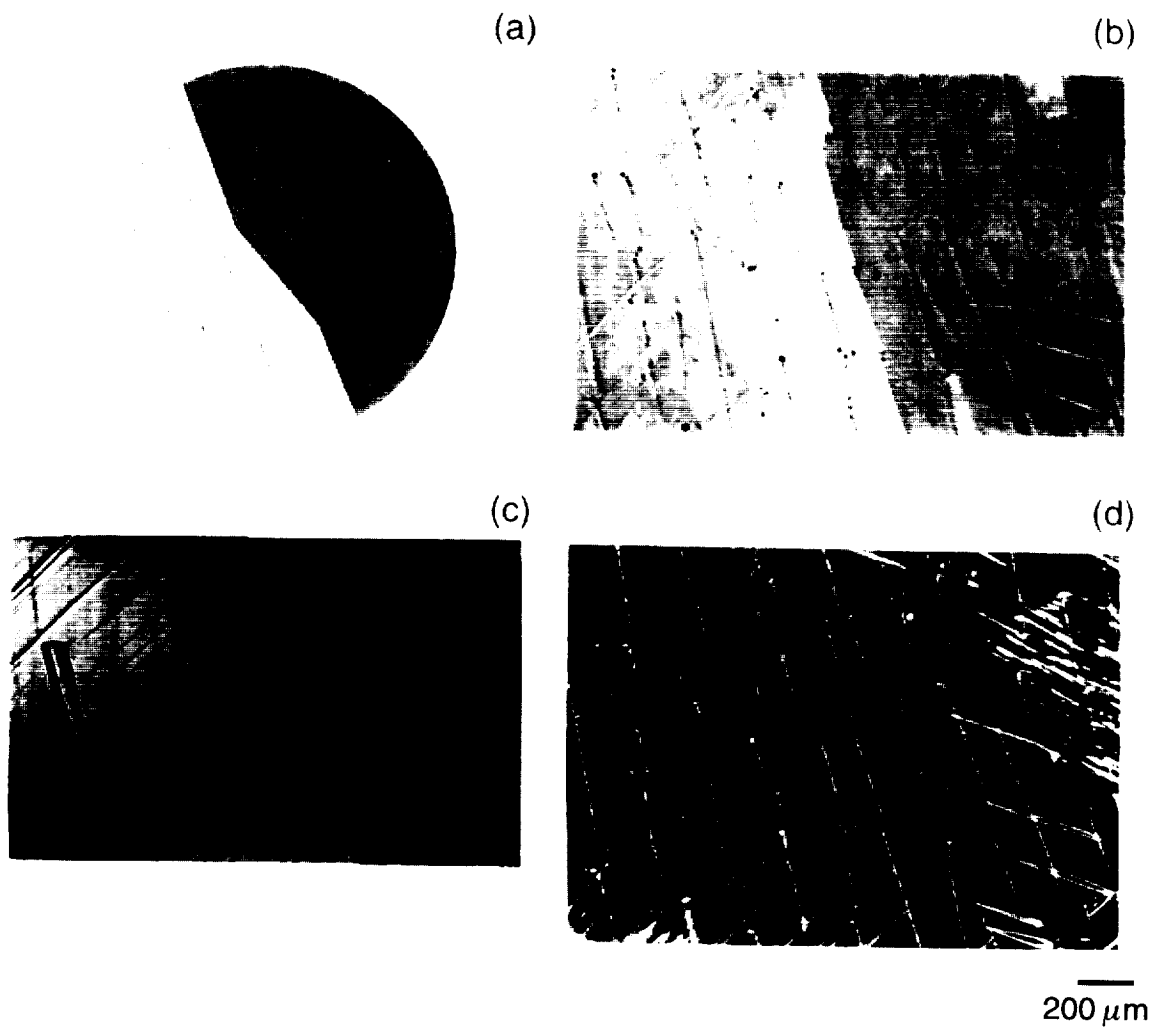


Figure 3-12. (a) Schematic of cellular growth, transverse section. Shows two dominant orientations. (b) Optical micrograph (B.F.) illustrating the cell boundaries. (c) Optical micrograph (P.L.S.T.) showing two dominant grains. (d) Optical micrograph (D.F.) showing cell boundaries.

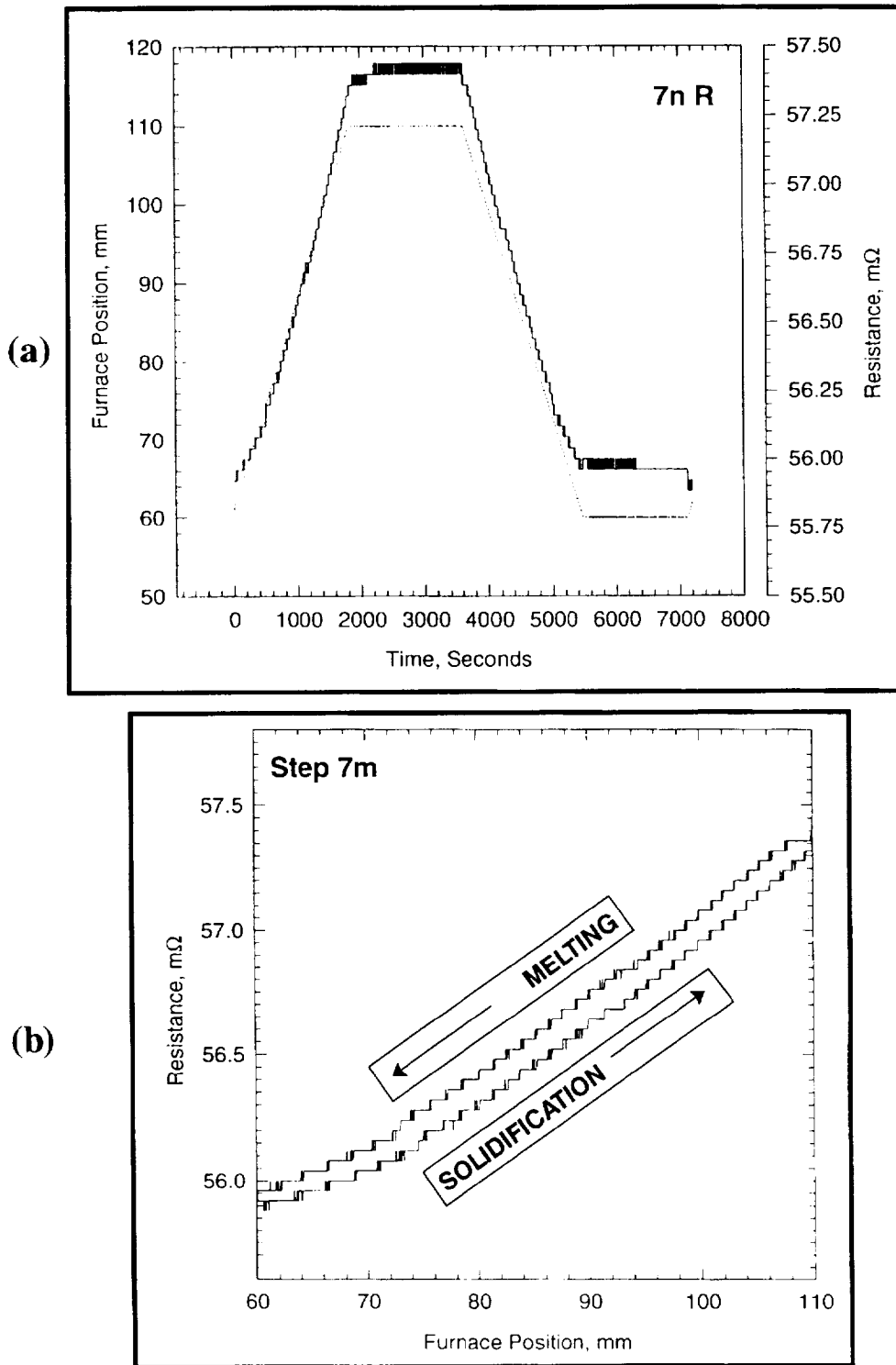


Figure 3-13. (a) Typical resistance tracking of interface position and measurement of furnace translation (by linear potentiometer) as a function of processing time. Typical Seebeck measurement cycle (solidification-stabilization-remelting-stabilization). (b) The hysteresis between resistance change during solidification (bottom curve) and that during symmetrical remelting (top curve).

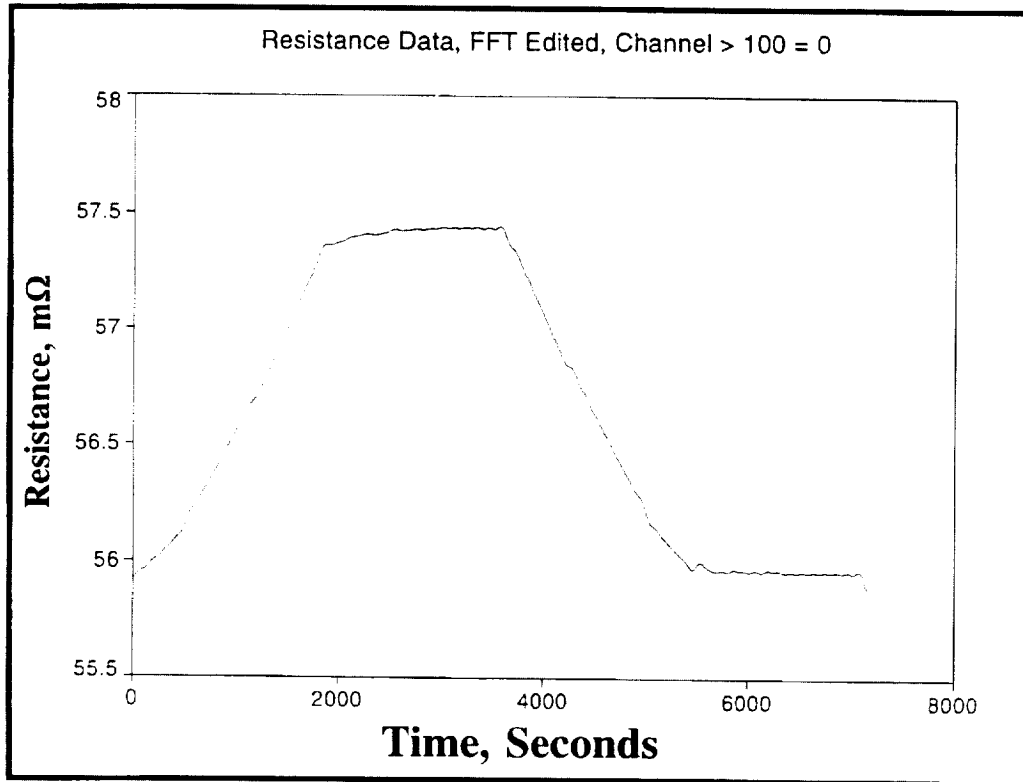


Figure 3-14. FFT editing of resistance measurement during a typical Seebeck cycle. Note the removal of superimposed noise so that fine slope changes during the resistance tracking can be detected.

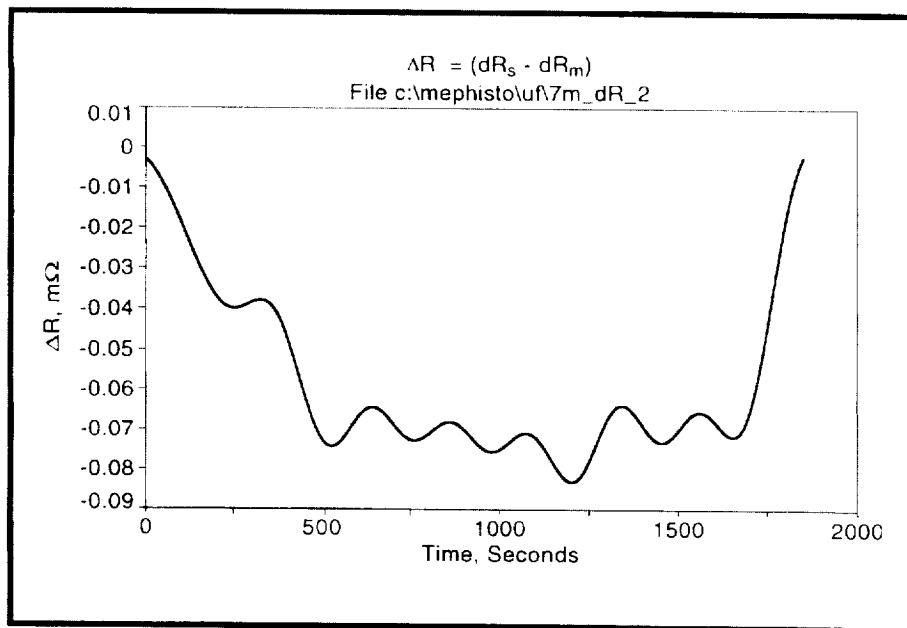


Figure 3-15. Subtraction of resistance change during solidification from that during symmetrical remelting. FFT edited data. The existence of a negative plateau indicates interfacial retardation during solidification.

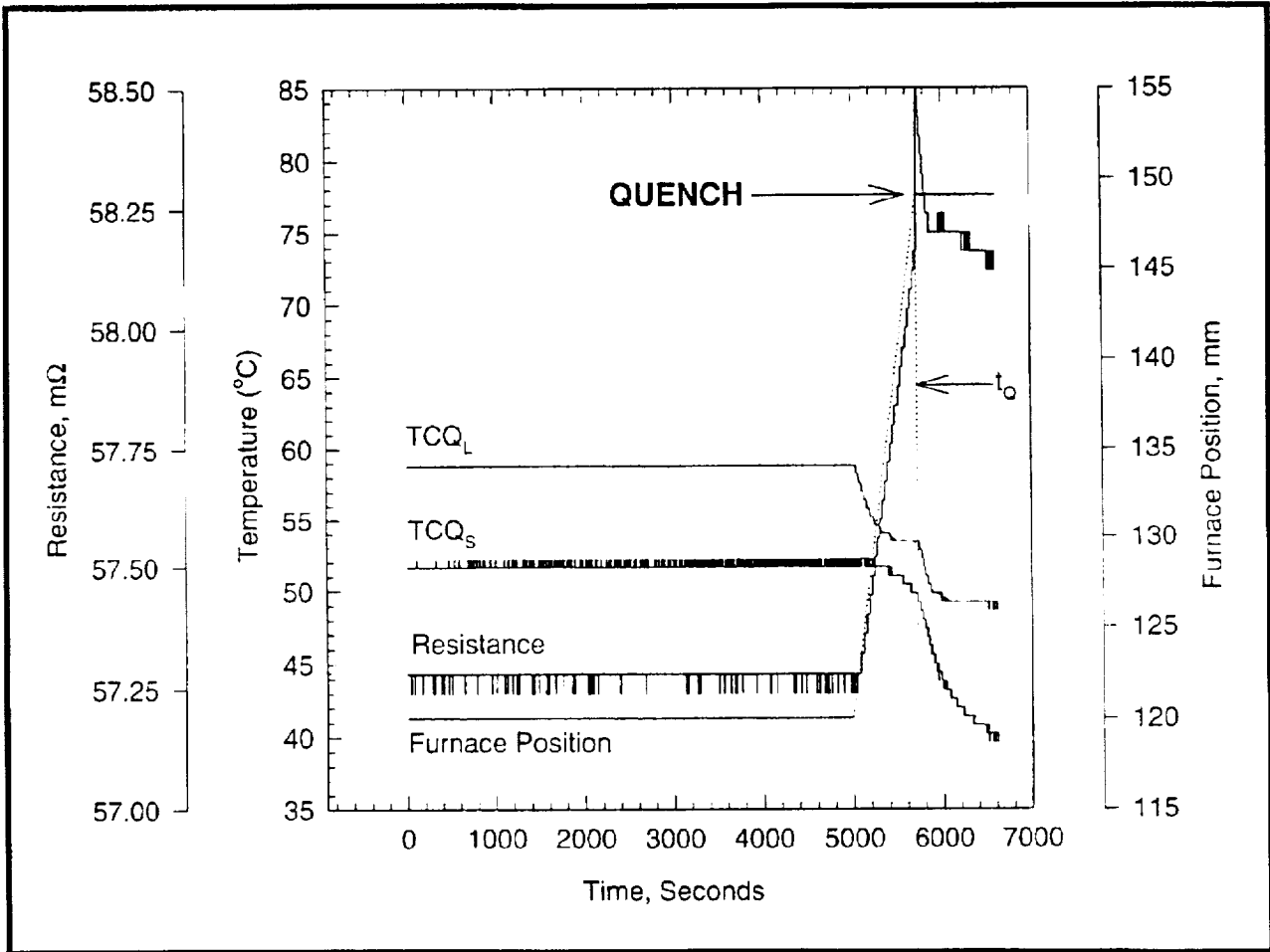


Figure 3-16. Resistance change during the final quench, shows a sharp increase in the resistance at the time of quench. The subsequent decay is due to the slower melting of the portion of the sample pushed into the hot zone during the quench. Also shown are furnace position and outputs of quenching sample thermocouples.

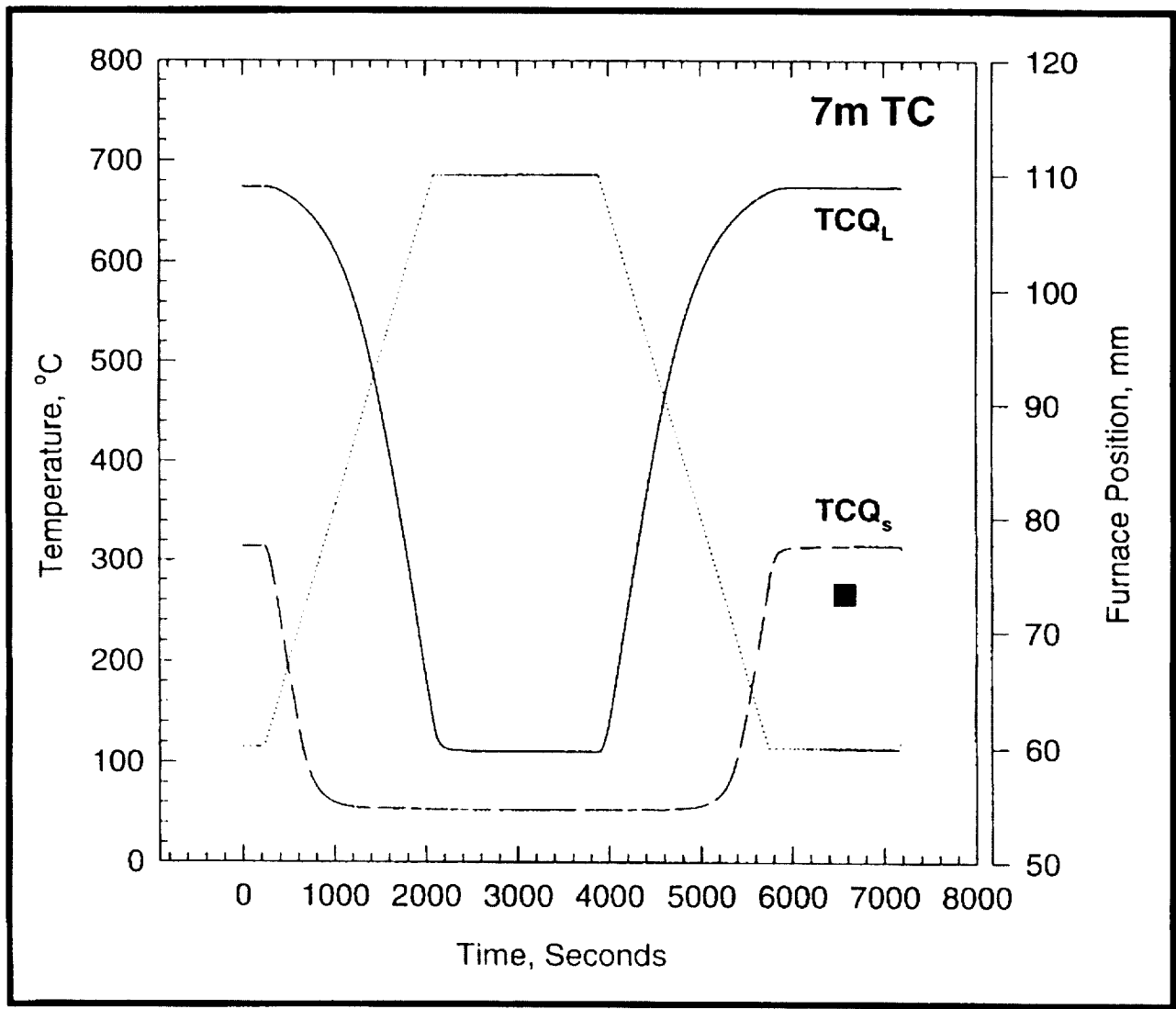


Figure 3-17. Output of short and long thermocouples in the quenching sample during a typical Seebeck measurement. Also shown is the corresponding furnace movement.

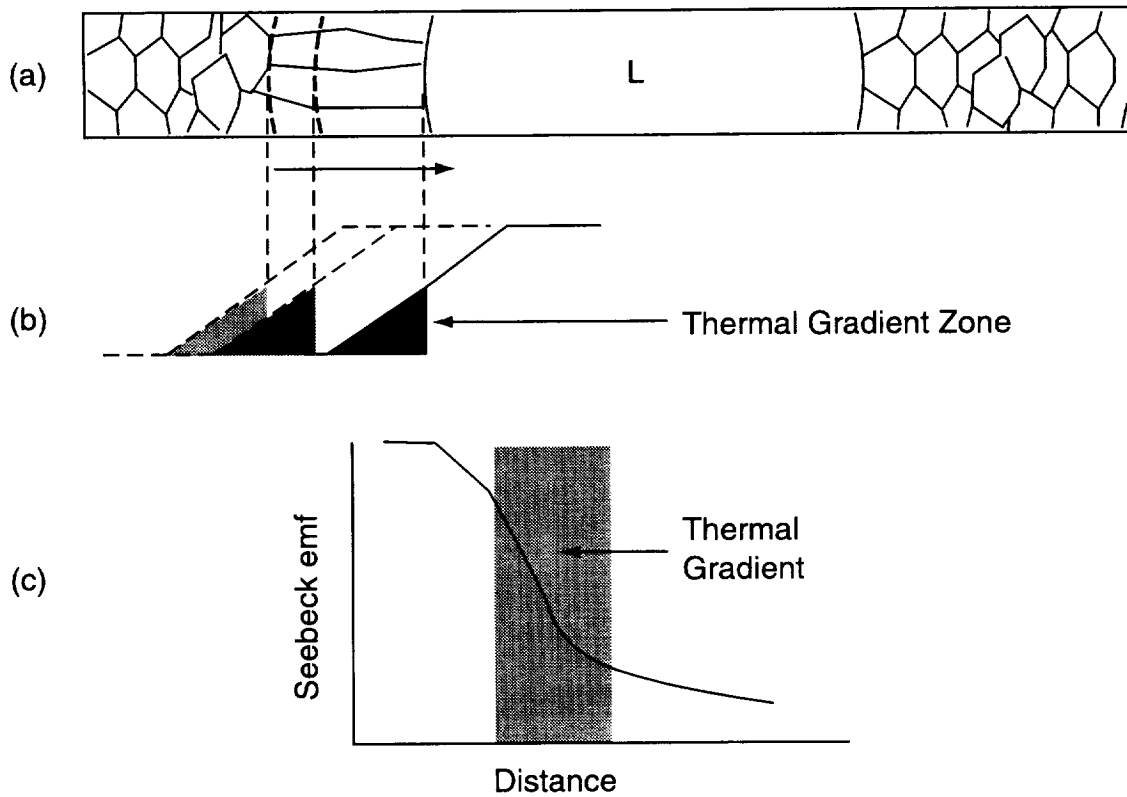


Figure 3-18. Evolution of differential Seebeck emf due to microstructure/thermal gradient interaction. (a) Initial and directional growth microstructure at two interfaces. (b) Thermal gradient zone during directional solidification. (c) Evolution of the Seebeck emf during translation of a thermal gradient.

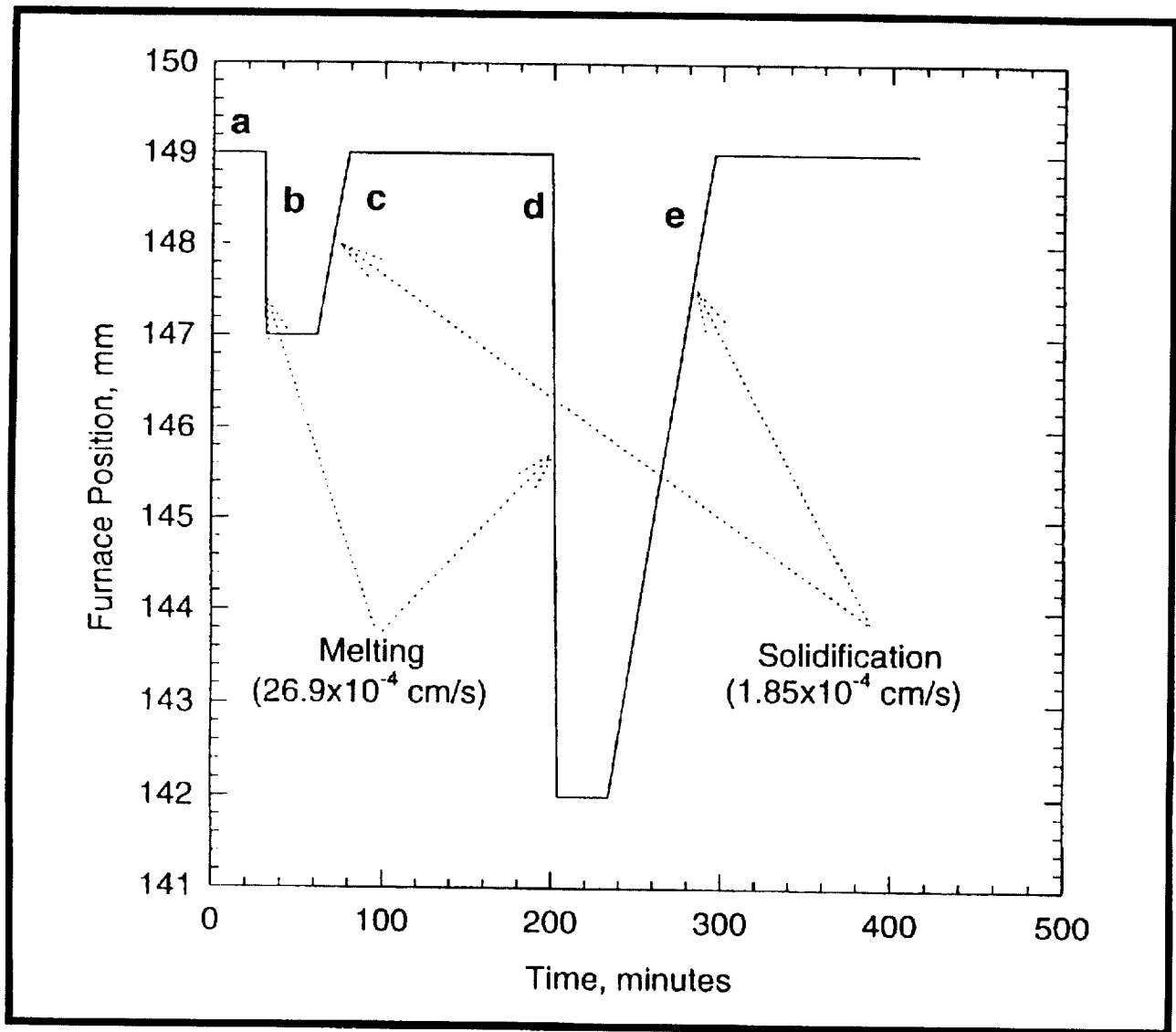


Figure 3-19. The processing sequence of microstructural/Seebeck emf evolution described in figures 20(a)–(e). Shows two melting cycles and two solidification cycles separated by stabilization periods. Each step in the process is identified by a letter (a through e), corresponding to figures 20 (a)–(e).

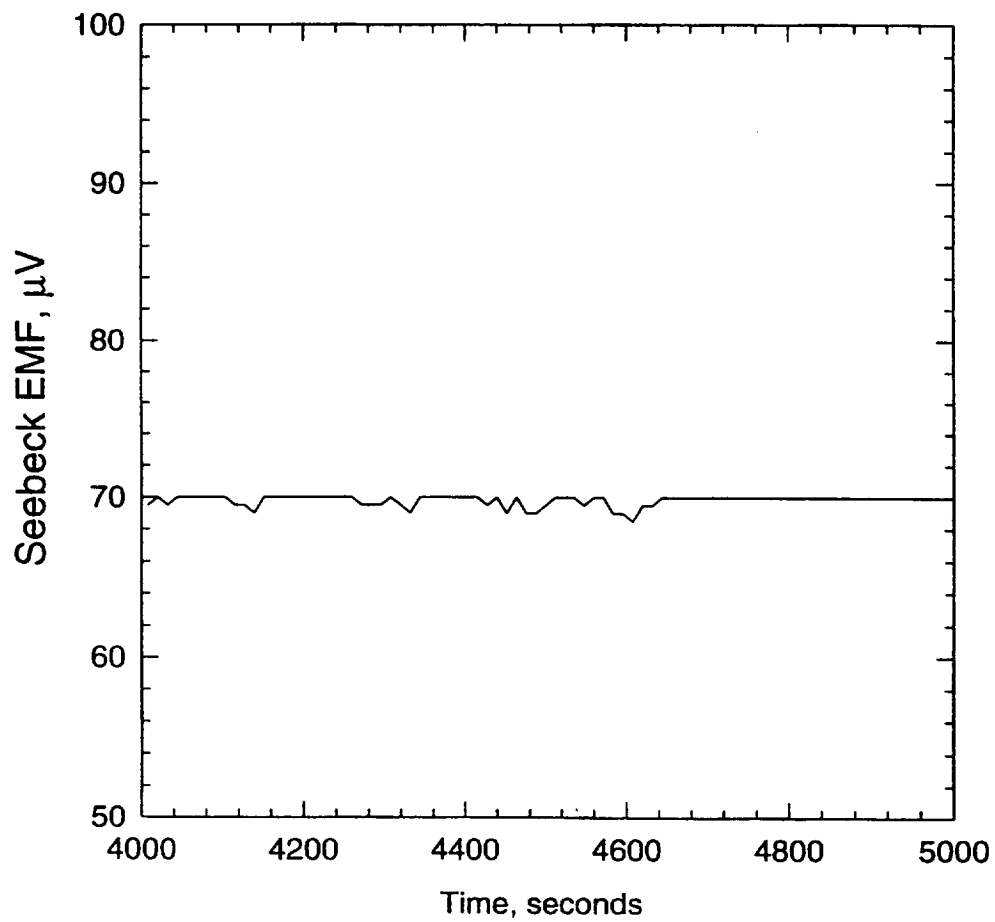
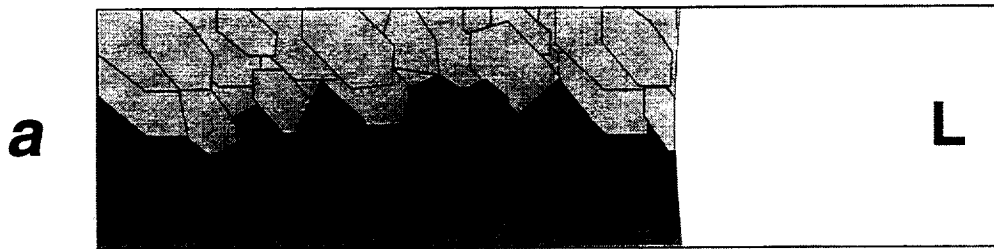


Figure 3-20. (a) Initial interface between the Earth-grown faceted cellular/dendritic microstructure and liquid alloy. The interface is slightly curved at the solid/liquid/crucible triple junction. The baseline Seebeck emf is steady with a mean value of $\sim 70 \mu V$.

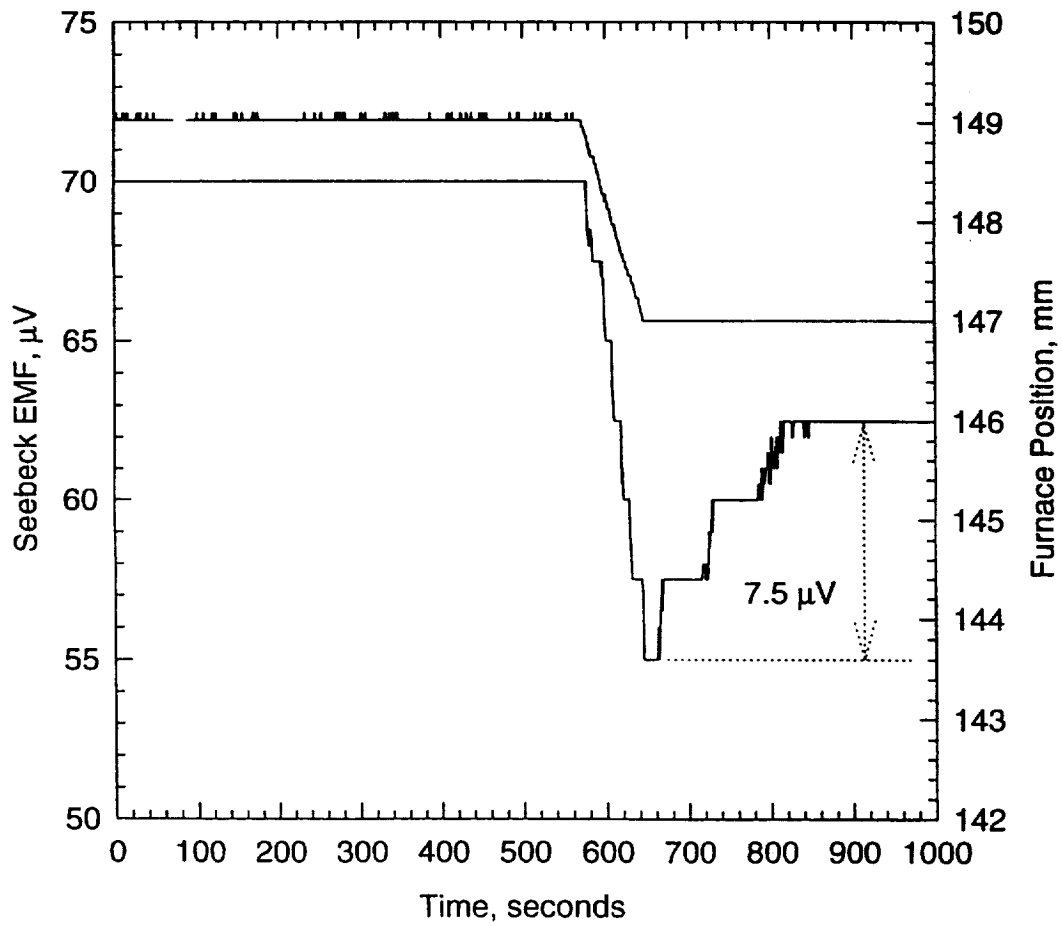
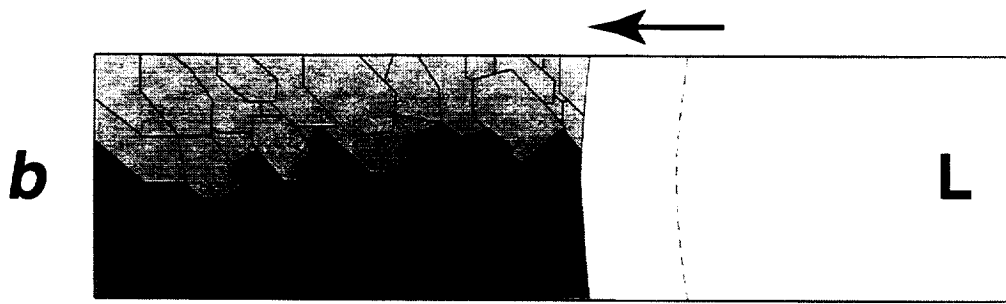


Figure 3-20. (b) Directional 2-mm melting of the initial interface and the corresponding Seebeck signal.

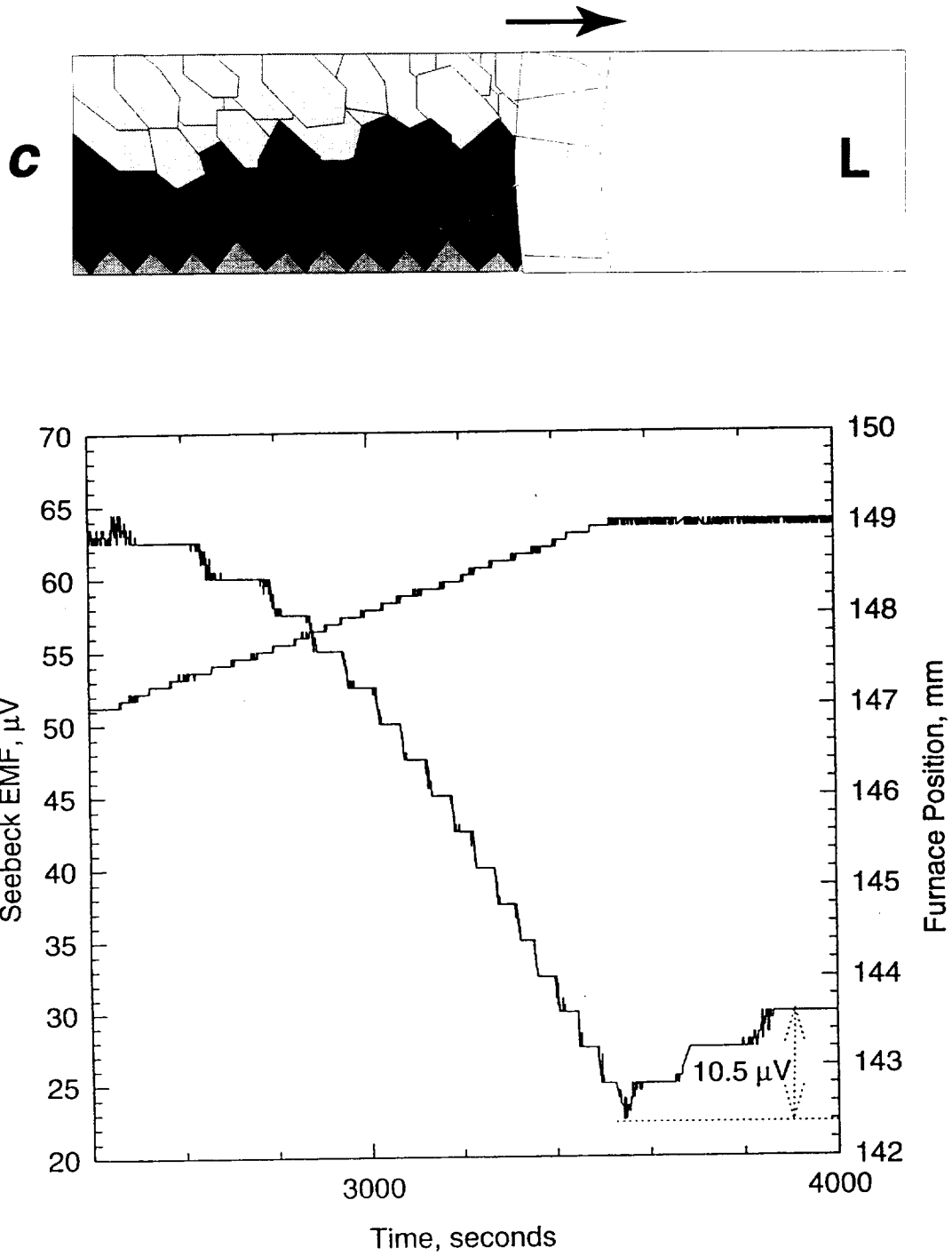


Figure 3-20. (c) Directional 2-mm solidification resulting in plane-front growth with columnar grains and the corresponding evolution of the Seebeck signal.

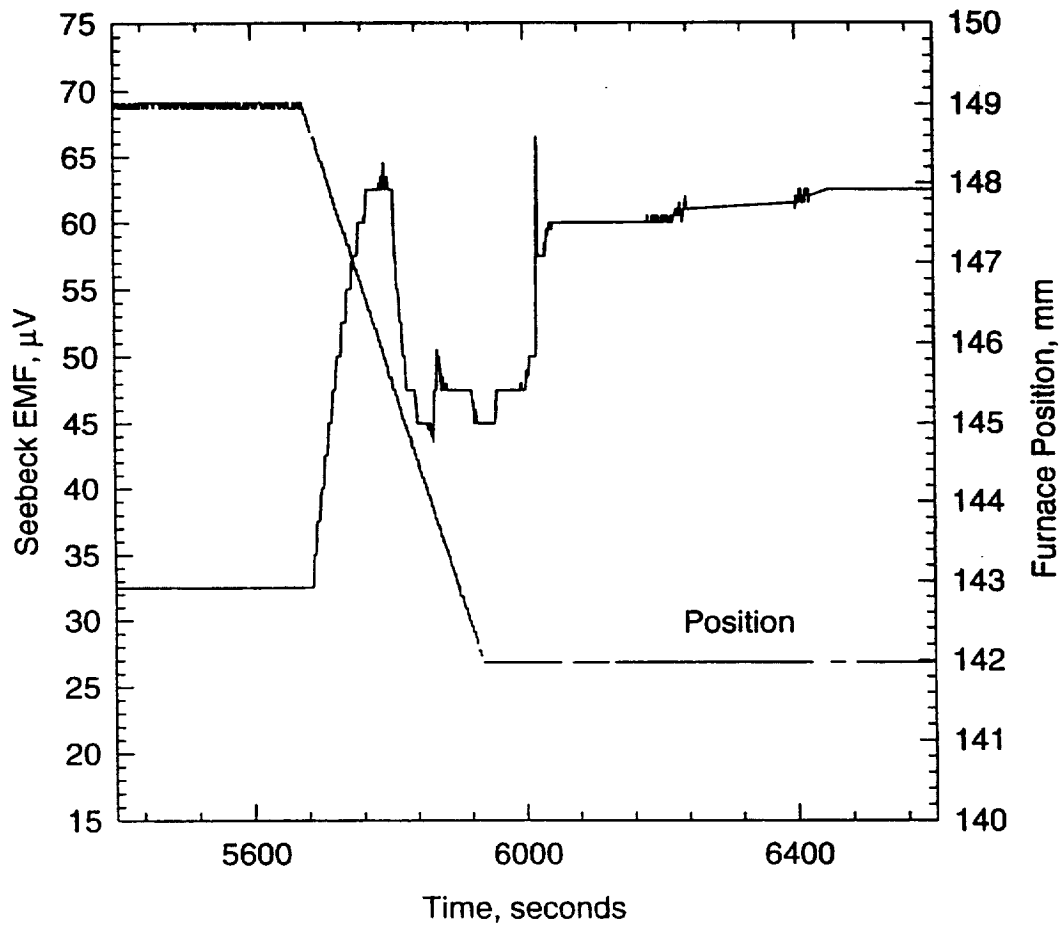
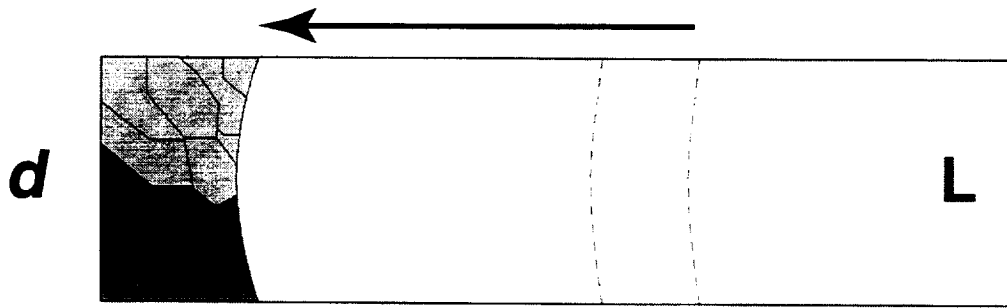


Figure 3-20. (d) Directional 7-mm melting of the plane-front (2 mm) and cellular/dendritic (last 5 mm) region and the corresponding evolution of the Seebeck signal.

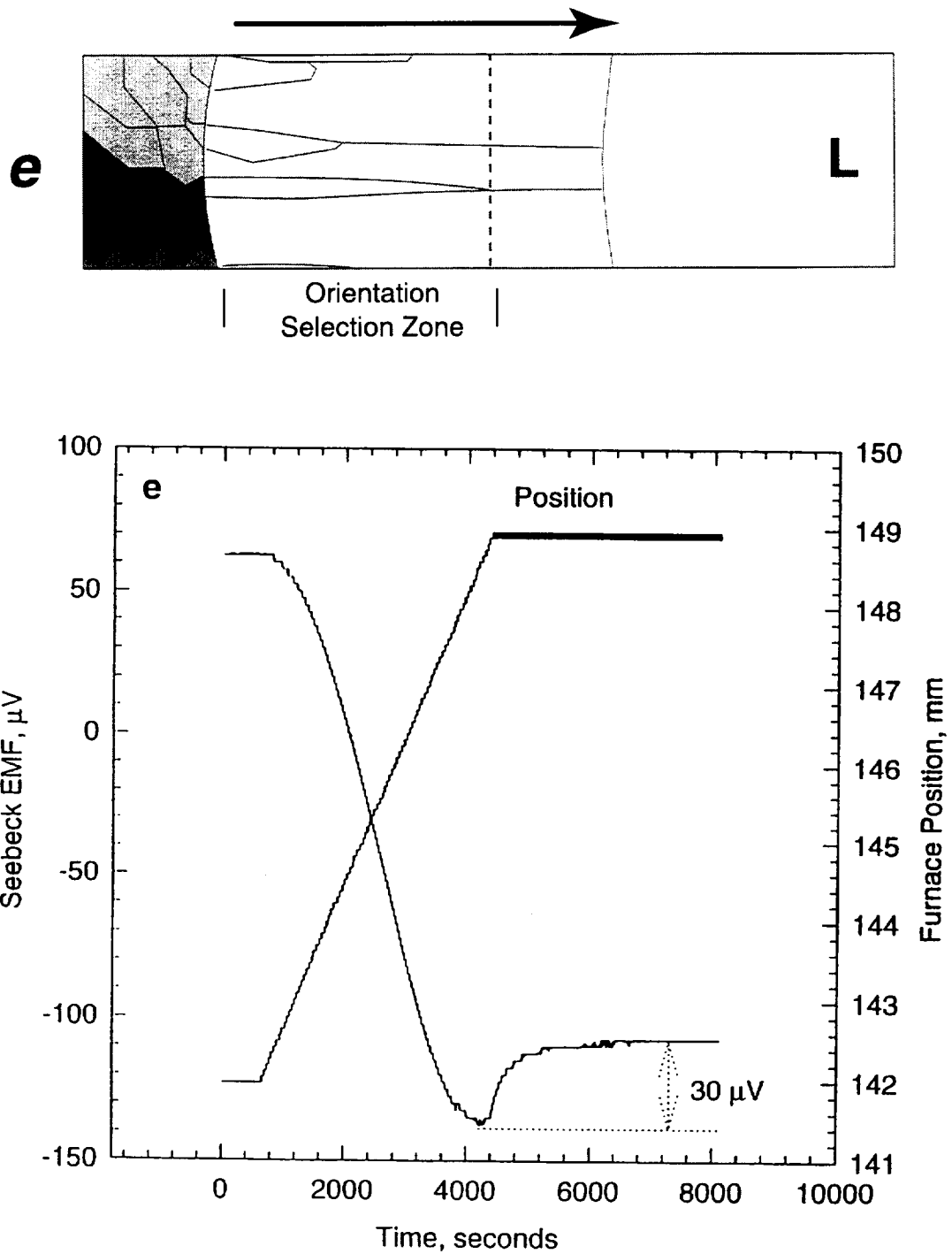


Figure 3-20. (e) Directional 7-mm solidification resulting in plane-front growth with columnar grain structure. Also shown is the disappearance of unfavorable orientations as growth proceeds and the corresponding evolution of the Seebeck signal.

SECTION IV.

GROWTH OF SOLID SOLUTION SINGLE CRYSTALS

Acknowledgments

Research was carried out in part at the National Synchrotron Light Source (NSLS), Brookhaven National Laboratory, which is supported by the U.S. Department of Energy, Division of Materials Sciences and Division of Chemical Sciences. Many persons have contributed to this effort. These include the AADSF Project Management team led by Fred Reeves, the Engineering team led by James Sledd, the test team led by Michael Cole, and the Teledyne Brown Engineering team. Bill Aldrich was responsible for much of the preliminary design of AADSF. Without their dedication and skillful efforts there would be no furnace. Strong collaboration from the Crystal Growth and Solidification Branch of Space Sciences Laboratory upon the experimental effort included the magnetic field growth experiments conducted by Dale Watring and Ching-Hua Su, growth experiments and characterization by Sharon Cobb, and skillful glass blowing by Mark Jones. Much of the preliminary crystal growth on this system was done by L.R. Holland, J.C. Clayton, and M.C. Davidson at MSFC. Important thermophysical property measurements have been made by D. Chandra, K. Mazuruk, and R.E. Taylor. Chris Coppens of the Structures and Design Laboratory designed the ampoule, while Greg Jerman of Materials and Processes Laboratory made the electron microprobe WDS measurements. Helga Alexander of Mevatec performed much of the optical and scanning electron microscopy work, while Gene Nelson of A.G. Scientific Glass Company prepared all the ampoules. Finally, we are indebted to Joel Kearns of NASA Headquarters for his encouragement and interest during the project.

GROWTH OF SOLID SOLUTION SINGLE CRYSTALS

Sandor L. Lehoczky, Frank R. Szofran, Donald C. Gillies

Space Sciences Laboratory
NASA/Marshall Space Flight Center, Alabama 35812

Abstract

The solidification of a solid solution semiconductor having a wide separation between liquidus and solidus has been extensively studied in ground-based, high magnetic field and Spacelab experiments. The material being studied, mercury cadmium telluride with 80 mole percent of HgTe and 20 mole percent of CdTe, is extremely difficult to grow by directional solidification on Earth due to high solutal and thermal density differences which give rise to fluid flow and consequent loss of interface shape and composition. Diffusion controlled growth is therefore impossible to achieve in conventional directional solidification. The ground-based experiments consisted of growing crystals in several different configurations of heat pipe furnaces, NASA's Advanced Automated Directional Solidification Furnace (AADSf), and a similar furnace incorporated in a superconducting magnet capable of operating up to 5T. The flight experiment took place during the flight of STS-62 in March 1994, with the AADSf installed on the second United States Microgravity Payload (USMP-2). The alloy was solidified at 3/4 inch per day over a 9-day period, and for the first time, a detailed evaluation was performed of residual acceleration effects.

The results of the ground-based experiments were compared with the crystal grown in orbit under microgravity conditions. On Earth, it has been found that the application of the magnetic field leads to a significant reduction in fluid flow, with improved homogeneity of composition. The field strength required to suppress flow increases with diameter of the material and the 8-mm diameter sample used was less than the upper limit for a 5T magnet.

The resulting material grown during the flight experiment was significantly different. One clear difference is that there is no hydrostatic force pushing the material against the ampoule wall during the solidification as is the case on Earth. During the mission the orbiter was maneuvered into several different attitudes with the result that the residual acceleration vector caused by drag on the orbiter and the distance of the AADSf from the center of gravity of the orbiter was aligned differently with respect to the growth axis of the solidifying material for distinct parts of the mission. Significant differences were observed during three long, but uninterrupted, periods at constant attitude. Compositional variations along the crystal circumference indicate residual fluid flows for the least favorable vector orientations. Identifiable regions exist in which a transverse vector has pushed the material against the ampoule wall and allowed it to readily contract away from the opposite wall. Such surfaces showed etch pits produced by preferential evaporation at defect sites. X-ray scattering showed that the regions pulled away from the wall tended to be less strained or of higher quality material than the opposite surface, and considerably better than the Earth-grown material. Composition determination on the surface of the material demonstrated significant difference, dependent on the direction of the residual acceleration vector. These are clear indications of three-dimensional fluid flow. A significant portion of the boule was grown with a component of the vector aligned in a direction from liquid to solid. Synchrotron x-ray studies of this material showed it to be single crystal and of much lower defect density than found in ground-based growths.

4.1. INTRODUCTION

The major objective of this research is to establish the limitations imposed by gravity during growth on the quality of bulk, solid-solution, semiconducting crystals having a large separation between their liquidus and solidus temperatures. An important goal is to explore the possible advantages of growth in the absence of gravity. The alloy system being investigated is $\text{Hg}_{1-x}\text{Cd}_x\text{Te}$ with x -values appropriate for infrared detector applications in the 8–14 μm region. Both melt and Te-solvent growth methods as well as growth in magnetic fields are being considered. The study consists of flight experimentation and ground-based experimental and theoretical work needed to establish material properties and optimum experimental parameters for the on-going flight experiments, and to assist material evaluation. $\text{Hg}_{1-x}\text{Cd}_x\text{Te}$ is representative of several II-VI alloys which have electrical and optical properties that can be compositionally tuned to meet a wide range of technological applications in the areas of sensors and lasers with applications to optical computing and communications as well as the national defense. The following specific objectives are deemed essential for accomplishing the primary objectives of the investigation: By means of ground laboratory and flight experiments and concurrent theoretical analysis, establish quantitative correlation between growth parameters (translation rates, thermal fields, alloy compositions, and sample geometries) and growth interface shapes during the melt growth of $\text{Hg}_{1-x}\text{Cd}_x\text{Te}$ alloy crystals by unidirectional solidification; establish correlation between growth interface shapes and microstructural characteristics; develop theoretical models to delineate the effects of segregation, diffusion, and fluid flow in two dimensions on sample homogeneity and the solid-liquid interface shape during the melt growth of $\text{Hg}_{1-x}\text{Cd}_x\text{Te}$ alloy crystals and thus establish a fundamental understanding of the growth process; ascertain the relative effectiveness of ground-based stabilizing techniques (e.g., applied magnetic fields) for suppressing convective flow during melt growth of the crystals; establish ternary phase-equilibrium parameters for selected regions of the Hg-Cd-Te constitutional phase diagram required to model the Te-solvent growth process; by means of growth experiments and theoretical analysis, establish quantitative correlation between growth parameters (growth rates, thermal fields, alloy compositions, and sample geometries), growth interface shapes, and microstructural characteristics for various Te-solvent growth processes; establish relationships between electrical characteristics and densities of charged and neutral defects for various growth conditions and thus correlate processing variables with the optical response of the processed alloy; evaluate the possible benefits of microgravity processing for device applications.

The investigation (Experiment No. MPS77F069) was originally selected based on the response to NASA OA-77-3 Announcement of Opportunity. The content of the current effort is based on an amended proposal submitted in response to Announcement of Opportunity OSTA-77-3 (formerly OA-77-3). Some of the initial work was done at McDonnell Douglas Research Laboratories under contract NAS8-33107.¹⁻⁷ The investigation is consistent with the committee recommendations resulting from the "Review of the Microgravity Science and Applications Flight Programs" conducted January–March of 1987. The majority of the ground-based studies are being performed in the Space Sciences Laboratory at the George C. Marshall Space Flight Center (MSFC).⁸⁻⁵⁷ In addition to crystal growth and characterization, this work has included thermophysical property determination, thermal modeling, phase diagram determination, fluid flow modeling, transient and diffusion analysis, and electronic property modeling. The flight portion of the investigation is being conducted using the AADSF developed by the MSFC and manifested for flights on the USMP series of missions. The first flight of the instrument took place in March 1994 on STS-62.⁵⁸

4.2. STUDY RATIONALE

Segregation during solidification, high volatility of one of the components (Hg), and strain fields associated with large temperature gradients make the preparation of homogeneous, high-quality, bulk crystals of the alloys an extremely challenging problem. The usual melt or solvent growth methods tend to yield crystals with significant alloy compositional variations, and second phase inclusions, e.g., Te-precipitates which we believe are at least partially caused by gravity-induced, thermosolutally-driven flows just ahead of the growth interface.

The reduction of the gravity-induced convection in a microgravity environment is expected to be advantageous for maintaining the crystal-melt interface shape required to minimize the densities of crystal defects while minimizing compositional variation transverse to the crystal growth direction. It is believed that CdTe, $\text{Hg}_{1-x}\text{Cd}_x\text{Te}$, etc. probably possess extremely small yield strengths near their growth temperatures. If this is the case, the high dislocation density ($\sim 10^5 \text{ cm}^{-2}$) usually seen in these crystals could be due at least in part, to stresses induced by the sample's own weight, that is, self-induced stresses. Therefore, a second goal of these experiments is to assess the validity of this hypothesis.

4.3. DRIVING FORCE FOR CONVECTION

As noted earlier, both melt and Se- and Te-solvent growth are subjects of the proposed investigation. Because of the relative maturity of the ground-based, melt-growth method compared with solvent growth, the unseeded melt growth of $\text{Hg}_{0.8}\text{Cd}_{0.2}\text{Te}$ alloys by Bridgman-Stockbarger-type directional solidification is the primary method selected for the initial USMP flight experiments. On Earth the Hg-rich component rejected during solidification is more dense than the original melt and the vertical Bridgman-Stockbarger growth process would appear to be both gravitationally and thermally stable against convection. However, this is not generally true. Due to the peculiar relationships between the thermal conductivities of the melt, solid, and ampoule, it is not practicable to completely avoid radial temperature gradients in the growth region in these alloys. Because of the high Hg partial vapor pressures involved at the processing temperatures, the confinement of the alloys requires the use of very thick fused silica ampoules which have thermal conductivities comparable to those of the alloys. This, when combined with the large (a factor of 4 to 10) decrease in the thermal conductivities of Hg alloys upon freezing, leads to isothermal surfaces near the melt/solid interface that are bowed into the solid. Although the interface under this condition is neither an isothermal nor an isocompositional surface, it is bowed in the same direction as the isotherms near it. We have developed a method that relies on a careful control of radiation heat transfer near the growth interface to minimize the effect for this type of growth system.²⁶ Nevertheless, the wide separation between the liquidus and solidus boundaries of each of the pseudobinary phase diagrams (by causing the growth interface temperature to undergo large changes during growth and yielding growth rate dependent thermophysical properties in the melt just ahead of the interface) makes a complete elimination of the radial temperature gradients in the vicinity of the interface nearly impossible. Thus, in spite of the stabilizing influence of the solutal density gradients, intense thermally-driven fluid flows will occur in a narrow region near the interface that will control the extent of radial compositional-segregation in a gravitational environment.⁵⁹

4.4. PREVIOUS RESULTS FOR COMPOSITIONAL REDISTRIBUTION

Over the past several years, we have performed an extensive evaluation of the effects of growth parameters on the axial and radial compositional uniformity in directionally solidified HgCdTe alloys.^{1 2 5 16 21 26 27 29 37} To obtain a measure of the relative importance of the various heat and mass transfer processes involved, detailed radial and axial composition mappings have been obtained for many ingots. For most cases, the compositional variation along the growth axis could be fit well by a set of one-dimensional diffusion equations, indicating that solute transport to the interface region during growth tends to be dominated by mass diffusion and that the vertical extent of the convective region above the crystal growth interface has to be small compared to the effective diffusion lengths. On the other hand, the extent of the typical measured radial segregation for practical growth rates ($\geq 0.1\text{--}0.4 \mu\text{m/s}$) was found to be significantly higher and at low growth rates ($\leq 0.1 \mu\text{m/s}$) significantly lower than would be expected from diffusion-limited lateral segregation alone, indicating that the crystal compositional distributions transverse to the growth axis are primarily determined by the nature of the thermally-driven fluid flows in the vicinity of the growth interface. This contention is strongly supported by the results of a linear-stability type analysis which indicates that the results are compatible with a transition from steady to time-dependent flows as the growth rates and thus the stabilizing composition gradients are reduced. In agreement with the conclusions suggested by the axial composition distribution data, such an analysis also suggests that the axial extent of the flow regions should be about a factor of 10 smaller than the estimated dimension of the effective diffusion lengths involved. Recent detailed numerical analysis for the HgCdTe system by D.H. Kim and R.A. Brown provides an excellent theoretical description of the overall heat and mass transport phenomenon and supports the main contentions of the proposition.^{59 60} Growth experiments performed in transverse and axial magnetic fields up to 0.6 and 5T, respectively, suggest strong fluid flow effects on radial compositional segregation.^{51 61}

4.5. PROBLEMS ASSOCIATED WITH GROWTH INTERFACE SHAPE CONTROL

Frequently, the desirable surface geometry for crystal growth is planar or nearly so. Usually, however, the optimum interface shapes tend to be those that bow slightly into the melt, because such interface shapes favor grain selection and the outgrowth of extended line defects. These shapes are expected to produce ingots with better crystal perfection. While such shapes are difficult to obtain for these alloys, they may be achievable with judiciously chosen thermal boundary conditions. Under the influence of the stable flow conditions during fast growth, such interface geometries exacerbate lateral alloy segregation because of the tendency of the more dense Hg-rich liquid to settle at portions of the surface having the lowest gravitational potential. Due to the decrease of the alloy solidus temperatures with increased Hg-concentration, the temperature at this portion of the interface will be lowered, causing an increase in the interface curvature. Thus, a potential interface instability can result from the "settling" of the rejected Hg-rich solvent into the lowest-lying regions of the interface. Lateral diffusion and incomplete convective mixing will have the tendency to drive the interface melt compositions to some equilibrium value, but most ground-based, melt-growth experiments involving the alloys show large radial compositional variations that are probably a direct consequence of such an interfacial fluid flow phenomenon. Although the growth at very slow rates, under the influence of reduced stabilizing composition gradients and thus nonsteady flow conditions, tends to yield radically more homogeneous ingots, generally, no ingots could be obtained by the Bridgman-Stockbarger method that were simultaneously radially and axially homogeneous for any substantial length.

4.6. ADVANTAGES OF MICROGRAVITY GROWTH

In microgravity it is expected that the highly desired, slightly convex growth surfaces will be easier to maintain because of the reduced tendency for stratification of the denser (Hg-rich) fluid components at the higher growth rates that are usually needed to obtain solute conserving steady-state growth and thus axial compositional uniformity. At the same time, the near-elimination of transverse temperature gradient-driven incomplete mixing effects is expected to provide for a better control of the lateral compositional distribution in the melts and stresses resulting from hydrostatic pressure will be nearly eliminated. We thus expect that by growing under the influence of low-gravity conditions, crystals with significantly improved crystallinity and compositional homogeneity can be prepared as compared to the best crystals that can be produced on Earth. It is also reasonable to expect that careful characterization of both the space- and ground-growth materials will lead to better insights into the peculiarities of the various growth mechanisms, permitting improvements in Earth-based processing of semiconductor alloy systems.

4.7. GROUND-BASED RESULTS

Over the past several years, a detailed evaluation has been performed on the effects of growth parameters on the axial and radial compositional uniformity, defect density, and optical properties in directionally solidified $\text{Hg}_{1-x}\text{Cd}_x\text{Te}$ and other similar compounds and pseudobinary alloys. A series of $\text{Hg}_{1-x}\text{Cd}_x\text{Te}$ alloy ingots ($0 < x < 0.6$) has been grown from pseudobinary melts by vertical Bridgman-Stockbarger type heat-pipe furnace assembly using a wide range of growth rates and thermal conditions. Several of the experiments were performed in transverse and axial magnetic fields of up to 5T.⁶¹ The effect of an axial field of 5T on the radial segregation is shown in figure 1. On the left is shown the superconducting magnet; the furnace resides in the central bore. On the right are shown the radial composition profiles. The two experiments were done in the same furnace with the same temperature settings and translation rates.^{26 27} Precision measurements were performed on the ingots to establish compositional distributions and defect density distributions.

Correlation between growth rates and thermal conditions and growth interface shapes have been established for the alloy system. To assist in the interpretation of the results and the selection of optimum in-flight growth parameters, the pseudobinary phase diagram ($0 < x < 1$),³ liquid and thermal diffusivities ($0 < x < 0.3$),¹⁹ melt viscosity,⁵⁵ and the specific volumes as a function of temperature ($0 < x < 0.15$) have been measured.²⁰ From these measurements and other available data, the heat capacity, enthalpy of mixing, and the thermal conductivity of pseudobinary melts have been calculated using a regular associated solution model for the liquid phase.

A one-dimensional diffusion model that treats the variation of the interface temperature, interface segregation coefficient, and growth velocity has been used to establish effective diffusion constants for the alloy system.¹⁴ Theoretical models have been developed for the temperature distribution and the axial and radial compositional redistribution during directional solidification of the alloys.^{10 11 59 60} These were used along with the experimental results to select the parameters for the first flight experiment flown on the USMP-2 mission.

A microscopic model for the calculation of point-defect energies, charge-carrier concentrations, Fermi energy, and conduction-electron mobility as functions of x , temperature, and both ionized and neutral defect densities has been developed.^{48 52-54} For selected samples, measurements were performed of electron concentration and mobility from 10–300 K. The experimental data were in reasonably good

agreement with theory and were successfully analyzed to obtain donor and acceptor concentrations for various processing conditions.

4.8. FLIGHT RESULTS

A five-zone Bridgman-Stockbarger-type furnace system designated as the AADSF has been designed and developed for operating in the cargo bay of the Space Transportation System (STS). Over 15 growth experiments were performed in the development and ground-based versions of the AADSF to establish optimum operating parameters and procedures for the initial flight experiment. Three other crystal growth experiments were made part of the ground-testing program of the flight unit. The experiment was successfully flown on the STS-62 mission as part of the USMP-2 mission in March 1994. An approximately 16-cm long and 0.7-cm diameter $\text{Hg}_{0.8}\text{Cd}_{0.2}\text{Te}$ alloy crystal was grown at a rate of 0.79-mm/hour over a period of approximately 11 days. Following the growth on the USMP-2 mission, an exact duplication of the experiment was conducted on the ground to provide a "ground truth" equivalent sample. Characterization of these two boules is in progress. Certain aspects of the characterization of the surface of the boules have been substantially completed, and much other work is in progress. The following paragraphs will describe the status of the characterization as of May 1, 1995.

4.9. FLIGHT TIMELINE

In order to optimize science results for all the experiments on the STS-62 mission, certain compromises were accepted with regard to the operation of the AADSF. First of all, the furnace was positioned some 13 feet in front of the center of gravity of the orbiter, 3 feet starboard of the center of gravity, and almost 4 feet above the center of gravity. This factor resulted in there being little or no possibility of avoiding a residual gravity vector acting parallel to the growth interface. While the most favorable attitude for flying the orbiter could be calculated, other mission-related issues affected the final decision. Such issues included the disposition of other experiments, and their desired residual gravity vectors, communications with other experiments, and orbiter safety-related issues including navigation and thermal aspects. Nevertheless, a substantial period of time was negotiated during which there were no orbiter maneuvers, and during which crystal growth could be initiated and continued well into the presumed "steady-state" region. The attitude during the AADSF operation of the mission remained faithful to the pre-mission timeline, and 153.5 contiguous hours within a $-ZLV/+YVV$ of the orbiter attitude were available. Sample translation occurred during some 147 hours, and actual crystal growth was estimated to take up some 140 hours of this time frame. The remainder of the crystal growth occurred during approximately 28 hours at $-XLV/-ZVV$ and 56 hours at $-XLV/+ZVV$. The final centimeter and a half (as calculated) grew during a period after the end of the dedicated microgravity part of the mission with a very noisy gravity environment and several changes of attitude. An estimated compositional profile based on diffusion controlled growth¹⁴ and a supercooled region of 1.7 cm is shown in figure 2. The graph is plotted against distance grown on a linear scale, with superimposed mission elapsed time (MET) adjusted to allow for changes in growth rate during the experiment. A decision was made during the mission to increase the translation velocity of the sample and hence force breakdown of the interface and thereby insert a time mark on the crystal. This marking was intended to demonstrate both position and shape of the interface and also to permit the correlation between crystal growth and mission activities to be determined. The chosen time for the "interface demarcation" was 4 hours before the first attitude change. The translation velocity was increased from a nominal value of 0.79 mm/hour to 10 mm/hour for 10 minutes and then returned to 0.79 mm/hour for the remainder of the mission. Figure 2 also shows the calculated effect of this change on the composition, again assuming diffusion control. It was anticipated that a 4-hour time period would be sufficient for the sample to re-establish the same conditions that had prevailed prior

to the change being made. The same timeline was used in the ground truth, with the furnace hot zone maintained on top.

4.10. RESIDUAL ACCELERATION RESULTS

Acceleration data of importance are now available, specifically the Orbital Atmospheric Research Experiment (OARE) data taken during the mission.⁶² OARE gives the quasi-steady component of the gravity vector at the instrument location which is close to and below the center of gravity of the orbiter. Figure 3 shows the z-component at the instrument for periods at the end of the AADSF primary attitude and through the change-over period to the second attitude. These data have been "transformed" to the center of gravity and then to the AADSF location. Of specific interest here is the degree of noise difference between the activity period and the crew sleep period. While most of the activity is believed to be in the high frequency range, the location of the change is significant, and will affect the characterization strategy as will be reported later. Figures 4 and 5 taken from the report of Rogers and DeLombard⁶² show a representative period of the -ZLV/+YVV attitude. In figure 5, the data have been transformed to the location of the crystal interface in the AADSF. To simplify some of the analysis, the orbital oscillations which are clearly seen in the X-Axis data are ignored and approximate steady-state components have been tabulated in table 1. These data are for the three primary attitudes and were calculated by Kim Destro-Sidik of Tal-Cut Company. Figure 6 is a schematic representation of the three main attitudes with the position of the AADSF with its hot and cold zones superimposed. The residual acceleration data from table 1 have been included.

The next step is to correlate such data with cross-sections of the crystal. Figure 7 shows the locations of the residual acceleration vectors relative to the crystal cross-section for the main primary attitudes. Three features are of note here: First, only during the first attitude is the total resolved value less than $1 \mu\text{g}$. Second, the vector points from the cold to the hot end of the furnace in the first and third attitudes, thus giving rise to an unstable convective situation liable to lead to fluid flow. The -ZVV/-XLV attitude has a small residual acceleration directed from liquid to solid and is thus stabilizing. Finally, the transverse vector across the solidifying interface is in all three cases lower than the perpendicular vector. This is also conducive to fluid flow. These parameters are mainly the result of the furnace being located some 13 feet aft of the center of gravity of the orbiter with a resulting acceleration component always driving in that direction, irrespective of drag contributions from the orbiter attitude. The significance of these residual components and the manner in which they affected the sample features will be discussed later in the characterization section.

4.11. RADIOGRAPHY

The first post-landing activity of characterization was to extract the cartridge from the furnace, photograph, and inspect for damage. The cartridge was in excellent shape and typical of all successful prior ground growths. A key issue here was the marking of the cartridge to ensure that the direction relative to the furnace frame and hence the orbiter frame was well established. This was done by identifying and then marking on the cartridge with a felt-tip pen the J7 position of the furnace, which corresponded to the forward direction of the orbiter. On-line radiography at Kennedy Space Center using a microfocuss tube and an image intensifier was used to examine the cartridge. The results were recorded on videotape. The main result was to confirm that the ampoule had not breached and that a single large boule of material had been produced. Closer examination of the video revealed that there were positions on the side of the boule, particularly near the end, where the surface was irregular. The other significant observation was that, on rotation of the cartridge in the x-ray beam, one side of the material at the very last to freeze showed a 180° contact with the wall, while the opposite face showed a 120° contact angle.

Ground-based results normally show angles of just over 90°. The 120° contact angle is most pronounced at and around the J7-45° position. These observations were later confirmed with film at Marshall Space Flight Center. A radiograph showing the flight sample and the ground truth is shown in figure 8. It is believed that the asymmetry of the end of the sample is caused by a transverse residual acceleration vector. This does not, however, correlate with the anticipated vector from the -XLV/+ZVV attitude shown in figure 7, but the final solidification takes place beyond the microgravity part of the mission, and the exact correlation of orbital maneuvers to crystal growth position is not exactly known due to the solidus temperature change associated with the final transient region and the thermal end effects of the cartridge.

4.12. PHOTOGRAPHY

During this stage of the characterization, all aspects of the removal of the cartridge from the furnace, the cutting open of the cartridge, and the removal of the ampoule and the boule itself following the dissolution of the fused silica in hydrofluoric acid were photographed. The cartridges, after processing, are shown in figure 9. Due to the attitude changes during the mission and the presumed presence of a residual acceleration component across the liquid-solid interface, radial asymmetry of the sample was anticipated and all photography was repeated at several locations around the ampoule and boule. Eight sets of photographs were taken at positions 45° apart with J7 as the reference point. The surface features changed both along the boule and also as one went around the boule at the same distance from the tip. A typical example is shown in figure 10. As on most of the orientations, the first 70 mm are smooth, and beyond 110 mm the surface is often rough. This is the J7 position and is fairly smooth throughout. At certain orientations there is a roughness associated with the solidifying material not being forced against the edge of the ampoule. A typical rough region is visible between 3 and 6 cm along the surface at about -45° or just below the center line of the boule as we observe it. Microscopy later confirmed the presence of thermal etch pits as one of the causes of such a surface. It should be noted that ground-based growths of this material invariably result in smooth, shiny surfaces, due to the hydrostatic force pushing the liquid against the ampoule wall during solidification. An interesting feature which was seen on the boule surface prior to dissolving away the ampoule was the presence of a thin ring approximately 11 cm from the tip of the ampoule. The ring passes completely around the boule and its presence was confirmed after the silica was removed. This ring is clearly shown in figure 10. Later analysis demonstrated that the position of the ring coincided with the change of attitude of the orbiter from -ZVV/-XLV to +ZVV/-XLV. The degree of smoothness at these various orientations is shown in table 2. In all ground-based experiments, the surface of the boule is smooth, with the exceptions of the occasional place where the material sticks and reacts with the ampoule wall. The table shows that the region between 9 and 11 cm is smooth completely round the boule; this is an indication of the presence of a downward force on the solidifying liquid and is similar to the hydrostatic force due to gravity as present in the ground-based work. This correlates well with the data shown in figure 7. The correlation is also good in the first part of the material to freeze, where the region near J7+180° has the smoothest surface. The rough surface close to J7 is due to the material being pulled from the wall by the residual acceleration as shown in figure 7. The nominal attitude for the crystal region in the range 11-15 cm was subjected to many disturbances. For example, the orbiter robot arm was in operation at day 8, hour 1 and extra vernier firings were deliberately made from day 8, hour 8 onwards. These may have contributed to the continuation of the banding starting at 11 cm and shown in figure 14.

4.13. X-RAY DIFFRACTION

Several options were considered prior to initiating surface characterization of the sample. The simplest techniques for observing grain structure and degree of crystallinity is by sand blasting the surface. This procedure, however, leads to considerable structural crystallographic damage to the surface, the removal of uneven amounts of material, and the destruction of surface effects. As has been shown in the

photographic section, the surface structure of the as-grown boule varies considerably from location to location; probably this is the result of the microgravity environment. It is important to retain such features for as long during the characterization phase as possible. A second possible preparation technique is to etch the surface with a bromine solution. This is much more controlled and, depending on time and concentration, can remove as little as 1 μ m/minute. The benefits are that the surface can be cleaned considerably, but delicate features such as etch pits may be removed. To reveal grain structure requires a considerable length of time in such an etch, and may be orientation dependent. The crystal structure, however, is not adversely disturbed by this technique. The third option is to use a strong acid etch such as Polisar or Straughan's reagent. This will clearly and rapidly reveal the grain structure and will not damage the crystallographic structure. The surface features, however, will be removed and the chemical reaction is dependent on both orientation and defect status. Such an acid etch produces etch pits in certain preferential directions and an oxidized surface in others. It is clear from the above rationale that grain structure of the surface cannot readily be revealed nondestructively.

One way out of this dilemma is to evaluate nondestructively the crystallinity and to find out where grains were and what orientation they were by taking x-ray back reflection Laue photographs. Some 60 patterns were taken on four surfaces at 90° to each other and at 0.5-mm intervals. There were significant differences between the four surfaces examined. The sample was mounted within a machined groove and attached with carbon paste to a graphite block. This arrangement was found to be suitable for x-ray diffraction in one direction, and for energy dispersion x-ray spectrometry (EDS) in a scanning electron microscope (SEM) at 90°, thus reducing the handling involved. The Laues showed that there was a long, single crystal stretching along the J7 surface from 35–90 mm. This would indicate that the crystal survived the interface marking translation rate increase which would have been at about 85 mm. As noted above this surface was rough, and the solidifying material was probably not being pressed strongly against the wall of the ampoule during the solidification. In contrast, the crystallographic orientation at J7+180° was changing every cm and the surface was smooth.

In order to get a quick estimate of the quality of the material, the collimator of the Laue camera was removed for some of the photographs; this produces a beam approximately 3 mm across and while it is by no means a parallel arrangement, it does simulate a topograph and does give an idea of crystal quality. Figure 11 shows the Laue patterns at a position 73 mm from the tip on the J7–90° surface. This pair were chosen at random, and it can be seen that the Laue pattern with the collimator in place (figure 11a) is close to [111] orientation, and with spots which are sharp, but split in places. This would indicate a structure with low angle boundaries. The accompanying topograph (figure 11b) shows well-defined spots with structural features within, indicative of a good but not perfect crystalline structure. Reflection topographs were recently taken at the National Synchrotron Light Source (NSLS) facility in Brookhaven, New York, in collaboration with Dr. Michael Dudley of the State University of New York (SUNY)-Stony Brook. The preliminary results will be reported in a subsequent paragraph.

These Laue patterns give the orientation of the crystal normal to the surface, but do not directly reveal the preferred direction of crystal growth. This can be done by transposing the normal plane through 90° towards the crystal growth axis. The procedure is as follows: First the normal to the surface is found by indexing the photograph with conventional techniques. If three known index planes which lie in different zones can be identified, then the angles made by these planes to the center will enable one to determine the $(h_c k_c l_c)$ for the center of the film. By repeating the procedure for an arbitrary position on the line joining hkl to the direction of crystal growth, a second plane can be found, and hence the zone $[uvw]$, which includes both the normal to the surface and the direction of crystal growth. The precision of the initial measurement is estimated to be about 0.5°, and the transformed orientation precision is approximately 4°. One can then determine the direction of crystal growth by determining the plane which makes an angle of 90° with $(h_c k_c l_c)$, and obeys the Weiss zone law for $[uvw]$. The resulting transformed

orientations are shown in table 3. As cutting of the boule has proceeded, the orientation of the directions of crystal growth can be measured directly from the Laue patterns. A cross-section of grains in the flight sample (MCT27-Q) taken with the back scattered signal in the SEM is shown in figure 12, together with the orientation of two of the largest crystals.

4.14. SCANNING ELECTRON MICROSCOPY (SEM)

The central part of the sample surface has been examined by SEM. Due to the size of the chamber and the movement of the stage, it is impossible to reach the first and last 3 cm of the sample without cutting the boule. As mentioned above, the surface features varied considerably and several hundred photographs have been taken. They included what are believed to be thermal etch pits (figures 13a and 13b) and several featureless areas. The etch pits change shape as one moves around the circumference of the sample, indicating the effect of orientation. Different grains can be readily recognized by an abrupt change in shape and orientation of the etch pit triangle. The circumferential mark at 11 cm is clearly visible as a brightly emitting band some 100 μm wide. Several other light bands were visible, but these were much narrower and were curved, and beyond the 11 cm mark. This part of the surface is shown in figure 14. These bands are also indications of interface breakdown as will be shown in the EDS section of this report.

4.15. ENERGY DISPERSION SPECTROMETRY (EDS)

In order to determine the compositional uniformity of the boule, EDS analysis in the SEM was employed. As a preliminary nondestructive evaluation was needed, the as-grown surface of the boule was examined first. While the results are not of optimum precision due to the fact that the surface is not flat, this is the most suitable chemical analysis technique known to us. Wavelength dispersion would give better results, but to justify its use one would need to examine a polished surface. Standards of elemental cadmium and mercury telluride were employed. Excitation energy of 10 kV was used with a take off angle of 35°, a working distance of 25 mm, and the L lines for Cd and Te and the M line for Hg were analyzed. Initially, separations of 5 mm were used, with better resolution employed when justified by the data. Two surfaces of the ground truth have been examined, and five of the flight sample. In addition, the flight sample was rotated about the growth axis within the SEM to obtain some area, as opposed to linear measurements.

The results are shown in figures 15–20. Figure 15 shows the ground-truth sample surface compositional values at the J7+90° position. The results are similar to those previously obtained in ground-based growth of mercury cadmium telluride and reflect primarily diffusion limited axial mass transport. As this is the surface analysis only and the interior of the sample has a lower cadmium telluride fraction, the curve is higher than normally seen with averaged density results. Of significance is the effect of the rate change, which is at 83 mm from the tip of the ampoule. Clearly, the sudden increase in translation velocity has forced the solidification of mercury-rich material which has not been replaced. The reversion back to the original velocity has then led to the opposite effect with cadmium-rich material being solidified. The same effect at the same position was found in the other surface examined. The increase in translation velocity for a short period has been successful in marking the location of the solidification front.

Figures 16–19 show the composition on the four “primary” surfaces of the flight sample. Figure 16 is the J7 position and shows the sharpest drop in composition. The behavior of the other three surfaces is similar, but with some significant differences. In all cases the initial transient region is more shallow than on the ground truth samples. Thus, the curve for flight grown material would seem to indicate a lower

effective mass transport coefficient. Preliminary fitting of the data to diffusion controlled growth conditions indicates a coefficient of $1 \times 10^{-4} \text{ cm}^2/\text{s}$, as opposed to a value of $5.5 \times 10^{-5} \text{ cm}^2/\text{s}$ normally found on the ground. Another significant difference is that the four surfaces are different from each other, thus supporting a notion that residual fluid flow is taking place. For example, the J7+90° curve lies above that for J7, the effect of the rate change is much less, and the reversion to the original rate results in a higher CdTe peak. While not showing on all the surface results, the light band at 11 cm noted above proved to be mercury telluride, this being a further indication of interface breakdown. The other light, narrow bands were all HgTe rich. EDS, particularly with unpolished surfaces, gives much scatter in the results, but the readings between the rate change region and the 11-cm mark are more widespread than normal, and more than the normal scatter. This region evidently contains more variations in composition than the remainder of the boule. Another feature is that the shape of the final "transient" is not that normally seen in this alloy in ground-based growth, the curve being the opposite direction to that which one would expect for diffusion-controlled conditions. These regions are being examined now that the sample has been cut. Figure 20 shows two-dimensional compositional analysis close to the rate change. The results show the spread of the rate change, but are not of sufficient fidelity to demonstrate the subtle trends that might be associated with changes of fluid flow.

4.16. CUTTING STRATEGY

The cutting strategy is crucial for optimizing characterization and obtaining maximum science return. Among the factors to be examined are the following: Compositional variations on a three-dimensional scale are required to determine the presence or absence of nonaxial rotational fluid flow caused by transverse residual acceleration vectors. [111] oriented slices are needed to examine defect structure by etch pit measurement, double axis diffractometry and for some x-ray synchrotron topography techniques. Finally, it is desirable to retain areas of material of reasonable homogeneity for the preparation of electrical test pieces. Such samples are not necessarily compatible with each other and so much precutting measurements have to be made. In both the ground truth and the flight sample tests, wafers were cut perpendicular to the growth direction and at a location just prior to the start of the rate change. These wafers were lapped and chemomechanically polished in 2 percent bromine-ethylene glycol. EDS readings were taken and later high precision, high spatial resolution wavelength dispersion spectrometry (WDS) readings also. These latter will be described in a later section of this report. During the preparation of these sections, careful monitoring of the J7 direction was maintained so that nonsymmetric analysis and presumed asymmetric fluid flow could be correlated with orbiter attitude and any residual acceleration vector. The cartridge was initially cut through with a wire saw to mark the fused silica ampoule, and the ampoule was cut after removal from the cartridge. The first cut was made into the glass at a location where there was no material, and corresponded to the J7 position of the furnace. The second cut had to penetrate the material and was made in the surface of the boule through the glass into the last-to-freeze portion. This position was deemed least destructive from the point of view of science return. A small cut was also made parallel to the growth direction close to the first-to-freeze end so that both ends would be marked after initial cuts were made. The surface features had already given some indication of the possibility of asymmetric fluid flow (see table 2). WDS results, however, showed no obvious asymmetry, and so the cutting strategy was to rely on the OARE calculated data shown in figure 7. The rough area seen in figure 10 is close to the OARE data. The cut was made at -16° with respect to J7 or along the resolved transverse vector calculated from the OARE data. The ground-truth sample was sectioned down the middle through the rate change region and EDS measurements made as shown in figure 21. The resolution was not good enough to determine exactly across the entire sample the position of the rate change, and the readings will be repeated with WDS measurements.

4.17. OPTICAL MICROSCOPY

This sectioned sample from the ground-truth growth was etched in Polisar II etch to examine for granularity and etch pits. The structure is shown in figure 22, and it is of interest that there is no breakdown of the crystallinity during the rate change. In fact there is no metallographic evidence of the interface position during the rate change. A comparison of this structure with the compositional variation shown in figure 21 indicates only roughly the history of the solidification and more solid conclusions will be drawn when the WDS results are available. This contrasts with the surface analysis (figure 15) on which the start of the rapid translation had an immediate and obvious effect. Similar cross-sections will be made in the two other primary attitudes of the orbiter. The material is prepared for structural evaluation by mounting the boule on a goniometer and then taking orientation photographs with the back reflection x-ray Laue technique. The feedback from the Laue photograph enables adjustments to be made on the goniometer so that the desired [111] orientation can be obtained. This has been done for one grain on the flight sample adjacent to the region from which the first wafer was cut. The etched surface is shown in figure 23. Once quantitative evaluation of the etch pits has been completed, the sample will be transferred to the double axis diffractometer and x-ray rocking curves and reciprocal lattice point scanning by means of $\theta/2\theta$ will be done. This same section will then be taken at Brookhaven National Laboratory for x-ray synchrotron topography. Similar cutting and sectioning will be done with the aim of examining one [111] oriented grain at each location of the surface. In this way it will be possible to observe any effects caused by the material being forced against the wall during solidification as compared to the regions of the crystal which grew in a "semicontainerless" configuration. The same procedure will be used for sections of material grown in all three major attitudes of the orbiter during growth, material permitting. The interface at 11 cm produced by the second attitude change will be examined in a cross section or slab.

A section cut from the ground-truth sample at a similar stage during the growth is shown in figure 24. While cut perpendicular to the growth axis rather than being oriented to [111], the Polisar etch has been effective in revealing the structure of one of the larger grains which lies 13° from the [111]. At first sight the structure and defect densities are not very different from the flight sample, but quantitative etch pit counting and correlation with compositionally dependent stresses due to differences in lattice constant will be carefully made to complete the characterization effort. A curiosity is the prominent twin present in this sample; twins are rare in bulk grown HgCdTe and the origin of this one will be carefully investigated.

4.18. WAVELENGTH DISPERSIVE SPECTROMETRY (WDS)

Results with WDS are more sensitive than those from EDS, and are now being done on polished samples with both high compositional resolution and high spatial resolution. The first samples studied were the cross sections prepared just prior to the rate change. This was done for both the ground-truth and the flight samples. Figure 25 shows a cross section for the ground-truth sample and indicates some asymmetry, possibly caused by the sample not being perfectly centered, not translating exactly along the center line of the furnace or, most likely, the furnace axis not being exactly vertical. Figure 26 shows a similar plot for the flight sample with a superimposed three-dimensional diffusion limited calculation done by Dr. J.C. Wang of Alabama A&M University. The calculation is for an interface deviation of 2 mm from being flat. It can be seen that this diametrical plot, which is in the J7 direction indicates a larger asymmetry than the ground truth sample. This may be an indication of three-dimensional fluid flow. The three-dimensional representation of the composition of the flight sample is shown in figure 27. This position includes material before, during, and after the rate change, and also beyond the attitude change. The first rate change has brought about a complete change in the solidification characteristics with an almost quenched in interface, particularly at the center of the boule. The surface data also show the interface as

has been shown, and it is reasonable to infer its exact position and shape at the instant of the first rate change. In figure 27, the red material is the heavier, low-x, HgTe rich material, and it can be seen that there is a slight asymmetry, denoted by the yellow material dominating the right center of the figure at the bottom.

Recently, much EDS data have become available on two wafers cut from the two first attitudes. These data were taken within 100 μm of the edge and proceeded at increasing intervals to the center. In all, some 280 points were measured. By this means good statistics are obtained, and figures 28 and 29 demonstrate certain effects very clearly. In figure 28, the resolved vector in the plane of the boule (but not in the plane of the solidifying interface, which is curved), is shown. At 62 mm from the first to freeze end there is a vector from the solid towards the liquid of 0.28 μg , and this has caused much stirring of the melt, resulting in considerable asymmetry in the resolved vector on the wafer. In contrast, the wafer cut at 106 mm, in the second attitude and shown in figure 29 has a small vector which points from the solid to the liquid, and the wafer is more homogeneous. There is still an asymmetry in the direction of the resolved vector, but it is much smaller than one would anticipate in comparison to the material at 62 mm. The inference here is that the stabilizing vector from liquid to solid is essential to reduce fluid flow. The data in figure 28 are worse than normally encountered in ground based growths, while the data of figure 29 are superior to ground based growths.

4.19. SYNCHROTRON RADIATION STUDIES

The entire boule surface was examined on beamline X19C at NSLS. This line operates as a white beam source with no monochromator and at an energy range up to 2.584 GeV. The operating current is initially at 250 mA and declines over a 20-hour period. It is ideally suited for Laue scattering experiments. While more information can be obtained from transmission synchrotron studies, the sample preparation involved is much longer and there is the possibility of losing some of the material; such studies will be left till later. No sample preparation is required for a study of the surface of the as grown boule. Initially the four surfaces at 90° were examined with an oblique incident beam along the length of the boule. The images of the ground-truth sample were generally of poor quality, indicative of both small crystal size and highly strained material. The flight sample, in general, was similar, but there were areas which were of much higher quality. Good quality reflection topographs were obtained from some of the rough, etch pit laden material, particularly the region between 38 and 42 mm at J7. Other good reflections were observed from the region close to 105 mm, which is the part of the crystal grown in the -XLV/-ZVV attitude. The crystal orientation seems to have been maintained entirely around the boule. It is significant that this is the region of the crystal grown with a stabilizing acceleration vector pointing from liquid to solid.

4.20. SUMMARY AND PRELIMINARY CONCLUSIONS

1. An approximately 16-cm long $\text{Hg}_{0.8}\text{Cd}_{0.2}\text{Te}$ alloy crystal was successfully grown over a period of 11 days during Mission STS-62 on USMP-2.

2. A rate change inserted into the growth timeline sequence produced in the crystal an effective time marker for correlating orbital and residual accelerations to various crystal features and alloy compositional changes. This allowed a detailed evaluation of the effects of the magnitude and direction of residual acceleration on crystal homogeneity and perfection to be made for the first time. The rate change did not cause the propagation of new crystals.

3. Circumferential variation of composition and topographic features around the boule indicated that residual acceleration vectors were present and having a considerable effect on the growth process.

4. Preliminary x-ray topographs of the portion grown in the most favorable attitude (-XLV,-ZVV) indicate that a region consisting of a complete single crystal of significantly higher quality than usually grown on the ground.

5. The OARE instrument proved to be an accurate predictor of the direction of residual acceleration vectors, as evidenced by the surface features of the boule.

6. The measured transient surface compositions indicate a lower effective mass transport coefficient than those observed in ground-based studies.

7. Certain attitude maneuvers of the orbiter can dramatically affect the growth stability. This is illustrated by the roll-around in tail-down attitude which reversed the direction of the residual acceleration perpendicular to the interface and caused thick compositional striations at 11 cm along the crystal.

8. Compositional maps of wafers taken from materials grown in two different orbiter attitudes with very different resulting residual accelerations vectors demonstrate conclusively the effect of residual accelerations on solidification of solid solution alloys with a wide separation between liquid and solid.

9. Further microstructural, optical and electrical characterizations of the crystal promise to provide a wealth of additional information on the growth in low-Earth orbit of solid solution alloy crystals having a large separation between their liquidus and solidus.

4.21. REFERENCES

1. Lehoczky, S.L., F.R. Szofran, and B.G. Martin, "Advanced Methods for Preparation and Characterization of Infrared Detector Materials," McDonnell Douglas Corporation Report No. MDC Q0717, July 5, 1980, (final report for the period December 5, 1978–July 5, 1980, for the George C. Marshall Space Flight Center, Contract No. NAS8-33107), pp. 1–151 (1980) (also NASA CR 161598, July 5, 1980).
2. Lehoczky, S.L., and F.R. Szofran, "Advanced Methods for Preparation and Characterization of Infrared Detector Materials," McDonnell Douglas Report No. MDC Q0744, September 30, 1981 (interim report for the period July 5, 1980–September 30, 1981, for the George C. Marshall Space Flight Center, Contract No. NAS8-33107), pp. 1–33 (1981) (also NASA CR 161949, September 30, 1981).
3. Szofran, F.R., and S.L. Lehoczky, "The Pseudobinary HgTe-CdTe Phase Diagram," *J. Electronic Matls.*, *10*, 1131–1150, 1981.
4. Kelley, J.D., B.G. Martin, F.R. Szofran, and S.L. Lehoczky, "Applications of the Regular-Associated-Solution Model to the Cd-Te and Hg-Te Binary Systems," *J. Electrochem. Soc.*, *129*, 2360–2365, 1982
5. Lehoczky, S.L., and F.R. Szofran, "Directional Solidification and Characterization of $\text{Hg}_{1-x}\text{Cd}_x\text{Te}$ Alloys," in *Materials Research Society Proceedings, Materials Processing in the Reduced Gravity Environment of Space*, ed., G.E. Rindone (Elsevier: New York), *9*, 409–420, 1982.
6. Lehoczky, S.L., C.J. Summers, F.R. Szofran, and B.G. Martin, "Electrical Characterization of $\text{Hg}_{1-x}\text{Cd}_x\text{Te}$ Alloys," in *Materials Research Society Proceedings, Materials Processing in the Reduced Gravity Environment of Space*, ed., G.E. Rindone (Elsevier: New York), *9*, 421–431, 1982.
7. Szofran, F.R., and S.L. Lehoczky, "Liquidus Temperatures of Hg-Rich Hg-Cd-Te Alloys," *J. Electronic Matls.*, *12*(4), 713–717, 1983.
8. Holland, L.R., "A Thermal Transmission Function for Fused Silica Ampoules," *J. Crystal Growth*, *49*, 246, 1980.
9. Holland, L.R., "Radiant Heating of Ampoule Contents," NASA Tech Briefs, 349, Fall/ Winter 1981.
10. Naumann, R.J., "An Analytical Approach to Thermal Modeling of Bridgman-Type Crystal Growth I. One-Dimensional Analysis," *J. Crystal Growth*, *58*, 554–568, 1982.
11. Naumann, R.J., "An Analytical Approach to Thermal Modeling of Bridgman-Type Crystal Growth II. Two-Dimensional Analysis," *J. Crystal Growth*, *59*, 569–584, 1982.
12. Clayton, J.C., "Transient and Diffusion Analysis of HgCdTe," NASA CR 162049, 1982.
13. Cothran, E.K., "An Analytical Approach to Thermal Modeling of Bridgman-Type Crystal Growth: One Dimensional Analysis, Computer Program Users Manual," NASA TM 82487, May 1982.

14. Clayton, J.C., M.C. Davidson, D.C. Gillies, and S.L. Lehoczky, "One Dimensional Analysis of Segregation in Directionally Solidified HgCdTe," *J. Crystal Growth*, 60, 374, 1982.
15. Gillies, D.C., "Analysis of Mercury Cadmium Telluride by Energy Dispersive Analysis," *J. Electronic Matls.*, 11, 689, 1982.
16. Lehoczky, S.L., F.R. Szofran, and R.J. Naumann, "Crystal Growth of Homogeneous Hg_{1-x}Cd_xTe Crystals from Pseudobinary Melts," *Bull. Am. Phys. Soc.*, 28, 294, 1982.
17. Naumann, R.J., and S.L. Lehoczky, "Effect of Variable Thermal Conductivity on Isotherms in Bridgman Growth," *J. Crystal Growth*, 61, 707-710, 1983.
18. Holland, L.R., R.P. Harris, and R. Smith, "High Temperature, High Pressure Optical Cells," *Review of Scientific Instruments*, 54, 993, 1983.
19. Holland, L.R., and R.E. Taylor, "Measured Thermal Diffusivity of Hg_{1-x}Cd_xTe Solids and Melts," *J. of Vacuum Science Technology*, A1, 1615, 1983.
20. Chandra, D., and L.R. Holland, "Density of Liquid Hg_{1-x}Cd_xTe," *J. of Vacuum Science and Technology*, A1, 1620, 1983.
21. Lehoczky, S.L., F.R. Szofran, D. Chandra, and J.C. Wang, "Growth Rate Dependence of the Axial Compositional Variations in Bridgman-Grown Hg_{1-x}Cd_xTe Crystals," Fall Meeting of the American Physical Society, San Francisco, CA, November 20-23, 1983, *Bull. APS*, 28, 1313, 1983.
22. Szofran, F.R., and S.L. Lehoczky, "High Temperature Electrical Properties of HgTe," *Bull. APS*, 28, 1313, 1983.
23. Lehoczky, S.L., and F.R. Szofran, "Growing Crystals for Infrared Detectors," *NASA Tech Briefs*, 8, 136, 1983.
24. Jasinski, T., and R.J. Naumann, "One-Dimensional Modeling of Vertical Bridgman-Type Crystal Growth," *J. Crystal Growth*, 66, 469, 1984.
25. Holland, L.R., "Sealed Silica Pressure Ampules for Crystal Growth," *J. Crystal Growth*, 66, 501, 1984.
26. Szofran, F.R., and S.L. Lehoczky, "A Method for Interface Shape Control During Bridgman Type Crystal Growth of HgCdTe Alloys," *J. Crystal Growth*, 70(1/2), 349-355, 1984.
27. Szofran, F.R., D. Chandra, J.C. Wang, E.K. Cothran, and S.L. Lehoczky, "Effect of Growth Parameters on Compositional Variations in Directionally Solidified HgCdTe Alloys," *J. Crystal Growth*, 70(1/2), 343-348, 1984.
28. Holland, L.R., "VLS Growth to Purify Elements of Groups II and VI," *J. Crystal Growth*, 70, 1984.
29. Lehoczky, S.L., and F.R. Szofran, "Further Comments on Segregation During Bridgman Growth of Hg_{1-x}Cd_xTe," *J. Crystal Growth (Lett.)*, 69, 201-203, 1984.

30. Lehoczky, S.L., and F.R. Szofran, "Solidification and Crystal Growth of Solid Solution Semiconducting Alloys," in NASA CP 2313, edited by Camille M. Jernigan, p. 320, 1984, Proceedings of the Second Symposium on Space Industrialization, Huntsville, AL, February 13–15, 1984.
31. Szofran, F.R., and P.N. Espy, "Automated AC Galvanomagnetic Measurement System," *Review of Scientific Instruments*, 56, 1363, 1985.
32. Chandra, D., "Anomalous Volume Expansion in $\text{Hg}_{1-x}\text{Cd}_x\text{Te}$ Melts: An Analysis Employing the Inhomogeneous Structure Model," *Phys. Rev.*, 331, 7706, 1985.
33. Lehoczky, S.L., and F.R. Szofran, "HCT Crystal Growth Method," U.S. Patent No. 4,545,848, October 1985.
34. Su, C.-H., S.L. Lehoczky, and F.R. Szofran, "A Method to Eliminate Wetting During the Homogenization of HgCdTe ," *J. Appl. Phys.*, 60(10), 3777–3778, 1986.
35. Su, Ching-Hua, "Heat Capacity, Enthalpy of Mixing and Thermal Conductivity of $\text{Hg}_{1-x}\text{Cd}_x\text{Te}$ Pseudobinary Melts," *J. Crystal Growth*, 78, 51, 1986.
36. Lehoczky, S.L., and F.R. Szofran, "Growth of Solid Solution Single Crystals," NASA TP 2787, December 1987.
37. Szofran, F.R., and S.L. Lehoczky, "Bridgman Growth of Mercury Cadmium Telluride Alloys," in *Processing of Electronic Materials*, eds., C.G. Law, Jr. and R. Pollard (American Institute of Chemical Engineers: New York), pp. 342–348, 1987, Proceedings of First International Conference on Processing of Electronic Materials, held Santa Barbara, CA, February 23–28, 1986.
38. Lehoczky, S.L., and F.R. Szofran, "Growth of Solid Solution Single Crystals," in *The Nation's Future Materials Needs, International SAMPE Technical Conference Series*, eds., T. Lynch, J. Persh, T. Wolf, and N. Rupert (SAMPE: Covina, CA), vol. 19, p. 332, 1987. Proceedings 19th International SAMPE Technical Conference, Arlington, VA, October 13–15, 1987.
39. Lehoczky, S.L., F.R. Szofran, C.-H. Su, S.D. Cobb, and R.N. Andrews, "Crystal Growth of Solid Solution Systems by Directional Solidification," Proceeding of ASM International '87 Materials Congress, Cincinnati, OH, October 12–15, 1987.
40. Naumann, R.J., S.L. Lehoczky, and D.O. Frazier, "Growing Single Crystals of Compound Semiconductors," in NASA Tech Briefs, vol. 11, No. 6, pp. 47–48, June 1987.
41. Naumann, R.J., D.O. Frazier, S. Lehoczky, M. Vlasse, and B. Facemire, "Crystal Growth in Liquid-Encapsulated Float Zone," in NASA Tech Briefs, vol. 11, No. 8, pp. 44–45, September 1987.
42. Su, C.-H., S.L. Lehoczky, and F.R. Szofran, "Growth of HgZnTe Alloy Crystals by Directional Solidification," *J. Crystal Growth*, 86, 87–92, 1988.
43. Szofran, F.R., G.L.E. Perry, and S.L. Lehoczky, "Highly Automated Transmission-Edge Mapping," *J. Crystal Growth*, 86, 650–655, 1988.

44. Dakhoul, Y.M., R. Farmer, S.L. Lehoczky, and F.R. Szofran, "Numerical Simulation of Heat Transfer During the Crystal Growth of HgCdTe Alloys," *J. Crystal Growth*, 86, 49–55, 1988.
45. Andrews, R.N., F.R. Szofran, and S.L. Lehoczky, "Growth and Characterization of $\text{Hg}_{1-x}\text{Cd}_x\text{Se}$ Alloys," *J. Crystal Growth*, 92(3/4), 445–453, 1988.
46. Andrews, R.N., F.R. Szofran, and S.L. Lehoczky, "Internal Temperature Gradient of Alloy Semiconductor Melts From Interrupted Growth Experiments," *J. Crystal Growth*, 86(1–4), 100–105, 1988.
47. Su, C.-H., G.L.E. Perry, F.R. Szofran, and S.L. Lehoczky, "Compositional Redistribution During Casting of $\text{Hg}_{0.8}\text{Cd}_{0.2}\text{Te}$ Alloys," *J. Crystal Growth*, 91, 20–26, 1988.
48. Patterson, J.D., and S.L. Lehoczky, "The Second Born Approximation and the Friedel Sum Rule," *Physics Lett. A*, 137(3), 137–138, 1989.
49. Lehoczky, S.L., and F.R. Szofran, "Method of Preparing Radially Homogeneous Mercury Cadmium Telluride Crystals," U.S. Patent No. 4,863,553, September 1989.
50. Andrews, R.N., S.D. Walck, M.W. Price, F.R. Szofran, C.-H. Su, and S.L. Lehoczky, "Microhardness Variations in II-VI Semiconducting Compounds as a Function of Composition," *J. Crystal Growth*, 99, 717–721, 1990.
51. Su, C.-H., S.L. Lehoczky, and F.R. Szofran, "Directional Solidification of HgCdTe and HgZnTe in a Transverse Magnetic Field," *J. Crystal Growth*, 109, 392–400, 1991.
52. Abdelhakiem, W., J.D. Patterson, and S.L. Lehoczky, "A Comparison Between Electron Mobility in N-Type $\text{Hg}_{1-x}\text{Cd}_x\text{Te}$ and $\text{Hg}_{1-x}\text{Zn}_x\text{Te}$," *Materials Lett.*, 11(1,2), 47–51, 1991.
53. Patterson, J.D., W.A. Gobba, and S.L. Lehoczky, "Electron Mobility in n-Type $\text{Hg}_{1-x}\text{Cd}_x\text{Te}$ and $\text{Hg}_{1-x}\text{Zn}_x\text{Te}$ Alloys," *J. Materials Res.*, 7(8), 2211–2218, 1992.
54. Gobba, W.A., J.D. Patterson, and S.L. Lehoczky, "A Comparison Between Electron Mobilities in $\text{Hg}_{1-x}\text{Mn}_x\text{Te}$ and $\text{Hg}_{1-x}\text{Cd}_x\text{Te}$," *Infrared Phys.*, 34(3), 311, 1993.
55. Mazuruk, K., C.-H. Su, S.L. Lehoczky, and F. Rosenberger, "Novel Oscillating Cup Viscometer - Application to Molten HgTe and $\text{Hg}_{0.8}\text{Cd}_{0.2}\text{Te}$," *J. Appl. Phys.*, 77 (10), 5098–5102, 1995.
56. Palosz, W., F.R. Szofran, and S.L. Lehoczky, "The Effect of Heat Treatment on the Magnitude and Composition of Residual Gas in Sealed Silica Glass Ampoules," *J. Crystal Growth*, 142, 215–224, 1994.
57. Price, M.W., R.N. Andrews, C.-H. Su, S.L. Lehoczky, and F.R. Szofran, "Effect of Transverse Magnetic Field on the Microstructure of Directionally Solidified CdTe," *J. Crystal Growth*, 142, 215–224, 1994.
58. Lehoczky, S.L., D.C. Gillies, F.R. Szofran, F.A. Reeves, J.D. Sledd, T.K. Pendergrass, D.A. Watring, C.R. Coppens, J.E. LeCroy and D. Popok, "Crystal Growth of HgCdTe in the AADSF on the USMP-2 Mission," Paper AIAA 95-0609, 33rd Aerospace Sciences Meeting and Exhibit, Reno, Nevada, 1995.

59. Kim, D.H., and R.A. Brown, "Modelling of the Dynamics of HgCdTe Growth by the Vertical Bridgman Method," *J. Crystal Growth*, 114, 411, 1991.
60. Kim, D.H., and R.A. Brown, "Models for Convection and Segregation in the Growth of HgCdTe by the Vertical Bridgman Method," *J. Crystal Growth*, 96, 609, 1989.
61. Watring, D.A., and S.L. Lehoczky, "Magneto Hydrodynamic Damping of Convection During Vertical Bridgman-Stockbarger Growth of HgCdTe," *J. Crystal Growth*, in press 1995.
62. Rogers, M.J.B., and R. DeLombard, "Summary Report of Mission Acceleration Measurements for STS-62," NASA TM 106773, November 1994.

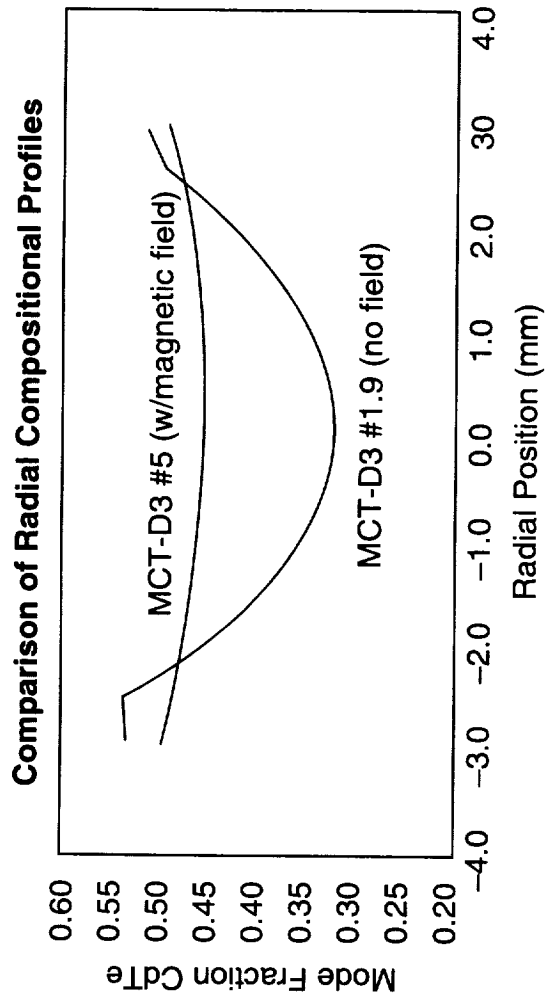
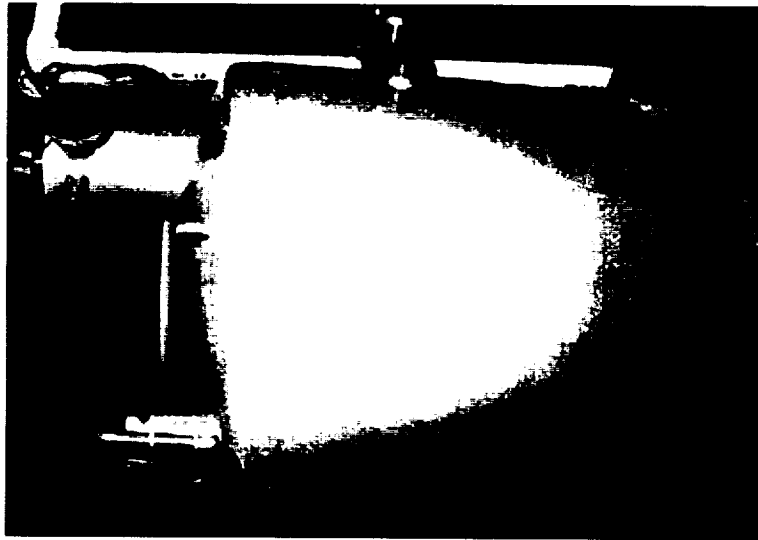


Figure 4-1. Superconducting magnet furnace.

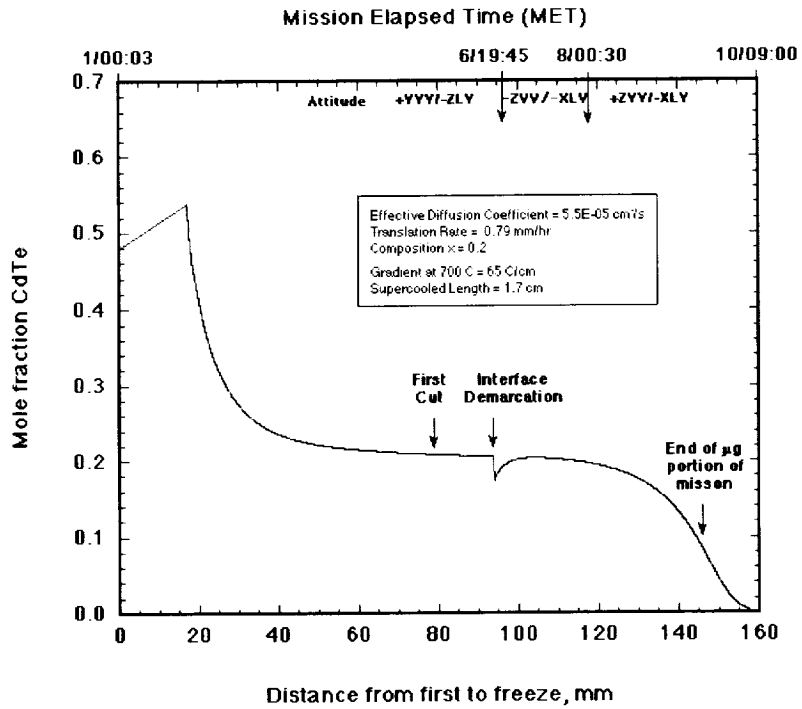


Figure 4-2. Estimated compositional profile based on diffusion controlled solidification.

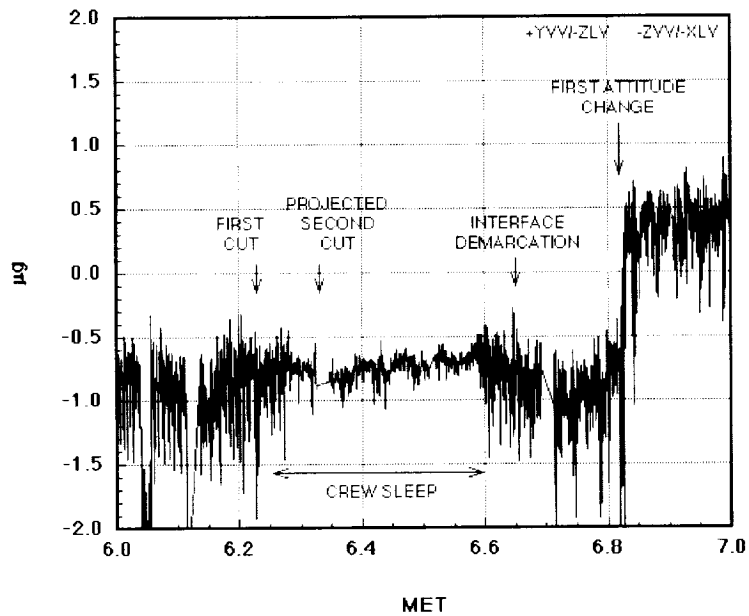


Figure 4-3. Z-component OARE data during attitude change.

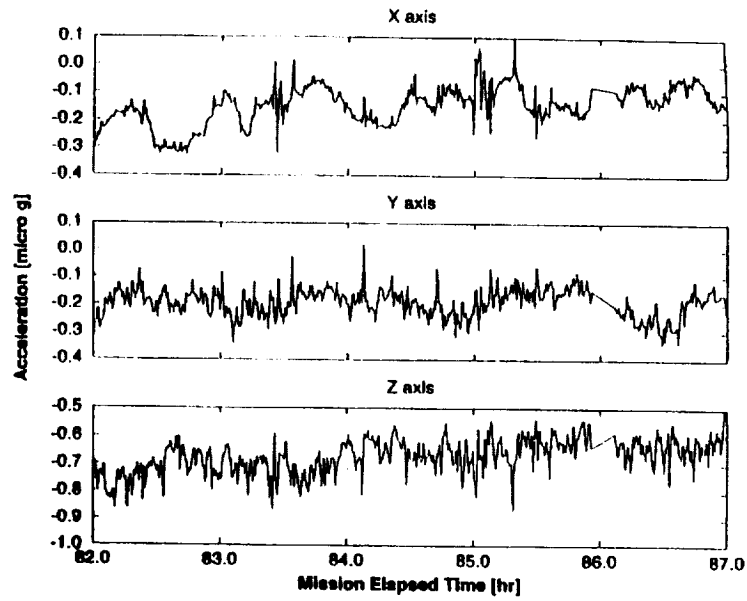


Figure 4-4. OARE data at instrument for $-ZLV/+YVV$ attitude.

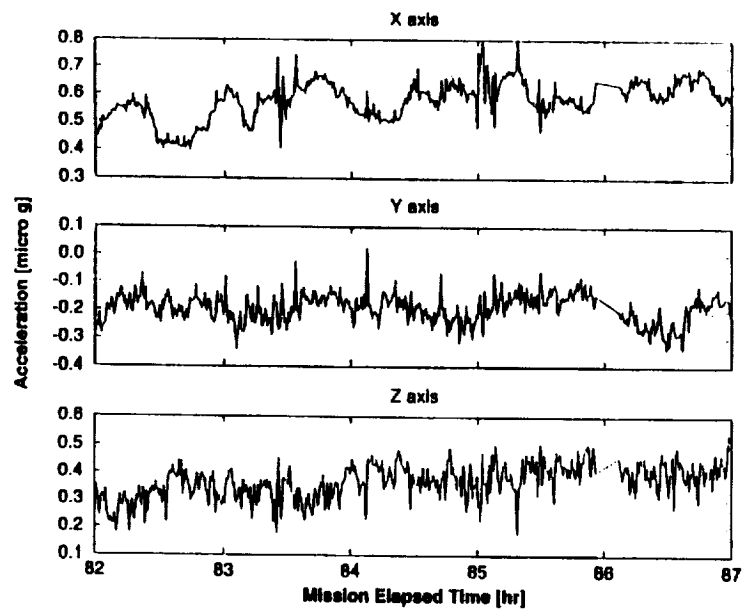


Figure 4-5. OARE data transformed to AADSF location for $-ZLV/+YVV$ attitude.

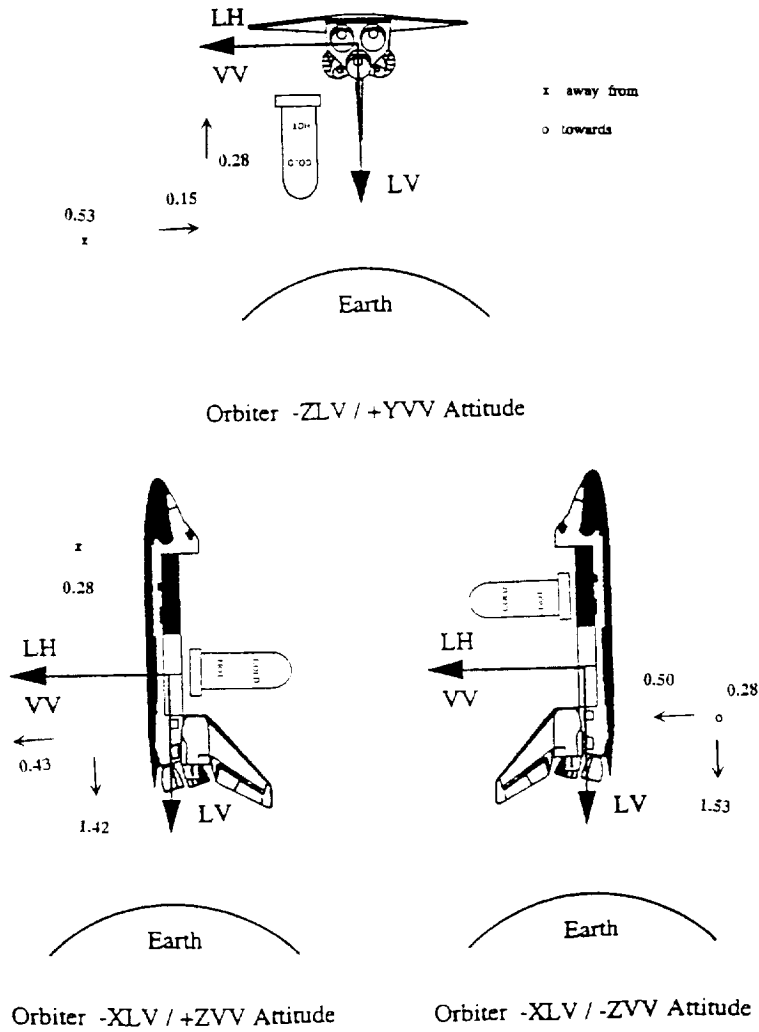


Figure 4-6. Directions of residual acceleration vectors with respect to AADSF and orbiter.

MCT 27Q Looking Towards First to Freeze End

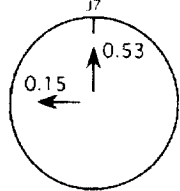
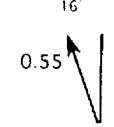
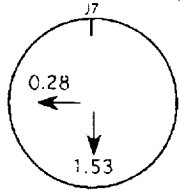
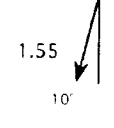
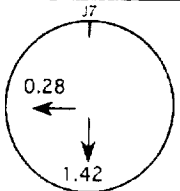

Orbiter Attitude	Transverse Residual Acceleration	Residual Axial Acceleration	Resolved Transverse	Axial/Transverse Ratio	Total Resolved
-ZLV/+YVV 0 - 9 cm		Hot ↑ 0.28 Cold	16 0.55 	-0.51	0.62
-XLV/-ZVV 9 - 11 cm		Hot ↓ 0.50 Cold	1.55 10° 	+0.32	1.63
-XLV/+ZVV 11 - 15 cm		Hot ↑ 0.43 Cold	1.45 11° 	-0.31	1.51

Figure 4-7. Resolved OARE data for AADSF flight sample.

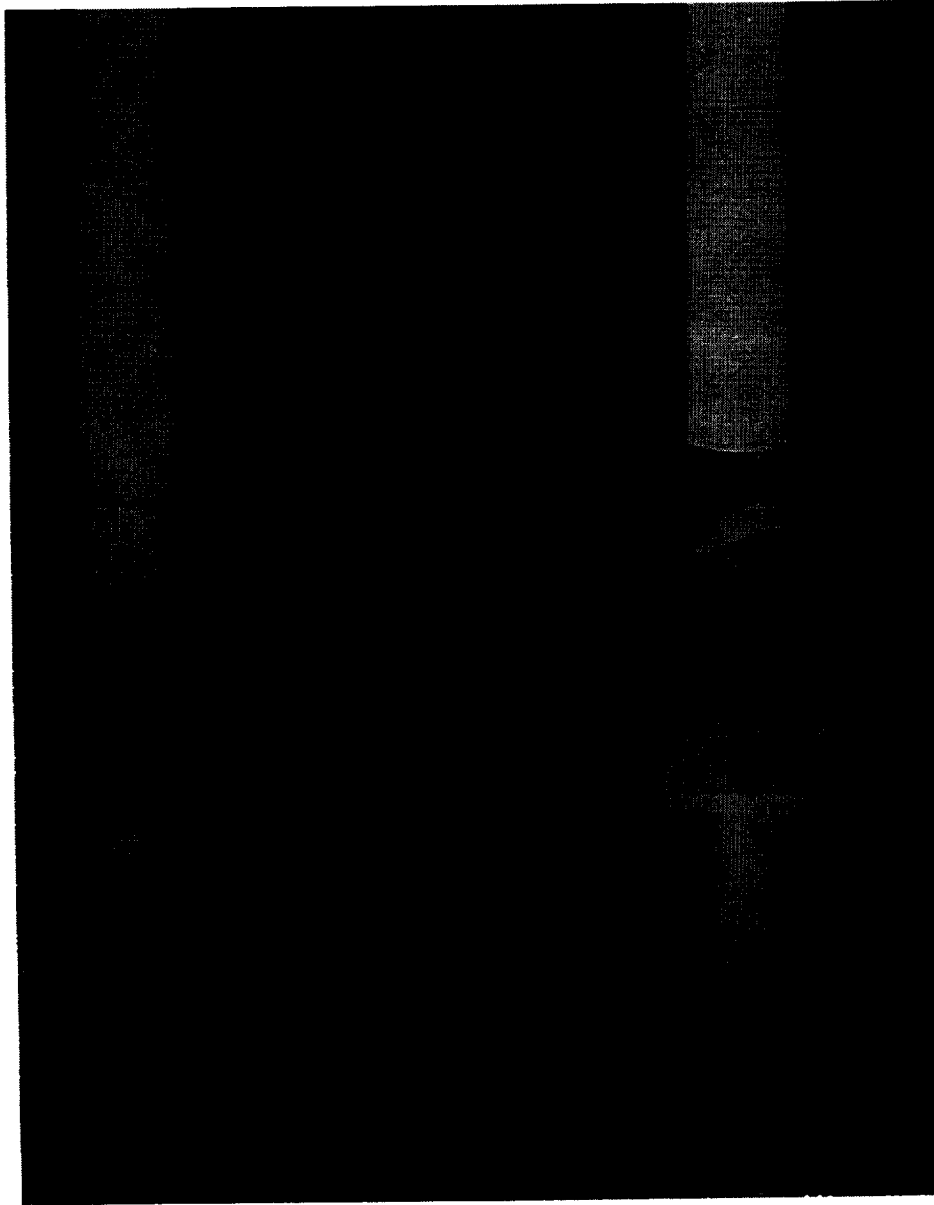


Figure 4-8. Radiographs of flight and ground-truth cartridges showing the last to freeze material.



Figure 4-9. Appearance of ground-truth and flight cartridges after processing.

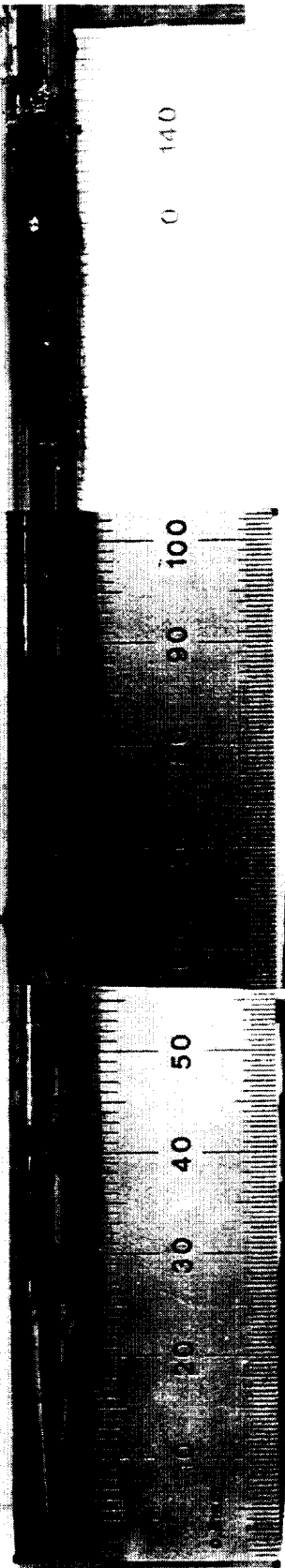


Figure 4-10. AADSF flight sample after removal from ampoule—J7 position

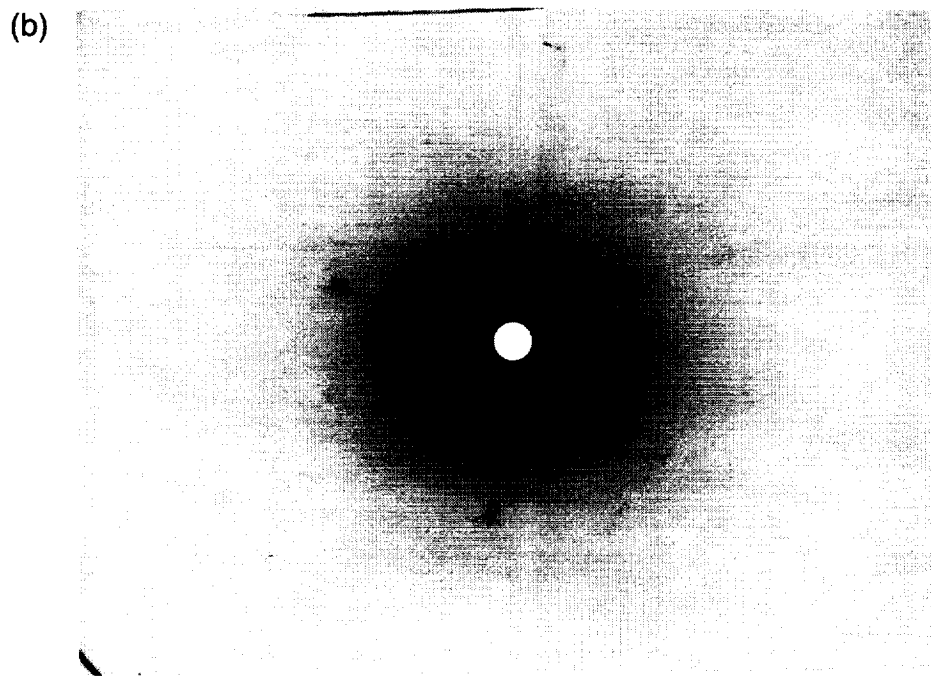
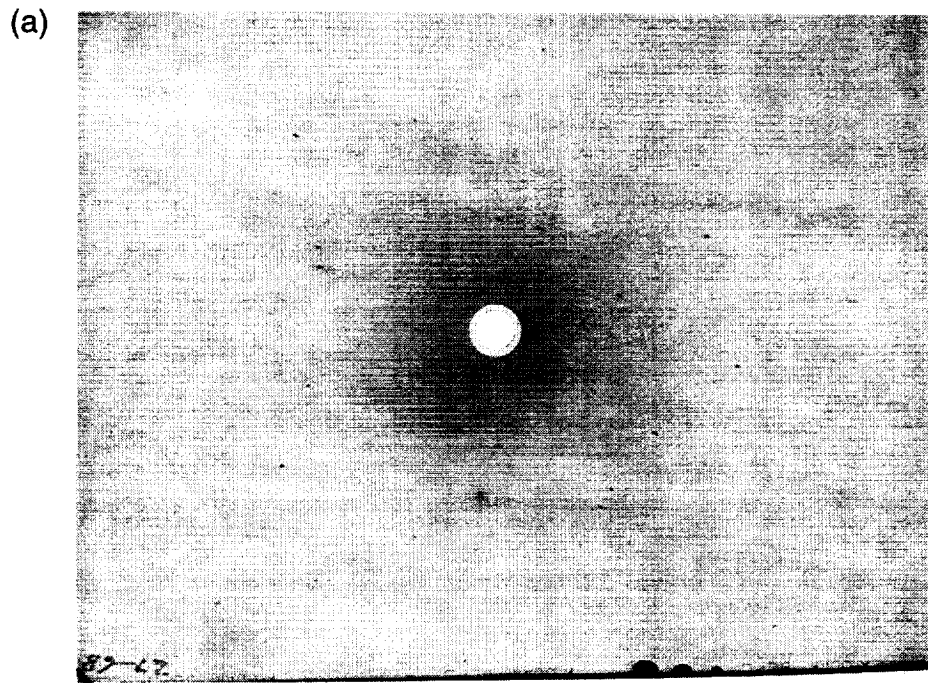


Figure 4-11. (a) Typical Laue back reflection pattern of surface of flight sample. (b) Broad beam back reflection Laue pattern—same region as figure 11a.

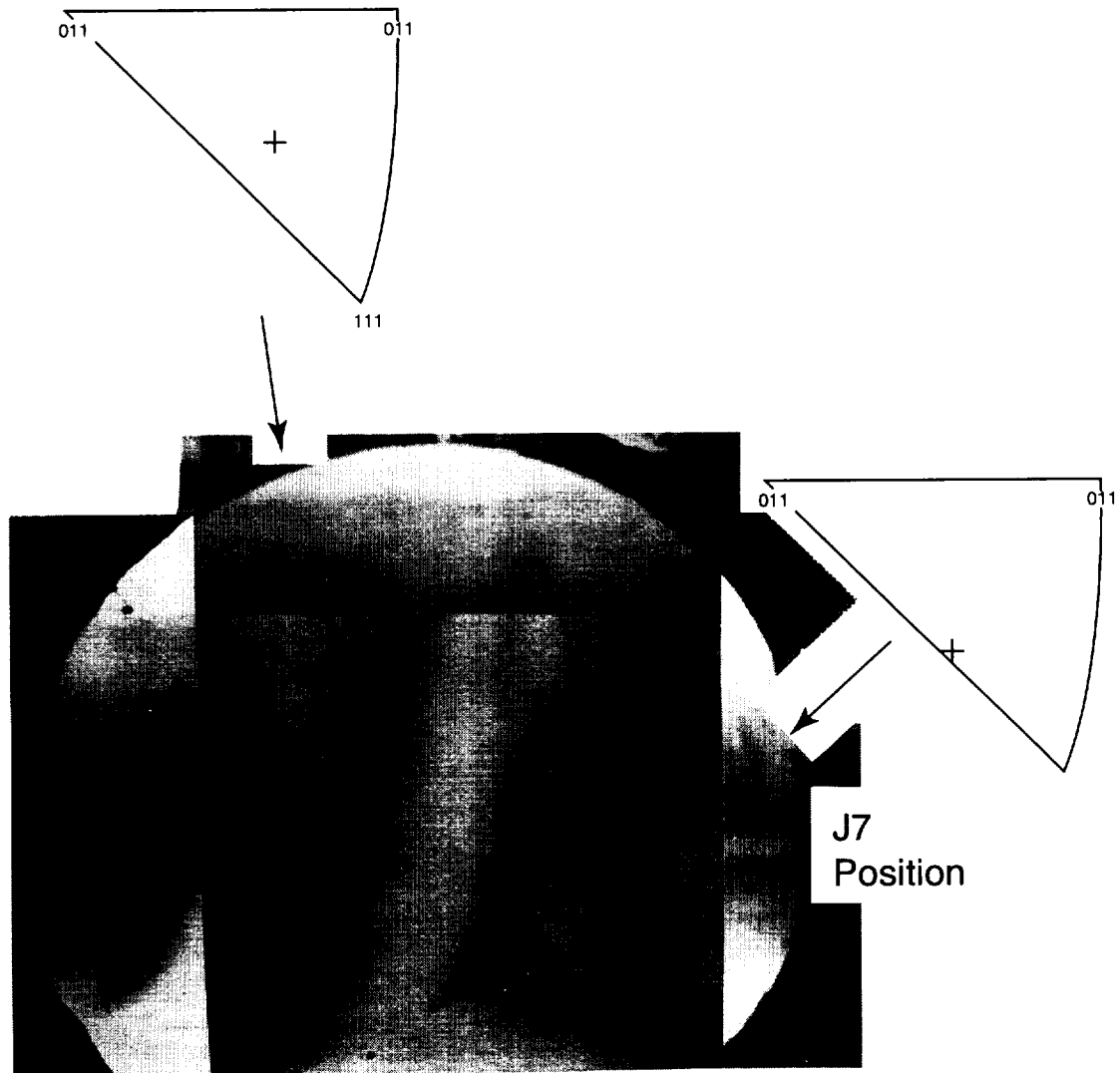


Figure 4-12. Back scattered electron image (SEM) from flight sample—note the channeling pattern.

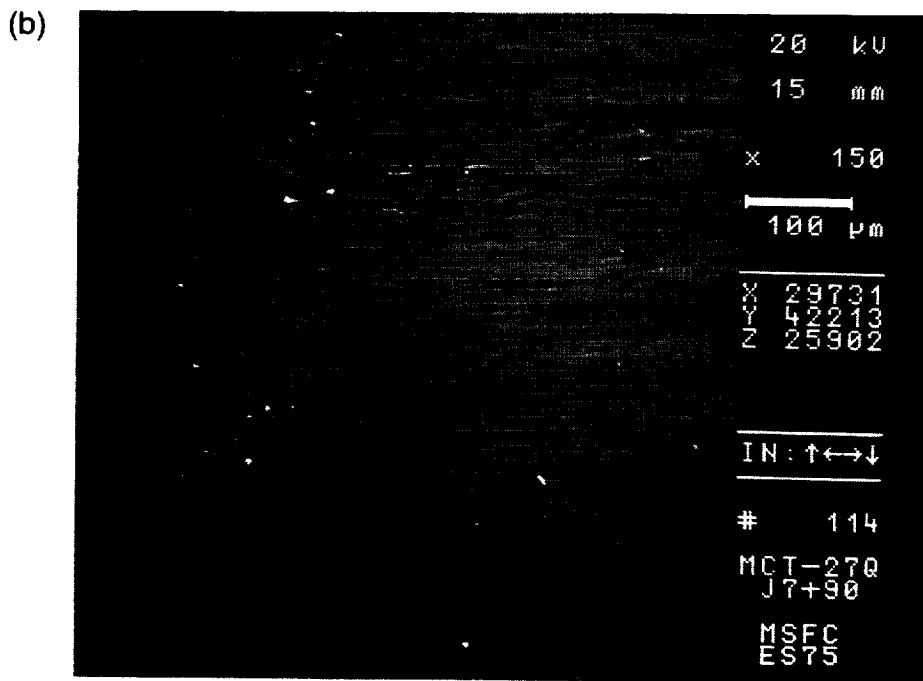
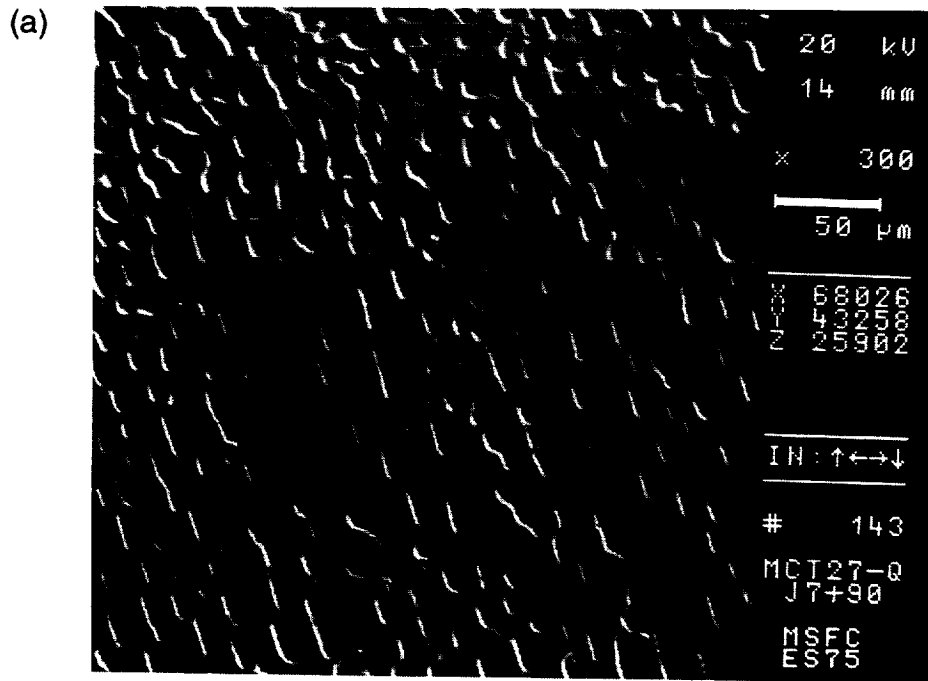


Figure 4-13. (a) Thermal etch pits on surface of flight sample—close to [111]. (b) Thermal etch pits on high index surface.

**Surface of Mercury Cadmium Telluride
Grown on USMP-2**

Top part grown during -ZVV/-XLV
Lower part grown during +ZVV/-XLV



Figure 4-14. Surface of flight sample showing interface breakdown during orbiter maneuver.

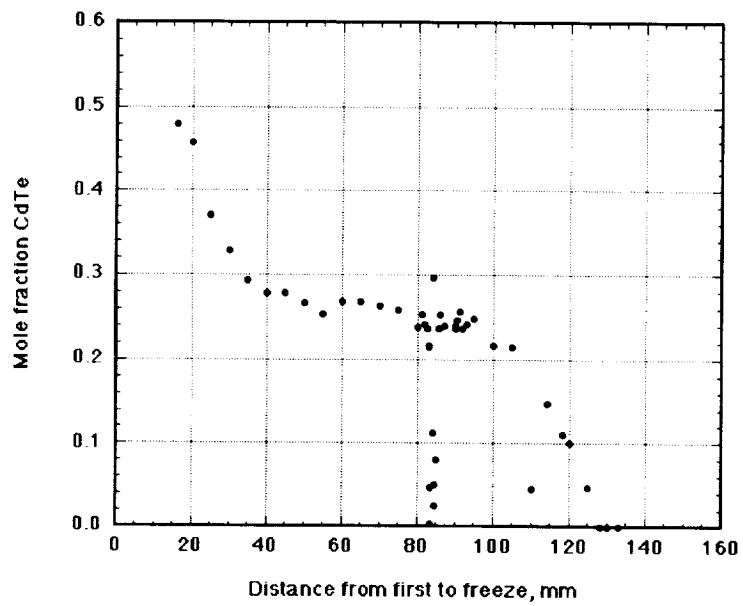


Figure 4-15. Surface composition of ground-truth sample along J7+90° orientation.

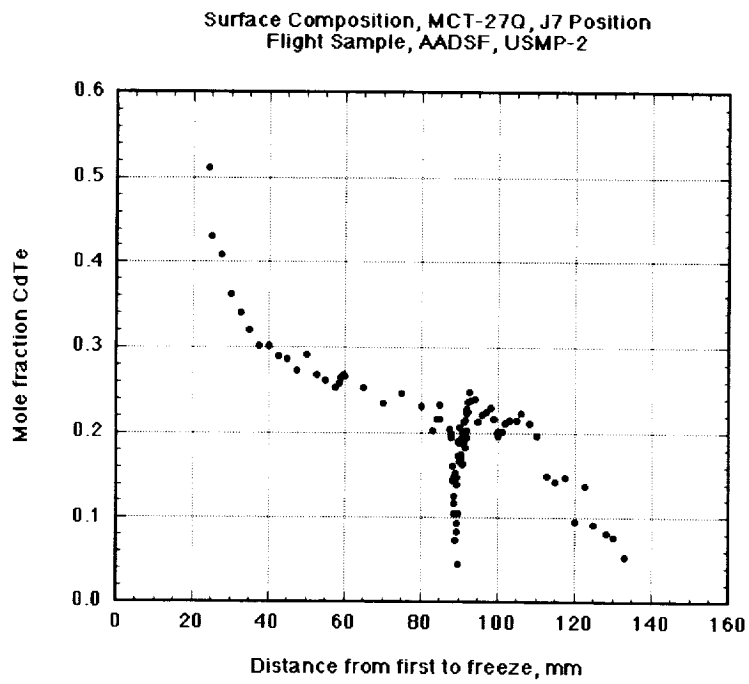


Figure 4-16. Surface composition of flight sample along J7 orientation.

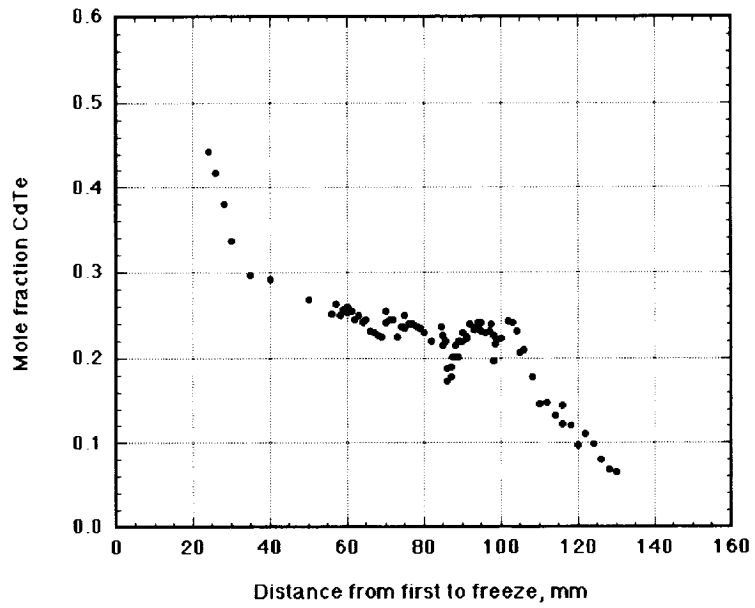


Figure 4-17. Surface composition of flight sample along J7-90° orientation.

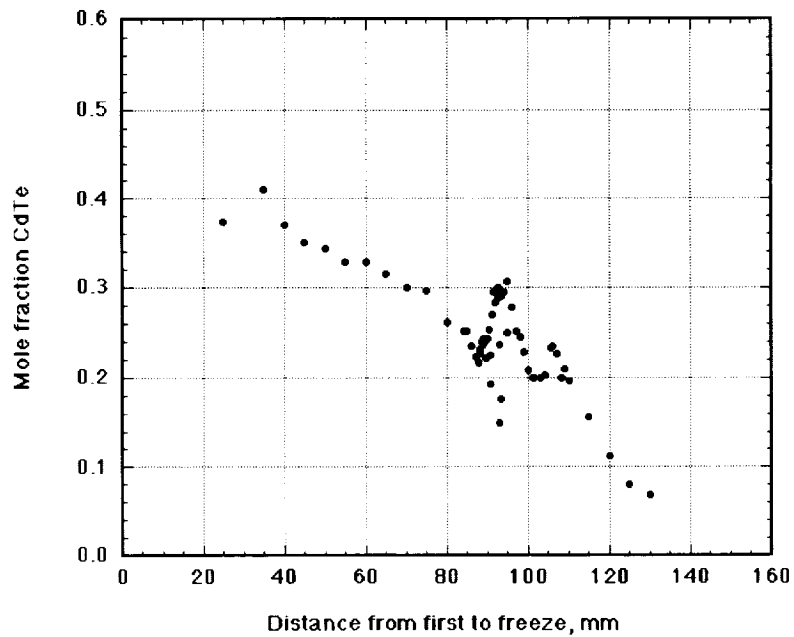


Figure 4-18. Surface composition of flight sample along J7+90° orientation.

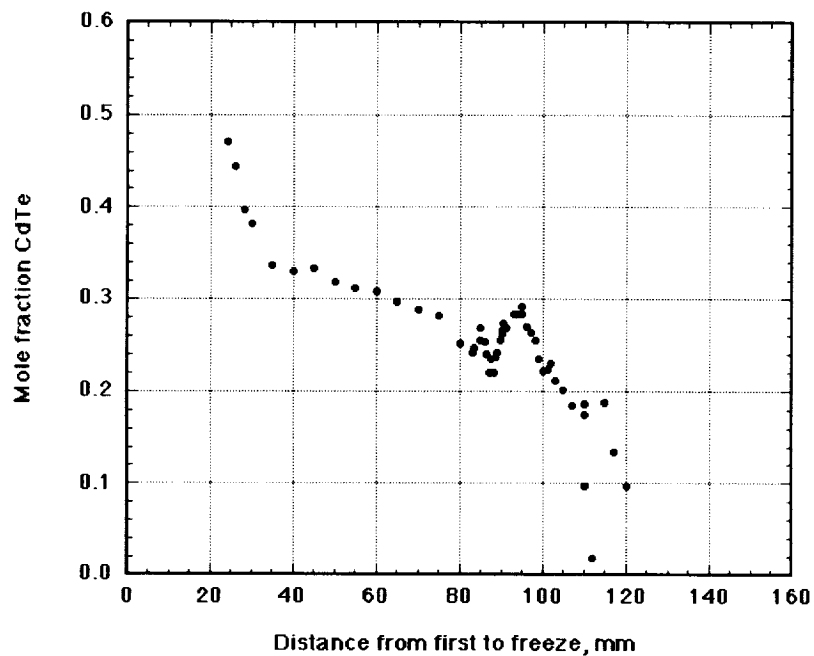


Figure 4-19. Surface composition of flight sample along J7+180° orientation.

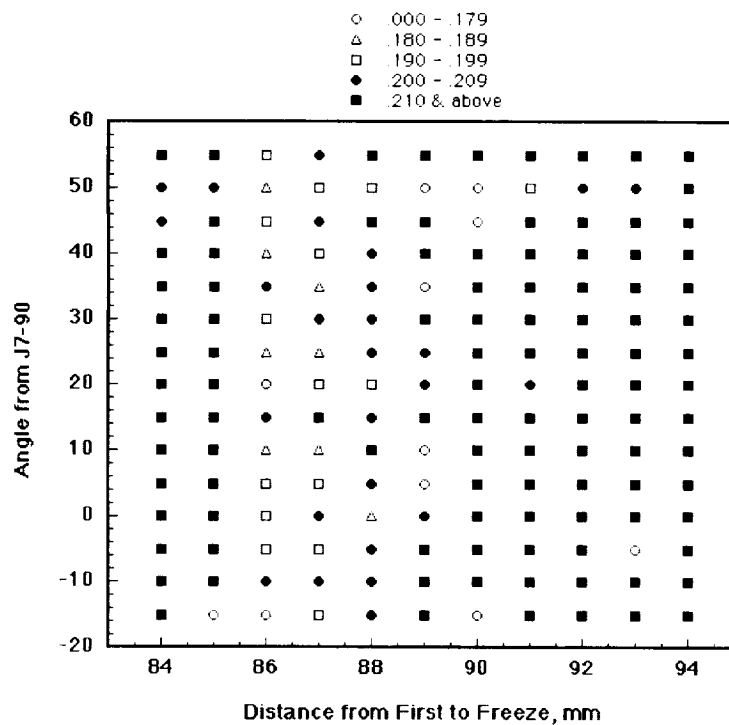


Figure 4-20. Surface composition of flight sample close to J7-90° orientation.

USMP-2 Ground Truth - Rate Change Region

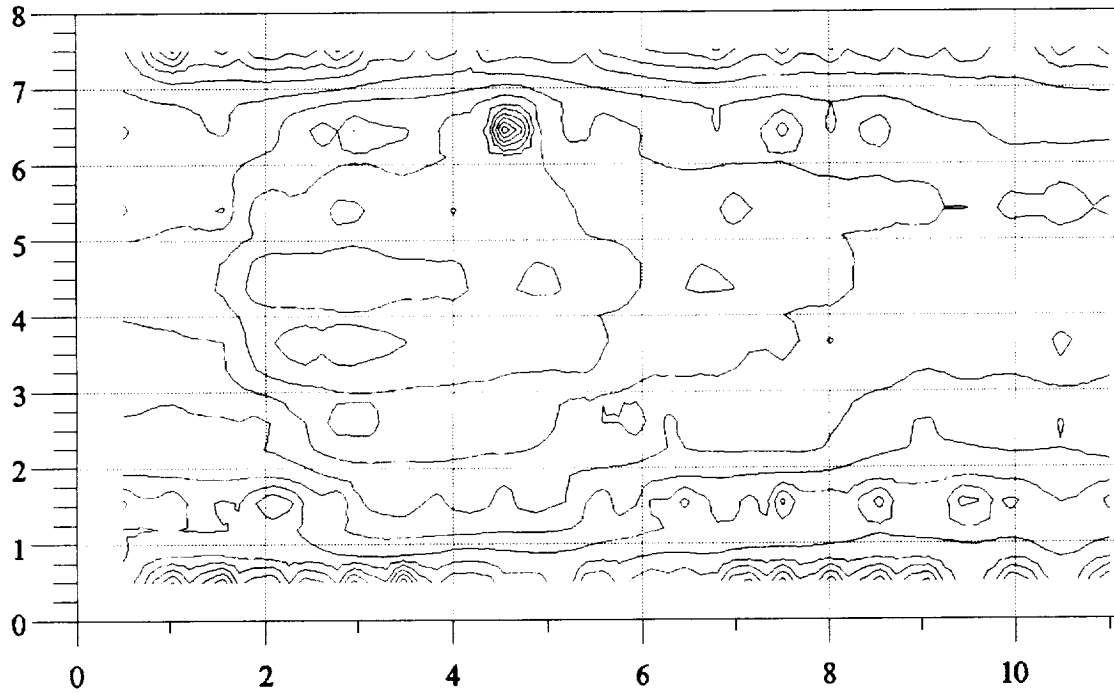


Figure 4-21. Two-dimensional analysis of a slab of the ground-truth sample cut through the rate change region—EDS results.

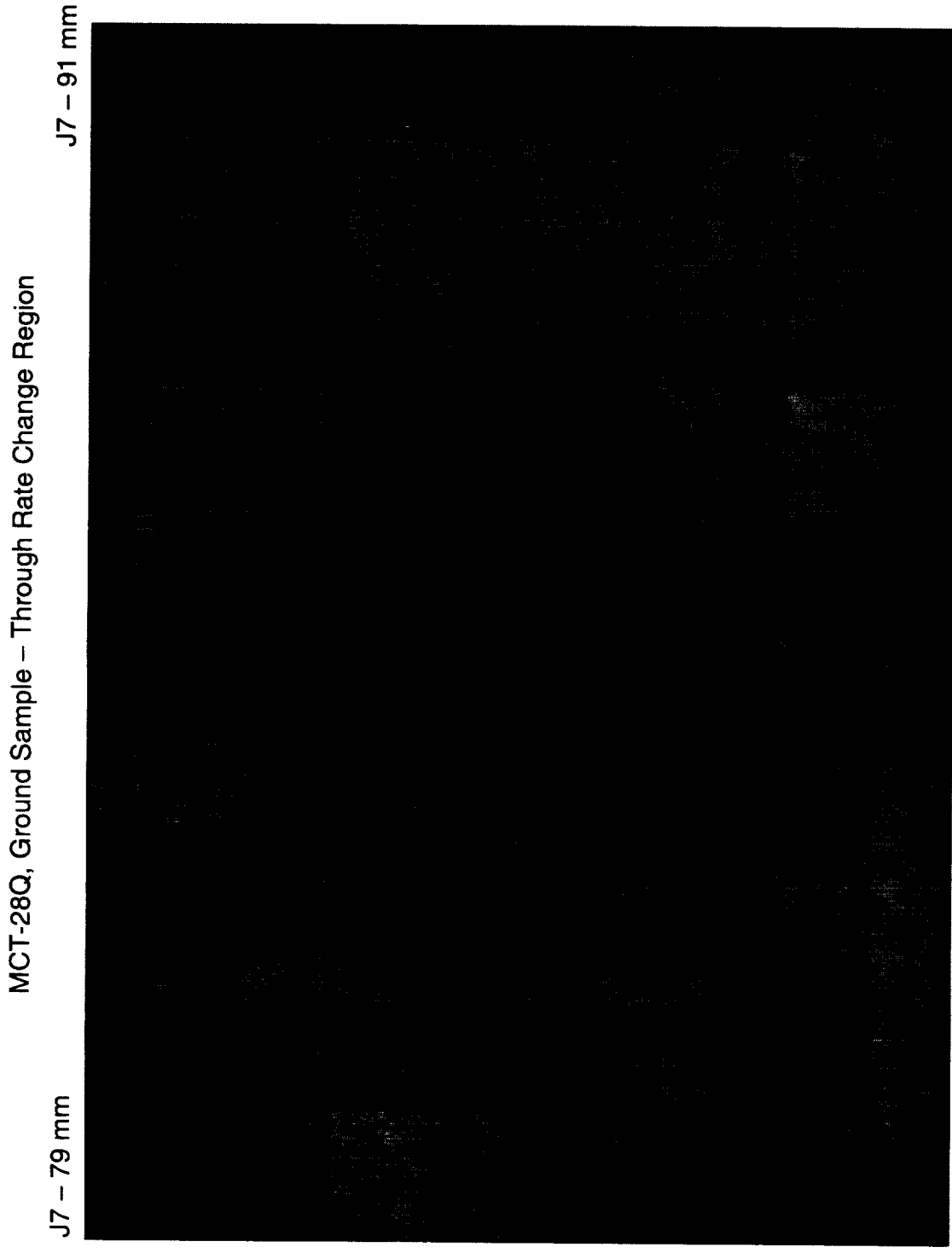


Figure 4-22. Microstructure of the slab shown in figure 21—ground-truth sample etched in Polisar II

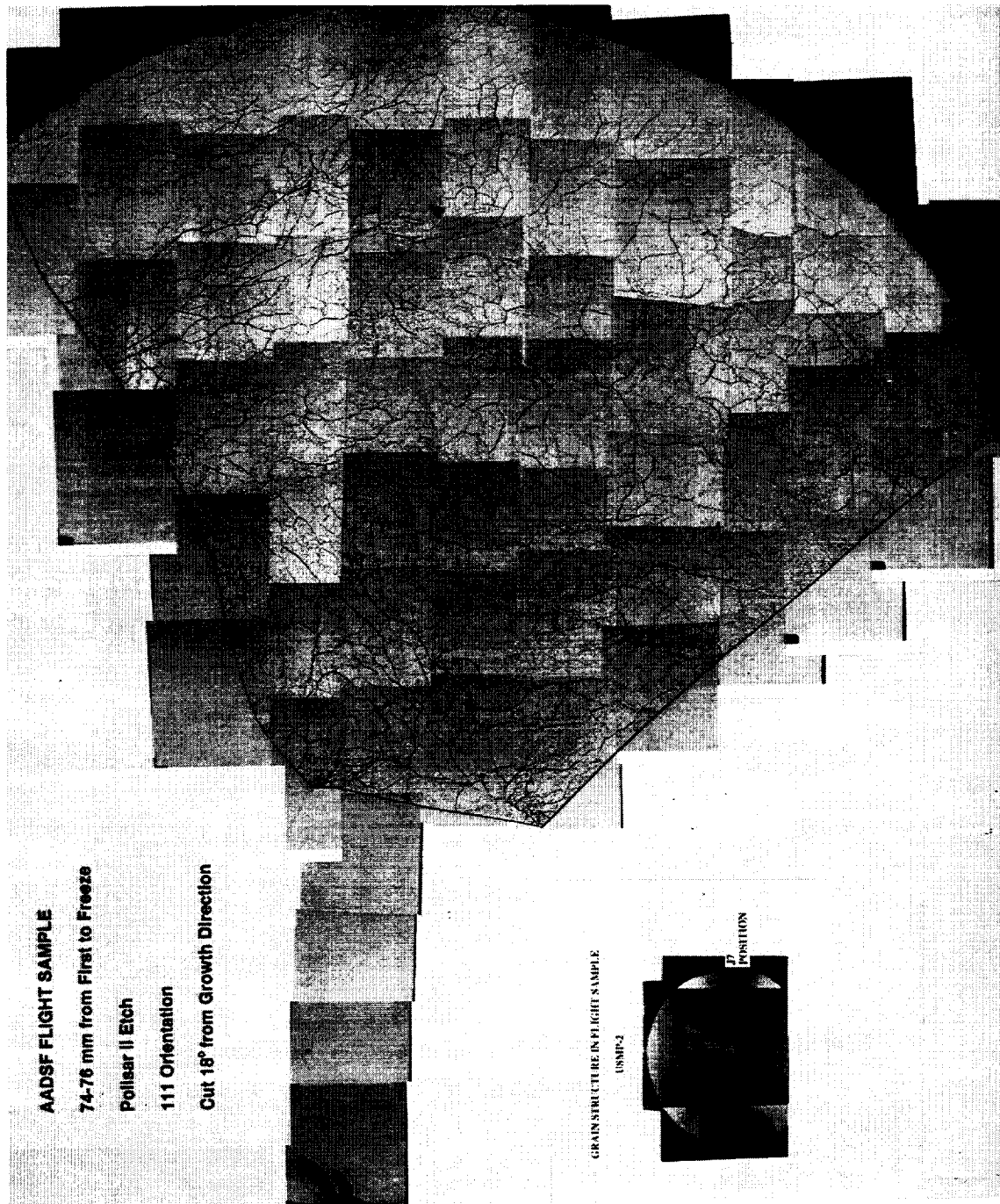


Figure 4-23. Flight sample cut to show major grain in [111] direction—etched in Polisar II.

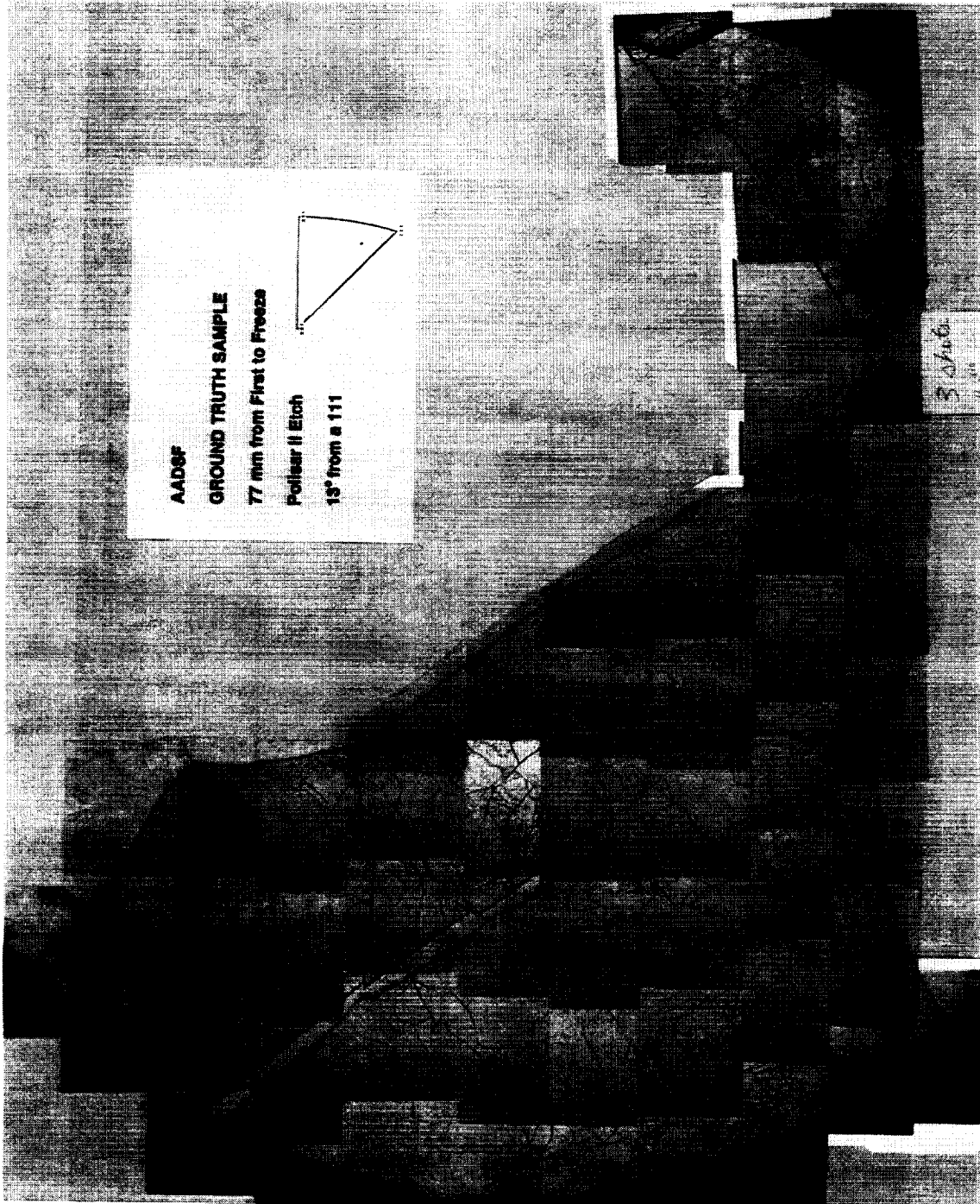


Figure 4-24. Ground-truth sample cut at right angles to growth axis—etched in Polisar II.

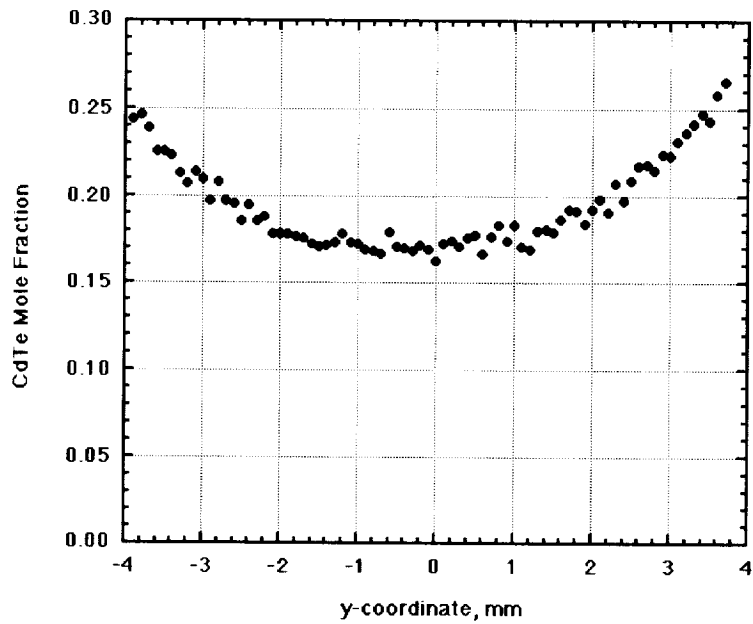


Figure 4-25. Composition across diameter of ground-truth sample—WDS results.

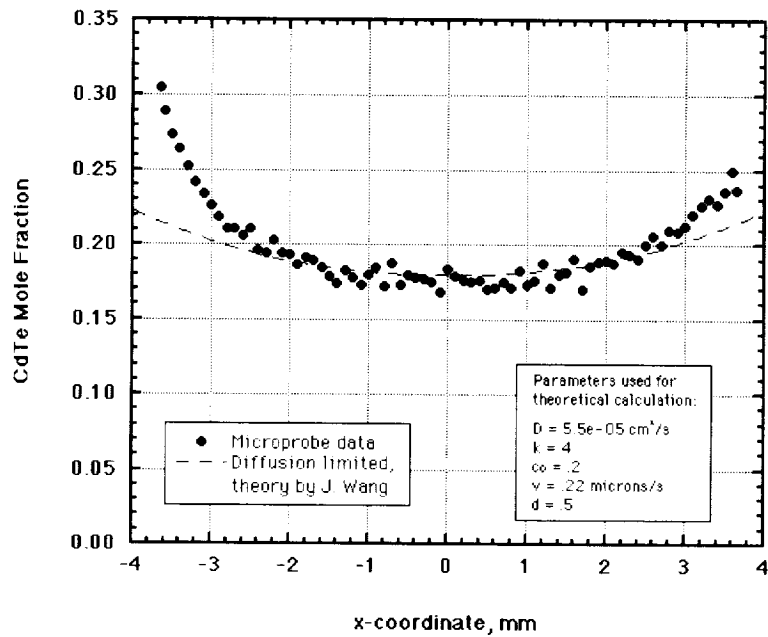


Figure 4-26. Composition across diameter of flight sample with superimposed diffusion profile.

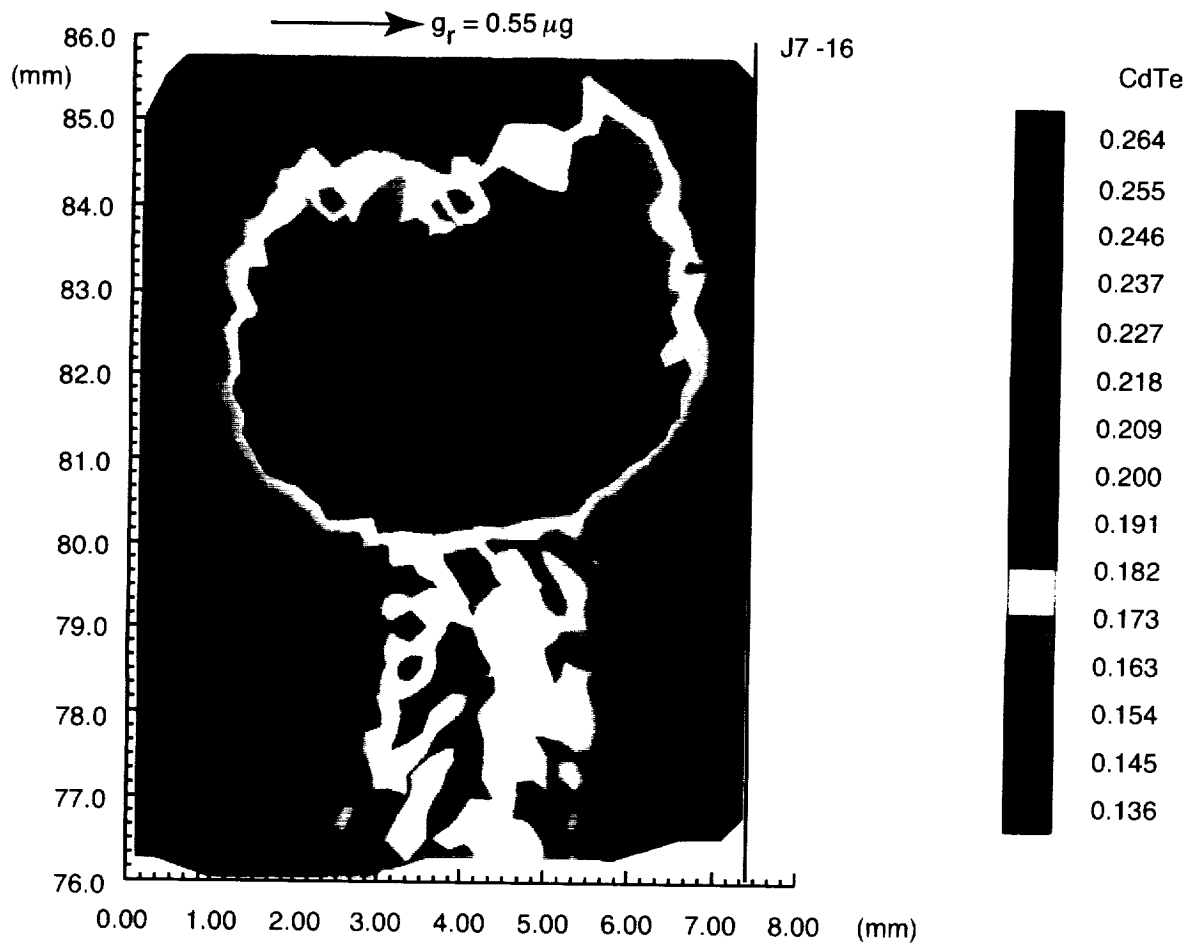


Figure 4-27. Three-dimensional representation of composition of flight sample—
WDS results through rate change

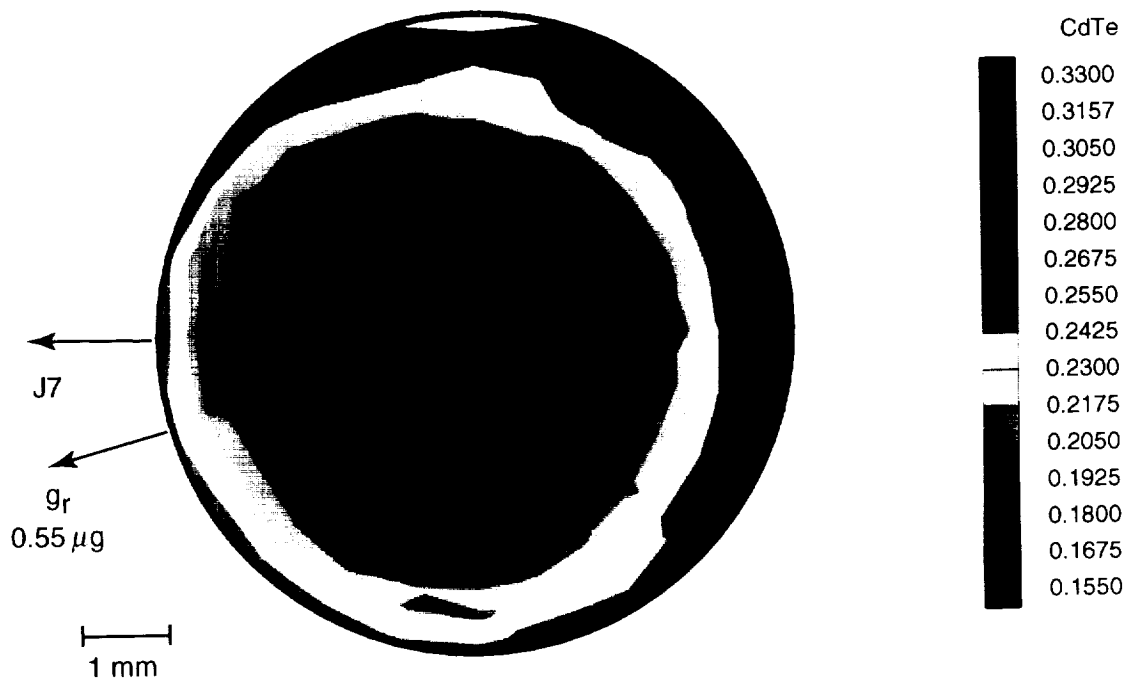


Figure 4-28. Composition map for flight sample in +YVV/-ZLV attitude (62 mm).

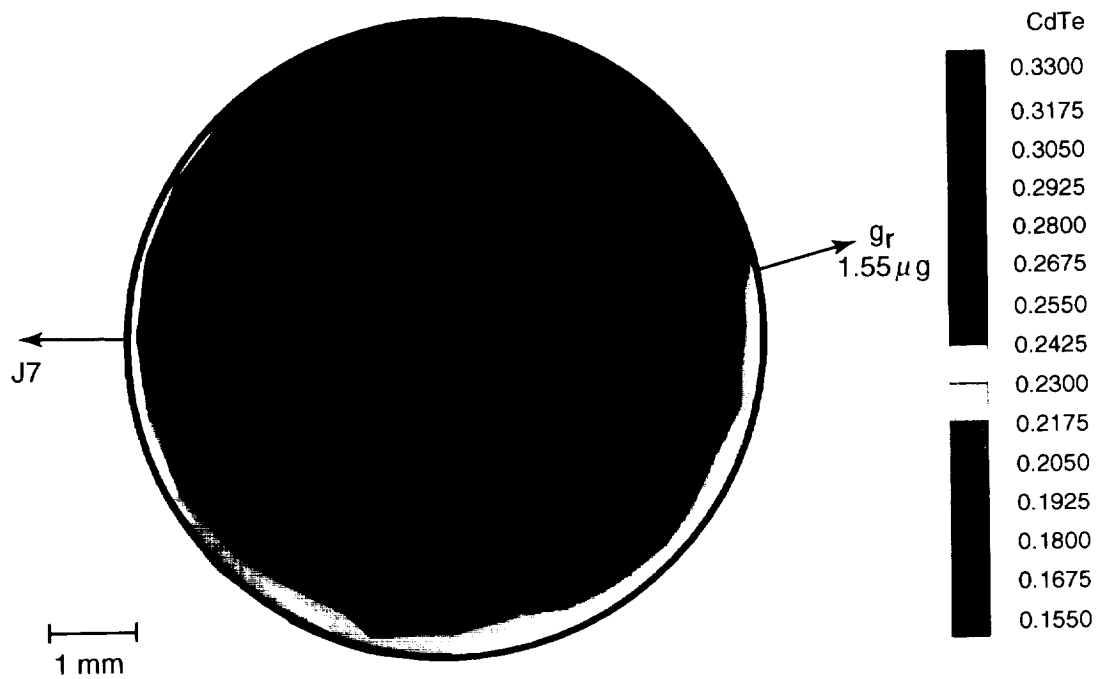


Figure 4-29. Composition map for flight sample in -XLV/-ZVV attitude (106 mm).

Table 4-1. OARE Data Transformed to AADSF Coordinates.

Average Acceleration (micro-g)

ATTITUDE	X-BODY	Y-BODY	Z-BODY
+YVV/-ZLV	+0.53	-0.15	+0.28
-ZVV/XLV	-1.53	-0.28	+0.50
+ZZV/-XLV	-1.42	-0.28	-0.43

Table 4-2. Quality of Surface on Flight Sample.

Surface Position Relative to J7

DISTANCE (CM)	J7	J7+45°	J7+90°	J7+135°	J7+180°	J7 - 135°	J7 - 90°	J7 - 45°
1-9	M	M	M	S	S	S	M	R
9-11	S	S	S	S	S	S	S	S
11-15	S	M	M	R	R	R	S	S

S—Smooth surface, M—Medium smooth surface, R—Rough surface

Table 4-3. Orientation of Flight Sample—Transformed Laue Patterns.

LAUES—AADSF—USMP-2
MCT27Q—FLIGHT SAMPLE

I.D.	Position (mm from first to freeze)	Surface	h k l (direction of crystal growth)		
			h	k	l
27-7	30	J7+90	0.29	0.68	1
27-13	35	J7+90	1	3.45	4.66
27-6	40	J7+90	1	3.45	4.66
27-5	50	J7+90	1	3.45	4.66
27-4	60	J7+90	1	3.45	4.66
27-1	70	J7+90	1	3.45	4.66
27-2	80	J7+90	1	3.45	4.66
27-3	90	J7+90	1	3.45	4.66
27-8	100	J7+90	1	3.45	4.66
27-9	110	J7+90	0.03	1	3.18
27-10	120	J7+90	0.03	1	3.18
27-11	130	J7+90	0.03	1	3.18
27-12	140	J7+90	0.03	1	3.18
27-29	30	J7-180	1	2.68	3.50
27-28	40	J7-180	0.04	1	1.78
27-27	50	J7-180	1	1.57	2.98
27-26	60	J7-180	1	3.46	3.93
27-25	70	J7-180	1	1.57	2.98
27-24	80	J7-180	1	2.68	3.50
27-23	90	J7-180	0	0.56	1
27-22	100	J7-180	0	0.56	1
27-21	110	J7-180	0.05	0.30	1
27-31	32	J7-90	0.04	0.55	1
27-32	42	J7-90	0.43	1	1.05
27-33	52	J7-90	0.31	0.73	1
27-47	55	J7-90	0.19	0.33	1
27-34	62	J7-90	0.05	1	2.81
27-45	65	J7-90	1	1.32	71.13
27-35	72	J7-90	0.14	0.55	1
27-53	73	J7-90	1	5.57	7.32
27-43	75	J7-90	0.34	1	1.01
27-36	82	J7-90	0.32	0.59	1
27-51	90	J7-90	0.12	0.46	1
27-37	90	J7-90	0.12	0.46	1
27-38	100	J7-90	0.97	1	1.44
27-39	110	J7-90	1	1.56	1.75
27-40	120	J7-90	0.46	1	3.80
27-41	130	J7-90	1	7.65	36.5
27-42	140	J7-90	1	7.65	36.5

Table 4-3. Orientation of Flight Sample—Transformed Laue Patterns Continued

LAUES—AADSF—USMP-2
MCT27Q—FLIGHT SAMPLE

I.D.	Position (mm from first to freeze)	Surface	h k l (direction of crystal growth)		
			h	k	l
27-104	30	J7	0.15	0.60	1
27-102	40	J7	0.23	0.59	1
27-100	50	J7	0.08	0.21	1
27-98	55	J7	0.10	1	1.37
27-96	60	J7	1	1.46	8.41
27-94	65	J7	0.41	1	1.40
27-92	70	J7	0.29	0.31	1
27-88	75	J7	1	1	1.93
27.86	80	J7	0.64	1	1.114
27-84	85	J7	0.64	1	1.14
27-82	87	J7	0.64	1	1.14
27-80	89	J7	0.64	1	1.14
27-78	92	J7	1	1.61	1.62
27-76	94	J7	0.58	0.98	1
27-74	96	J7	0.58	0.98	1
27-72	98	J7	0.17	1	1.03
27-71	100	J7	0.17	1	1.03
27-68	110	J7	0.45	1	2.98
27-65	120	J7	1	1.34	4.22
27-63	130	J7	multigrains		
27-61	140	J7	multigrains		

SECTION V.

**HIGHLIGHTS OF THE ZENO RESULTS
FROM THE USMP-2 MISSION**

Acknowledgments

We are grateful for the work of many colleagues who contributed so much to the success of this mission. At the University of Maryland: John Borden, David Torrealba, Dan Swann, Mark Sienkiewicz, Paul Mahata, Lori Mora, Matt Bieneman, Meade Larson, John Pickett, Kai-Chang Zhang, Ed Cole, and Jan Sengers. At Lewis Research Center: Richard Lauver, Andrew Peddie, Greg Zimmerli, Geoff Elliott, and Klaus Gumperto. At Ball Aerospace: Richard Reinker, Mike Dials, Robert Stack, and Robert Woodruff. At the National Institute of Standards and Technology: Svetlana Avramov, Nile Oldham, M.R. Moldover, and Robert Berg.

SECTION V. HIGHLIGHTS OF THE ZENO RESULTS FROM THE USMP-2 MISSION

**Robert W. Gammon, J. N. Shaumeyer, Matthew E. Briggs, Hacène Boukari,
and David A. Gent**

Institute for Physical Science and Technology,
University of Maryland, College Park, Maryland 20740

R. Allen Wilkinson

NASA Lewis Research Center, Cleveland, Ohio 44135

5.1. INTRODUCTION

When a pure fluid is near its liquid-vapor critical point the otherwise small, statistical fluctuations in its density become very large, as large as the wavelength of light when the system is still only 10 mK from the critical temperature, T_c . These large fluctuations scatter light very strongly and the previously clear fluid turns milky white, a phenomenon known as critical opalescence.

Indeed, many different systems have critical points, and large fluctuations of some thermodynamic parameter are a universal feature. Because critical fluctuations become macroscopic in size and involve enormous numbers of molecules, many features of critical-point behavior are controlled by the statistical behavior of the fluctuations, so that many types of systems exhibit the same behavior near the critical point.

Light scattering from critical fluctuations in a fluid is a simple and accurate technique to measure one fundamental property of the fluctuations: Their decay rates (the inverse of their lifetimes). However, near the critical point, the fluid becomes highly compressible, so that just the weight of the fluid itself causes severe density gradients in the sample, distorting these measurements in a terrestrial laboratory.

The goal of the Zeno experiment was to build a precision, light-scattering spectrometer to measure the fundamental fluctuation decay rates in a sample of xenon, which would operate in the low-gravity environment of the space shuttle, thus removing the gravity-induced distortion of the measurements. The instrument performed beautifully on its first mission, and we were able to make our projected measurements with 1 percent precision to within 100 μ K of the critical temperature (16.7 °C).

The light-scattering spectrometer is shown schematically in figure 1. Light from the low-power, helium-neon laser was directed into the sample along one of two beam paths determined by the beamsplitter B1; the path was chosen by shutters (not shown). Light scattered by the sample (located in the cylindrical thermostat at the center of the figure) was then collected by the apertured photomultiplier tubes (PMT1 and PMT2), the primary signal which was processed to obtain the decay rate information. In addition, photodiodes (PD1 and PD2) placed behind partially reflecting mirrors (M2 and M3) measured the intensity of the light entering and exiting the sample. These two signals were then ratioed electronically to give us information about the turbidity of the fluid, itself an important measurement and our primary method of locating the critical temperature of the sample.

The collection angles for the scattered light (determined by apertures A1, A2, A3, and A4) were precisely aligned so that the two scattering angles were supplements. This accomplished two things: It simplified data analysis, and it allowed us to measure decay rates at the same pair of widely-spaced angles regardless of the beam path through the sample.

The instrument was housed in two separate containers attached to the USMP carrier. The optics module contained the light-scattering spectrometer, built on a stiff, optical bench, in addition to temperature-sensitive signal amplifiers and ratio transformers for the thermostat's temperature control and measurement system. All additional electronics, including the instrument's computer system, were housed in the Electronics Module.

5.2. TIMELINE

The instrument operated continuously for 13 days and 17 hours, probably a record. Figure 2 shows the timeline of the experiment as the temperature of the sample (in distance from T_c) versus mission elapsed time (MET). The principle events are delineated by times where the sample was warmed to T_c+1 K in order to bring it back to a state of uniform density, and times where the sample was closer than 1 μ K to T_c .

During MET day 0 the instrument was primarily in a warm-up and initialization phase. Then, just prior to the start of MET Day 1 the sample was warmed to 1 K, and the first scan to locate T_c began. The scan was followed by two warming periods. The slow cooling that spans MET days 2 and 3 represents a zig-zag search for T_c which extended into MET day 4, followed by another warming procedure.

The first period of data collection began midway through MET day 4. Decay rate measurements were collected at a geometrically spaced set of temperatures progressively nearer T_c , the first one starting at 100 mK. The last measurements of this set, during MET day 7, were at temperatures within 100 μ K of T_c , and actually contained some measurements at temperatures just below T_c .

MET Day 8 began with another warming cycle, followed by another period of data collection at various temperatures between 560 mK and 30 μ K above T_c . Between MET days 9 and 12 we took some additional measurements at temperatures further from T_c , as well as repeating selected measurements from earlier in the mission. Near the beginning of MET day 11 we began a series of 100 μ K cooling steps which would again take the sample below T_c , recording decay rate measurements during the process with the hope of getting measurements which would show the effects of crossing the critical point into the two-phase region at temperatures at which it is impossible to make measurements on Earth.

5.3. INSTRUMENT PERFORMANCE

5.3.1. Thermostat and Thermometry

The thermostat was a small device, 23-cm long and 8 cm in diameter, which provided a stable, controlled thermal environment for the xenon sample cell. It was made of three coaxial, cylindrical shells, each with a heater and feedback temperature controller. In addition, each shell and the sample cell had separate temperature-monitoring devices. Thermometry was provided by thermistors inside the thermostat and sample-cell walls, wired to standard resistors inside the thermostat to form one arm of an alternating current resistance bridge. The other part of the bridge was made up of ratio transformers. In all there were

three control bridges and one, multiplexed measurement bridge. There were three 6-decade ratio transformers and one 8-decade transformer, all calibrated through a collaboration with workers at the National Institute of Standards and Technology [see bibliography: dissertation of S. Avramov; papers of S. Avramov and N. Oldham].

In flight, the thermostat required a stable thermal environment to do its job: The temperature control of the optics module by radiative heat leak and control heaters was excellent. Because of the length of the mission and the long periods of constant shuttle attitude, we were able to maximize the temperature control. Thus, the thermostat was able to achieve a routine control level of better than $\pm 3 \mu\text{K}$ rms noise for periods of 3 hours or longer. Figure 3 shows one period of 4 hours when the sample-cell temperature was controlled to $10 \mu\text{K}$ peak-to-peak (with a 5-second time constant in the measurement) and $1.7 \mu\text{K}$ rms. This level of control easily met the requirements for the Zeno experiment.

To change the temperature of the sample, the set points of all three control shells of the thermostat were moved. Figure 4 shows an example of a simple temperature change (cooling) of 2 mK; the temperature of the sample cell follows with a time constant of about 30 minutes.

For smaller temperature changes, we were able to make “fast steps” where the set points of the control shells were temporarily moved well beyond the target temperature and then returned just as the sample cell reached the desired temperature. Figure 5 illustrates the fast change, which is finished in a matter of minutes.

5.3.2. The Light-Scattering Spectrometer

Scattered light was detected by a pair of ruggedized, EMI 9863 photomultiplier tubes. These tubes had better than 5 percent quantum efficiency at 633 nm, total afterpulsing of less than 0.06 percent, and dark counts of less than 1 s^{-1} at the operating temperature of the optics module of 9°C . The background photon count rates were low enough that we could easily see the 20 counts/second from increased radiation when the shuttle passed through the South Atlantic Anomaly.

The photomultiplier tubes were operated in photon-counting mode and the two signals were passed to the dual inputs of an ALV-5000 digital correlator, adapted specifically for this instrument. With this correlator we were able to make simultaneous measurements of forward-scattered and backscattered light. The correlator is a special-purpose, digital signal processor, which produces an accurate autocorrelation function of the stream of photocounts from the photomultipliers. This correlator is designed to cover a broad range in delay times by calculating the autocorrelation function on a geometrically expanding time scale so it is natural to plot the resulting correlograms with a logarithmic time scale. Figure 6 shows a sample correlogram; note that this shape represents an exponential decay of the autocorrelation function.

The experiment was performed with very low light levels. The windows of the sample cell absorb small amounts of the incident light at their surface (measured to be about 2 ppm). Because the thermal expansion coefficient of the sample diverges at the critical point, the increase in temperature of the window surface due to absorbed light can lead to unwelcome perturbations in the density of the fluid, and measurements would no longer represent the behavior of the fluid at the temperature we measured for the bulk [see bibliography: dissertation of M.E. Briggs].

To avoid these problems, we reduced the power of the laser light by placing filters in the beam paths, selecting two different power levels that allowed us to cover two temperature ranges with density perturbations of less than 1 percent. A power level of $17 \mu\text{W}$ was used between 1 K and 1 mK from T_c , and the lower level of $1.7 \mu\text{W}$ was used at temperatures closer than 1 mK, with overlapping

measurements made with both powers near 1 mK. With this combination of incident light powers we were able to cover a wide range of temperature with enough signal to reach our precision requirement of 1 percent in the decay-rate measurements within the length of the mission.

5.4. DETERMINING T_c ON ORBIT

Since all of the measurements in the Zeno experiment are made relative to the critical temperature of the xenon sample, it was important to understanding the results that we locate T_c precisely using our experimental thermometry. The possibility that the thermometry would be sensitive to the harsh mechanical environment of a shuttle launch meant that locating T_c on orbit was a significant part of our mission activities.

In general, locating T_c involved moving the sample to a region very near the critical temperature and then adjusting its temperature in a controlled way and watching for signs that the critical point has been crossed. The signal which we monitored during the searches measured the turbidity of the sample, given by the logarithm of the ratio of the intensity of the light transmitted by the sample to the intensity of the incident beam. We attempted two techniques with different expected levels of precision; one worked, and one did not.

The zig-zag technique, which we used to try to increase our level of precision for the value of T_c and did not work successfully, is a technique that we had previously used to locate the critical-mixing temperature of density-matched mixture of two fluids. In a density-matched critical mixture gravity has little effect and the technique gave clear indications, with 10 μK precision, whenever T_c was crossed. However, we were not able to try the technique with a pure-fluid system on Earth because the dynamics of density stratification were too rapid. Our single zig-zag search on orbit was the first time that this technique had been tried in a pure fluid.

The zig-zag search started only 200 μK above the critical temperature. Figure 7 shows the manner in which the temperature of the sample changed, alternately cooling by 20 μK and then warming by 10 μK ; Figure 8 shows the response of the turbidity signal during the same portion of the search. Although it is clear that the sample is responding to the changes in temperature, we never detected a clear hysteresis in the turbidity which we expected to indicate that we had crossed T_c . We believe now that several unexpected effects in the turbidity signal (see the next section) combined to obscure the transition. The entire period of the zig-zag search is shown in figure 9. At some point just past MET day 3, hour 12, the sample first crossed T_c and began the early stages of spinodal decomposition, indicated by the increasing amplitude of the variations in the signal. However, we will not be able to extract more precise information until we understand all of the effects in the turbidity response better.

Our second technique for locating T_c , which was successful, is a simple scanning procedure. The set point of the thermostat's control shells was changed in small steps of 50 μK every 6 minutes (figure 10), which caused the temperature of the sample to change at a uniform rate of 500 $\mu\text{K}/\text{hour}$ (figure 11).

During the scan we monitored two signals as the sample crossed T_c : The turbidity of the sample, and the photon count rates of the light scattered by the sample. Figure 12 shows the turbidity signal during the first of the three scans done during the mission. Between hour 4 and hour 6 the signal increased steadily as the critical temperature was approached. At a few minutes past hour 6 there was a small break in the increase, followed by a swift rise, then decline, in the signal. The break marked the sample's crossing T_c ; the large peak was caused by the sudden increase in density fluctuations as the fluid

began spinodal decomposition, the initial stages of phase separation in which the fluctuations first become unstable and begin to grow in size. This increase passed as the fluid began to resolve itself into distinct gas and liquid phases, and the turbidity signal dropped.

That this rather unassuming feature in the turbidity signal marked the phase boundary was confirmed by the intensity of the forward-scattered light, shown over the same time period in figure 13. The light scattered at this angle increased as the critical point was approached, and then dropped as fluctuations at this wavelength lost stability and the fluid began phase separation. The position of the peak in the scattering-intensity curve matched that of the feature in the turbidity curve.

For comparison, figure 14 shows a scan done on the instrument during preflight testing on the ground, at the same rate as the one in figure 12. There are two notable differences in the curves, both related to the effects of gravity. In the second hour of the terrestrial scan the turbidity appeared to be decreasing rather than increasing steadily. This was caused by the slowly forming density gradient in the highly compressible sample: As the gradient became more severe, the amount of fluid near enough to its critical density to show increasing turbidity decreased, and the net effect was a decrease in the turbidity signal. In addition, the small feature immediately preceding the phase-decomposition peak that marked the phase transition is not even visible. At this level of resolution, gravity had broadened the critical point to such an extent that it effectively disappears from the turbidity response.

During the mission the collection of three scans and the zig-zag T_c determinations seemed to show a drift in the critical temperature of $800 \mu\text{K}$, substantially larger than we had seen during all testing with this instrument and with the functionally identical engineering model. However, we now believe that this may have been caused by small density rarifications in the beam path that resulted from repeated crossings into the two-phase region that were not completely removed by the warming procedures which we used to rehomogenize the sample. Subsequent ground scans with the instrument, along with the first on-orbit scan and previous ground measurements now tell us unambiguously that the critical temperature of the sample had indeed been stable during the mission to within the precision of our measurement of $\pm 50 \mu\text{K}$. This gives an upper boundary of $120 \mu\text{K}/\text{year}$ on the stability of this sample, a drift rate spectacularly better than any previously experienced.

5.5. TURBIDITY MEASUREMENTS AND RELATED EFFECTS

Turbidity is the natural logarithm of the sample transmission, per unit length, and is a measure of the overall cloudiness of the sample. We measured the intensity of the light leaving the sample and ratioed that with the intensity of the light entering the sample; special electronics then calculated the logarithm of this ratio, giving us a measurement proportional to the turbidity of the xenon sample.

The turbidity of a fluid increases as the fluid is taken nearer to its critical point; measuring the turbidity gives information about the average size (the correlation length) of critical fluctuations. The turbidity measurements which we made during the mission have proved to be the biggest challenge to our understanding of the flight data. During the mission the turbidity signal showed small, long-time drifts at constant temperatures, sometimes to smaller values, sometimes to larger values. We believe that this was related to the small density inhomogeneities which we conjecture caused the apparent drifts in T_c . However, the analysis of these data are far from complete at this point.

Extracting values which actually represent the turbidity of the sample is complicated by two known effects which make difficult a direct, simple turbidity measurement. We have modeled these effects extensively and we now have a better understanding of their contribution. The first has to do with the

optical properties of the sample cell itself; the second is a manifestation of the thermal response of a fluid near its critical point.

The interior of the sample cell created a 100- μm thick disk of xenon, the portion of the sample through which the laser beam passed, by bounding the region with two polished, parallel, fused-quartz windows. Reflections of the beam from the window surfaces can interfere, changing the intensity of the transmitted beam depending on the spacing of the windows. When the temperature of the sample cell was changed, thermal expansion or contraction of its components altered the window spacing and produced a measurable change in the turbidity signal, independent of the turbidity of the xenon itself.

Figure 15 shows the turbidity signal responding to 100 mK steps in the temperature of the sample cell, which warmed the cell from 1 to 5 K above the critical temperature of the xenon; this curve is from preflight testing of the instrument. At these temperatures the actual turbidity of the fluid is negligible and we are viewing the interferometric behavior of the sample cell only.

The large, sinusoidal variations in the curve were the result of the interference effect, showing that the separation of the windows changed by about 0.75 orders of interference per Kelvin, at approximately 400 orders of interference. This corresponded to a change in the window separation of 0.28 $\mu\text{m}/\text{K}$, a rather small effect. Nevertheless, it is clear from the magnitude of the change in figure 15 that in order to make good use of our turbidity measurements it is vital that we know where on this interference curve the measurements were made.

We were able to fit curves like this one with ample precision to make the necessary correction to the turbidity measurements. Important questions about how this characteristic of the instrument changes with time are now settled as well. We have found, from analysis of testing both before and after the mission, that the amplitude of this curve was stable and predictable. However, the phase of the interference showed a drift with time which suggests that the sample cell exhibits a small mechanical creep of its longitudinal spacing of about 10 nm/month. With this information we can be confident that we have placed the flight measurements at the appropriate place on the interference curve.

There is a second feature evident in figure 15 that is related to the fluid behavior itself. With each temperature step the turbidity signal, rather than simply moving to a new value appropriate to that temperature, overshoot and then returned to the expected value; all of these temperature steps were of the fast-change variety. Although the fluid at these temperatures showed no critical enhancement to its turbidity, it was still near enough to the critical point that it was highly compressible. We have shown in previous work [see bibliography: papers of H. Boukari, J.N. Shaumeyer, M.E. Bridges, and R.W. Gammon; H. Bourkari, M.E. Briggs, J.N. Shaumeyer, and R.W. Gammon; dissertation of H. Boukari] that highly-compressible critical fluids can make very fast changes in their density via an adiabatic heat-transfer mechanism; this phenomenon is a manifestation of the adiabatic mechanism.

As the temperature change began, heat entered the outer walls of the sample cell and quickly caused a large thermal expansion of a thin layer (order 10 μm) of fluid near the wall. As a result, because of high compressibility, the bulk of the fluid was subject to adiabatic compression, which caused the bulk to heat rapidly. Significantly, the density of the bulk had changed, changing its index of refraction, hence the optical path length of the laser beam passing through that part of the sample. Thus, during the temperature change itself, the fluid in the optical path of the cell executed density changes which affected the interference characteristics of the cell. Note that this transient response depends on the temperature of the fluid and decreased as the sample was moved further from T_c .

We have been modeling this phenomenon extensively, as well as performing controlled experiments with our engineering model of the instrument. These analyses have now converged in a satisfying way.

Figure 16 demonstrates the adiabatic effect, using data from the engineering model. The sample cell was subjected to a fast change of 100 mK, far enough from T_c that the actual turbidity of the xenon is negligible. Recorded in the lower curve is the response in the measured turbidity signal showing the overshoot and then return to its final, equilibrium value. It is significant that the final value is reached at precisely the same time as the temperature change is completed.

The upper curve in figure 16 shows data from our calibration of the apparent change in turbidity, represented as a change in phase along the interference curve, due solely to the interference effects of cell expansion. The difference between these two curves, shown in figure 17, shows the effect due solely to a change in the fluid density from adiabatic heating effects. Since the adiabatic effects came into play only in response to a changing temperature, we can verify this relationship by comparing the adiabatic response in figure 17 to figure 18, which is the derivative of the sample-cell temperature measured during the temperature change: They have exactly the same shape. Note that the temperature is measured at the cell wall, approximately 1.5 cm from the region of fluid probed by the laser, confirming the long-range action of the adiabatic effect.

All of the mysteries of the flight turbidity data have not been settled. Figure 19 shows the transient response of the turbidity signal when the sample-cell temperature was changed by 70 mK (starting from $T_c+0.1$ K). The adiabatic contribution that we have measured on Earth is evident here in the initial sudden decrease in the signal as the temperature change began. However, this was soon overwhelmed by a much larger change in the opposite direction, followed by a slower settling to the final value. We know that this response is apparent because gravity has been removed: We had never seen it in data taken during ground testing. We believe that it is related to later stages in an adiabatic response that is quenched by convection in 1 g, but we have not yet completed the modeling of the behavior.

5.6. CRITICAL-POINT FLUCTUATION DECAY RATES

During the mission we collected 32 sets of correlograms at 23 different temperature set-points, covering a temperature range from 560 mK to 10 μ K above the critical temperature, as well as three temperatures below critical. In all, there are 500 correlograms for each of the two scattering angles (in the fluid) of 10.4478° (forward scattering) and 169.5636° (backscattering); forward-scattering and backscattering correlograms were collected simultaneously. The data were taken with two different incident-beam intensities: 17 and 1.7 μ W.

The next several figures show representative correlograms, illustrating the range of temperatures and incident-beam intensities. Figure 20 shows a pair of correlograms taken 560 mK from T_c , the furthest from the critical temperature at which we made measurements. As in all the correlograms, the upper curve with the slower decay is the forward-scattering correlogram. At this temperature the intensity of the scattered light was at its lowest, although we were using the higher power beam path. The decays of the two curves, particularly the backscattering curve, are barely discernible, although the measurements are statistically meaningful.

Figure 21 shows a pair of correlograms taken 1 mK above the critical temperature, using the higher-intensity beam path. At this temperature the critical fluctuations were well developed, the intensity of the scattered light was relatively high in both directions, and the correlograms appeared virtually noiseless. However, a new feature is evident here in the backscattering correlogram: It shows two decays.

The second decay, which has the same time scale as the forward scattering correlogram, is actually forward scattered light.

The forward-scattering cross section had become large enough, 100 times the backscattering cross section, that the small amount of light reflected in the backward direction at the exit window of the sample cell contributed a forward-scattering correlation to this signal. It was for this reason that the two scattering angles were chosen to be precise supplements: Results from the analysis of the forward-scattering correlograms could be used to remove this contribution from the backscattering correlograms.

For comparison, figure 22 shows a pair of correlograms at the same temperature as in figure 21, but at the lower beam-intensity of $1.7 \mu\text{W}$. The backscattering correlogram shows an increased amount of noise (due to the statistical process of the light detection), but the decay rate obtained from it is still precisely determined. Finally, figure 23 shows correlograms collected at $T_c+100 \mu\text{K}$. These measurements are well inside a region in which, on Earth, the observation of fluctuation correlations is completely distorted by gravity.

The data sets were collected for a total amount of time which we had predicted would result in fluctuation decay-rate measurements with a precision of 1 percent or better. We achieved this precision with all of the measurements except for the backscattering measurement at the warmest temperature, where the extremely low intensity of the scattered light precluded it. Each data set was made up of 10–15 separate correlograms so that we could examine our results statistically.

The decay rate values were extracted from the correlograms by nonlinear, least-squares fitting. The forward-scattering correlograms were fit to a simple decaying exponential; for the backscattering correlograms the forward-scattering contribution was first removed where necessary, and then a simple decaying exponential was used.

The results of the fluctuation decay-rate measurements are shown in figure 24, the backscattering decay rates, and figure 25, the forward-scattering decay rates. In both figures we have included data from ground testing on the instrument (in both cases the upper curve of symbols), as well as a line representing the best available theoretical predictions.

Quite evident in these graphs is the effect of removing gravity and the distortions it creates in the density of the sample, already apparent as far as 30 mK from the critical temperature. The limiting values of these curves is a significant measurement, and it is clear from these graphs that it is not possible to make accurate measurements of the limits on Earth, whereas we have been able to penetrate well into the limiting region without the distortions due to gravity. As measurements were made closer yet to T_c , the density gradient in the Earth-bound sample as probed by the $100\text{-}\mu\text{m}$ diameter of our focused laser beam led to errors of 100 percent, doubling the apparent decay rate in the terrestrial measurements compared with the measurements in μg .

We believe that the limiting values of the fluctuation decay rates from our data set will be the key contributions from this flight of the Zeno instrument. It is true that some questions remain about the homogeneity and precise density of the xenon at each temperature, questions raised by the drifts in the turbidity signal. Nevertheless, we have made measurements so close to the critical temperature that we have been able to make accurate measurements of the limiting values of the decay rate, accurate regardless of the possibly small variations in density. These limits are beyond the predictive capabilities of current theories and represent a challenge and target for future calculations of transport properties in near-critical systems.

To conclude, we present our results for the limits. From the backscattering, the limiting decay rate is $\Gamma = (51.2 \pm 0.4) \times 10^3$ rad/s at a scattering angle in the fluid of 169.5636° . From the forward scattering, the limiting decay rate is $\Gamma = 36.8 \pm 0.3$ rad/second at a scattering angle inside the fluid of 10.4478° .

5.7. CONCLUSION

The Zeno instrument and the special flight opportunity of the USMP-2 mission, with its exceptional commitment of mission time to making fundamental scientific measurements, have given us an excellent data set to contribute to measurements on liquid-vapor critical points. The data are beautiful and precise. The outstanding performance of the Zeno instrument during the mission gave a fine demonstration of the possibility of making high-precision, materials measurements in low-gravity, as well as the power of a flexible, ground-commanded experiment.

5.8. SELECTED BIBLIOGRAPHY

Zeno Publications

1. Kopelman, R.B., "Light Scattering Measurements of Critical Fluctuations in an Optically Thin Binary Liquid Sample," Ph.D. Dissertation, University of Maryland, College Park, MD, 1983 (University Microfilms, Ann Arbor, #AAD84-05662).
2. Moldover, M.R., and R.W. Gammon, "Capillary Rise, Wetting Layers, and Critical Phenomena in Confined Geometry," *J. Chem. Phys.*, *80*, 528–535, 1984.
3. Kopelman, R.K., R.W. Gammon, and M.R. Moldover, "Turbidity Very Near the Critical Point of Methanol-Cyclohexane Mixtures," *Phys. Rev.*, *A29*, 2084, 1984.
4. Takagi, Y., and R.W. Gammon, "Brillouin-Scattering in Thin Samples: Observation of Backscattering Components by 90° Scattering," *J. Appl. Phys.*, *61*, 2030–2034, 1987.
5. Gammon, R.W., "Critical Fluid Light Scattering," in *The Nation's Future Material Needs*, T. Lynch, J. Persh, T. Wolf, and N. Rupert, eds., Soc. Adv. Mater. & Process Eng., Covina, CA, 1987, Proceedings of the 19th International Technical Conference of the Society for the Advancement of Material and Process Engineering (SAMPE), Oct. 13–15, 1987.
6. Gammon, R.W., and J.N. Shaumeyer, "Science Requirements Document for Zeno," NASA, Washington, DC, 1988.
7. Shaumeyer, J.N., and R.W. Gammon, "Optimizing Fitting Statistics in Photon Correlation Spectroscopy," in *OSA Proceedings on Photon Correlation Techniques and Applications, Volume I*, J.B. Abbiss and A.E. Smart, eds., Optical Society of America, Washington, DC, pp. 14–17, 1988.
8. Gammon, R.W., "Description of the Photon-Correlation Instrument for Zeno," NASA Laser Light Scattering Advanced Technology Development Workshop, NASA Lewis Research Center, September 1988, NASA Conference Publication 10033, 1989.
9. Boukari, H., J.N. Shaumeyer, M.E. Briggs, and R.W. Gammon, "Critical Speeding Up in Pure Fluids," *Phys. Rev.*, *A41*, 2260–2263, 1990.
10. Boukari, H., M.E. Briggs, J.N. Shaumeyer, and R.W. Gammon, "Critical Speeding Up Observed," *Phys. Rev. Lett.*, *65*, 2654–2657, 1990.
11. Gammon, R.W., "Investigations of Fundamental Phenomena in Microgravity," Proceedings IKI/AIAA Microgravity Symposium, American Institute of Aeronautics and Astronautics, pp. 379–381, 1991.
12. Shaumeyer, J.N., R.W. Gammon, and J.V. Sengers, "Photon-Correlation Spectroscopy," in *Measurement of the Transport Properties of Fluids, Experimental Thermodynamics, Volume III*, W.A. Wakeham, A. Nagashima, and J.V. Sengers, eds., Blackwell Scientific, Oxford, pp. 197–213, 1991.

13. Boukari, H., "Adiabatic Effects in a Fluid Near its Liquid-Gas Critical Point: Theory and Experiment," Ph.D. Dissertation, University of Maryland, College Park, MD, 1992.
14. Zhang, K.C., M.E. Briggs, and R.W. Gammon, "The Susceptibility Critical Exponent for a Nonaqueous Ionic Binary Mixture Near a Consolute Point," *J. Chem. Phys.*, *97*, 8692–8697, 1992.
15. Briggs, M.E., "Photothermal Deflection in a Supercritical Fluid," Ph.D. Dissertation, University of Maryland, College Park, MD, 1993.
16. Briggs, M.E., R.W. Gammon, and J.N. Shaumeyer, "Measurement of the Temperature Coefficient of Ratio Transformers," *Rev. Sci. Instrum.*, *64*, 756–759, 1993.
17. Avramov, S., and N.M. Oldham, "Automatic Calibration of Inductive Voltage Dividers for the NASA Zeno Experiment," *Rev. Sci. Instrum.*, *64*, 2676–2678, 1993.
18. Avramov, S., and N.M. Oldham, "Inductive Voltage Divider Calibration for a NASA Flight Experiment," Proceedings of National Conference of Standards Laboratories Workshop and Symposium, Albuquerque, NM, July 1993, pp. 225–232, July 1993.
19. Shaumeyer, J.N., M.E. Briggs, and R.W. Gammon, "Statistical Fitting Accuracy in Photon Correlation Spectroscopy," *Appl. Optics*, *32*, 3871–3879 (1993).
20. Avramov, S., "Voltage Ratio Measurements Using Inductive Voltage Dividers," Ph.D. Dissertation, University of Maryland, College Park, MD, 1994.
21. Palik, E.D., H. Boukari, and R.W. Gammon, "Line-Shape Studies for Single- and Triple-Pass Fabry-Perot Interferometer Systems," *Appl. Optics*, *34*, 58–68, 1995.
22. Boukari, H., E.D. Palik, and R.W. Gammon, "Closed-Form Expressions to Fit Data Obtained with a Multipass Fabry-Perot Interferometer System," *Appl. Optics*, *34*, 69–86, 1995.
23. Boukari, H., R.L. Pego, and R.W. Gammon, "Calculation of the Dynamics of Gravity-Induced Density Profiles Near a Liquid-Vapor Critical Point," *Phys. Rev. E*, in press 1995.

NASA Reports

1. Gammon, R.W., and M.R. Moldover, "Light Scattering Tests of Fundamental Theories of Transport Properties," in *Microgravity Science and Applications Program Tasks*, NASA TM 89607, NASA Office of Space Science and Applications, Washington, DC, p. 240, February 1985.
2. Gammon, R.W., and M.R. Moldover, "Light Scattering Tests of Fundamental Theories of Transport Properties," in *Microgravity Science and Applications Program Tasks*, NASA TM 87568, NASA Office of Space Science and Applications, Washington, DC, p. 106, May 1986.
3. Gammon, R.W., "Critical Fluid Light Scattering," in *Microgravity Science and Applications Flight Programs, January–March 1987, Selected Papers*, NASA TM 4069, Vol. 2, NASA Office of Space Science and Applications, Washington, DC, p. 805, 1988.

4. Gammon, R.W., J.N. Shaumeyer, and M.R. Moldover, "Zeno: Critical Fluid Light Scattering," in *Microgravity Science and Applications Program Tasks: 1987 Revision*, NASA TM 4068, NASA Office of Space Science and Applications, Washington, DC, p. 189, September 1988.
5. Gammon, R.W., J.N. Shaumeyer, and M.R. Moldover, "Zeno: Critical Fluid Light Scattering," in *Microgravity Science and Applications Program Tasks: 1988 Revision*, NASA TM 4097, NASA Office of Space Science and Applications, Washington, DC, p. 245, January 1989.
6. Gammon, R.W., and J.N. Shaumeyer, "Critical Fluid Light Scattering (Zeno)," in *Microgravity Science and Applications Program Tasks: 1989 Revision*, NASA TM 4191, NASA Office of Space Science and Applications, Washington, DC, p. 201, May 1990.
7. Gammon, R.W., and J.N. Shaumeyer, "Critical Fluid Light Scattering (Zeno)," in *Microgravity Science and Applications Program Tasks: 1990 Revision*, NASA TM 4284, NASA Office of Space Science and Applications, Washington, DC, p. 261, May 1991.
8. Gammon, R.W., and J.N. Shaumeyer, "Critical Fluid Light Scattering (Zeno)," in *Microgravity Science and Applications Program Tasks: 1991 Revision*, NASA TM 4349, NASA Office of Space Science and Applications, Washington, DC, p. 261, February 1992.
9. Gammon, R.W., "Critical Fluid Light Scattering (Zeno)," in *Microgravity Science and Applications Program Tasks and Bibliography for FY 1992*, NASA TM 4469, NASA Office of Space Science and Applications, Washington, DC, p. II-69, March 1993.

Critical Phenomena

Static Critical Phenomena

1. Einstein, A., *Ann. Phys. (Leipzig)*, 33, 1275 (1910); English translation: "Theory of Opalescence of Homogeneous Liquids and Mixtures of Liquids in the Vicinity of the Critical State," in *Colloid Chemistry*, J. Alexander, ed., Rheinhold, New York, vol. I, p. 323, 1913.
2. Stanley, H.E., *Introduction to Phase Transitions and Critical Phenomena*, Oxford, New York, 1971.
3. Wilson, K.G., and J. Kogut, "The Renormalization Group and the ϵ Expansion," *Phys. Rep.*, 12C, 77, 1974.

Dynamic Critical Phenomena

1. Swinney, H.L., and D.L. Henry, "Dynamics of Fluids Near the Critical Point: Decay Rate of Order-Parameter Fluctuations," *Phys. Rev.*, A8, 2586, 1973.
2. Kawasaki, K., in *Phase Transitions and Critical Phenomena*, C. Domb and M.S. Green, eds., Academic, New York, vol. 5a, p. 165, 1975.
3. Siggia, E.D., B.I. Halperin, and P.C. Hohenberg, "Renormalization-Group Treatment of the Critical Dynamics of the Binary-Fluid and Gas-Liquid Transitions," *Phys. Rev.*, B13, 2110, 1976.

4. Güttinger, H., and D.S. Cannell, "Correlation Range and Rayleigh Linewidth of Xenon Near the Critical Point," *Phys. Rev.*, A22, 285, 1980.
5. Sengers, J.V. "Universality of Critical Phenomena in Classical Fluids," in *Phase Transitions: Cargese 1980*, M. Levy, J.-C. LeGuillou, and J. Zinn-Justin, eds., Plenum Publishing Corp., New York, 1982.
6. Bhattacharjee, J.K, and R.A. Ferrell, "Critical Viscosity Exponent for a Classical Fluid," *Phys. Rev.*, A28, 2363. 1983.
7. Burstyn, H.C., J.V. Sengers, J.K. Bhattacharjee, and R.A. Ferrell, "Dynamic Scaling Function for Critical Fluctuations in Classical Fluids," *Phys. Rev.*, A28, 1567, 1983.
8. Berg, R.F., and M.R. Moldover, "Critical Exponent for the Viscosity of Carbon-Dioxide and Xenon," *J. Chem. Phys.*, 93, 1926, 1990.
9. Hao, H., "Aspects of Dynamic Critical Phenomena in a Single-Component Fluid," Ph.D. Dissertation, University of Maryland, College Park, Maryland, 1991.

Critical-Fluid Light Scattering

1. Puglielli, V.G., and N.C. Ford, Jr., "Turbidity Measurements in SF₆ Near its Critical Point," *Phys. Rev. Lett.*, 25, 143, 1970.
2. Degiorgio, V., and J.B. Lastovka, "Intensity-Correlation Spectroscopy," *Phys. Rev.*, A4, 2033, 1971.
3. Lunacek, J.H., and D.S. Cannell, "Long-Range Correlation Length and Isothermal Compressibility of Carbon Dioxide Near the Critical Point," *Phys. Rev. Lett.*, 27, 841, 1971.
4. Ford, Jr., N.C., "Light Scattering Apparatus," in *Dynamical Light Scattering, Application of Photon Correlation Spectroscopy*, R. Pecora, ed., p. 7, Plenum, New York, 1985.

Low-Gravity Critical Phenomena

1. Hohenberg, P.C., and M. Barmatz, "Gravity Effects Near the Gas-Liquid Critical Point," *Phys. Rev.*, A6, 289, 1977.
2. Moldover, M.R., R.J. Hocken, R.W. Gammon, and J.V. Sengers, *Overviews and Justifications for Low Gravity Experiments on Phase Transitions and Critical Phenomena in Fluids*, National Bureau of Standards Technical Note 925, U.S. Government Printing Office, Washington, DC, 1976.
3. Moldover, M.R., J.V. Sengers, R.W. Gammon, and R.J. Hocken, "Gravity Effects in Fluids Near the Gas-Liquid Critical Point," *Rev. Mod. Phys.*, 51, 79, 1979.
4. Beysens, D., "Critical Phenomena," in *Materials Sciences in Space, A Contribution to the Scientific Basis of Space Processing*, B. Feuerbacher, H. Hamacher, and R.J. Naumann, eds., p. 91, Springer, Berlin, 1986.

5. Beysens, D., J. Straub, and D.J. Turner, "Phase Transitions and Near-Critical Phenomena," in *Fluid Sciences and Materials Science in Space, A European Perspective*, H.U. Walter, ed., p. 221, Springer, Berlin, 1987.
6. Beysens, D., "Recent Developments in Critical and Near-Critical Point Phenomena," in *Proceedings VIIth European Symposium on Materials and Fluid Sciences in Micro-gravity*, ESA SP-295, 1990.
7. Guenoun, P., B. Khalil, D. Beysens, Y. Garrabos, F. Kammoun, B. Le Neindre, and B. Zappoli, "Thermal Cycle Around the Critical-Point of Carbon-Dioxide Under Reduced Gravity," *Phys. Rev.*, *E47*, 1531, 1993.

Adiabatic Effects Near the Critical Point

1. Dahl, D., and M.R. Moldover, "Thermal Relaxation Near the Critical Point," *Phys. Rev.*, *A6*, 1915, 1972.
2. Onuki, A., H. Hong, and R.A. Ferrell, "Fast Equilibration in a Single-Component Fluid Near the Liquid-Vapor Critical Point," *Phys. Rev.*, *A41*, 2256, 1990.
3. Onuki, A., and R.A. Ferrell, "Adiabatic Heating Effect Near the Gas-Liquid Critical Point," *Physica*, *A164*, 245, 1990.
4. Behringer, R.P., A. Onuki, and H. Meyer, "Thermal Equilibration of Fluids Near the Liquid-Vapor Critical-Point—³He and ⁴He Mixtures," *J. Low Temp. Phys.*, *81*, 71, 1990.
5. Zappoli, B., D. Baily, Y. Garrabos, B. Le Neindre, P. Guenoun, and D. Beysens, "Anomalous Heat Transport by the Piston Effect in Supercritical Fluids Under Zero Gravity," *Phys. Rev.*, *A41*, 2264, 1991.
6. Ferrell, R.A., and H. Hao, "Adiabatic Temperature Changes in a One-Component Fluid Near the Liquid-Vapor Critical Point," *Physica*, *A197*, 23, 1993.
7. Berg, R.F., "Thermal Equilibration Near the Critical Point: Effects Due to Three Dimensions and Gravity," *Phys. Rev.*, *E48*, 1799, 1993.
8. Zhong, F., and H. Meyer, "Numerical Calculation of Density Equilibration Above the ³He Liquid-Vapor Critical Point," in *Proceedings of NASA/JPL Microgravity Low Temperature Workshop, Washington, DC (1994)*, U. Israelson and D. Strayer, eds., NASA Document JPL D-11775, p. 73, NASA, Washington DC, 1994.

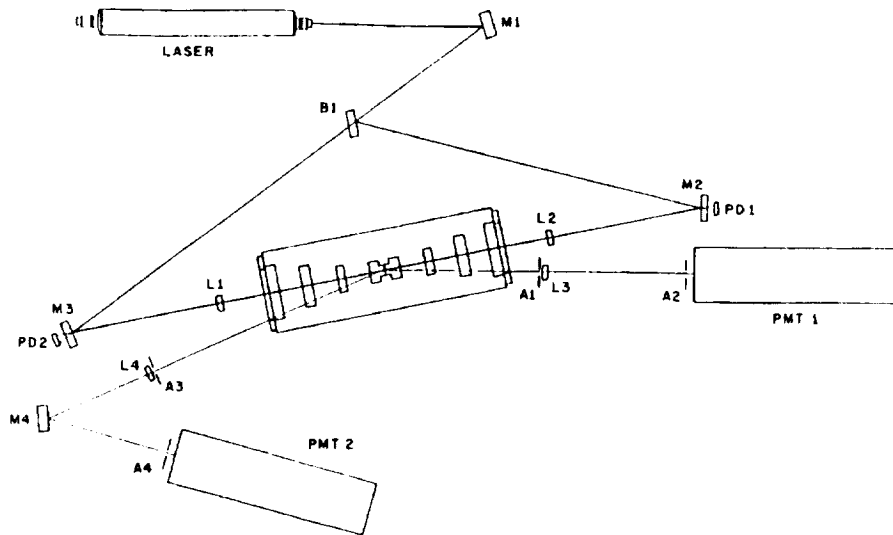


Figure 5-1. A schematic of the optical layout of the instrument, showing its main components: Beamsplitter (B1), mirrors (M1, M2, and M3), apertures (A1–A4), photodiodes (PD1 and PD2), and photomultiplier tubes (PMT1 and PMT2). The thermostat is the cylindrical object in the center.

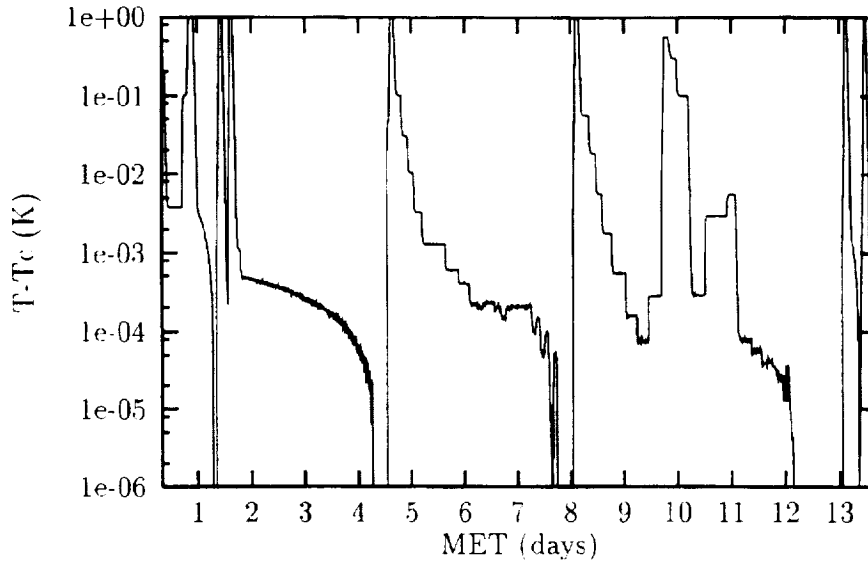


Figure 5-2. The timeline of the experiment, given as the temperature of the sample (measured in distance from T_c) versus MET in days.

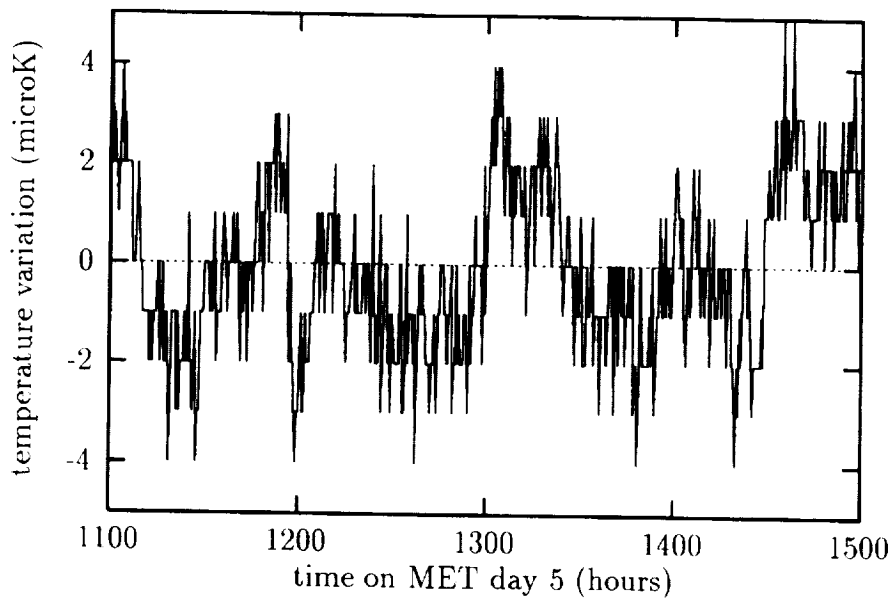


Figure 5-3. The stability of the sample temperature at 1 mK, over a four-hour period while collecting correlograms. The rms of the variations is $1.7 \mu\text{K}$. (Time is in *hhmm* format.)

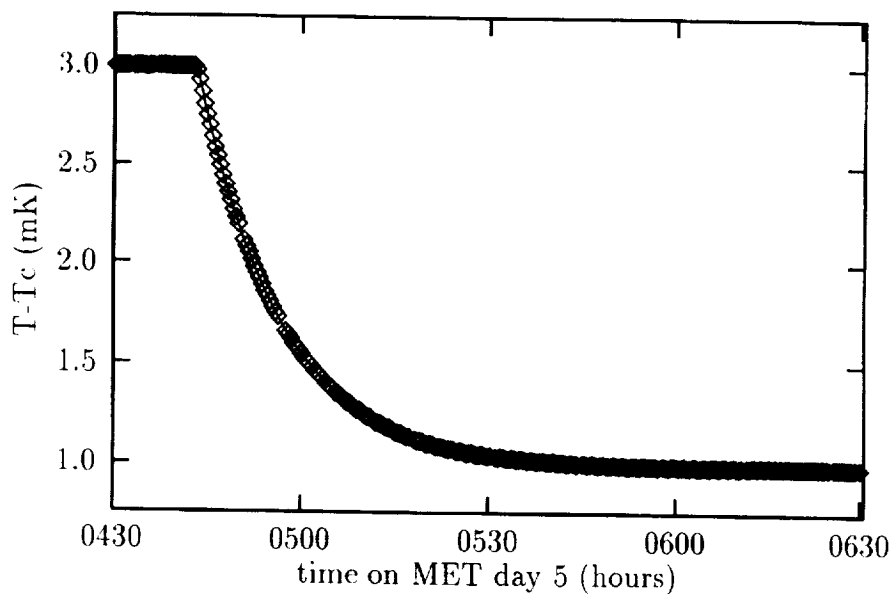


Figure 5-4. The temperature of the sample cell during a slow temperature step of -2 mK , shown as distance from T_c . The time constant for thermal relaxation of the sample cell is about 30 minutes. (Time is in *hhmm* format.)

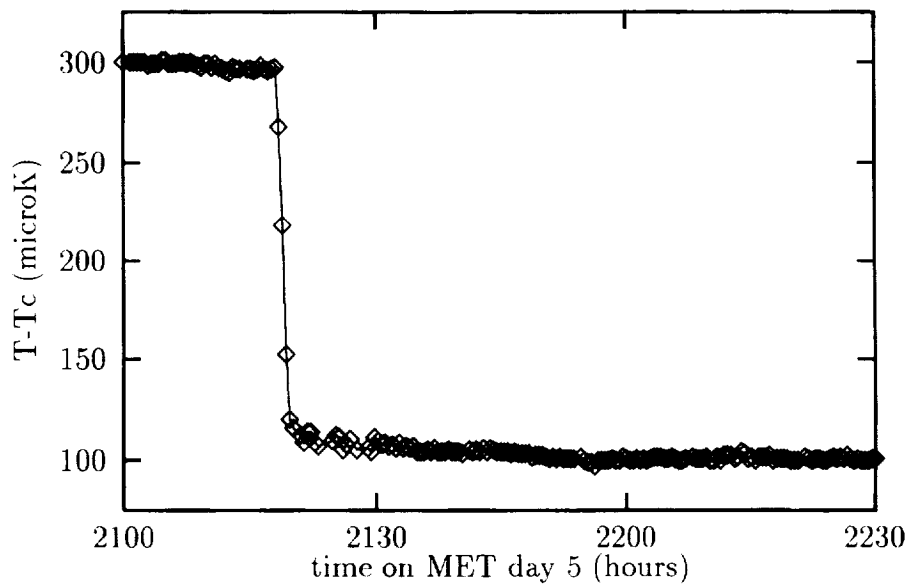


Figure 5-5. The temperature of the sample cell during a fast temperature step of $-200 \mu\text{K}$, shown as distance from T_c . (Time is in *hhmm* format.)

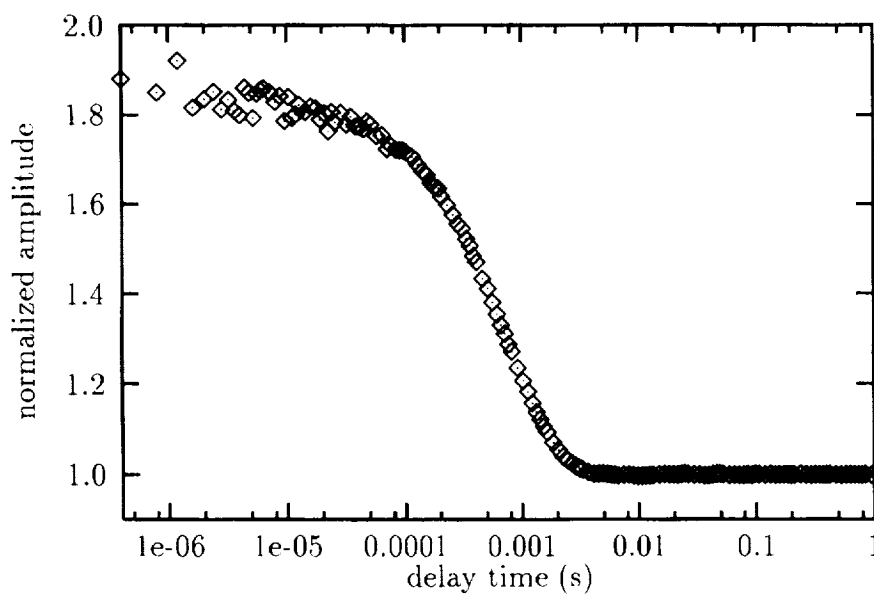


Figure 5-6. A correlogram example showing simple exponential decay on a logarithmic time scale. Taken at $T - T_c = 100 \text{ mK}$ at a laser power of $17 \mu\text{W}$, this is a forward-scattering correlogram.

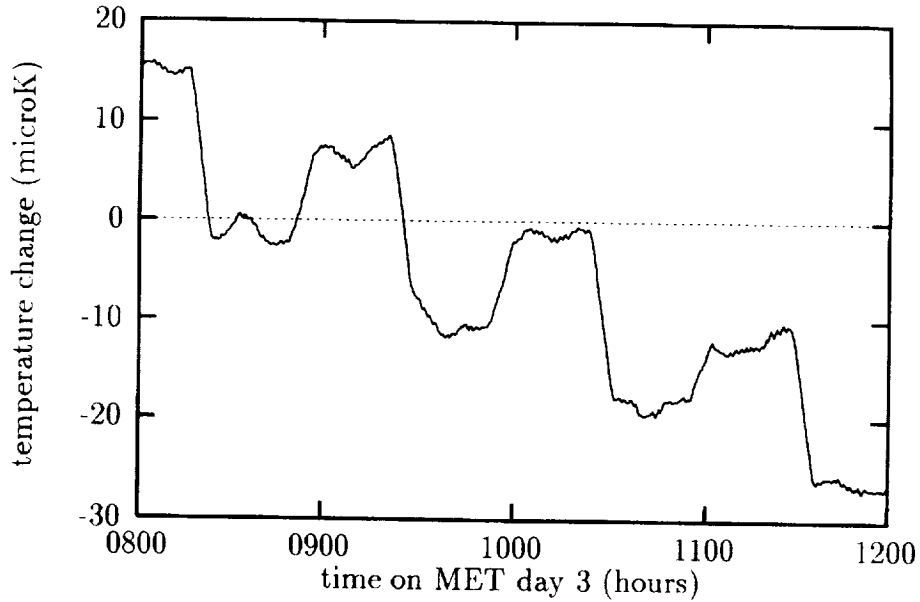


Figure 5-7. A section of the zig-zag T_c search, showing the pattern of sample temperature changes: Cooler by 20 μK , then warmer by 10 μK . The data are smoothed over a 300-second interval. The turbidity during this same time is shown in figure 8. (Time is in *hhmm* format.)

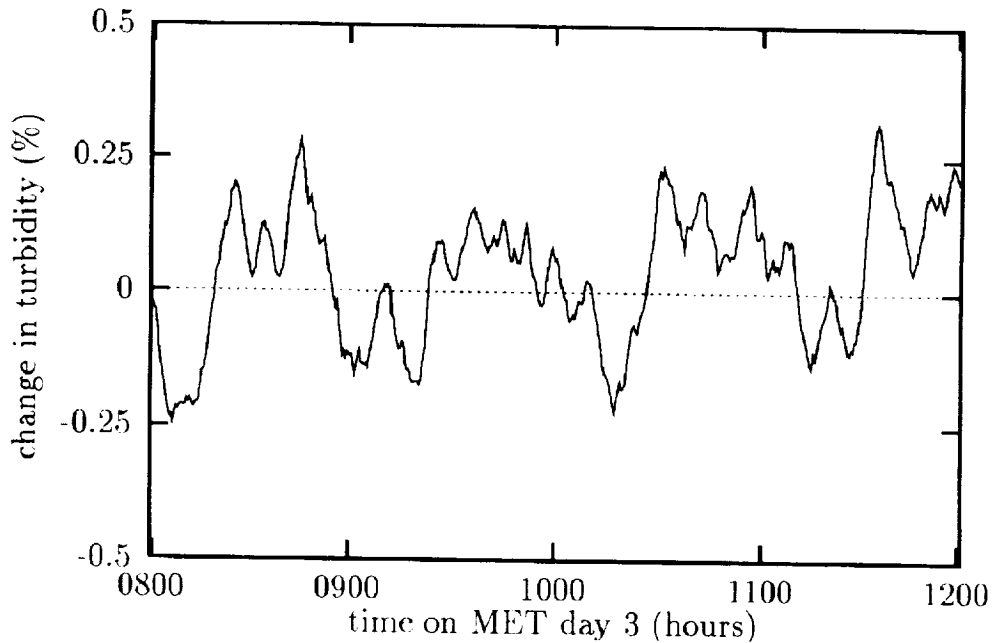


Figure 5-8. A section of the zig-zag T_c search, showing the response of the sample turbidity to the zig-zag temperature steps shown in figure 7 for the same time period. The data are smoothed over a 300-second interval. (Time is in *hhmm* format.)

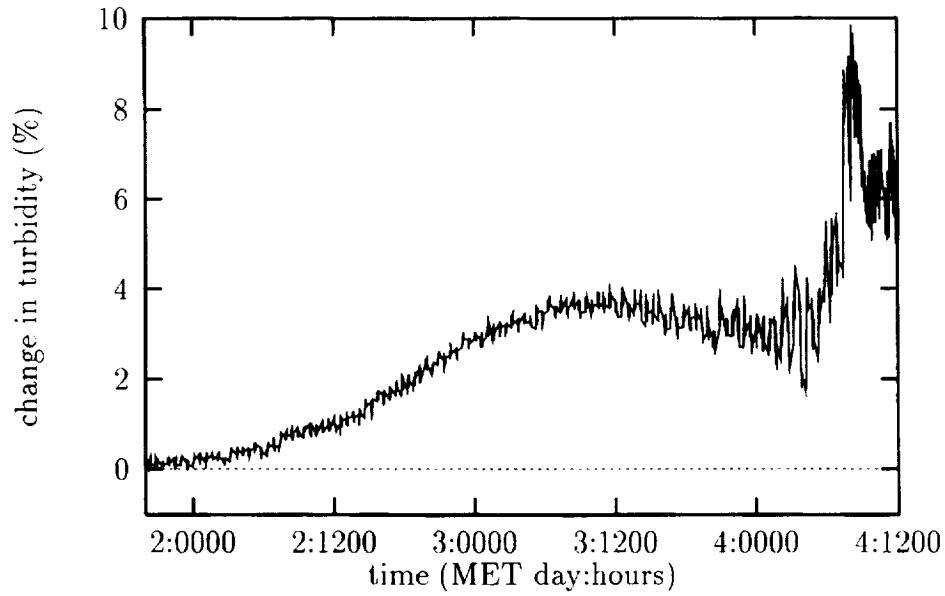


Figure 5-9. The turbidity signal during the entire 64-hour zig-zag T_c search. (Time is in day: *hhmm* format.)

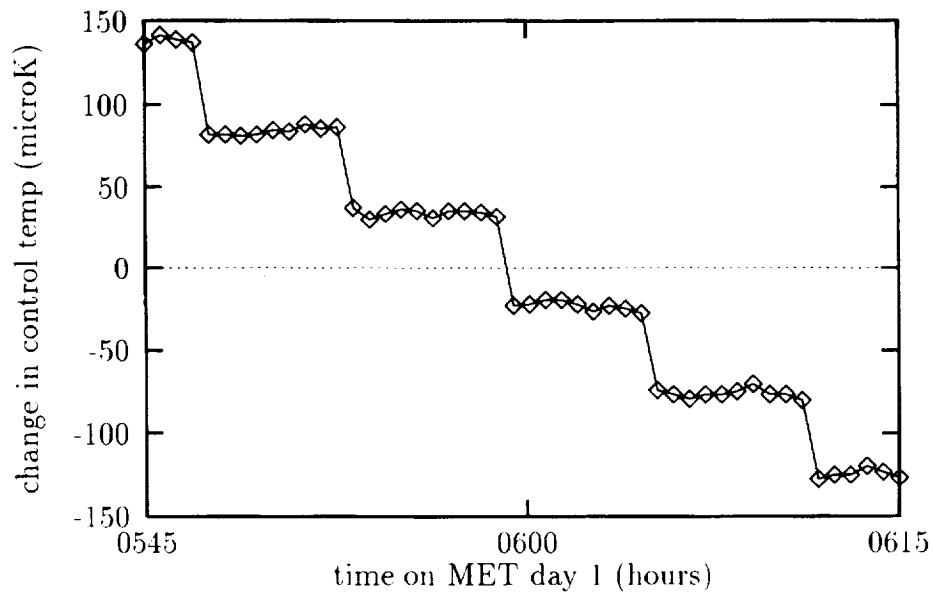


Figure 5-10. The temperature of the high-precision control shell of the thermostat, during the first scan for T_c . The temperature of this shell, shown making $-50 \mu\text{K}$ steps, determines the sample temperature, shown in figure 11. (Time is in *hhmm* format.)

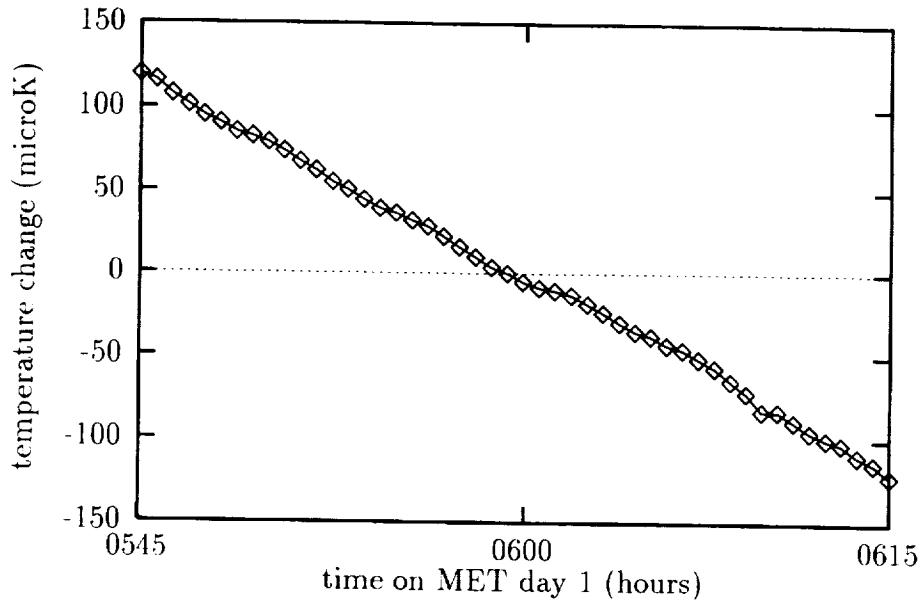


Figure 5-11. The sample temperature during the first scan for T_c , in response to the control-shell steps shown in figure 10. The result is a uniform sample cooling of $500 \mu\text{K}/\text{hour}$. (Time is in *hhmm* format.)

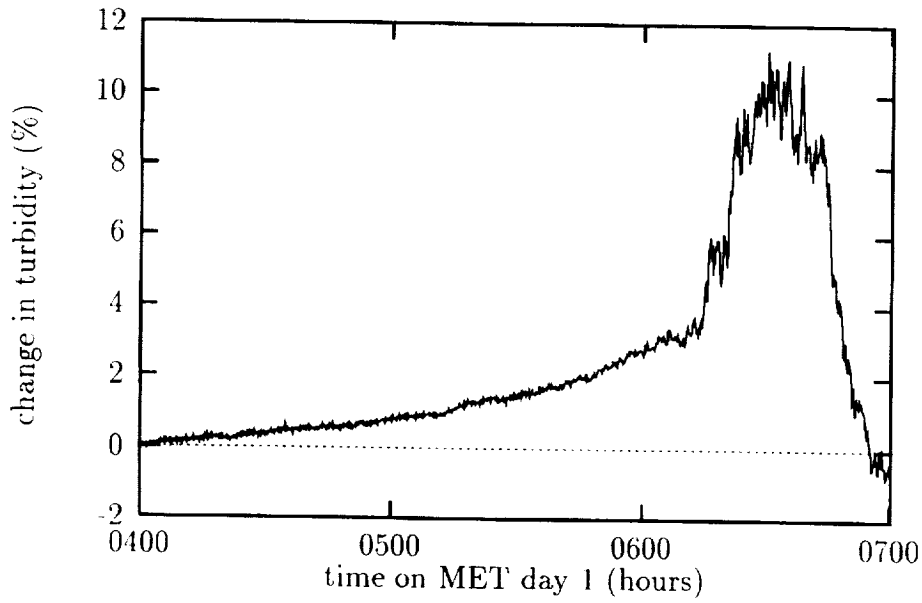


Figure 5-12. The turbidity signal during the first scan for T_c . The small feature just past 0600 hours is where the sample crosses T_c ; the large peak is spinodal decomposition. (Time is in *hhmm* format.)

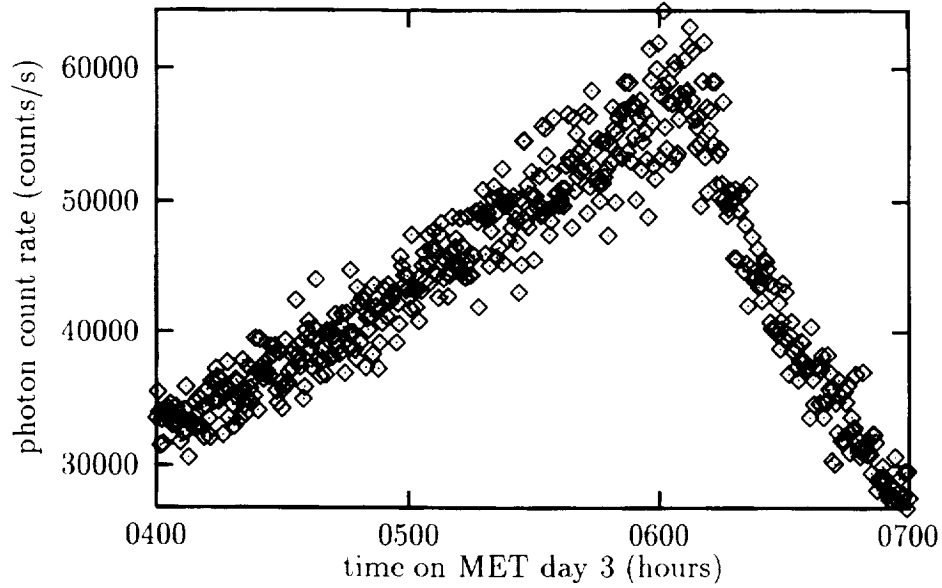


Figure 5-13. Forward-scattering photon count rate during the first scan for T_c , showing from the break in slope that the sample crosses T_c just past 0600 hours. (Time is in *hhmm* format.)

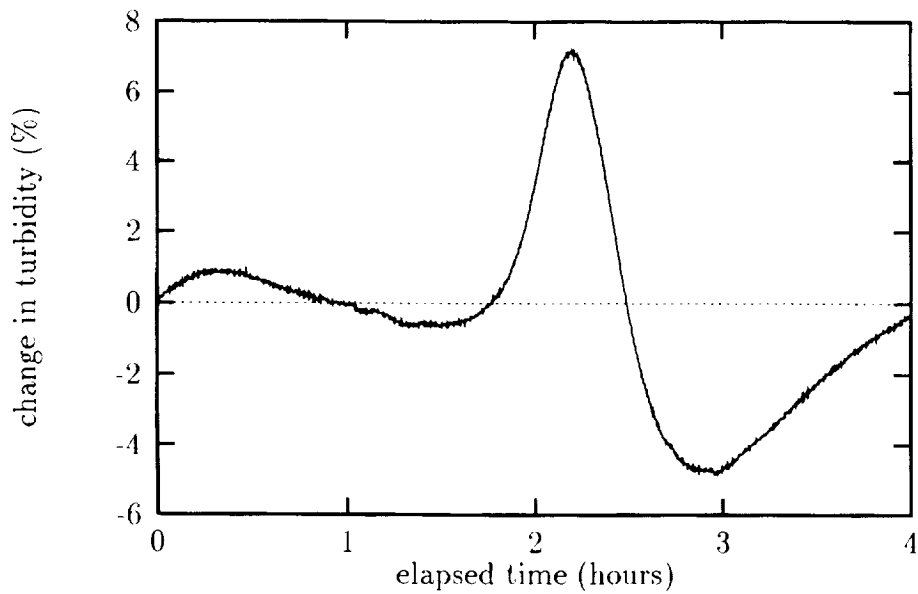


Figure 5-14. The turbidity signal during a $500 \mu\text{K}/\text{hour}$ scan for T_c done in 1-g during preflight testing. Compare this scan with the $\mu\text{-g}$ scan shown in figure 12.

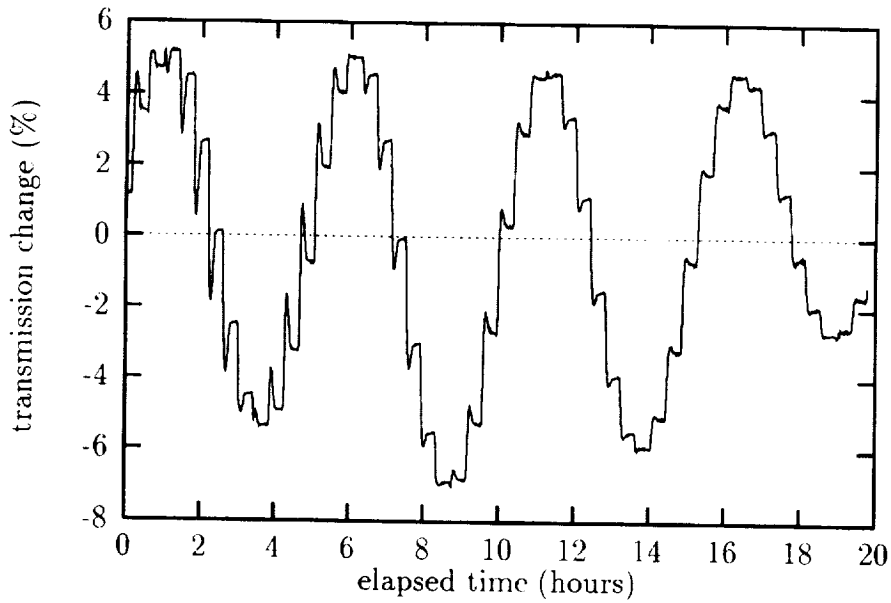


Figure 5-15. The turbidity signal, in preflight testing, during a warming sequence between T_c+1 K to T_c+5 K, made in steps of 0.1 K. The sinusoidal shape is due to cell expansion; the small spikes result from changes in fluid density.

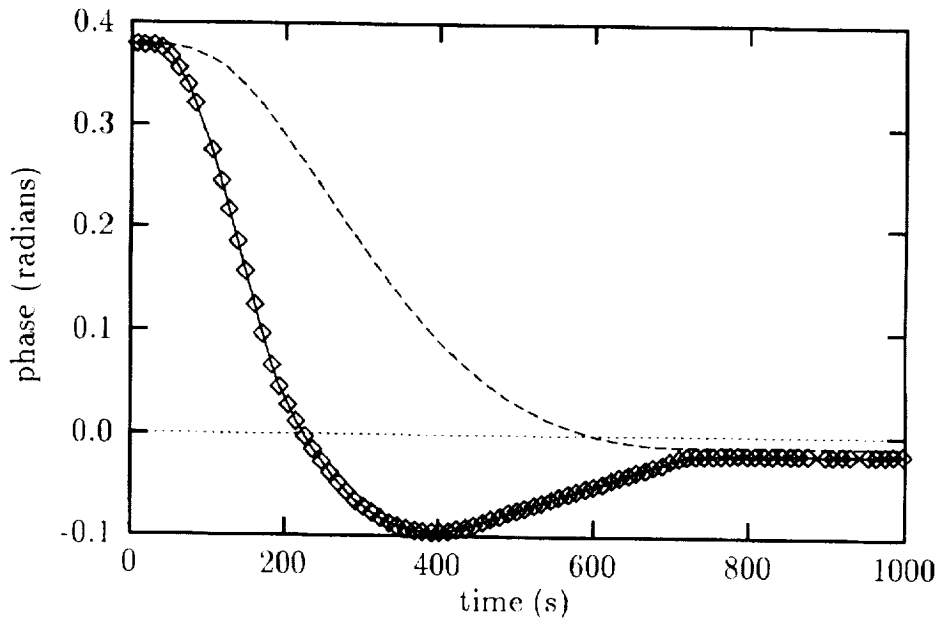


Figure 5-16. Data taken on the engineering model of the instrument show, in the lower curve, the response of the turbidity signal to a change in temperature from $T_c+0.6$ K to $T_c+0.7$ K. The upper curve is the change due solely to cell expansion. The vertical units are the phase along the interference curve for the cell.

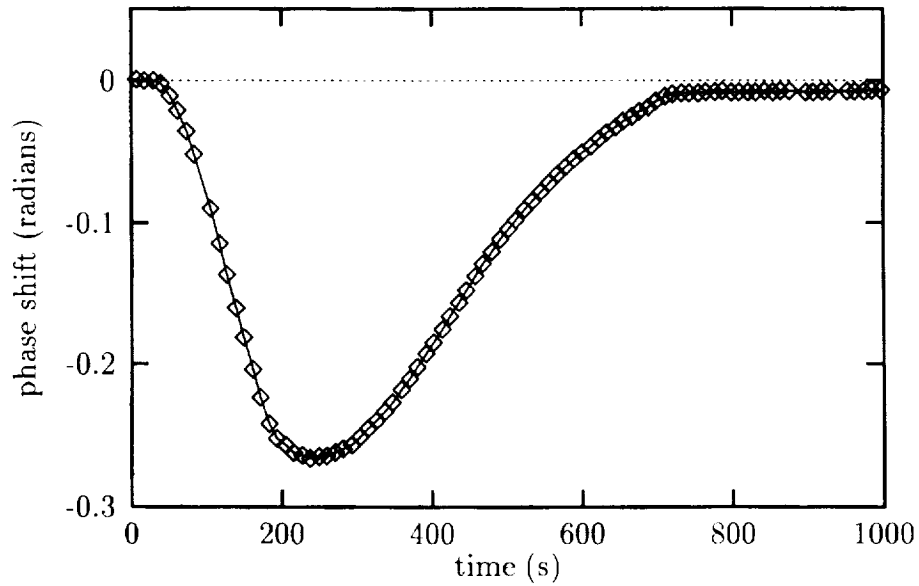


Figure 5-17. The difference between the two curves in figure 16, showing the response of the turbidity signal due solely to changes in the fluid density. Compare with figure 18. (These data are from the engineering model of the instrument.)

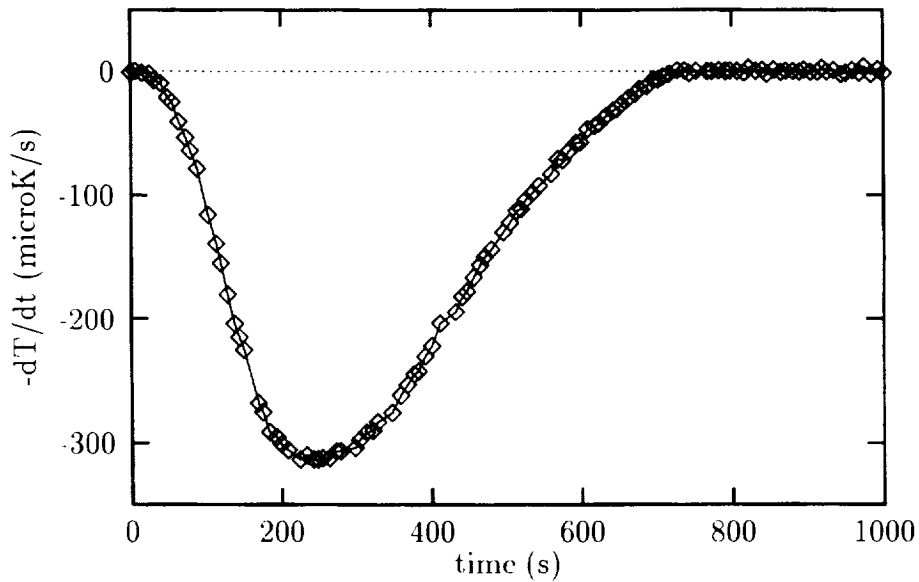


Figure 5-18. The time derivative of the temperature change which produced the turbidity signal shown in figure 16; this curve has the same shape as the curve in figure 17. (These data are from the engineering model of the instrument.)

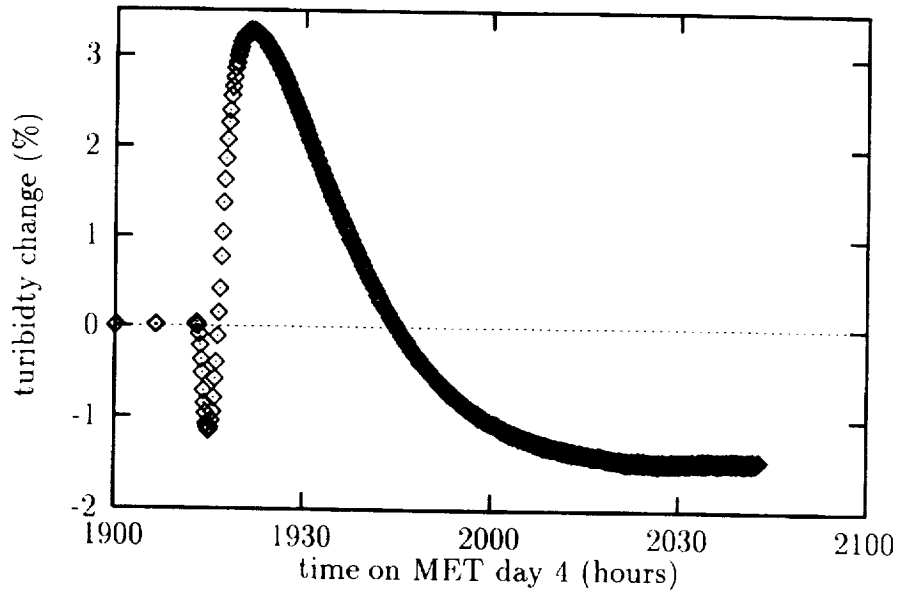


Figure 5-19. The turbidity response to a temperature change of -70 mK, starting at $T_c+0.1$ K, showing cell interference, adiabatic response, and an as-yet unidentified feature.

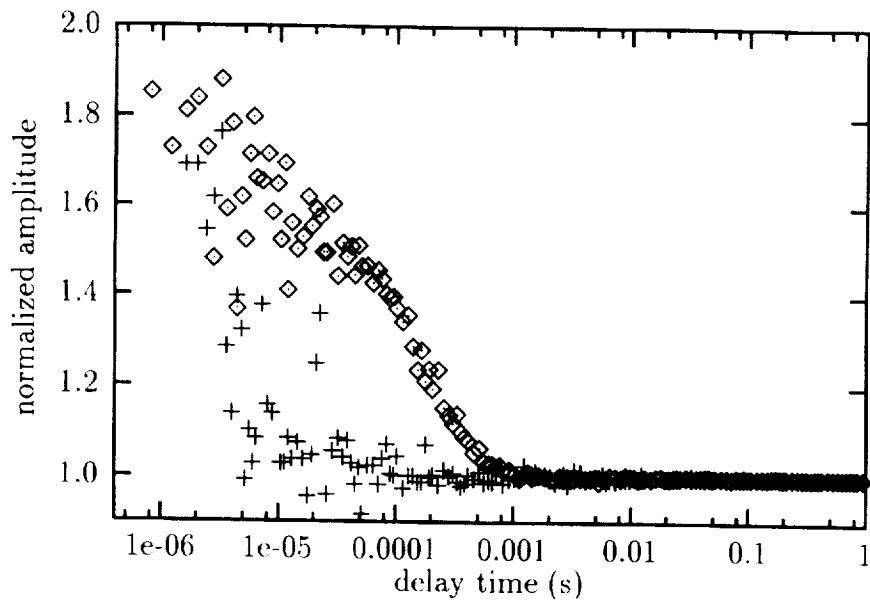


Figure 5-20. Dual correlogram taken at $T_c + 560$ mK with $17 \mu\text{W}$ of laser power; the integration time was 6 minutes. Forward scattering (upper curve) had an average count rate of 710 counts/second; backscattering (lower curve) had 435 counts/second.

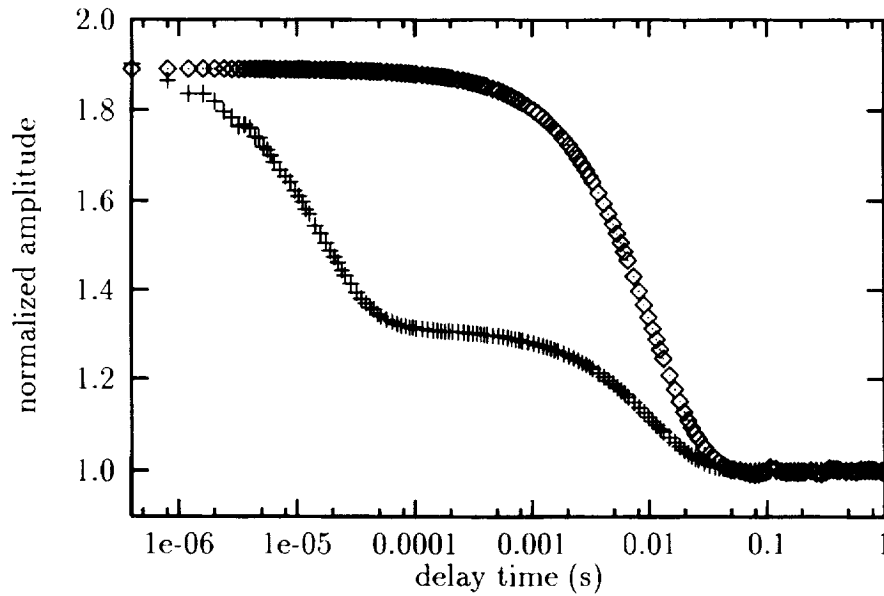


Figure 5-21. Dual correlogram taken at T_c+1 mK with $17 \mu\text{W}$ of laser power; the integration time was 10 minutes. Forward scattering (upper curve) had an average count rate of 446,000 counts/second; backscattering (lower curve) had 17,800 counts/second.

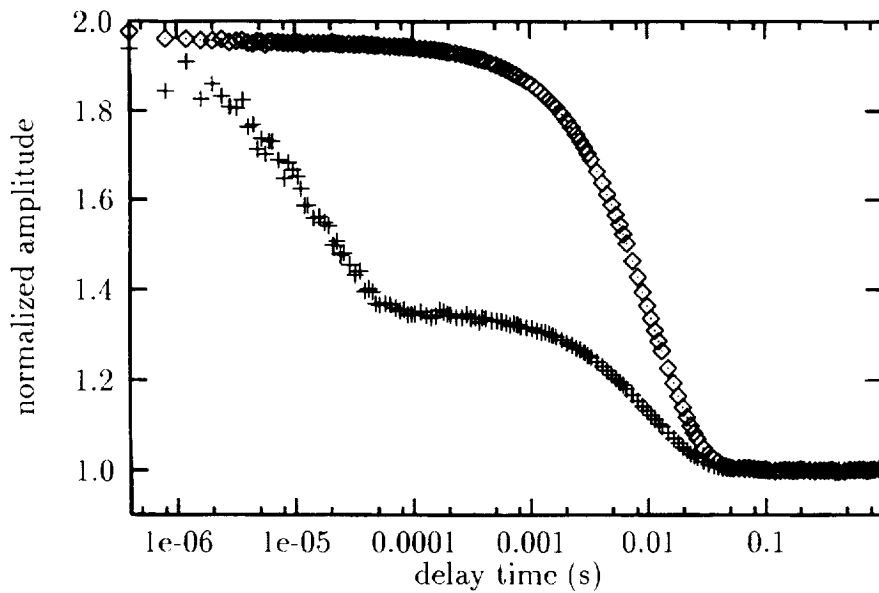


Figure 5-22. Dual correlogram taken at T_c+1 mK with $1.7 \mu\text{W}$ of laser power; the integration time was 15 minutes. Forward scattering (upper curve) had an average count rate of 27,100 counts/second; backscattering (lower curve) had 2,200 counts/second.

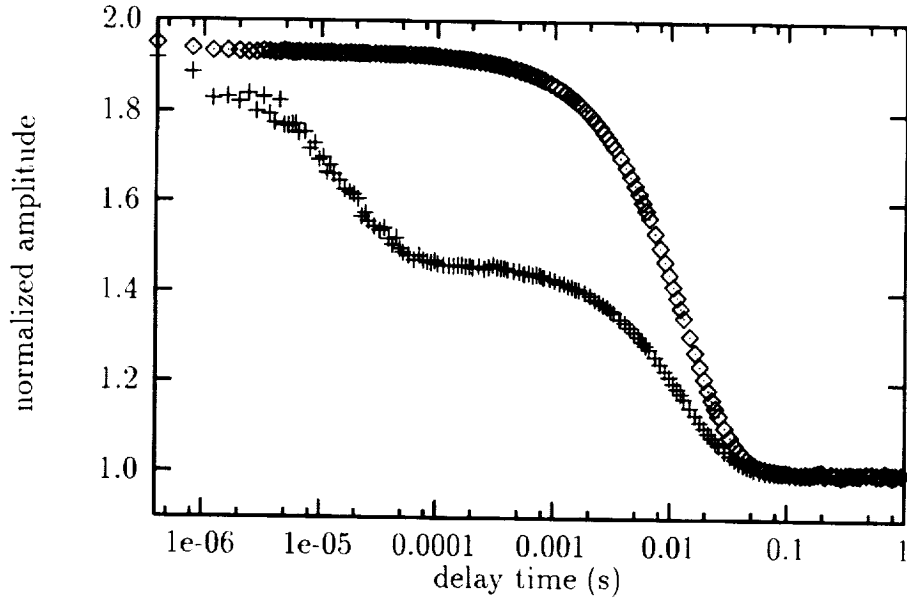


Figure 5-23. Dual correlogram taken at $T_c+100 \mu\text{K}$ with $1.7 \mu\text{W}$ of laser power; the integration time was 15 minutes. Forward scattering (upper curve) had an average count rate of 45,000 counts/second; backscattering (lower curve) had 3,000 counts/second.

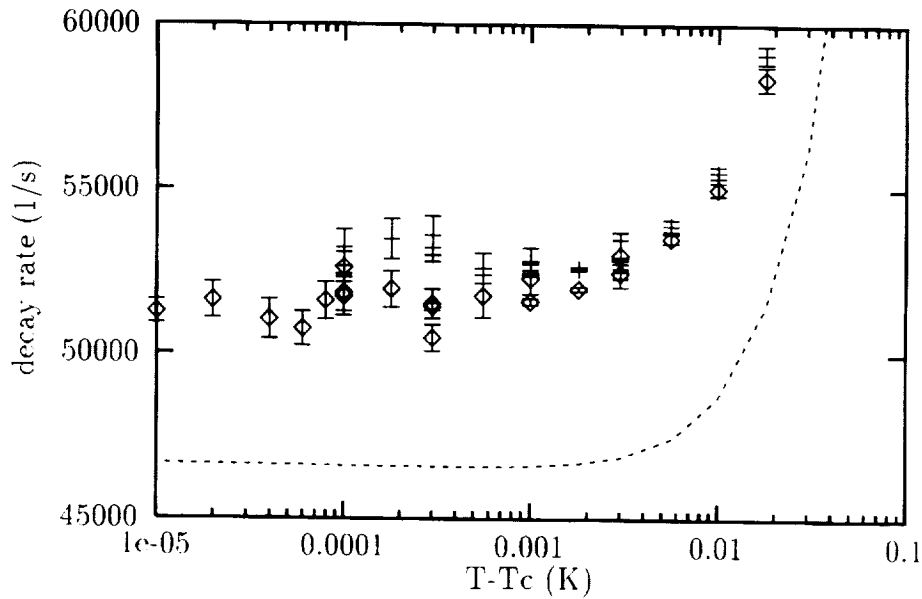


Figure 5-24. Backscattering decay rates as a function of temperature; the vertical scale is linear, the horizontal scale logarithmic. The crosses are 1-g data from preflight testing; the diamonds are the mission data. The curve is our best theoretical estimate. The error bars show the rms of the data.

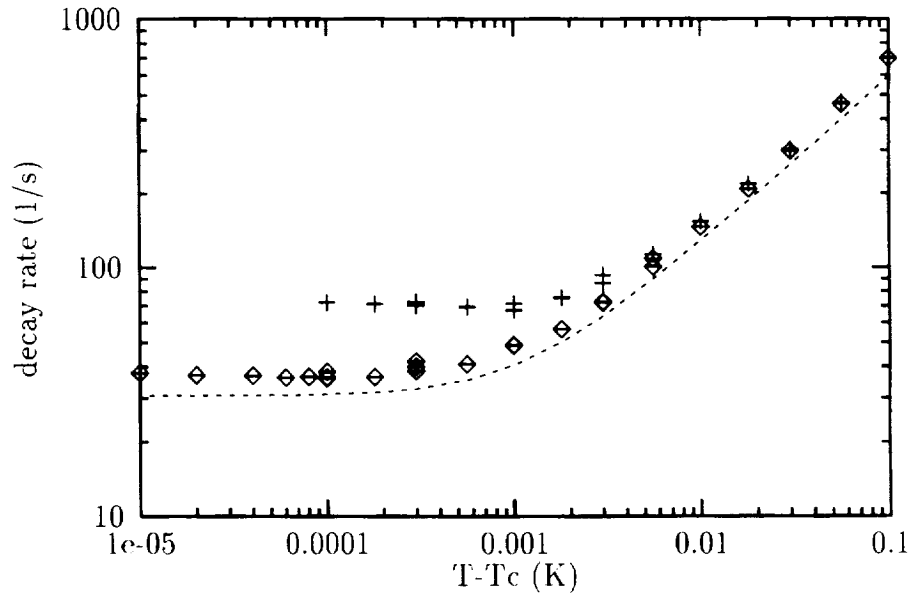


Figure 5-25. Forward-scattering decay rates as a function of temperature; both scales are logarithmic. The crosses are 1-g data from preflight testing; the diamonds are the mission data. The curve is our best theoretical estimate. The error bars, generally smaller than the symbols, show the rms of the data.

REPORT DOCUMENTATION PAGE			Form Approved OMB No. 0704-0188	
Public reporting burden for this collection of information is estimated to average 1 hour per response, including the time for reviewing instructions, searching existing data sources, gathering and maintaining the data needed, and completing and reviewing the collection of information. Send comments regarding this burden estimate or any other aspect of this collection of information, including suggestions for reducing this burden, to Washington Headquarters Services, Directorate for Information Operations and Reports, 1215 Jefferson Davis Highway, Suite 1204, Arlington, Va 22202-4302, and to the Office of Management and Budget, Paperwork Reduction Project (0704-0188), Washington, DC 20503.				
1. AGENCY USE ONLY (Leave Blank)	2. REPORT DATE April 1996	3. REPORT TYPE AND DATES COVERED Technical Memorandum		
4. TITLE AND SUBTITLE Second United States Microgravity Payload: One Year Report			5. FUNDING NUMBERS	
6. AUTHOR(S) Peter A. Curreri and Dannah E. McCauley.* Editors				
7. PERFORMING ORGANIZATION NAME(S) AND ADDRESS(ES) George C. Marshall Space Flight Center Marshall Space Flight Center, Alabama 35812			8. PERFORMING ORGANIZATION REPORT NUMBERS M-806	
9. SPONSORING/MONITORING AGENCY NAME(S) AND ADDRESS(ES) National Aeronautics and Space Administration Washington, DC 20546-0001			10. SPONSORING/MONITORING AGENCY REPORT NUMBER NASA TM-4737	
11. SUPPLEMENTARY NOTES Prepared by Space Sciences Laboratory, Science and Engineering Directorate *University of Alabama in Huntsville				
12a. DISTRIBUTION/AVAILABILITY STATEMENT Unclassified-Unlimited Subject Category 39			12b. DISTRIBUTION CODE	
13. ABSTRACT (Maximum 200 words) The second United States Microgravity Payload (USMP-2), flown in March 1994, carried four major microgravity experiments plus a sophisticated accelerometer system. The USMP program is designed to accommodate experiments requiring extensive resources short of a full Spacelab mission. The four USMP-2 experiments dealt with understanding fundamental aspects of materials behavior, three with the formation of crystals from melts and one with the critical point of a noble gas. This successful, scientifically rich mission also demonstrated telescience operations.				
14. SUBJECT TERMS microgravity, USMP, crystal growth, critical point, metal alloys, Seebeck, Peltier, telescience			15. NUMBER OF PAGES 185	
			16. PRICE CODE A09	
17. SECURITY CLASSIFICATION Unclassified	18. SECURITY CLASSIFICATION OF THIS PAGE Unclassified	19. SECURITY CLASSIFICATION OF ABSTRACT Unclassified	20. LIMITATION OF ABSTRACT Unlimited	